

Wireless Communications and Mobile Computing

Energy Conservation and Harvesting in Wireless Sensor Networks

Lead Guest Editor: Mile Stojcev

Guest Editors: Zoran Stamenkovic and Bojan Dimitrijevic





Energy Conservation and Harvesting in Wireless Sensor Networks

Wireless Communications and Mobile Computing

Energy Conservation and Harvesting in Wireless Sensor Networks

Lead Guest Editor: Mile Stojcev

Guest Editors: Zoran Stamenkovic and Bojan Dimitrijevic



Copyright © 2019 Hindawi. All rights reserved.

This is a special issue published in “Wireless Communications and Mobile Computing.” All articles are open access articles distributed under the Creative Commons Attribution License, which permits unrestricted use, distribution, and reproduction in any medium, provided the original work is properly cited.

Editorial Board

- Javier Aguiar, Spain
Ghufran Ahmed, Pakistan
Wessam Ajib, Canada
Muhammad Alam, China
Eva Antonino-Daviu, Spain
Shlomi Arnon, Israel
Leyre Azpilicueta, Mexico
Paolo Barsocchi, Italy
Alessandro Bazzi, Italy
Zdenek Becvar, Czech Republic
Francesco Benedetto, Italy
Olivier Berder, France
Ana M. Bernardos, Spain
Mauro Biagi, Italy
Dario Bruneo, Italy
Jun Cai, Canada
Zhipeng Cai, USA
Claudia Campolo, Italy
Gerardo Canfora, Italy
Rolando Carrasco, UK
Vicente Casares-Giner, Spain
Luis Castedo, Spain
Ioannis Chatzigiannakis, Italy
Lin Chen, France
Yu Chen, USA
Hui Cheng, UK
Ernestina Cianca, Italy
Riccardo Colella, Italy
Mario Collotta, Italy
Massimo Condoluci, Sweden
Daniel G. Costa, Brazil
Bernard Cousin, France
Telmo Reis Cunha, Portugal
Laurie Cuthbert, Macau
Donatella Darsena, Italy
Pham Tien Dat, Japan
André L. F. de Almeida, Brazil
Antonio De Domenico, France
Antonio de la Oliva, Spain
Gianluca De Marco, Italy
Luca De Nardis, Italy
Liang Dong, USA
Mohammed El-Hajjar, UK
Oscar Esparza, Spain
- Maria Fazio, Italy
Mauro Femminella, Italy
Manuel Fernandez-Veiga, Spain
Gianluigi Ferrari, Italy
Ilario Filippini, Italy
Jesus Fontecha, Spain
Luca Foschini, Italy
A. G. Fragkiadakis, Greece
Sabrina Gaito, Italy
Óscar García, Spain
Manuel García Sánchez, Spain
L. J. García Villalba, Spain
José A. García-Naya, Spain
Miguel Garcia-Pineda, Spain
A. - J. García-Sánchez, Spain
Piedad Garrido, Spain
Vincent Gauthier, France
Carlo Giannelli, Italy
Carles Gomez, Spain
Juan A. Gómez-Pulido, Spain
Ke Guan, China
Antonio Guerrieri, Italy
Daojing He, China
Paul Honeine, France
Sergio Ilarri, Spain
Antonio Jara, Switzerland
Xiaohong Jiang, Japan
Minho Jo, Republic of Korea
Shigeru Kashiara, Japan
Dimitrios Katsaros, Greece
Minseok Kim, Japan
Mario Kolberg, UK
Nikos Komninos, UK
Juan A. L. Riquelme, Spain
Pavlos I. Lazaridis, UK
Tuan Anh Le, UK
Xianfu Lei, China
Hoa Le-Minh, UK
Jaime Lloret, Spain
Miguel López-Benítez, UK
Martín López-Nores, Spain
Javier D. S. Lorente, Spain
Tony T. Luo, Singapore
Maode Ma, Singapore
- Imadeldin Mahgoub, USA
Pietro Manzoni, Spain
Álvaro Marco, Spain
Gustavo Marfia, Italy
Francisco J. Martinez, Spain
Davide Mattera, Italy
Michael McGuire, Canada
Nathalie Mitton, France
Klaus Moessner, UK
Antonella Molinaro, Italy
Simone Morosi, Italy
Kumudu S. Munasinghe, Australia
Enrico Natalizio, France
Keivan Navaie, UK
Thomas Newe, Ireland
Tuan M. Nguyen, Vietnam
Petros Nicopolitidis, Greece
Giovanni Pau, Italy
Rafael Pérez-Jiménez, Spain
Matteo Petracca, Italy
Nada Y. Philip, UK
Marco Picone, Italy
Daniele Pinchera, Italy
Giuseppe Piro, Italy
Sara Pizzi, Italy
Vicent Pla, Spain
Javier Prieto, Spain
Rüdiger C. Pryss, Germany
Sujan Rajbhandari, UK
Rajib Rana, Australia
Luca Reggiani, Italy
Daniel G. Reina, Spain
Jose Santa, Spain
Stefano Savazzi, Italy
Hans Schotten, Germany
Patrick Seeling, USA
Muhammad Z. Shakir, UK
Mohammad Shojaraf, Italy
Giovanni Stea, Italy
Enrique Stevens-Navarro, Mexico
Zhou Su, Japan
Luis Suarez, Russia
Ville Syrjälä, Finland
Hwee Pink Tan, Singapore



Pierre-Martin Tardif, Canada
Mauro Tortonesi, Italy
Federico Tramarin, Italy
Reza Monir Vaghefi, USA

Juan F. Valenzuela-Valdés, Spain
Aline C. Viana, France
Enrico M. Vitucci, Italy
Honggang Wang, USA

Jie Yang, USA
Sherali Zeadally, USA
Jie Zhang, UK
Meiling Zhu, UK

Contents

Energy Conservation and Harvesting in Wireless Sensor Networks

Mile Stojcev , Zoran Stamenkovic, and Bojan Dimitrijevic
Editorial (2 pages), Article ID 7640232, Volume 2019 (2019)

Actor-Critic-Algorithm-Based Accurate Spectrum Sensing and Transmission Framework and Energy Conservation in Energy-Constrained Wireless Sensor Network-Based Cognitive Radios

Hurmat Ali Shah , Insoo Koo , and Kyung Sup Kwak 
Research Article (12 pages), Article ID 6051201, Volume 2019 (2019)

The Smaller the Better: Designing Solar Energy Harvesting Sensor Nodes for Long-Range Monitoring

Malo Mabon, Matthieu Gautier , Baptiste Vrigneau, Mickaël Le Gentil, and Olivier Berder
Research Article (11 pages), Article ID 2878545, Volume 2019 (2019)

Harvested Energy Maximization of SWIPT System with Popularity Cache Scheme in Dense Small Cell Networks

Xuefei Peng and Jiandong Li 
Research Article (14 pages), Article ID 1949638, Volume 2019 (2019)

Robust Power Allocation for Cooperative Localization in Jammed Wireless Sensor Networks

Mingxing Ke, Shiwei Tian , Lu Lu, and Chuang Wang
Research Article (9 pages), Article ID 6904687, Volume 2019 (2019)

A Self-Powered PMFC-Based Wireless Sensor Node for Smart City Applications

Daniel Ayala-Ruiz, Alejandro Castillo Atoche, Erica Ruiz-Ibarra , Edith Osorio de la Rosa, and Javier Vázquez Castillo 
Research Article (10 pages), Article ID 8986302, Volume 2019 (2019)

Novel Energy-Efficient Data Gathering Scheme Exploiting Spatial-Temporal Correlation for Wireless Sensor Networks

Ying Zhou , Lihua Yang , Longxiang Yang, and Meng Ni
Research Article (10 pages), Article ID 4182563, Volume 2019 (2019)

Priority-Based Pipelined-Forwarding MAC Protocol for EH-WSNs

Kyuwook Shim and Hyung-Kun Park 
Research Article (7 pages), Article ID 5418516, Volume 2019 (2019)

Relaying Communications in Energy Scavenging Cognitive Networks: Secrecy Outage Probability Analysis

Khuong Ho-Van  and Thiem Do-Dac 
Research Article (13 pages), Article ID 2109837, Volume 2019 (2019)

EEHRT: Energy Efficient Technique for Handling Redundant Traffic in Zone-Based Routing for Wireless Sensor Networks

Rab Nawaz Jadoon , WuYang Zhou , Iftikhar Ahmed Khan, Muhammad Amir Khan , and Waqas Jadoon
Research Article (12 pages), Article ID 7502140, Volume 2019 (2019)

Editorial

Energy Conservation and Harvesting in Wireless Sensor Networks

Mile Stojcev ¹, Zoran Stamenkovic,² and Bojan Dimitrijevic¹

¹University of Nis, Niš, Serbia

²IHP-Leibniz-Institut für Innovative Mikroelektronik, Frankfurt (Oder), Germany

Correspondence should be addressed to Mile Stojcev; mile.stojcev@elfak.ni.ac.rs

Received 14 July 2019; Accepted 15 July 2019; Published 29 August 2019

Copyright © 2019 Mile Stojcev et al. This is an open access article distributed under the Creative Commons Attribution License, which permits unrestricted use, distribution, and reproduction in any medium, provided the original work is properly cited.

Wireless Sensor Networks (WSNs) have attracted significant attention in monitoring and controlling plants, resources, and infrastructures. These networks are composed of a large number of smart devices called Sensor Nodes (SNs) aimed to work autonomously. The spatially distributed nature of WSNs often requires that the individual SNs be powered by batteries. One of the major limitations on performance and lifetime of SN is the limited capacity of its finite power source, which must be manually replaced when its battery runs out. A viable alternative then is to endow the SNs with appropriate harvesting technologies such as solar, vibrational, wind/water flow, thermal gradient scavenging, electromagnetic direct conversion, and others. These sources can supplement or even entirely replace the battery energy supply. There are complex tradeoffs to be considered when designing energy harvesting and conservation circuits for WSNs arising from the characteristics of the energy sources, energy storage devices used, power management functionality of the SNs and protocols, and the applications' requirements. This special issue contains nine papers that roughly cover some topics that are important for future applications of harvesting and conservation techniques in WSNs. The following paragraphs give an overview regarding the content of this special issue.

In the paper “Harvested Energy Maximization of SWIPT System with Popularity Cache Scheme in Dense Small Cell Networks,” X. Peng and J. Li, from Xidian University, China, concentrate on energy minimization problem of simultaneous wireless information and power transfer (SWIPT) system.

K. Ho-Van and T. Do-Dac, from HCMUT, Vietnam, in “Relaying Communications in Energy Scavenging Cognitive Networks: Secrecy Outage Probability Analysis” evaluate the

performance of relaying communications system in terms of the secrecy outage probability.

“The Smaller the Better: Designing Solar Energy Harvesting Sensor Nodes for Long-Range Monitoring” by M. Mabon et al., from University Rennes, France, describe an energy autonomous node architecture with long-range communication capabilities. In addition, an optimization methodology for energy harvesting and storage elements of the sensor node is presented.

In “Novel Energy-Efficient Data Gathering Scheme Exploiting Spatial-Temporal Correlation for Wireless Sensor Networks,” Y. Zhou et al., from Nanjing University of Posts and Telecommunications, Nanjing, China, propose an energy-efficient data gathering scheme exploiting both spatial and temporal correlations for clustered WSNs.

In the paper “Priority-Based Pipelined-Forwarding MAC Protocol for EH-WSNs,” K. Shim and H.-K. Park, from KOREATECH, Cheonan, Republic of Korea, concentrate on priority-based pipelined forwarding MAC protocol that determines the priority of relay nodes based on the residual power and energy-harvesting rate.

In the paper entitled as “Actor-Critic-Algorithm-Based Accurate Spectrum Sensing and Transmission Framework and Energy Conservation in Energy-Constrained Wireless Sensor Network-Based Cognitive Radios,” H. A. Shah et al., from Inha and Ulsan Universities, Republic of Korea, focus on solving the Markov decision process problem which deals with an actor-critic-algorithm-based solution intended for optimization the action taken in a sensing-transmission framework.

M. Ke et al., from PLA Army Engineering University, Nanjing, China, in the paper entitled as “Robust Power Allocation for Cooperative Localization in Jammed Wireless

Sensor Networks” investigate the robust power allocation strategies for cooperation in jammed wireless sensor localization systems.

R. N. Jadoon et al., from University of Science and Technology of China, Hefei, China, and COMSATS University, Islamabad, Pakistan, describe an efficient data delivery technique called RD²T for wireless sensor networks. This technique divides the network into static zones by eliminating the control overhead and hence extends the network lifetime.

Finally, in the paper “A Self-Powered PMFC-Based Wireless Sensor Node for Smart City Applications,” D. Ayala-Ruiz et al., from Technology Institute of Sonora, Autonomous University of Yucatan and University of Quintana Roo, Mexico, propose a WSN composed of self-powered plant microbial fuel cells as long-range sensor nodes for environmental analysis in smart cities.

We sincerely thank the authors for their outstanding work and the anonymous reviewers who made contribution to the review process. Both the authors’ and the reviewers’ efforts guaranteed the high quality of the published papers in this special issue. A special thank goes to the Editorial Board who has the overall responsibility of the journal quality and to Monica Nabil for assistance during the publication process. We believe that the technical details presented in the papers in this special issue will be interesting and useful to the journal readers and will provide a good snapshot of the state of art in WSNs.

Conflicts of Interest

The guest editors declare no (existing and anticipated) conflicts of interest.

*Mile Stojcev
Zoran Stamenkovic
Bojan Dimitrijevic*

Research Article

Actor–Critic–Algorithm–Based Accurate Spectrum Sensing and Transmission Framework and Energy Conservation in Energy-Constrained Wireless Sensor Network-Based Cognitive Radios

Hurmat Ali Shah ¹, Insoo Koo ², and Kyung Sup Kwak ¹

¹Department of Information and Communication Engineering, Inha University, Incheon, Republic of Korea

²School of Electrical and Computer Engineering, University of Ulsan, Ulsan, Republic of Korea

Correspondence should be addressed to Insoo Koo; iskoo@ulsan.ac.kr

Received 22 March 2019; Revised 30 June 2019; Accepted 8 July 2019; Published 14 August 2019

Guest Editor: Bojan Dimitrijevic

Copyright © 2019 Hurmat Ali Shah et al. This is an open access article distributed under the Creative Commons Attribution License, which permits unrestricted use, distribution, and reproduction in any medium, provided the original work is properly cited.

Spectrum sensing is of the utmost importance to the workings of a cognitive radio network (CRN). The spectrum has to be sensed to decide whether the cognitive radio (CR) user can transmit or not. Transmitting on unoccupied spectrum becomes a hard task if energy-constrained networks are considered. CRNs are ad hoc networks, and thus, they are energy-limited, but energy harvesting can ensure that enough energy is available for transmission, thus enabling the CRN to have a theoretically infinite lifetime. The residual energy, along with the sensing decision, determines the action in the current time slot. The transmission decision has to be grounded on the sensing outcome, and thus, a combined sensing–transmission framework for the CRN has to be considered. The sensing–transmission framework forms a Markov decision process (MDP), and solving the MDP problem exhaustively through conventional methods cannot be a plausible solution for ad hoc networks such as a CRN. In this paper, to solve the MDP problem, an actor–critic–algorithm-based solution for optimizing the action taken in a sensing–transmission framework is proposed. The proposed scheme solves an optimization problem on the basis of the actor–critic algorithm, and the action that brings the highest reward is selected. The optimal policy is determined by updating the optimization problem parameters. The reward is calculated by the critic component through interaction with the environment, and the value function for each state is updated, which then updates the policy function. Simulation results show that the proposed scheme closely follows the exhaustive search scheme and outperforms a myopic scheme in terms of average throughput achieved.

1. Introduction

Wireless sensor networks are pervasive. They are employed in a variety of applications and services ranging from smart grids, Internet of things, to cognitive radios. Wireless sensor networks have sensing at its core. Sensing is required not only to gather information about events, i.e., to record events and behavior of processes, but also to decide the occurrence of a phenomena. When sensor networks are employed to decide the occurrence of an event or a phenomenon, it can be generalized as the basis of diverse set of communication networks. In this way, sensor networks form the basis for cognitive radios when cognitive radios are deployed overlay,

i.e., the cognitive radios have to use the licensed spectrum when not in use by the licensed user. Wireless sensor networks form the sensing base for cognitive radios in deciding whether the spectrum is free or not. So, spectrum sensing is an important task in cognitive radio networks (CRNs). The spectrum has to be sensed and the whole spectrum appropriated for the cognitive radio (CR) user if the full promise of the CRN is to be exploited. On the basis of spectrum sensing, the CR user can transmit, provided it vacates as soon as the primary user (PU) appears. This is more complicated if energy-constrained networks are considered. CRNs are ad hoc networks, and the energy for transmission may not always be available. Given the limited energy budget, the CR

user has to take into consideration the long-term operation of the network. So, one of the multiple levels of transmission power can be selected, or given that transmission power is unavailable, no transmission will happen.

In an uncertain but stochastically known environment, behavior can be learned and the policy of the CR user can be adjusted. The CR user can be seen as an agent in terms of reinforcement learning, and through the acknowledgment (ACK) signal, the environment can be known. In each time frame, the optimal decision has to be taken on the basis of the sensing decision and other system parameters, such as historical information about the belief of the presence or absence of the PU. The optimal decision can be learned, but it will take a lot of iterations by the system to reach it. This is the biggest drawback of simple reinforcement learning (RL) [1]. Instead, deep RL algorithms can be considered to make the optimal decision in the current time slot and to design an optimal policy for the agent.

RL and deep RL solutions and algorithms are most effective in situations where there are patterns and models, so they can be learned. The abstractions of the environment are translated into parameters on the basis of which decision can be taken. In the area of communications, the methods of deep RL can be effective in solving many challenges, particularly in emerging fields varying from the CRN to the Internet of things (IoT) to heterogeneous networks. As communications networks become more and more autonomous and decentralized, the need for optimal operation on the basis of both the environment and gained knowledge becomes paramount. The problems of the CRN, such as spectrum access and transmission power level in energy-constrained situations to optimize different network parameters, can be devised as a decision problem. In the stochastic nature of wireless communications, the decision-making problem can be modeled as a Markov decision process (MDP). An MDP can be solved through deep RL techniques. The sensing–transmission problem is an MDP problem, and it is solved in this paper.

After the sensing decision is made, CR users either transmit or stay silent. The decision to transmit is based on the current state and the transition probability to the next state, as well as the remaining energy, if energy constraints of the network are considered. The states for transition are limited by the current state. The set of actions is also determined by the current state, which may be a combination of spectrum-sensing decision, the belief function, and the remaining energy. In Markov decision systems, the state transition should strictly follow the Markov chain. So, all the possible states and possible actions for those states will have to be computed. In this case, the computation becomes complex and expensive.

This paper presents a model-free reinforcement learning algorithm called an actor–critic algorithm [2, 3]. The advantage of the actor–critic algorithm is that it is not as computationally complex as partially observable MDP (POMDP) approaches and it does not need all of the state transition information to make a decision. In the training phase, the critic updates the approximation of state information on the basis of simulation parameters and feeds

this information to the actor to update the policy parameters. The actor–critic algorithm may converge to a local optimal policy, but it generates the policy directly from training, so much less computational complexity and formulation are required. The actor–critic algorithm obtains a solution to the nonconvex optimization problem as presented in this paper without complete and accurate information about the wireless network environment.

Deep learning is composed of a set of algorithms and techniques that attempt to find important features of data and that try to model high-level abstractions. The main goal of deep learning is to avoid manual descriptions of a data structure (like handwritten features) by automatically learning from the data. Typically, deep learning structures are any neural network which has two or more hidden layers. The algorithms can be divided into policy optimization and dynamic programming. In policy optimization, the policy is parameterized, and the expected reward is maximized. Methods in this category include policy gradients and derivative-free optimization and evolutionary algorithms, whereas dynamic programming methods can exactly solve some simple control problems (i.e., MDPs) through iteration and subdivision. Dynamic programming includes policy iteration and value iteration, and (for more useful and realistic problems) approximate versions of these algorithms are considered (e.g., Q-learning). The actor–critic methods are policy-gradient methods that use value functions.

The notion of learning from the environment is embedded in the concept of cognitive radio. CR users are meant to monitor the environment and adapt their operating characteristics (operating frequency, transmitting power, etc.) to the changing conditions. To enable CR users to learn from the environment, several authors have considered machine learning algorithms for spectrum sensing [4–12]. In [4], a dynamic game is formulated where the secondary users incur sensing charges as a result of PU activity and then after a successful completion of a bidding also pay for transmission opportunities. To solve the problem of bidding, a Bayesian nonparametric belief update is used and learning algorithms are employed, so the users can decide whether to participate in the bidding process or not. In [5], to maximize the available spectrum for secondary users' transmission, a select number of CR users sense multiple bands simultaneously through RL. Q-learning is also employed for diverse purposes. In [7], it is employed to mitigate interference in CRNs while in [8], it is employed for detection of primary signal for spectrum sensing. In [9], two kinds of approaches in a no-regret-based machine learning framework with the presence of malicious activity were proposed with two different algorithms, one had perfect observation of the environment and the other had a partial observation, while in [10], pattern classification techniques as SVM and KNN were investigated for spectrum sensing. In [11, 12], a TV white space database was constructed through machine learning and data fusion was carried for global spectrum sensing decision, respectively. In [11], k-nearest neighbors (KNN) were simply used for data recovery in a white space database as a mechanism for majority voting.

Recently, there has been much interest in the efficient use of energy resources for the sake of energy-aware network architectures and to reduce energy costs [13, 14]. To that end, energy resources have to be used according to system performance requirements. Energy harvesting from renewable energy sources (thermal, vibration, solar, acoustic, and ambient radio power) is designed to meet energy requirements, as well as contribute towards reducing harmful emissions [13]. Energy harvesting allows for theoretically perpetual lifetime operation of an ad hoc network without any need for an external power source or battery replacement. This is an attractive model for many kinds of future wireless and cellular networks and is most important for CRNs. Pei et al. [15] studied an energy-efficient design of a spectrum-sensing scheme in cognitive radio networks. Chen et al. [16] maximized throughput given an energy budget, whereas Hoang et al. [17] designed a utility-based objective function for penalizing energy consumption. Studies have been conducted on exploiting energy harvesting in ad hoc networks [18]. For multiple relay channels, energy harvesting-based schemes were proposed [19, 20]. Wang et al. [21] studied energy harvesting in heterogeneous networks, and both they and Anisi et al. [22] studied the effect of energy harvesting in sensing and body-area networks.

Deep learning is a vast area and is now excessively used in all aspects of communications, particularly in intelligent communications such as cognitive radios, so giving an exhaustive list of literature references is out of the scope of this work, but here, the application of deep learning to spectrum sensing and spectrum access in CRN will be discussed briefly. In [23] a deep Q-learning (DQL) algorithm is used to select the channels for sensing and ultimately access to achieve maximum rate. The action is selected on the basis of the channel SINR exceeding a particular QoS requirement. In [24], a DQL is proposed in a heterogeneous network which consists of multiple users and base stations. The base stations for the users to be associated with are selected through DQL. The simulation results in [24] also confirmed that DQL has better performance than a simple Q-learning scheme. In [25], a deep learning scheme was proposed for a joint user association, spectrum access, and content caching problem in an LTE network. The users are controlled by cloud-based servers, and they are able to access both licensed and unlicensed spectrum. Different actions are selected on the basis of the DQL algorithm such as optimal user association, the bandwidth allocated to users, the time slot allowed to the users, and deciding the content popularity for caching. In [26], a dynamic channel access scheme for a sensor-based IoT is proposed which employs deep learning, while in [27], experience replay is used to find the optimal policy. In [28], a joint channel selection and packet forwarding scheme is proposed in a multisensor scenario, while to counter the energy limitation problem in [29], channel access in an energy harvesting-based IoT system is investigated.

In this paper, an energy-constrained CRN is considered. When transmission is considered jointly with the results from sensing, then in an energy-constrained CRN,

that becomes a hard problem to solve. In the literature, machine learning was applied extensively (as shown above) to the process of spectrum sensing, but not to taking a combined sensing–transmission decision. The problem of transmission is considered an MDP, and the conventional methods are used for solving the problem [30–32]. The wireless environment is a partially observable MDP, and thus, on the basis of some observations, the next state is transitioned to. The problem of the POMDP is solved by visiting all the next possible states from taking all possible actions in the current state and selecting an action that optimizes certain network parameters. When sensing decisions along with the remaining energy in energy-constrained CRNs are considered to be the state, the state space becomes too large to compute and solve. Another problem with such POMDP solutions is that the environment is not aptly learned. As an alternative to the conventional POMDP, the actor–critic algorithm is emerging as a promising alternative. In an actor–critic algorithm, the agent has two parts. The actor takes an action according to a policy, whereas the critic adjusts the policy through parameters like temporal difference. The policy in the actor is optimized on the basis of optimal value function. The value function can have two definitions: (1) the total accumulated reward while starting in the current state and (2) going to the next states according to the given policy. In the state-action value function, the expected accumulated rewards are calculated while taking an action in the current state, and then, in the next state taking other actions according to the given policy. The value function adjusts the policy function in the actor on the basis of observations from the environment. Convergence in the actor–critic algorithm is possible. It is achieved with less complexity and fewer iterations and computations in the state space. Also, in the actor–critic algorithm, the policy is directly learned from the operational environment.

In this paper, an actor–critic-algorithm-based sensing and transmission framework is proposed. CR users take a local sensing decision and then send it to the fusion center (FC) to take a global decision, and these two form part of the local state. The belief function and the remaining energy form the rest of the state. The action space is formed of either the silent mode or transmission with a level of energy that is able to fulfil the long-term energy requirements of the system. CR users are able to harvest energy, and the transmission energy in the current slot also has to take into consideration the long-term energy requirements. On the basis of the transmission and ACK signal, a reward is assigned to each action. The critic evaluates the reward brought by the action and updates the policy function. At the end of the training phase, the optimal value function and the optimal policy function are obtained.

The rest of this paper is organized as follows. Section 2 presents the system model. In Section 3, the system energy constraints, the energy harvesting process, and the Markov decision process are explained. In Section 4, the actor–critic algorithm is presented, while Section 5 presents simulation results and Section 6 concludes the paper.

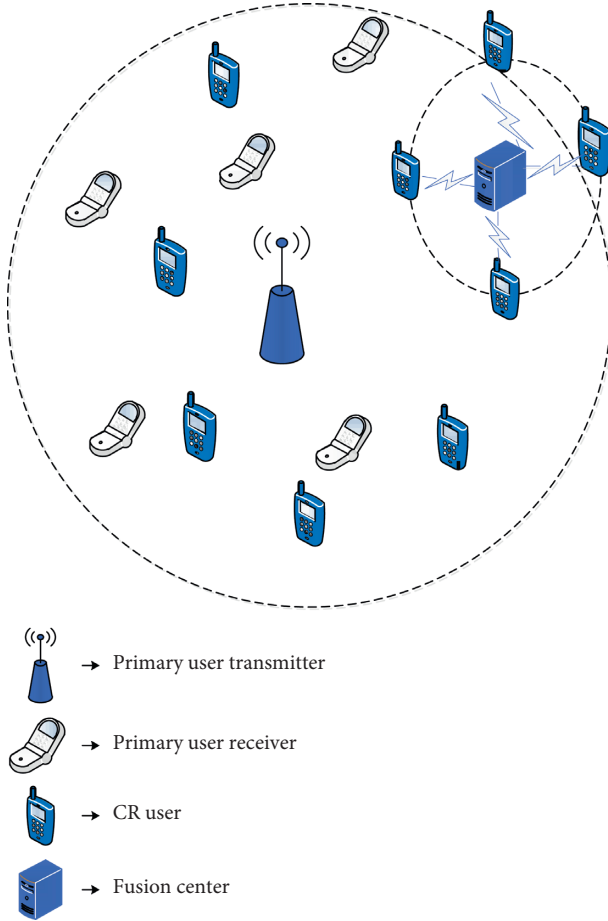


FIGURE 1: Basic system model.

2. System Model and Methods

We consider that a single PU is active and a CRN that consists of N CR users, as shown in Figure 1, monitors the activity of the PU. Considering multiple PUs complicates the sensing process as well as involves other processes such as scheduling and spectrum-handoff. These particular problems are beyond the scope of this paper. The CR users perform spectrum sensing and report their results to the FC. We assume a slotted time-frame structure where each slot is divided into two slots: a sensing slot for spectrum sensing and a transmission slot, which is used for data transmission. The slotted frame structure is considered in [33–41]. In this method of spectrum sensing, the time frame is divided into two parts. The first part of the time frame is known as sensing slot while the other is transmission slot. Spectrum is sensed in the first while the CR users either transmit or stay silent in the transmission slot on the basis of global decision. The durations of both slots among CR users are synchronized through a common control channel and by the FC.

Each CR user employs the energy detection scheme for spectrum sensing. CR users receive energy and on the basis of received energy take a decision. Energy detection is the simplest technique, given the limited resources (e.g., energy and computational power) of most CR users. Common spectrum sensing problems such as multipath fading and

shadowing can be overcome by exploiting spatial diversity using cooperative spectrum sensing, thereby ensuring that PU constraints are met [33]. CR users can either report the actual value of energy received or take a decision locally or report it to the FC. The first one is called soft decision combination and results in optimal detection performance but theoretically requires infinite bandwidth [34], while the latter is hard decision combination which saves bandwidth but produces inferior results as compared to soft reporting. To balance performance and bandwidth efficiency, a combination of both soft and hard decisions can be used where the energy range can be quantized, as in references [34, 37]. In [34], the authors used a so-called softened hard combination scheme, in which the observed energy is quantized into four regions using two bits, where each region is represented by a label. This achieves an acceptable trade-off between the improved performance resulting from soft reporting and information loss during quantization process [41]. In this paper, quantization is considered where the received energy is quantized into four quantization zones.

The signal received by the i -th CR user, during the sensing slot, when the PU is absent, i.e., H_0 , and when the PU is present, i.e., H_1 , is given as

$$y_i = \begin{cases} w(n), & H_0, \\ s(n) + w(n), & H_1, \end{cases} \quad (1)$$

where $w(n)$ is additive white Gaussian noise and $s(n)$ is the energy received from the PU's signal. The received energy is quantized as

$$l_i = \begin{cases} H_0 \begin{cases} Z_1, & Y_i \leq \lambda_{Z_1}, \\ Z_2, & Y_i \leq \lambda_{Z_2}, \end{cases} \\ H_1 \begin{cases} Z_3, & Y_i \leq \lambda_{Z_3}, \\ Z_4, & Y_i > \lambda_{Z_3}, \end{cases} \end{cases} \quad (2)$$

where λ_{Z_1} , λ_{Z_2} , and λ_{Z_3} are the quantization thresholds and $\{Z_1, Z_2, Z_3, Z_4\}$ represent different quantization zones in which the received energies are quantized. A global decision is taken on the basis of majority rule, i.e., the majority of the reported symbols become the global decision, denoted by D_t , where t represents the time index. The combination of local and global decisions determines the state of the CR in the current slot.

3. System Constraints and Definitions

In the section below, the system constraints and processes are explained in detail.

3.1. Energy Harvesting Process. The CR users are able to harvest energy. If the energy arrival process, $e_h^t \in R^+$, is assumed to be independent and identically distributed (i.i.d.) sequences of variables, then $E\{e_h^t\} = e_h$ [13]. It is also assumed that the energy harvested in time slot t is immediately available in slot $t + 1$.

The total energy spent in the current slot, t , if the CR user transmits, is given as

$$e_c(t) = e_s + \alpha_t e_r, \quad (3)$$

where e_s is the sensing energy, e_r is the transmission energy, and α_t is given as

$$\alpha_t = \begin{cases} 1, & \text{if the CR user transmits,} \\ 0, & \text{otherwise.} \end{cases} \quad (4)$$

The residual energy for the next time slot, if the CR user transmits in the current time slot, is

$$e_{\text{rem}}(t+1) = \min\{e_{\text{cap}}, e_{\text{rem}}(t) - e_c(t) + e_h\}, \quad (5)$$

where e_{cap} is the maximum battery capacity and $e_{\text{rem}}(t)$ is the residual energy at time t .

To ensure long-term operation of the network, the energy remaining in the current time slot has to satisfy the energy requirements for some future time slots. Because the transmission energy is dependent upon the sensing decision, its future value cannot be estimated. There is assumed to be a number of future time slots for which energy is required. To maintain energy conservation and long-term operation of the network, it is necessary to save energy in the current time slot. The sensing energy for future time slots remains fixed as sensing happens in each time slot in the sensing slot. The consumption by transmission energy is dependent on the sensing decision, so it cannot be determined in advance. Thus, on the basis of sensing energy, a constraint for energy preservation to ensure long-term operation of the network can be formulated. Let us suppose that we want the CRN to be functional for next N future slots; then, the constraint for long-term energy availability can be formulated as

$$e_{\text{rem}} \geq N(e_s - e_h). \quad (6)$$

3.2. The Markov Process. Let the PU activity follow a two-state Markov process, as shown in Figure 2. Figure 2 illustrates the Markov process where the CR user either transitions to another state or remains in the same state. On the edges, the transition probabilities are given. For the sake of simplicity, H is not written as the subscript of P.

The sensing and transmission framework is formulated as a Markov decision process. The Markov decision process tuple is $\langle S, A, P, R \rangle$, where S represents the state, A is the action taken, P is the transition probability, and R is the reward received on taking an action given a state.

The state is composed of the local and global sensing decisions, the remaining energy, and the transition probability, denoted by $\mu(t)$. For simplicity, let us denote the combination of local and sensing decisions as Q_{id} . The state at time t is given as

$$s(t) = \{Q_{\text{id}}, e_{\text{rem}}(t), \mu(t)\}. \quad (7)$$

The transition probabilities are dependent upon the current local and global sensing decisions. They will be presented in detail later.

The CR user, after sensing, can either be silent or transmit at different levels of transmission energy to meet long-term energy requirements. Two transmission energy

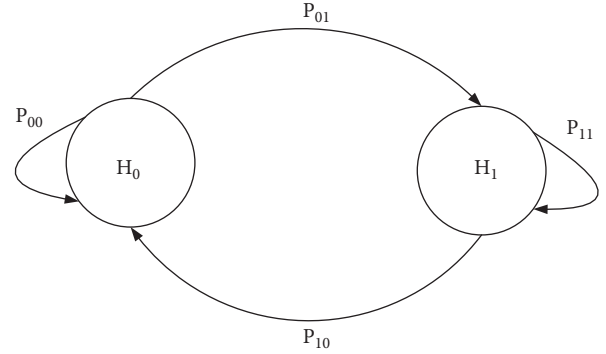


FIGURE 2: The Markov process.

levels are considered. There can be many levels, but the formulation and the solution will become untenable. The action space is defined as

$$A = \{\text{SIL}, e_r^1(t), e_r^2(t)\}, \quad (8)$$

where $e_r^1(t)$ represents transmitting with transmission energy e^1 and $e_r^2(t)$ denotes transmitting with energy level e^2 , while SIL indicates no transmission.

The reward is based on the ACK signal. The rewards are assigned as follows, where $T^{(i)}$ represents the throughput achieved with the given state and transmission energy:

$$\begin{aligned} R\left(\frac{s(t), e_r^1(t)}{\text{ACK}}\right) &= T^{(e^1(t))}, \\ R\left(\frac{s(t), e_r^2(t)}{\text{ACK}}\right) &= T^{(e^2(t))}, \\ R\left(\frac{s(t), e_r^i(t)}{\text{ACK}}\right) &= 0, \quad \text{and } i = 1, 2, \end{aligned} \quad (9)$$

where $T = \log_2(1 + e_r \ell_i)$ and ℓ_i is the SNR received by i -th CR user.

4. Actor-Critic Algorithm

The CR user can take an action, given a particular state, and transition to another state in the current time slot, determined as follows:

$$P\left(\frac{s'}{s(t), a(t)}\right) = \begin{cases} 1, & \text{if } s' = s(t+1), \\ 0, & \text{otherwise.} \end{cases} \quad (10)$$

The reward associated with each state is given in (9).

The total discounted reward in the t -th time slot is given by a value function when the current state is $s(t)$, computed as follows [3]:

$$V(s(t)) = \sum_{k=t}^{\infty} \gamma^k R(s(t), a(t)). \quad (11)$$

The policy function is given as follows [3]:

$$\pi\left(\frac{a(t)}{s(t)}\right) = P\left(\frac{a(t) \in A}{s(t)}\right) = \frac{e^{\phi(a(t), s(t))}}{\sum_{a \in A} e^{\phi(a(t), s(t))}}, \quad (12)$$

where $e^{\phi(a(t), s(t))}$ is the tendency to select action $a(t)$ in state $s(t)$.

After the action is taken, the reward will be calculated. After calculating the reward, the temporal difference is determined as follows:

$$\delta(t) = [R(s(t), a(t)) + \gamma V(s(t+1)) - V(s(t))], \quad (13)$$

where γ determines the effect of the state transition from the current state to the next state.

On the basis of the temporal difference, the value function is updated by the critic as

$$B_{Z_1}^i = P_{\text{ACK}} \times \{R(Q_{l_1}, e_{\text{rem}}(t), \mu(t), e_r^i(t))\} + P_{\text{ACK}} \times \sum_{\left\{ \begin{array}{l} t=t+1 \\ e_{\text{rem}}(t+1) \end{array} \right\}} P[*]V(s(t)) + P_{\text{ACK}} \times \sum_{\left\{ \begin{array}{l} t=t+1 \\ e_{\text{rem}}(t+1) \end{array} \right\}} P[*]V(s(t)). \quad (16)$$

For Z_2 , it is

$$B_{Z_2}^i = P_{\text{ACK}} \times \{R(Q_{l_2}, e_{\text{rem}}(t), \mu(t), e_r^i(t))\} + P_{\text{ACK}} \times \sum_{\left\{ \begin{array}{l} t=t+1 \\ e_{\text{rem}}(t+1) \end{array} \right\}} P[*]V(s(t)) + P_{\text{ACK}} \times \sum_{\left\{ \begin{array}{l} t=t+1 \\ e_{\text{rem}}(t+1) \end{array} \right\}} P[*]V(s(t)), \quad (17)$$

where $P[*]$ gives the probability that (6) will be satisfied and $i \in (1, 2)$. The decision function for the current time slot can then be formulated as

$$B_0(e_{\text{rem}}(t+1), \mu(t), Q_{ld}) = \text{Arg max}_A \{B_{Z_1}^i, B_{Z_2}^i\}, \quad (18)$$

where $l, d \in (Z_1, Z_2)$, and A is given by (8).

The training process is meant to find the set comprising the policy and the optimal value function corresponding to each state. The CR users take a local decision and send the quantized energy zone to the FC. The FC takes a global decision and sends it to the CR users. Based on the local decision and the global decision, the CR users can stay silent or transmit at one of two levels of transmission energy. At the beginning of each time slot, a CR user takes action $a(t) \in A$ according to policy $\pi(a(t)/s(t))$ in a given state. There will be a transition to another state or the current state will be retained, and the next state will be $s(t+1)$ based on the residual energy and the feedback. The rewards will be calculated according to (9). The temporal difference is calculated according to (12) after calculating the reward on the basis of temporal differences, updating the value function in (13). The tendency to select action $a(t)$ in state $s(t)$ is updated in (13). After the convergence is achieved, there will be an optimal value function, $V(s)$, and an optimal set of

$$V(s(t)) = V(s(t) + \beta \cdot \delta(t)), \quad (14)$$

where β is the positive parameter of the critic. The tendency to select an action, given a state, is updated as

$$\varphi(s(t), a(t)) = \varphi(s(t), a(t)) + \chi \cdot \delta(t), \quad (15)$$

where χ is a positive step-size parameter, which determines the number of states to be visited.

The decision in the current time slot is based on the sum of the reward in the current time slot and the expected future reward in the next time slot. If the global decision is Z_1 , calculating the reward from the current and future time slots on the basis of the status of the ACK signal is

policies, π . The following are the possible cases for CR users, on the basis of which the value function is updated and the policy function found. These cases are determined by the system model and the level of transmission energy. They are run till the optimal value function and optimal policy function are obtained.

Case 1. If $D_t = Z_1$ or Z_2 & $l_1 = Z_1$, then stay silent. The belief that the PU is absent in the current time slot is updated using Bayes' rule [2] as

$$\mu^*(t) = \frac{\mu(t)P_f^{Z_1}}{\mu(t)P_f^{Z_1} + (1 - \mu(t))P_d^{Z_1}}, \quad (19)$$

where $P_f^{Z_i}$ is the local probability of false alarm for zone Z_i and $P_d^{Z_i}$ is the local probability of detection for zone Z_i , with $i \in (1, 2, 3, 4)$. The belief for the next time slot is given as

$$\mu(t+1) = \mu^*(t)P_{11} + (1 - \mu^*(t))P_{01}. \quad (20)$$

The residual energy for the next time slot is updated as

$$e_{\text{rem}}(t+1) = \min\{e_{\text{cap}}, e_{\text{rem}}(t) - e_s + e_h\}. \quad (21)$$

Case 2. If $D_t = Z_1$ or Z_2 & $l_1 = Z_2$, then stay silent. The belief that the PU is absent in the current time slot is updated using Bayes' rule as

$$\mu^*(t) = \frac{\mu(t)P_f^{Z_2}}{\mu(t)P_f^{Z_2} + (1 - \mu(t))P_d^{Z_2}}. \quad (22)$$

The belief for next time slot and the residual energy for next time slot for cases 2 to 5 are given in (20) and (21), respectively.

Case 3. If $D_t = Z_1$ or Z_2 & $l_1 = Z_3$, then stay silent. The belief that the PU is absent in the current time slot is updated using Bayes' rule as

$$\mu^*(t) = \frac{\mu(t)P_f^{Z_3}}{\mu(t)P_f^{Z_3} + (1 - \mu(t))P_d^{Z_3}}. \quad (23)$$

Case 4. If $D_t = Z_1$ or Z_2 & $l_1 = Z_4$, then stay silent. The belief that the PU is absent in the current time slot is updated using Bayes' rule as

$$\mu^*(t) = \frac{\mu(t)P_f^{Z_4}}{\mu(t)P_f^{Z_4} + (1 - \mu(t))P_d^{Z_4}}. \quad (24)$$

Case 5. If $D_t = Z_1$ or Z_2 & $l_1 = Z_1$, then take a decision according to (18). The belief that the PU is truly absent in the current time slot is given by Bayes' rule (if transmission happens and ACK is received) as follows:

$$\mu^*(t) = \frac{\mu(t)P_f^{Z_1}}{\mu(t)P_f^{Z_1} + (1 - \mu(t))P_d^{Z_1}}. \quad (25)$$

The residual energy at the CR user for the next time slot is given as

$$e_{\text{rem}}(t+1) = \min\{e_{\text{cap}}, e_{\text{rem}}(t) - e_r^j - e_s + e_h\}, \quad (26)$$

where $j \in (1, 2)$.

The belief that the PU will be absent in the next time slot is given as

$$\mu(t+1) = P_{01}. \quad (27)$$

Case 6. If $D_t = Z_2$ or Z_2 & $l_1 = Z_1$, then take a decision according to (18). The belief that the PU is truly absent in the current time slot is given by Bayes' rule (if transmission happens and ACK is received) as follows:

$$\mu^*(t) = \frac{\mu(t)(1 - P_f^{Z_2})}{\mu(t)(1 - P_f^{Z_2}) + (1 - \mu(t))(1 - P_d^{Z_2})}. \quad (28)$$

The residual energy at the CR user for the next time slot and the belief are given in (23) and (24), respectively. In the absence of an ACK signal, in both Case 5 and Case 6, the belief probability for the next time slot is updated according to (20).

Based on the ACK signal, the rewards are assigned if Case 5 and Case 6 occur on the basis of (9).

In Figure 3, the basic flow chart of the proposed scheme is presented. First, the local and global sensing decisions are made. Combined with the remaining energy and the belief function, a decision is taken according to the cases explained above. The decision is taken by the actor component of the actor-critic algorithm. On the basis of the action taken, there is interaction with the environment. On the basis of observations, the belief function (along with remaining energy) is updated and the reward calculated. The parameters of the optimization problem given in (18) are updated, and the value function is calculated by the critic. On the basis of the updated value function, the temporal difference as given in (13) is determined. Ultimately, the policy is updated implicitly by updating the tendency to select an action, given a state, according to (15).

5. Simulation Results

In this section, the performance of the proposed actor-critic-algorithm-based sensing and transmission framework is assessed through simulation. In the simulation, the proposed scheme is compared with an exhaustive search scheme where the reward brought by each action in each state is calculated and the best selected, rather than finding the transition probabilities for each state to another state. This scheme can be considered an upper bound for the proposed scheme. A myopic scheme is also considered, where energy is harvested, but the long-term energy constraint is not considered, and the maximum available power is used for transmission.

The exhaustive search scheme has precedent in the literature, where in [42], an offline scheme was proposed as an upper bound for a deep Q-network based scheme. The offline scheme assumed that the base station has perfect knowledge of all the random process and thus it can take the optimal decision. The proposed scheme does not have noncausal knowledge of the processes involved, i.e., the future state of battery and the PU activity. The number of mathematical operations involved for the exhaustive search scheme depends on the state space and action space but with the added advantage of having knowledge of all the random processes. The maximum number of mathematical operations, i.e., computational complexity, for the exhaustive search scheme is $O(S_t \times A)$, while the computational complexity of the proposed scheme is given by $O(S_t \times A \times \gamma \times \chi)$. As both γ and χ are positive values below 1, the computational complexity of the proposed scheme is less than the exhaustive search scheme.

When simulating the proposed scheme, the initial value of residual energy is assumed to be $0.6(e_c + e_r^1)$; e_r^1 is 150 mW, and e_r^2 is 110 mW. The circuit power consumption was kept fixed at 210 [13–15]. These energy settings parameters are considered because of the energy harvesting model. The energy harvesting model considered in this paper was investigated in detail by the authors in [13] and the values for the parameters are based on simulation results as obtained there. The two different values of transmission energies are considered to be realistic in comparison with

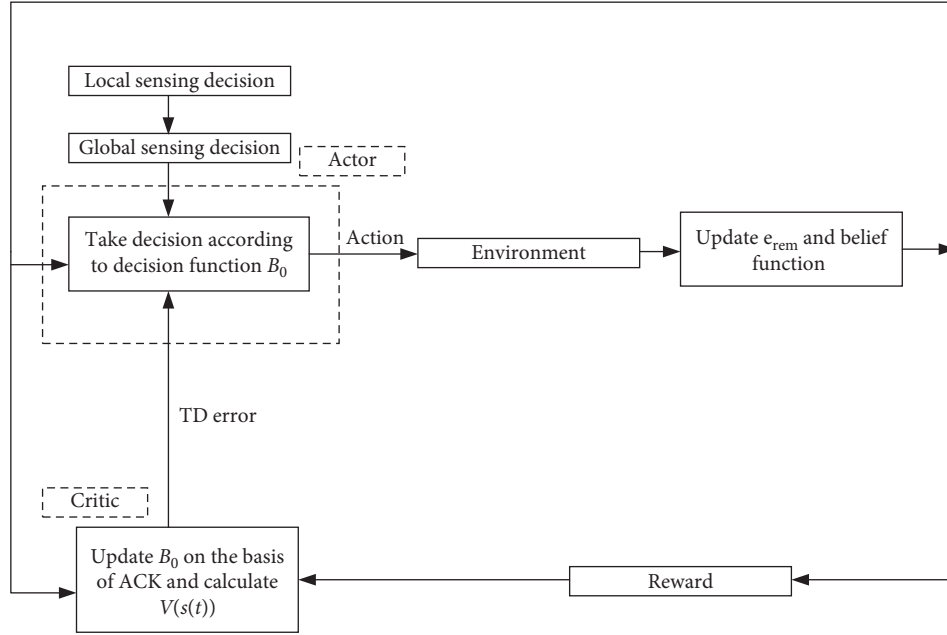


FIGURE 3: Flow chart of the proposed scheme.

sensing energy and overall circuit consumption. The transmit power was varied for the different simulation results and is given for each. The time slot duration was 200 ms, and the sensing duration was eight of the total slot durations. The noise spectrum density was taken to be 4.4×10^{-21} W/Hz [43]. The number of CR users considered was three. The probability of detection is 0.9, and the false alarm probability is 0.1, while the initial belief about the PU is 0. The state transition probabilities of the channel are 0.2. The value of γ was kept at 0.4, while χ was 0.3. These values were taken experimentally for achieving convergence, and different values will have different convergence behavior.

Figure 4 presents the comparison of the proposed scheme with the exhaustive search scheme. We can see from the figure that the proposed scheme closely follows the exhaustive search scheme, which acts as the upper bound for the proposed scheme. The average SNR of all the CR users was taken to be the value given on the x -axis, and it was changed as shown in the figure. The number of iterations was taken to be 5000. The average rate was calculated for all the slots according to (9). SNR is important both for sensing and for success of transmission. When the SNR is low, the CR users will not be able to sense properly, and even when the CR users decide to transmit, the rate achieved will be less because of the higher ratio of the noise signal. So, checking the performance at different levels of SNR is important. At a very low SNR of -9 dB, the proposed scheme starts to converge, and the behavior is the same as the upper bound. The exhaustive search scheme, rather than taking an optimized decision, searches the subspace of available actions, and thus, the one selected is the global optimum. The proposed scheme, on the other hand, may at best converge to a locally optimal policy, and thus, there is always a gap, even after the training converges to an optimal value function and policy. Because the subspace of all available actions is

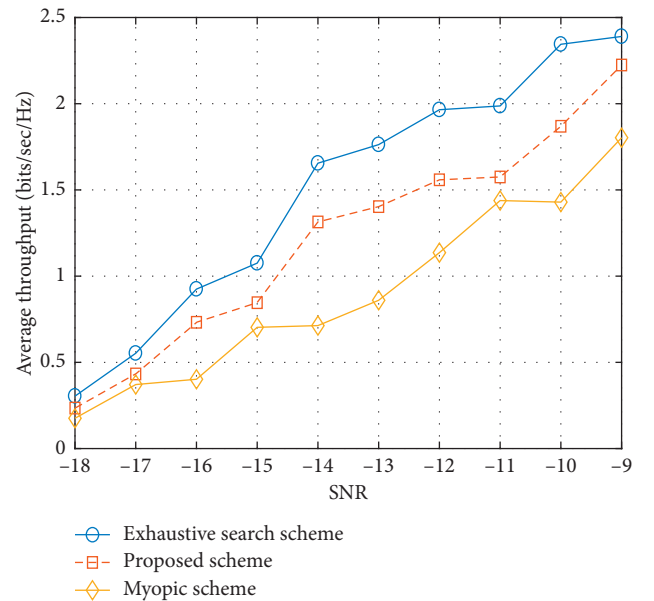


FIGURE 4: Average throughput of the system.

checked thoroughly in the exhaustive search scheme and all the rewards brought by all possible next states are calculated, it is computationally expensive. The proposed scheme, on the other hand, has less computational complexity but gives performance closely following the upper bound. On the other hand, the proposed scheme outperforms the myopic scheme, which transmits with all the transmission power available. It may achieve high throughput in some slots, but it eventually runs out of transmission energy. The state space is continuous as the energy harvested and the remaining energy are continuous functions. The size of the state space cannot be predetermined; however, the positive step

parameters given in (14) and (15) determine the rate of convergence at the expense of not visiting all the states. In simulation for exhaustive search schemes, all states are visited unless there is convergence, and the reward returned does not change significantly. So, the positive step parameters in (14) and (15) determine the complexity of the proposed scheme while for exhaustive search scheme, all the states will be visited unless there is a convergence to a stable reward value.

Figure 5 presents the false decision rate, which is represented by P_{fd} . The false decision rate measures the probability that the PU is absent and the CR user does not transmit or that the PU is absent and the CR user does transmit. The sensing part is the same for both schemes, but in the exhaustive search scheme, all the states and actions are visited, and the best is selected; in the proposed scheme, only the optimization problem is solved, and that may not be accurate. Though both schemes follow the same quantization-based sensing scheme, the error performance from the exhaustive search scheme is better than with the proposed scheme because the proposed scheme is based on estimating the next state, whereas the exhaustive search scheme checks the reward brought by all the next possible states and selects the best one. In that scenario, the exhaustive search scheme assumes correct information for all the possible states.

Figure 6 shows the convergence of the proposed scheme. The x -axis is the number of iterations. We can see that as the number of iterations increases, system performance improves. The system performance is dependent upon the information obtained from the environment, and the optimization problem presented here learns both the probability that the CR user will have enough energy to transmit and the reward brought by each action taken in a given state. With the increase in the system run, the critic component of the proposed scheme is able to calculate and thus to limit the temporal difference. On the basis of the temporal difference, the policy parameters are optimized. As many times as the proposed scheme is invoked, there is the same number of updates to the temporal difference error, and hence, the best action (given a state) can be selected. When the number of iterations reaches a certain point, we can see that system performance reaches a stable position, and despite further increases in the number of iterations, the performance improves no more. Thus, there is also a limit to performance improvement in terms of the number of iterations, and performance improvement beyond that point would need a new model of energy harvesting or changing the other system's parameters and constraints.

In Figure 7, the effect of the energy harvesting rate is shown. The effect is determined by r which is the energy harvesting rate. The energy harvesting rate affects the harvested energy which is given by $e_h = r(e_c + e_r^1)$. The x -axis in Figure 7 shows different values of r . The proposed scheme closely matches the exhaustive search scheme when the harvested energy is below a certain limit. This is because when there is limited energy available, a transmission cannot be made, despite having the best information about the operating environment, and thus, the exhaustive search scheme cannot outperform the proposed scheme by a big

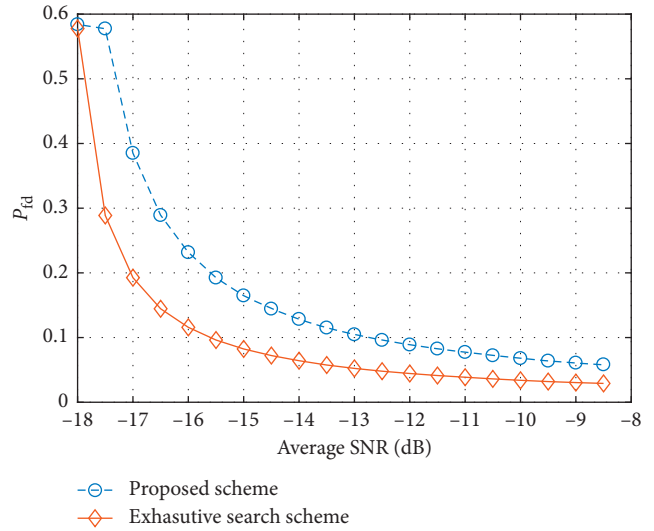


FIGURE 5: Comparison of the probability of false alarm.

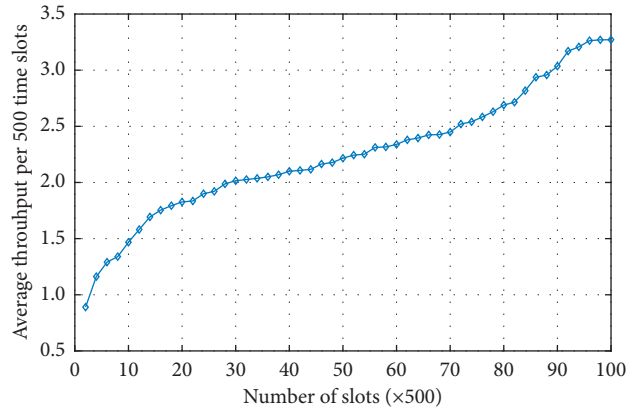


FIGURE 6: Convergence rate of the proposed scheme.

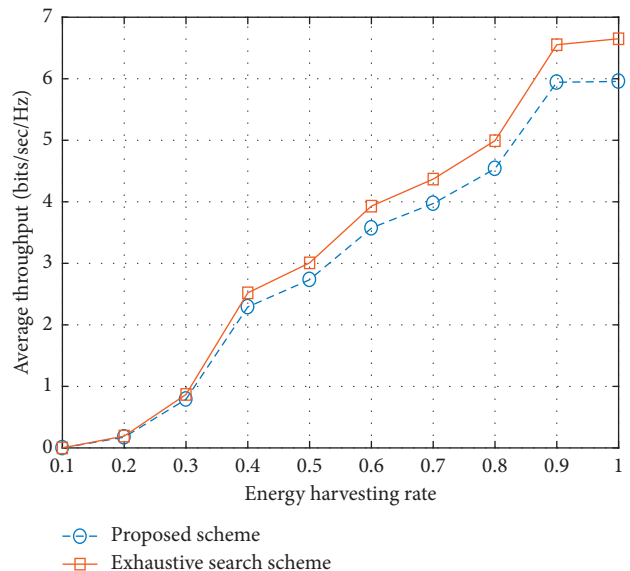


FIGURE 7: Effect of harvested energy on average throughput.

margin. When there is sufficient transmission energy available and when the energy harvesting rate improves, there is sufficient energy available for transmission, and thus, the decision taken on the basis of the exhaustive search scheme outperforms the solution to the optimization problem, which does not check all the possible solutions. The exhaustive search scheme calculates the next possible states and calculates the actions that can be taken in all future states and thus can better know the future energy state. The proposed scheme, on the other hand, makes a decision on the basis of the probability of receiving the ACK signal and on the energy constraint. Because it solves the optimization problem, rather than visiting all possible states and calculating the reward brought by each action in every possible state, the proposed scheme settles for low transmission energy to satisfy the system's energy constraints. But despite not visiting all possible states, the proposed scheme closely follows the exhaustive search scheme, and under practical conditions (when information about all possible states is not available), the proposed scheme based on the actor-critic algorithm comes across as an acceptable alternative.

As the harvested energy remains low, there is a slight chance that transmission with higher level of power will be selected. Thus, the performance of both the proposed scheme and the exhaustive search scheme remains the same in terms of average throughput despite the exhaustive search scheme visiting more states as ultimately the transmission is carried out with low transmission power. But as the harvested energy increases, the exhaustive search scheme performs better because it can predict well the future state of energy, and so transmission with higher level of power can be carried out. On the other hand, because of having inexact knowledge of the energy harvesting process and thus the future state of the remaining energy, the proposed scheme opts to transmit with low level of transmission power because of the constrain given in (6). Thus, the exhaustive search scheme gives better average throughput than the proposed scheme when the energy harvesting rate increases.

6. Conclusion

In this paper, a joint sensing and transmission framework was considered. The transition probabilities from one state to another and the set of available actions are determined from the sensing result and the amount of residual energy. This allows for a robust framework where the CRN ensures there is energy available for future time slots while achieving throughput in the current slot. The actor-critic algorithm is formulated to decide the next state and the amount of transmission energy, if there is a transmission. The value function takes care to come up with an optimal policy, which associates an optimal action with each state. After the training is complete, there is an optimal policy function as the environment is learned through the interplay of the actor and critic functions. The proposed scheme avoids computing all the state and action space and rather finds an action which optimizes the reward in a given state. The optimal policy is updated in each time slot, and the critic acts to reduce the deviation from the optimal path. The proposed

scheme which is based on reinforcement learning-based actor-critic algorithm is less computationally expensive and less exhaustive while solves the optimization problem to find the optimal action in a given state. The simulation results show that the proposed scheme closely follows the exhaustive search scheme despite having less computations and solving an optimal solution.

Data Availability

The data used to support the findings of this study are available from the corresponding author upon request.

Conflicts of Interest

The authors declare that they have no conflicts of interest.

Acknowledgments

This work was supported by the National Research Foundation (NRF) grant through the Korean Government (MSIT) under grant NFR-2018R1AB6001714.

References

- [1] N. C. Luong, N. C. Luong, D. T. Hoang, S. Gong et al., "Applications of deep reinforcement learning in communications and networking: a survey," 2018, <http://arxiv.org/abs/1810.07862>.
- [2] V. R. Konda and J. N. Tsitsiklis, "Actor-critic algorithms," in *Advances in Neural Information Processing Systems*, S. A. Solla, T. K. Leen, and K.-R. Müller, Eds., Vol. 12, MIT Press, Cambridge, MA, USA, 2000.
- [3] R. S. Sutton and A. G. Barto, *Reinforcement Learning: An Introduction*, MIT Press, Cambridge, MA, USA, 1998.
- [4] Z. Han, R. Zheng, and H. V. Poor, "Repeated auctions with Bayesian nonparametric learning for spectrum access in cognitive radio networks," *IEEE Transactions on Wireless Communications*, vol. 10, no. 3, pp. 890–900, 2011.
- [5] J. Lundén, V. Koivunen, S. R. Kulkarni, and H. V. Poor, "Reinforcement learning based distributed multiagent sensing policy for cognitive radio networks," in *Proceedings of the 2011 IEEE International Symposium on Dynamic Spectrum Access Networks (DySPAN)*, IEEE Aachen, Germany, May 2011.
- [6] M. Bkassiny, K. J. Sudharman, and K. A. Avery, "Distributed reinforcement learning based MAC protocols for autonomous cognitive secondary users," in *Proceedings of the 2011 20th Annual Wireless and Optical Communications Conference (WOCC)*, IEEE Newark, NJ, USA, April 2011.
- [7] A. Galindo-Serrano and L. Giupponi, "Distributed Q-learning for aggregated interference control in cognitive radio networks," *IEEE Transactions on Vehicular Technology*, vol. 59, no. 4, pp. 1823–1834, 2010.
- [8] B. Y. Reddy, "Detecting primary signals for efficient utilization of spectrum using Q-learning," in *Proceedings of the Fifth International Conference on Information Technology: New Generations (ITNG 2008)*, IEEE Las Vegas, NV, USA, April 2008.
- [9] Q. Zhu, Z. Han, and T. Başar, "No-regret learning in collaborative spectrum sensing with malicious nodes," in *Proceedings of the 2010 IEEE International Conference on Communications*, IEEE, Cape Town, South Africa, May 2010.

- [10] K. M. Thilina, K. W. Choi, N. Saquib, and E. Hossain, "Pattern classification techniques for cooperative spectrum sensing in cognitive radio networks: SVM and W-KNN approaches," in *Proceedings of the 2012 IEEE Global Communications Conference (GLOBECOM)*, pp. 1260–1265, IEEE, Anaheim, CA, USA, December 2012.
- [11] M. Tang, Z. Zheng, G. Ding, and Z. Xue, "Efficient TV white space database construction via spectrum sensing and spatial inference," in *Proceedings of the 2015 IEEE 34th International Performance Computing and Communications Conference (IPCCC)*, pp. 1–5, IEEE, Nanjing, China, December 2015.
- [12] A. M. Mikaeil, B. Guo, and Z. Wang, "Machine learning to data fusion approach for cooperative spectrum sensing," in *Proceedings of the 2014 International Conference on Cyber-Enabled Distributed Computing and Knowledge Discovery*, pp. 429–434, IEEE, Shanghai, China, October 2014.
- [13] S. Park, H. Kim, and D. Hong, "Cognitive radio networks with energy harvesting," *IEEE Transactions on Wireless Communications*, vol. 12, no. 3, pp. 1386–1397, 2013.
- [14] L. Cai, H. Poor, Y. Liu, T. Luan, X. Shen, and J. Mark, "Dimensioning network deployment and resource management in green mesh networks," *IEEE Wireless Communications*, vol. 18, no. 5, pp. 58–65, 2011.
- [15] Y. Pei, Y.-C. Liang, K. C. Teh, and K. H. Li, "Energy-efficient design of sequential channel sensing in cognitive radio networks: optimal sensing strategy, power allocation, and sensing order," *IEEE Journal on Selected Areas in Communications*, vol. 29, no. 8, pp. 1648–1659, 2011.
- [16] Y. Chen, Q. Zhao, and A. Swami, "Distributed spectrum sensing and access in cognitive radio networks with energy constraint," *IEEE Transactions on Signal Processing*, vol. 57, no. 2, pp. 783–797, 2009.
- [17] A. T. Hoang, Y.-C. Liang, D. T. C. Wong, Y. Zeng, and R. Zhang, "Opportunistic spectrum access for energy-constrained cognitive radios," *IEEE Transactions on Wireless Communications*, vol. 8, no. 3, pp. 1206–1211, 2009.
- [18] J. Yang, O. Ozel, and S. Ulukus, "Broadcasting with an energy harvesting rechargeable transmitter," *IEEE Transactions on Wireless Communications*, vol. 11, no. 2, pp. 571–583, 2012.
- [19] H. Li, N. Jaggi, and B. Sikdar, "Relay scheduling for cooperative communications in sensor networks with energy harvesting," *IEEE Transactions on Wireless Communications*, vol. 10, no. 9, pp. 2918–2928, 2011.
- [20] I. Krikidis, T. Charalambous, and J. S. Thompson, "Stability analysis and power optimization for energy harvesting cooperative networks," *IEEE Signal Processing Letters*, vol. 19, no. 1, pp. 20–23, 2012.
- [21] L. Wang, K.-K. Wong, S. Jin, G. Zheng, and R. W. Heath, "A new look at physical layer security, caching, and wireless energy harvesting for heterogeneous ultra-dense networks," *IEEE Communications Magazine*, vol. 56, no. 6, pp. 49–55, 2018.
- [22] M. H. Anisi, G. Abdul-Salaam, M. Y. I. Idris, A. W. A. Wahab, and I. Ahmedy, "Energy harvesting and battery power based routing in wireless sensor networks," *Wireless Networks*, vol. 23, no. 1, pp. 249–266, 2017.
- [23] Y. Lin, X. Dai, L. Li, and F.-Y. Wang, "An efficient deep reinforcement learning model for urban traffic control," 2018, <http://arxiv.org/abs/1808.01876>.
- [24] S. Gu, E. Holly, T. Lillicrap, and S. Levine, "Deep reinforcement learning for robotic manipulation with synchronous off-policy updates," in *Proceedings of the 2017 IEEE International Conference on Robotics and Automation (ICRA)*, pp. 3389–3396, IEEE, Singapore, June 2017.
- [25] X. Di, K. Xiong, P. Fan, H.-C. Yang, and K. B. Letaief, "Optimal resource allocation in wireless powered communication networks with user cooperation," *IEEE Transactions on Wireless Communications*, vol. 16, no. 12, pp. 7936–7949, 2017.
- [26] D. Zhao, H. Wang, K. Shao, and Y. Zhu, "Deep reinforcement learning with experience replay based on SARSA," in *Proceedings of the IEEE Symposium Series on Computational Intelligence (SSCI)*, pp. 1–6, IEEE, Athens, Greece, December 2016.
- [27] W. Wang, J. Hao, Y. Wang, and M. Taylor, "Towards cooperation in sequential prisoner's dilemmas: a deep multi-agent reinforcement learning approach," 2018, <http://arxiv.org/abs/1803.00162>.
- [28] S. Wang, H. Liu, P. H. Gomes, and B. Krishnamachari, "Deep reinforcement learning for dynamic multichannel access," in *Proceedings of the International Conference on Computing, Networking and Communications (ICNC)*, IEEE, Guilin, China, July 2017.
- [29] Q. Zhao, B. Krishnamachari, and K. Liu, "On myopic sensing for multi-channel opportunistic access: structure, optimality, and performance," *IEEE Transactions on Wireless Communications*, vol. 7, no. 12, pp. 5431–5440, 2008.
- [30] B. C. Jung, J. Park, T.-W. Ban, W. Lee, and J. M. Kim, "Full-duplex generalized spatial modulation: a compressed sensing-based signal detection," in *Proceedings of the 2017 Ninth International Conference on Ubiquitous and Future Networks (ICUFN)*, IEEE, Milan, Italy, July 2017.
- [31] Y. Cui, W. Xu, and J. Lin, "A novel compressed data transmission scheme in slowly time-varying channel," in *Proceedings of the 2016 IEEE 27th Annual International Symposium on Personal, Indoor, and Mobile Radio Communications (PIMRC)*, IEEE, Valencia, Spain, September 2016.
- [32] M. Hirzallah, W. Afifi, and M. Krunz, "Full-duplex-based rate/mode adaptation strategies for Wi-Fi/LTE-U coexistence: a POMDP approach," *IEEE Journal on Selected Areas in Communications*, vol. 35, no. 1, pp. 20–29, 2017.
- [33] F. Rongfei and H. Jiang, "Optimal multi-channel cooperative sensing in cognitive radio networks," *IEEE Transactions on Wireless Communications*, vol. 9, no. 3, pp. 1128–1138, 2010.
- [34] J. Ma, G. Zhao, and Y. Li, "Soft combination and detection for cooperative spectrum sensing in cognitive radio networks," *IEEE Transactions on Wireless Communications*, vol. 7, no. 11, pp. 4502–4507, 2008.
- [35] S. Kyperountas, N. Correal, and Q. Shi, *A Comparison of Fusion Rules for Cooperative Spectrum Sensing in Fading Channels*, EMS Research, Motorola, Libertyville, IL, USA, 2010.
- [36] H. Guo, W. Jiang, and W. Luo, "Linear soft combination for cooperative spectrum sensing in cognitive radio networks," *IEEE Communications Letters*, vol. 21, no. 7, pp. 1573–1576, 2017.
- [37] H. Sakran and M. Shokair, "Hard and softened combination for cooperative spectrum sensing over imperfect channels in cognitive radio networks," *Telecommunication Systems*, vol. 52, no. 1, pp. 61–71, 2013.
- [38] H. A. Shah, M. Usman, and I. Koo, "Bioinformatics-inspired quantized hard combination-based abnormality detection for cooperative spectrum sensing in cognitive radio networks," *IEEE Sensors Journal*, vol. 15, no. 4, pp. 2324–2334, 2015.
- [39] P. Kaligineedi and V. K. Bhargava, "Sensor allocation and quantization schemes for multi-band cognitive radio cooperative sensing system," *IEEE Transactions on Wireless Communications*, vol. 10, no. 11, pp. 284–293, 2011.

- [40] R. Chen, J. M. Park, and K. Bian, "Robust distributed spectrum sensing in cognitive radio networks," in *Proceedings of the 2008 IEEE INFOCOM-The 27th Conference on Computer Communications*, pp. 31–35, IEEE, Phoenix, AZ, USA, April 2008.
- [41] H. A. Shah and I. Koo, "Reliable machine learning based spectrum sensing in cognitive radio," *Wireless Communications and Mobile Computing*, vol. 2018, Article ID 5906097, 17 pages, 2018.
- [42] M. Chu, H. Li, X. Liao, and S. Cui, "Reinforcement learning-based Multiaccess control and battery prediction with energy harvesting in IoT systems," *IEEE Internet of Things Journal*, vol. 6, no. 2, pp. 2009–2020, 2019.
- [43] H. Mu, M. Tao, W. Dang, and Y. Xiao, "Joint subcarrier-relay assignment and power allocation for decode-and-forward multi-relay OFDM systems," in *Proceedings of the 2009 Fourth International Conference on Communications and Networking in China*, pp. 1–6, IEEE, Xian, China, August 2009.

Research Article

The Smaller the Better: Designing Solar Energy Harvesting Sensor Nodes for Long-Range Monitoring

Malo Mabon, Matthieu Gautier , Baptiste Vrigneau, Mickaël Le Gentil, and Olivier Berder

Univ Rennes, CNRS, IRISA, France

Correspondence should be addressed to Matthieu Gautier; matthieu.gautier@irisa.fr

Received 5 April 2019; Accepted 13 June 2019; Published 15 July 2019

Guest Editor: Zoran Stamenkovic

Copyright © 2019 Malo Mabon et al. This is an open access article distributed under the Creative Commons Attribution License, which permits unrestricted use, distribution, and reproduction in any medium, provided the original work is properly cited.

Emerging Low Power Wide Area Networks (LPWAN) represent a real breakthrough for monitoring applications, since they give the possibility to generate and transmit data over dozens of kilometers while consuming few energy. To further increase the autonomy of such wireless systems, the present paper proposes an original methodology to correctly dimension the key elements of an energy autonomous node, namely, the supercapacitor and the battery that mainly give the form factor of the node. Among the LPWAN candidates, LoRa is chosen for real field experiments with a custom wireless platform that proves its energy neutrality over a finite horizon. Different LoRa configurations are explored, leading to adequate dimensioning. As an example, it is shown that, for the same quality of service, the size of the solar panel needed to keep a LoRa node autonomous in the South of France is less than half of the size required in North of France.

1. Introduction

Future wireless standards such as the fifth generation of mobile communications are evolving to allow simultaneously high datarate transmissions for classical end-user applications such as telephony or video, very low latency for vehicle, and safety applications but also low power transmission required by the connected thing. The latter class, also known as Internet of Things (IoT), needs to accept an exponentially growing number of nodes due to a large panel of applications. While mobile operators are able to upgrade their base stations in order to deal with the IoT by allowing the 4G Cat-M or NB-IoT standards, several technologies dedicated to very low power consumption recently emerged in nonlicensed-ISM (Industrial Scientific and Medical) bands, among which we can cite LoRa, SigFox, or Weightless [1]. As the radio range of most of these technologies can reach several kilometers and even tens of kilometers, they are called Low Power Wide Area Networks (LPWAN).

These wireless nodes generally embed several sensors to monitor their direct environment and regularly transmit a low amount of data to a base station. Smart agriculture typically represents an application domain where LPWAN nodes are very useful, due to the huge number of nodes

required to monitor fields or farm buildings and the distance to cover from remote places to the main site. Of course, the more you deploy sensors, the less you want to have to change the batteries, especially if some of them are deployed in harsh environment. Energy consumption therefore becomes a critical issue for wireless node designers, and huge efforts were recently devoted to increase node lifetime [2].

Besides, some harvesters are able to collect surrounding energy from various sources [3], e.g., light, heat, vibrations, electromagnetic waves, or even microbial fuel cell. Provided that energy managers [4, 5] are carefully designed, it is therefore even possible to optimize the Quality of Service (QoS) while keeping a total energy autonomy. Among all harvesters, photovoltaic panels offer from far the best power outcome and are able to efficiently transform outdoor light to feed wireless nodes [6]. However, to avoid battery failures that either could be very disadvantageous for farm monitoring or even be dangerous for the node longevity, the panels are generally oversized [7]. As they represent the element that decides the form factor of nodes, this leads to larger, more expensive, and also more visible nodes and therefore it is subject to intentional or unintentional damages. To overcome these drawbacks, the present paper proposes a methodology to reduce as much as possible the energy harvesting and

storage elements while guarantying the desired quality of service, namely, the data rate.

Our contributions are the following:

- (i) An energy autonomous node architecture with LoRa communication capabilities.
- (ii) An optimization methodology for the energy harvesting and storage elements of the wireless node.
- (iii) The exploration of both application requirements and light conditions and the impact on the node dimensioning.

The remainder of this paper is organized as follows. Section 2 presents related works on existing long-range oriented standards and energy harvesting. Our wireless node architecture is introduced in Section 3. Section 4 focuses on the LoRa standard and our energy consumption characterization process, followed by a experimental validation in Section 5. Finally, Section 6 concludes this paper and discusses further works.

2. Related Works on Energy Harvesting for Long-Range Platforms

In order to enable sustainable operation of IoT nodes, energy harvesting technologies have been considered for a long time by improving both hardware components and platforms and the associated software methods to properly manage the energy consumption [4, 8, 9]. These software components are often referred to as energy managers and are not addressed in this study. At hardware level, efforts focus on three main components of the energy harvesting system: the harvester, the energy converter, and the energy storage. Converting energy from the harvester to the storage is crucial for any energy harvesting circuit. The energy converter of the platform aims to transform the incoming energy into a suitable voltage in order to charge the energy storage (super-capacitor or battery). Different power converter architectures can be used to regulate the energy from the energy harvesting source voltage to a suitable output voltage. While the simplest architecture relies on a Low DropOut (LDO) regulator, many solutions use an SMPS (Switched Mode Power Supply) architecture in which a switch between the energy source and the energy load is rapidly opened and closed. SMPS can easily provide good conversion efficiency, from 70% to 90%, can boost a low harvested voltage but are more complex and expensive than LDOs. Moreover, each energy harvesting source has an optimal operating point, called Maximum Power Point (MPP). In order to maximize harvesting efficiency, the energy converter can use MPPT (MPP Tracking) techniques in order to keep its input voltage close to the operating voltage for which the harvested power is maximized. All functions (voltage conversion, battery charging, and MPPT) are now integrated in a single Integrated Circuit (IC), such as the LTC3108 [10] from Linear Technology, the BQ25570 [11] from Texas Instruments, or the SPV1050 [12] from ST Microelectronics.

At an industrial level, few devices powered by energy harvesting are currently available and they mostly use short-range communications [13–15]. For instance, Z-Beacon from Zoliton Technology [13] uses solar energy to power a Bluetooth 5 communication node and MVA 00X family from Micropelt [14] uses a thermoelectric generator to power an EnOcean short-range transceiver. To the best of our knowledge, Z-Node [13] is the only industrial LPWAN node powered by solar energy harvesting. It uses Sigfox [16] for its long-range communication but also includes short-range communications (Bluetooth 5 and NFC) and many sensors (temperature, acceleration, illumination, GPS, and magnetic fields). However, the problem of these devices is a lack of methodology for efficiently choosing both harvester and energy storage device according to a target quality of service. Indeed, most of them are designed for a given data and/or sensing rate. However, new LPWAN standards such as LoRa allow a wide range of data and packet rates. The node energy consumption of the node can consequently vary of several orders of magnitude from one configuration to another.

Powering LoRa based devices with energy harvesting is, as far as we know, still a research work [17–19]. Reference [17] presents an energy-efficient multi-sensing platform that exploits energy harvesting, long-range, communication and ultra-low-power short-range wake-up radio to achieve self sustainability in a kilometer range network. Energy harvesting is designed around the BQ25570 IC from Texas Instruments, which allows a conversion efficiency of 90% and provides MPPT capability. The multisource energy harvesting platform proposed in [19] relies on a circuit which switches between multiple heterogeneous energy sources and uses a single power conditioning block. A prototype has been developed and validated with a LoRaWAN platform. A single Power Management IC (PMIC) is used, the SPV1050 from ST Microelectronics, allowing a wide input voltage range. However, due the multiple energy sources, the MPPT can not be used, thus reducing consequently the harvesting efficiency.

To sum up, there is currently no commercial LoRa-based platform powered by energy harvesting but only few research works that mainly focus on the validation of the SW (energy manager) part [18, 20] and do not address the dimensioning of the hardware elements [7].

3. Methodology for Dimensioning Energy Harvesting Platforms

3.1. Platform Model. The goal of the platform studied in this paper is to measure information with several sensors and to transmit this collected data using a radio transceiver, while being powered by solar energy harvesting. The model of such a sensor node is shown in Figure 1. Two main parts can be identified: the energy harvesting part and the processing part. Firstly, the energy harvesting part is made up of the energy harvester (i.e., solar panel), the energy manager chip, a way to store the harvested energy (a supercapacitor and/or a battery), and a chip able to measure the current and voltage of the battery. Secondly, the processing part consists of a micro-controller unit (MCU) which manages both the sensors and

TABLE 1: Input parameters description.

Name	Unit	Description
I_{Rad}	mA	consumed current of the radio module in active mode
$I_{RadSleep}$	mA	consumed current of the radio module in sleep mode
I_{MCU}	mA	consumed current of the MCU in active mode
$I_{MCUSleep}$	mA	consumed current of the MCU in sleep mode
T_{oA}	s	Time On Air: duration of active radio
T_{Send}	s	period between two transmissions
T_{Act}	s	time when MCU is active for a transmission
I_{Sens}	mA	consumed current of the sensor in active mode
$I_{SensSleep}$	mA	consumed current of the sensor in sleep mode
$T_{MCUSens}$	s	duration of active MCU for sensing operation
T_S	s	period between two sensing operations
T_{Sens}	s	duration of active sensor
I_{BM}	mA	consumed current of the battery manager
V_{EoC}	V	supercapacity maximum voltage (End of Charge)
V_{UVP}	V	supercapacity minimum voltage (Under Voltage Protection)
μ_{MPPT}		efficiency rate of the MPPT device
nb_{WD}	day	number of working days for the node
nb_{TD}	day	number of days without harvesting
T_{EH}	s	duration with harvesting over one day
$T_{\overline{EH}}$	s	duration without harvesting over one day

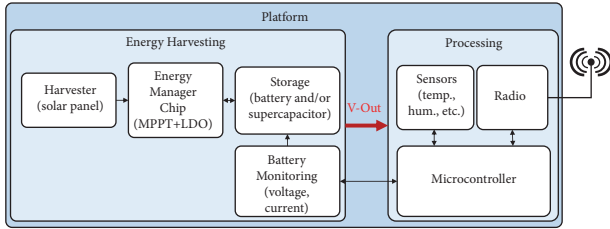


FIGURE 1: Platform block diagram.

a radio communication module. The proposed methodology is quite generic and does not depend on the types of radio transceiver, MCU, and sensors. Thanks to power characterization using microbenchmarks, any technology can be used in this framework. In our experimentation, the LoRa LPWAN will be addressed but other radio standards can be used. All parameters of the proposed model are given in Table 1 for the required input values and in Table 2 for the intermediate results and the outputs.

3.2. Dimensioning Energy Harvesting Components

3.2.1. Energy Consumption Model of the Platform. In order to dimension energy harvesting components, a duty-cycle model is proposed in which the node switches between a sleep state (the radio is turned off) and an awoken state for transmitting the data according to a periodical schedule. The time interval between two consecutive transmissions is called the wake up interval and is denoted T_{send} . However, to get a flexible and accurate model, two independent and distinct

operations are defined: one for the radio transmission and one for the sensing. The time profiles of these operations are described in Figure 2.

Figure 2(a) introduces the cycle of a radio transmission. The MCU is firstly awoken and consumes I_{MCU} . It then turns on the radio module that transmits the data. The radio module creates a current peak I_{Rad} during the Time on Air denoted T_{oA} . Finally, the MCU goes back to sleep. The total time of activity is denoted T_{Act} . The cycle can be split into two parts, the active and the sleep states, and the average current per each part is defined by

$$\bar{I}_{Act} = I_{MCU} + I_{Rad} \frac{T_{oA}}{T_{Act}} + I_{RadSleep} \left(1 - \frac{T_{oA}}{T_{Act}} \right), \quad (1)$$

and

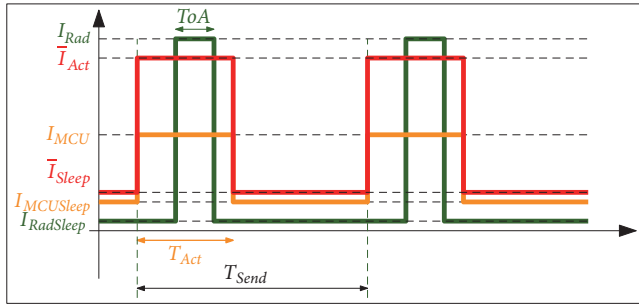
$$\bar{I}_{Sleep} = I_{MCUSleep} + I_{RadSleep}. \quad (2)$$

Figure 2(b) introduces the cycle of a data sensing. First the MCU is awoken and then orders the sensor to acquire the measure. The sensing consumes I_{Sens} and lasts T_{Sens} while the MCU is turned on during $T_{MCUSens}$. However, in order to avoid considering several times the sensor current in sleep mode, it is considered equal to zero in this case. The period between two sensing operations is denoted T_S , and the average current can be computed as

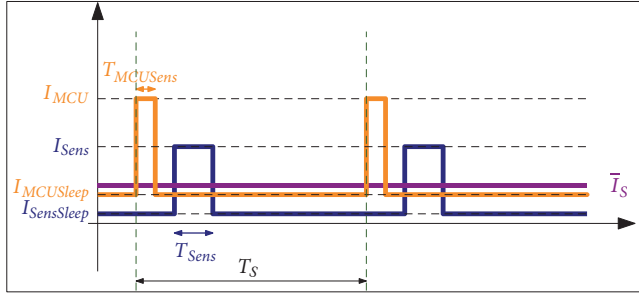
$$\begin{aligned} \bar{I}_S = & I_{MCU} \cdot \frac{T_{MCUSens}}{T_S} + I_{Sens} \cdot \frac{T_{Sens}}{T_S} \\ & + I_{SensSleep} \cdot \left(1 - \frac{T_{Sens}}{T_S} \right). \end{aligned} \quad (3)$$

TABLE 2: Intermediate and output parameters description.

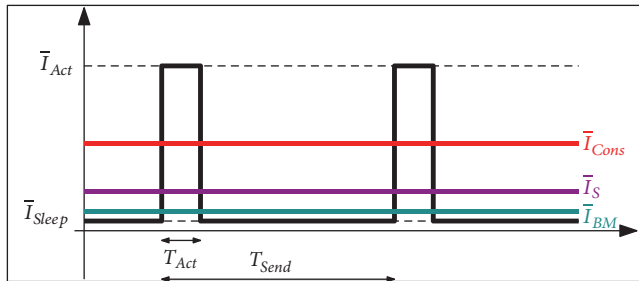
Name	Unit	Description
\bar{I}_{Act}	mA	average consumed current of a transmission in active mode
\bar{I}_{Sleep}	mA	average consumed current of a transmission in sleep mode
\bar{I}_S	mA	average consumed current of a sensing operation
\bar{I}_{Cons}	mA	average consumed current of a radio transmission
\bar{I}_C	mA	total average consumed current
V_{SC}	V	supercapacity voltage
V_B	V	battery voltage
C_S	F	capacity of the supercapacity
Q_B	mA.s	electric charge of the battery
E_{CD}	mJ	consumed energy during a day
E_{RD}	mJ	harvested energy over one available day
P_{Inst}	mW	instantaneous power of the supply



(a) Cycle of a radio transmission: MCU (orange) and radio (green) current consumptions



(b) Cycle of a sensing operation: MCU (orange) and sensor (purple) current consumptions



(c) Behavior of average currents

FIGURE 2: Current time descriptions of the cycles of both radio transmission (a) and data sensing (b) operations and the simplified cycle of the total consumption (c).

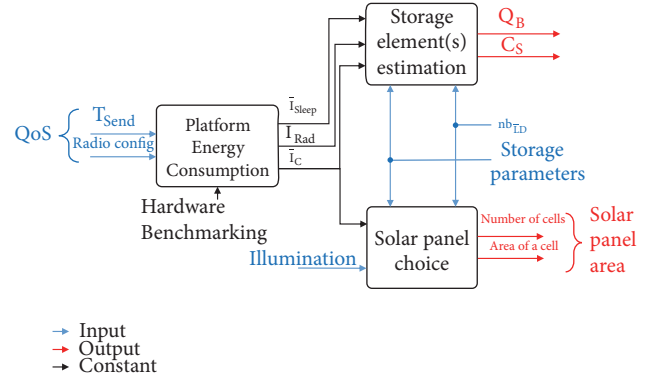


FIGURE 3: Sizing methodology diagram.

Figure 2(c) recaps the model with the currents of both transmission and sensing cycles as well as the current consumption of the battery manager \bar{I}_{BM} . Then the overall current \bar{I}_{cons} is defined as the mean of the sum of those three components:

$$\bar{I}_{Cons} = \bar{I}_{Act} \cdot \frac{T_{Act}}{T_{Send}} + \bar{I}_{Sleep} \cdot \left(1 - \frac{T_{Act}}{T_{Send}}\right) + \bar{I}_S + \bar{I}_{BM}. \quad (4)$$

Based on this two-step model (i.e., transmission and sensing), Figure 3 introduces the proposed methodology for choosing sizes of energy storage devices (i.e., both battery and capacitor) and harvesting components (i.e., solar panel area) of the previously introduced platform. These elements depend on QoS parameters, hardware characteristics, and environmental harvesting conditions. To this aim, the first step is to precisely control the consumed energy of the board.

Assuming that all parameters of (4) are known, the average consumed current \bar{I}_C can be computed according to the efficiency rate μ_{MPPT} of MPPT device:

$$\bar{I}_C = \frac{\bar{I}_{Cons}}{\mu_{MPPT}}. \quad (5)$$

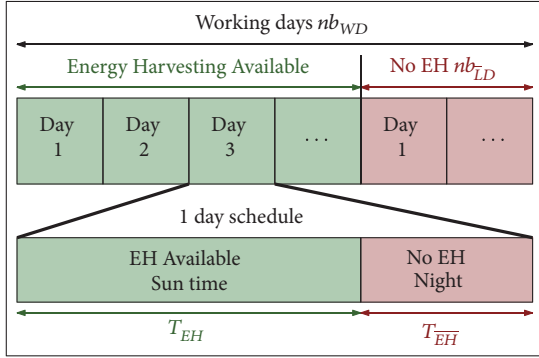


FIGURE 4: Harvesting schedule on several days and on one day.

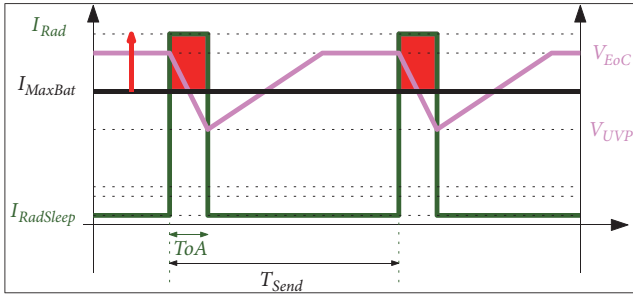


FIGURE 5: Absorption of the current peak of the radio module with capacity and battery.

3.2.2. Sizing Energy Storage Devices. The storage capacity is directly linked to both the node activity and the harvesting capabilities. The model of the solar energy harvesting considered in this work is illustrated in Figure 4 and is composed of two scales: (i) the large scale is based on the number of working days nb_{WD} split into the available and no available harvesting days (nb_{LD}), for example, when a climatic event occurs like a storm; (ii) the small scale is about a day (24 hours) composed of the durations T_{EH} and $T_{\overline{EH}}$ during which energy harvesting is available or not, respectively.

In our platform model, the node embeds both a battery and a supercapacitor. The battery should be able to provide the current \bar{I}_C during nb_{LD} days or $T_{\overline{EH}}$ and leads to the inequality constraints on the battery size Q_B :

$$Q_B \geq \bar{I}_C \times 3600 \times 24 \times nb_{LD}. \quad (6)$$

$$Q_B \geq \bar{I}_C \times T_{\overline{EH}}. \quad (7)$$

The capacitor goal is to absorb the peak of current during the transmission. The behaviors of both the current and the voltage are described in Figure 5. We assume that the battery is undersized compared to the current peak of the radio module; i.e., the maximum current provided by the battery I_{MaxBat} is lower than the current I_{Rad} . In this case, the capacitor size is computed by considering the current variation during ToA between I_{Rad} and I_{MaxBat} while the capacitor voltage drops. Indeed, the storage capacitor voltage V_{SC} varies between the maximum value V_{EoC} corresponding to the End of Charge and the minimum value V_{UVP} . Under

Voltage Protection in order to avoid destruction. The worst case during the current peak is a total variation from V_{EoC}^C to V_{UVP}^C and leads to the constraint:

$$C_S \geq ToA \times \frac{I_{Rad} - I_{MaxBat}}{V_{EoC} - V_{UVP}}. \quad (8)$$

The node can also be powered by using of only a supercapacitor. In this case, the supercapacitor should provide all the electric charge Q_B (instead of only the current peak). However, for most QoS scenarii, its size will be very high (several Farads), leading to an over-pricing of the node. The cheapest solution is therefore to associate a battery and a supercapacity.

3.2.3. Sizing Solar Panel. The simplest way to calculate the solar panel size is to define the energy budget. Firstly, the average consumed energy of the system during a day is calculated:

$$E_{CD} = \bar{I}_C \times V_{EoC} \times 24 \times 3600. \quad (9)$$

Knowing the number of working days and the number of days without light, the energy that has to be harvested during one available day is

$$E_{RD} = \frac{E_{CD} \times nb_{WD}}{nb_{WD} - nb_{LD}}. \quad (10)$$

The instantaneous power of the supply is then given by

$$P_{Inst} = \frac{E_{RD}}{T_{EH}}. \quad (11)$$

The final step requires some more information related to the geographical position of the system and the solar panel. To this aim, Look-Up Tables (LUTs) of the following parameters are used:

- (i) produced current density of the photo-voltaic panel (mA/cm^2) as a function of the illuminance (lx),
- (ii) voltage of a photo-voltaic cell (V/cell) as a function of the illuminance (lx),
- (iii) produced current density of the photo-voltaic panel (mA/cm^2) as a function of the output voltage (V) which allows us to extract optimum voltage and current and consequently the maximum output power.

These LUTs are given by the Panasonic amorphous silicon solar cell specifications [21]. Using these LUTs, the minimum solar panel size according to the number of cells and the area of each cell for a given illumination can be computed according to the previously defined instantaneous power P_{Inst} .

4. Designing Platform for LoRa Communication

This section aims to apply the proposed methodology to design a LoRa-based platform powered by solar energy

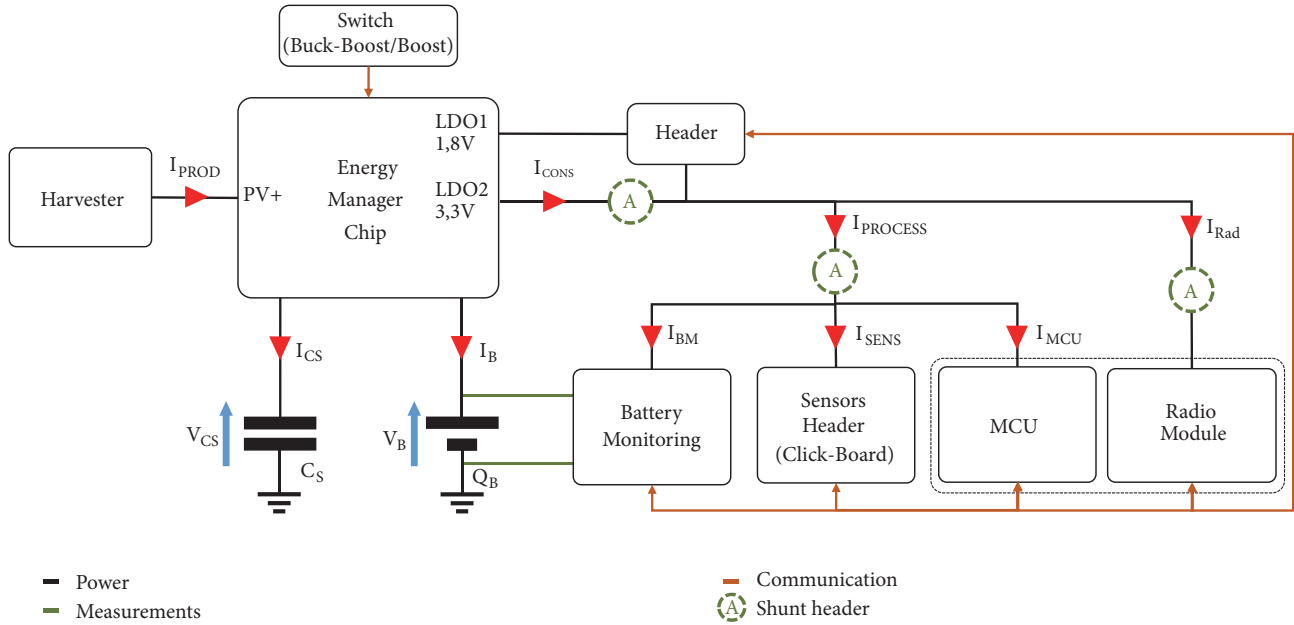


FIGURE 6: Board block diagram with energy harvesting source.

source. First, a platform has been designed using the model introduced in Section 3.1. Then, the dimensioning methodology is applied to explore the design space of the platform. As described in Figure 3, the energy consumption of the platform must be firstly characterized thanks to microbenchmarking. Then, using energy measurement values for different LoRa configurations, a design exploration is performed to see the influence of different configurations (QoS and illumination) on the hardware sizing (solar panel area and energy storage size).

4.1. Platform Design. A platform combining LoRa communication and energy has been designed and implemented using off-the-shelf components. The block diagram of the platform is given in Figure 6 while a picture of the board is shown in Figure 7. This part introduces the different blocks of both the energy harvesting part and the processing part.

4.1.1. Energy Harvesting Part. The energy harvesting part aims to supply the processing part. It is made up of the energy manager chip (SPV1050), the harvester (solar panel, Peltier module, ...), a way to store the harvested energy (a supercapacitor and/or a battery), and a chip able to measure the current and voltage of the battery.

The energy manager is implemented using the SPV1050 chip because it embeds MPPT technique, requires few external components, has a large input voltage operating range (from 150 mV to 18 V), and has a relatively low cost. However, its efficiency is a little bit lower than other PMICs having smaller input voltage operating range. A 4P2T slide switch enables changing the SPV1050 configuration from Buck-Boost to Boost. With this feature, the type of harvesters (e.g., solar panels or Peltier module) can be easily changed.

For the energy storage, both previously mentioned configurations are available (i.e., using a battery and a

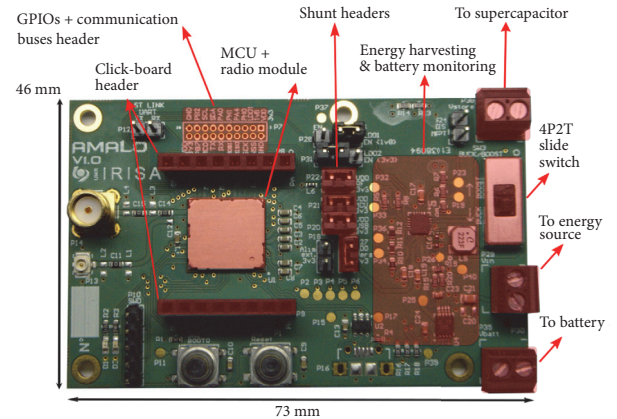


FIGURE 7: Prototype of the energy harvesting LoRa platform.

supercapacitor, or only a capacitor). Indeed, it is possible to connect a supercapacitor in order to absorb the current peaks that can occur for a transmission for instance. In addition, the SPV1050 allows the charge of any battery by configuring the protection voltages V_{EoC} and V_{UVP} .

In order to monitor at run-time the battery state-of-charge, the INA226 chip from Texas Instruments is implemented in the platform. It allows measuring both the battery voltage and the current and is connected to the MCU thanks to an I²C serial port. This feature allows to dynamically manage the processing block consumption by modifying the QoS for example.

4.1.2. Processing Part. The processing part allows the system to perform measurements of its environment using diverse

sensors and to send them to a gateway using a LoRa long-range radio. This part relies on the CMWX1ZZABZ-078 chip from the ABZ Murata because it gathers a micro-controller (STM32L082CZ), a LoRa module (SX1276), and an impedance matching line on a single system-on-chip. The STM32 micro-controller is a Cortex M0+ optimized for low power applications. Its 192kB flash memory enables embedding both the LoRaWAN stack and the application code. In addition to the radio module, the micro-controller is connected to the sensors and to the battery monitoring chip (INA226).

The connection to sensors is achieved by dedicated Click-Board headers or by the other pin headers with several interfaces (SPI, UART, and I²C) and GPIOs. These interfaces are shown on Figure 7. Moreover, in order to characterize the platform by monitoring the current consumptions of the different parts, several shunt headers have been placed on the board to perform external current measurements (I_{CONS} , $I_{PROCESS}$, and I_{Rad}). Figure 6 gives the block diagram of the board with the different ICs and the headers.

4.2. Energy Consumption Evaluation. Different current measurements can be performed using the shunt headers shown in Figure 6: the total current consumption of the system, the current consumption of the LoRa module, and the current consumption of the processing part (MCU, battery monitoring, and sensors). These measurements are important to characterize the different configurations of the platform that depend on the MCU modes and LoRa parameters.

Indeed, using LoRa transmission, the more range we want, the more consumption we will have. A trade-off between energy consumption and the range of the communication must be considered [22]. This trade-off is controlled by the spreading factor (SF), the bandwidth (B), the coding rate (CR), and the transmission power (P_{Tx}). The CR parameter corresponds to the additional data overhead ratio incurred by the cyclic error coding to perform forward error detection and correction and takes value in the range between 4/8 and 4/5. The SF takes value in the range between 6 and 12 and BW between 125 kHz and 500 kHz. The bitrate denoted R_b , for a LoRa communication, is calculated as follows:

$$R_b = SF \cdot \frac{B}{2^{SF}} \cdot CR. \quad (12)$$

The modification of just one of the four parameters can significantly change the time on air of a LoRa communication and therefore the energy consumption. Because the space defined by these parameters is large, 3 setups corresponding, respectively, to the highest bit-rate setup (SH), the LoRa default setup (SD), and the lowest bit-rate setup (SL) were considered in this work. Table 3 shows the parameter values for each setup. Because the resulting datarates are different, the packet ToA depends on the used setup.

Figure 8 gives the different steps of the packet transmission process and the corresponding states are indicated. These steps are the ones introduced in Figure 2. The accuracy of the measurements shows that hardware and software overheads occur at the beginning and at the end of the

TABLE 3: LoRa setups used for energy measurement.

	SH	SD	SL
CR	$\frac{4}{5}$	$\frac{4}{5}$	$\frac{4}{8}$
B (kHz)	500	125	125
SF	6	7	12
R_b (kbps)	37.5	5.47	0.183

TABLE 4: Current consumption of the transmission process steps.

	Mode	Current
Transceiver	I_{Rad}	cf. Figure 9
	$I_{RadSleep}$	$0.5 \mu A$
MCU	I_{MCU}	$9.5 mA$
	$I_{MCUSleep}$	$2.8 \mu A$

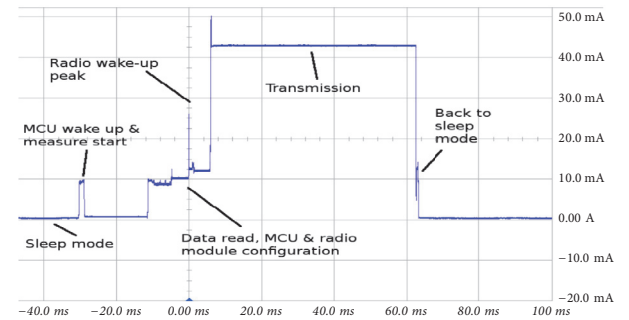


FIGURE 8: Microbenchmark of both MCU and LoRa transmission.

processes. Table 4 shows the current consumption of the most significant operation states.

The current consumption I_{Rad} of LoRa transceiver is given in Figure 9 for different transmission powers P_{Tx} . The figure shows that increasing the transmission power from 0 dBm to 14 dBm only doubles the current consumption. Therefore, the packet ToA will have a higher influence on the energy required for sending a packet than the transmission power. Table 5 gives the energy required for sending a 25 bytes payload using each setup and for different transmission powers P_{Tx} . The energy required to send a packet using the SL setup is two orders of magnitude higher than the energy required to send a packet using the SH setup. This is due to the much lower bit-rate incurred by the lower bandwidth and the higher spreading factor, as well as the data overhead caused by a higher code rate.

4.3. Design Exploration. The experimental characterization of the proposed platform results in a fine knowledge of the current consumption for all processing steps. By combining these measurements and the QoS requirements (the method is detailed in the above Section 3), both the solar panel area and the energy storage size can be computed. This part aims to show the impact of the QoS on the hardware dimensioning. The influence of the illuminance is also evaluated.

First, the solar panel area is clearly linked to the illuminance where the node is deployed. Figure 10 explores

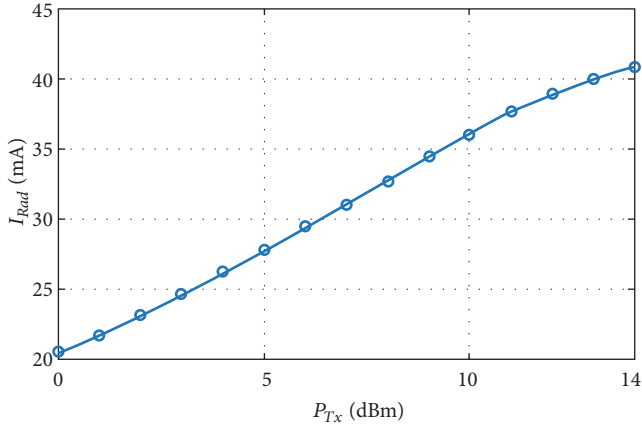


FIGURE 9: Current consumption I_{Rad} of LoRa transceiver for different transmission powers P_{Tx} .

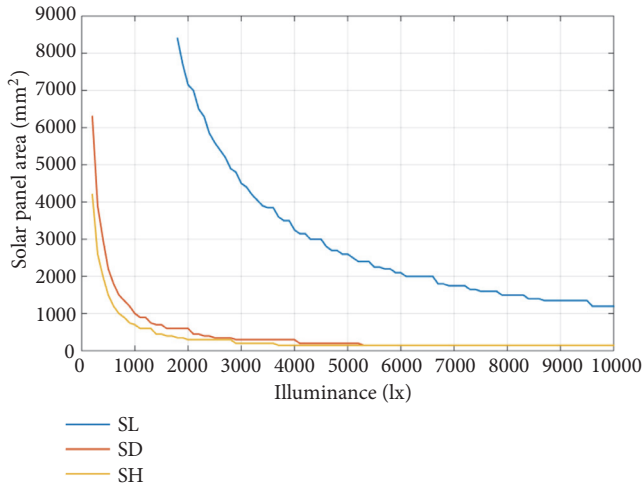


FIGURE 10: Solar panel area with respect to illuminance for different LoRa configurations.

this relation for the three LoRa setups with a 14 dBm transmission power, a 25B payload, and T_{send} set to 5 mn. The illuminance ranges from 200 lx, corresponding to minimum indoor irradiance allowed in offices to 10000 lx, which is the maximum outdoor irradiance [23, 24]. First, results show that the minimal solar panel area can be orders of magnitude (in mm^2) different depending of the illuminance of the node. For instance, a 60 cm^2 is required for the SD setup in an indoor deployment while only a 5 cm^2 can be used in a sunny outdoor environment. The LoRa setup has also a huge impact on the solar panel area. For a 5000 lx illuminance, an area of 25 cm^2 must be used for SL setup while less than 5 cm^2 is required for SD and SH setups.

The impact of the QoS on the battery size is also evaluated. Figure 11 gives the minimal value of the battery needed to respect a given QoS expressed by T_{send} . The same configurations as for Figure 10 are used. However, another key parameter to setup the capacity is the margin needed to respect the QoS during periods of energy scarcity. This parameter is set to 2 days per week without any illuminance.

TABLE 5: Energy consumption according to LoRa configurations.

LoRa Setup	ToA (ms)	P_{Tx} (dBm)	Energy (mJ)
SH	8.99	0	0.99
		10	1.45
		14	1.59
SD	61.7	0	4.58
		10	7.73
		14	8.70
SL	1974.27	0	134.72
		10	235.57
		14	266.65

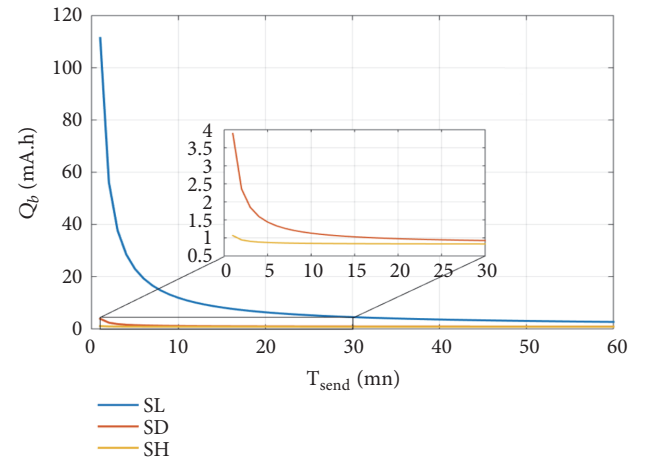


FIGURE 11: Battery sizes with respect to packet generation periods T_{send} for different LoRa configurations.

Moreover, by applying (8), the supercapacitor needs to be set to 148.87 mF in order to absorb the current peaks of the transmission process (40.9 mA for P_{Tx} of 14 dBm). Results show that increasing T_{send} from 1 mn to 60 mn induces a battery reduction factor of 41 for SL setup, of 4.5 for SD setup and 1.3 for SH setup. The more energy the setup consumes, the higher the factor will be. Moreover, this reduction depends on a compromise between the QoS and the number of days without any illuminance.

Finally, to illustrate the benefit of a fine computation of the solar panel area, the impact of the platform localization is given in Figure 12. In this figure, the solar panel area is computed according to the minimum illuminance for each region of France. The same configurations and QoS are targeted for all regions: LoRa SL setup is used with a 14 dBm transmission power and a 25B payload, T_{send} is set to 5 mn, and the margin is set to 1 day without any light. Dimensioning results show that the solar panel area can range from 17.5 cm^2 in the South of France to 44 cm^2 in North of France. Therefore, an area reduction more than 2 times can be achieved to keep a LoRa node autonomous depending of its localization.

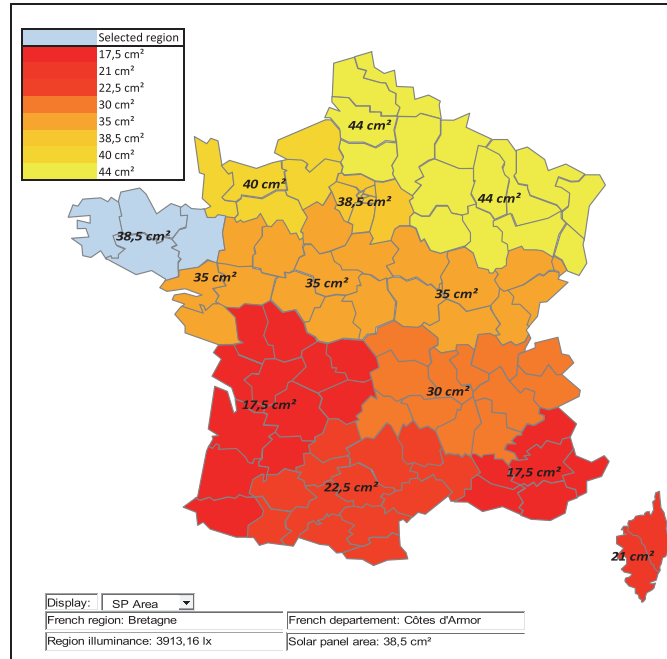


FIGURE 12: French map of solar panel area.

5. Experimental Validation: In-Field Deployment

5.1. Experimental Setup. The proposed methodology was applied for two different QoS and two LoRa-based platforms were implemented. Node 1 used the SL setup (i.e., spreading factor SF=12) with a 14 dBm transmission power and had a sending period T_{send} of 5 mn. Node 2 used the same configuration but its SF was reduced to 10 and T_{send} set to 1 mn. Node 1 has therefore a longer ToA (1974.27 ms) than Node 2 (411.65 ms) but a longer sending period. Node 1 senses temperature and humidity while Node 2 also embeds a pluviometer (inducing a negligible power consumption overhead). The battery size is set with a margin so that nodes can operate during two days without any light.

To set both solar panel area and battery size of Node 1, Figures 12 and 11 are used as they address the same configuration. Considering a deployment in the French Brittany region, Figure 12 shows that a minimal solar panel area of 38.5 cm^2 is required. Figure 11 shows that SL setup achieves T_{send} of 5 mn when a battery size of at least 26.3 mA.h is used. Constrained by off-the-shelf components, the platform has been implemented with a 40.7 cm^2 ($7.4 \times 5.5 \text{ cm}$) solar panel, a 35 mA.h LiPo battery, and a 220 mF supercapacity from Murata. For Node 2, its configuration was chosen in order to achieve the same hardware dimensioning.

For validation purpose, both nodes were deployed on the roof of the laboratory building, as shown in Figure 13. The nodes were deployed under the same illuminance conditions. The gateway was installed in an office room and at around 20 m far from the nodes. The range was not considered in this experimentation to evaluate only the impact of the energy harvesting on the QoS. The gateway was battery powered to

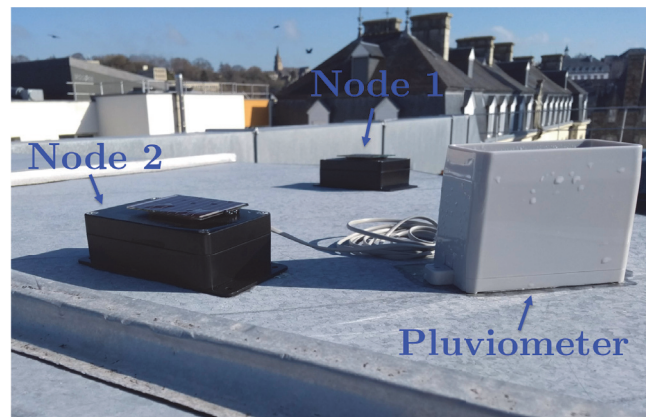


FIGURE 13: Photography of the two nodes deployed on the building roof.

gather data from both nodes, i.e., the 25B payload composed of all sensed values and the battery state-of-charge. The experiment lasted 15 days from March 8th to March 22nd.

5.2. Experimental Results. The values from the sensors show that the weather was quite favourable during these days. The average temperatures were 21.1 degrees during days and 8.2 degrees during nights for Node 1; 20.7 degrees during days and 8.35 degrees during nights for Node 2. The pluviometer of Node 2 measured no rain precipitation over experimentation. These values are higher than the normal ones for this season: 11.5 degrees during days, 5.4 degrees during nights, and 95.7 mm of precipitation. The illuminance was also very high compared to the value used to set the solar panel area.

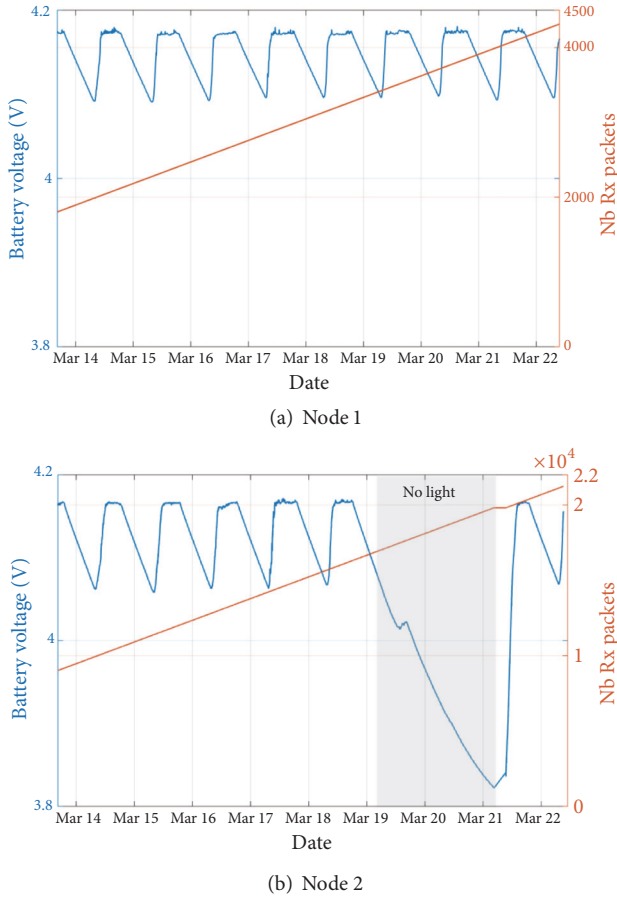


FIGURE 14: Battery voltage and frame counter for the two nodes.

Figure 14 shows the obtained results. The battery state-of-charge and the frame counter are plotted for the last 9 days. Figure 14(a) gives the results for Node 1 with the lowest QoS ($T_{send}=5$ mn) and Figure 14(b) the results for Node 2 with the highest QoS ($T_{send}=1$ mn). Results show that both nodes operate without any packet loss during the 15 days, reaching a total of 4308 packets for Node 1 and 21233 packets for Node 2. In order to evaluate the robustness against periods of energy scarcity, Node 2 was turned upside down at the beginning of March 19th so that it does not harvest any energy. In these conditions, Node 2 still operates during more than two days, as expected, showing the good sizing of the battery. After the first packet losses, the node was powered again and quickly reached its periodic behavior.

6. Conclusion

LPWAN technologies represent a real opportunity for applications requiring both long-range and low power consumption, such as environmental monitoring or connected farms. We proposed in this paper an energy autonomous wireless node platform leveraging LoRa technology. Optimizing the size of the energy storage and harvesting elements of the platform is of prime importance, because it will directly impact the form factor of the global platform. On the one

hand, to deal with the distance to the base station and channel impairments, LoRa offers several configurations by properly tuning the spreading factor or the error correcting code, but this dramatically changes the time-on-air, therefore leading to very different energy consumption for transmitting the same amount of data. On the other hand, the climate of the area where nodes are deployed also means very different light conditions. Thanks to hybrid energy modelling including accurate benchmarking on our platform, a methodology was proposed to optimize the key elements of the wireless node, ensuring application requirements while taking into account node environment. An exploration was driven to highlight the impacts of both time-on-air and illuminance on this sizing. As a toy example, it was shown that, for the same quality of service, the size of the solar panel has to be twice in the North of France than in the South, and this ratio is directly linked to the size of the whole wireless sensor node.

Data Availability

No data were used to support this study.

Conflicts of Interest

The authors declare that there are no conflicts of interest regarding the publication of this paper.

Acknowledgments

This work has been conducted in the context of the AAP PME ALAMO project labelled by the “Pôle Images & Réseaux” and funded by “Région Bretagne” and “Lannion Trégor Communauté”.

References

- [1] M. Centenaro, L. Vangelista, A. Zanella, and M. Zorzi, “Long-range communications in unlicensed bands: The rising stars in the IoT and smart city scenarios,” *IEEE Wireless Communications Magazine*, vol. 23, no. 5, pp. 60–67, 2016.
- [2] F. A. Aoudia, M. Gautier, M. Magno, M. L. Gentil, O. Berder, and L. Benini, “Long-short range communication network leveraging LoRa™ and wake-up receiver,” *Microprocessors and Microsystems*, vol. 56, pp. 184–192, 2018.
- [3] R. J. M. Vullers, R. V. Schaijk, H. J. Visser, J. Penders, and C. Hoof, “Energy harvesting for autonomous wireless sensor networks,” *IEEE Journal of Solid-State Circuits*, vol. 2, no. 2, pp. 29–38, 2010.
- [4] A. Kansal, J. Hsu, S. Zahedi, and M. B. Srivastava, “Power management in energy harvesting sensor networks,” *ACM Transactions on Embedded Computing Systems*, vol. 6, no. 4, article 32, 2007.
- [5] T. N. Le, A. Pegatoquet, O. Berder, O. Sentieys, and A. Carer, “Energy-neutral design framework for supercapacitor-based autonomous wireless sensor networks,” *ACM Journal on Emerging Technologies in Computing Systems*, vol. 12, no. 2, pp. 1–19, 2015.
- [6] M. A. Green, Y. Hishikawa, W. Warta et al., “Solar cell efficiency tables (version 50),” *Wiley Journal of Progress in Photovoltaics: Research and Applications*, vol. 25, no. 7, pp. 668–676, 2010.

- [7] W. Lee, M. J. Schubert, B. Ooi, and S. J. Ho, "Multi-source energy harvesting and storage for floating wireless sensor network nodes with long range communication capability," *IEEE Transactions on Industry Applications*, vol. 54, no. 3, pp. 2606–2615, 2018.
- [8] F. Ait Aoudia, M. Gautier, and O. Berder, "RLMan: an energy manager based on reinforcement learning for energy harvesting wireless sensor networks," *IEEE Transactions on Green Communications and Networking*, vol. 2, no. 2, pp. 408–417, 2018.
- [9] F. A. Aoudia, M. Gautier, and O. Berder, "Fuzzy power management for energy harvesting Wireless Sensor Nodes," in *Proceedings of the ICC 2016 - 2016 IEEE International Conference on Communications*, pp. 1–6, Kuala Lumpur, Malaysia, May 2016.
- [10] I. Analog Devices, "LTC3108 - Ultralow voltage step-up converter and power manage," <http://www.analog.com/en/products/power-management/energy-harvesting/ltc3108.html>.
- [11] T. I. Inc., "BQ25570 - ultra low power harvester power management IC with boost charger, and nanopower buck converter," <http://www.ti.com/product/bq25570>.
- [12] STMicroelectronics, "SPV1050 - Ultra low power energy harvester and battery charger with embedded MPPT and LDOs," <https://www.st.com/en/power-management/spv1050.html>.
- [13] Zoliton, "Z-Node: World's first and only autonomous cognitive sensor," <https://zoliton.com/our-products/zoliton-z-node/>.
- [14] Micropelt, "Self-powered radiator valve," http://www.micropelt.com/fileadmin/user_upload/_PDF_MVA004_datasheet_IDSMVA004_0817v11e.pdf.
- [15] Trameto, "Delivering any-many-multi source, micro-energy harvesting," <https://trameto.com/technology/>.
- [16] C. Goursaud and J. M. Gorce, "Dedicated networks for IoT: PHY / MAC state of the art and challenges," *EAI Endorsed Transactions on Internet of Things*, vol. 1, no. 1, p. 150597, 2015.
- [17] M. Magno, F. A. Aoudia, M. Gautier, O. Berder, and L. Benini, "WULoRa: An energy efficient IoT end-node for energy harvesting and heterogeneous communication," in *Proceedings of the 20th Design, Automation and Test in Europe, DATE 2017*, pp. 1528–1533, Lausanne, Switzerland, March 2017.
- [18] F. Wu, J. Redoute, and M. R. Yuce, "WE-Safe: a self-powered wearable IoT sensor network for safety applications based on LoRa," *IEEE Access*, vol. 6, pp. 40846–40853, 2018.
- [19] P.-D. Gleonec, J. Ardouin, M. Gautier, and O. Berder, "Architecture exploration of multi-source energy harvester for IoT nodes," in *Proceedings of the 2016 6th Annual IEEE Online Conference on Green Communications, OnlineGreenComm 2016*, pp. 27–32, November 2016.
- [20] P. Gleonec, J. Ardouin, M. Gautier, and O. Berder, "A real-world evaluation of energy budget estimation algorithms for autonomous long range IoT nodes," in *Proceedings of the 2018 25th International Conference on Telecommunications (ICT)*, pp. 561–565, Saint-Malo, France, June 2018.
- [21] Panasonic, "Amorphous Silicon Solar Cells Amorphous Photosensors," https://www.panasonic-electric-works.com/cps/rde/xbcr/pew_eu_en/ca_amorton_solar_cells_2018_en.pdf.
- [22] X.-C. Le, B. Vrigneau, M. Gautier, M. Mabon, and O. Berder, "Energy/Reliability Trade-off of LoRa Communications over Fading Channels," in *Proceedings of the 25th International Conference on Telecommunications, ICT 2018*, pp. 544–548, France, June 2018.
- [23] Y. Xie, M. Sengupta, and M. Dooraghi, "Assessment of uncertainty in the numerical simulation of solar irradiance over inclined PV panels: New algorithms using measurements and modeling tools," *Solar Energy*, vol. 165, pp. 55–64, 2018.
- [24] National Renewable Energy Laboratory (NREL), <http://www.nrel.gov/>.

Research Article

Harvested Energy Maximization of SWIPT System with Popularity Cache Scheme in Dense Small Cell Networks

Xuefei Peng and Jiandong Li 

The State Key Laboratory of Integrated Service Networks, Xidian University, Xi'an 710071, China

Correspondence should be addressed to Jiandong Li; jdli@xidian.edu.cn

Received 10 January 2019; Revised 7 March 2019; Accepted 27 March 2019; Published 1 July 2019

Guest Editor: Zoran Stamenkovic

Copyright © 2019 Xuefei Peng and Jiandong Li. This is an open access article distributed under the Creative Commons Attribution License, which permits unrestricted use, distribution, and reproduction in any medium, provided the original work is properly cited.

In this paper, we propose a harvested energy maximization problem of simultaneous wireless information and power transfer (SWIPT) system with popularity cache scheme in dense small cell networks. Firstly, network model, content request, and popularity cache schemes are provided in the system model. Then, we establish a harvested energy maximization problem of SWIPT system with popularity cache scheme in dense small cell networks, where maximum transmit power of small cell base stations (SBSs), minimum rate requirement, i.e., quality of service (QoS) of user terminals (UTs), and power splitting ratio are considered. Further, an iterative power splitting ratio and power allocation optimization (IPSPA) algorithm is proposed to solve the formulated problem. Finally, the better performance of our proposed method is demonstrated through a number of simulations. These results are of significance for maximizing harvesting energy of UTs and reducing consumption of backhaul resources and energy.

1. Introduction

In future, the fifth generation (5G) wireless network will be characterized by energy-limited environment that is inconvenient to connect with fixed charging facilities [1–3]. Energy storage can provide power for UTs by storing energy in their batteries. Traditional energy harvesting method cannot achieve information transmission when it stores energy. Compared with traditional energy storage methods, simultaneous wireless information and power transfer (SWIPT) is a promising energy harvesting technology that allows UTs to harvest energy from radio signals by sensing radio frequency sent by surrounding small cell base stations (SBSs). Moreover, SWIPT system can guarantee UTs performing information decoding (ID) and energy harvesting (EH) simultaneously without interrupting data transmission through adopting power splitters. SWIPT is a key technical innovation that promotes the development of the energy field and may bring vital changes to wireless communication networks [1–3]. Nevertheless, dense small cell deployment in 5G wireless communication networks will introduce several major technical challenges. On the one hand, spectrum sharing among small cells leads to severe interference in the networks.

On the other hand, this large deployment creates a new burden on backhaul links for all the SBSs. Therefore, it is necessary to maximize harvested energy of SWIPT system by exploring interference and increasing the time for energy harvesting, as well as save backhaul resources and energy through reducing backhaul load. In this paper, we explore both useful and interference radio frequency signals in dense small cell networks as the energy harvesting source and introduce SBSs with the ability of caching in SWIPT system to decrease the distance between UTs and their desired contents. Here, note that contents in this paper refer to voice, video, data or files, etc. Aiming at maximizing harvested energy of the SWIPT system with popularity cache scheme and reducing backhaul load, we propose a harvested energy maximization problem considering constraints of the transmit power of SBSs, quality of service (QoS) of UTs, and power splitting ratio of SWIPT system. We firstly determine content request and popularity cache schemes. Then, we provide the popularity cache-based user association scheme and resource allocation scheme. Further, we propose an iterative power splitting ratio and power allocation optimization (IPSPA) algorithm to solve the formulated problem. Our proposed scheme has two advantages compared to traditional SWIPT

system in which SBSs do not have the capability of caching from local SBSs and have to fetch each content (voice, video, data or a file, etc.) from the core network through backhaul links. One advantage is reduction of the time of fetching contents from core network by obtaining some of the contents from local SBSs, thereby providing more time to harvest energy and improve energy harvesting efficiency. The other advantage is the reduction of backhaul links load through employing the proposed popularity caching scheme of SBSs.

The paper is organized as follows. The description of related work is given in Section 2. In Section 3, we outline the system model including network model, content request, and popularity cache schemes. In Section 4, we formulate and solve the harvested energy maximization problem of SWIPT system with popularity cache scheme in dense small cell networks. Complexity analysis of the proposed solution is given in Section 5. In Section 6, a number of simulations are provided. Finally, Section 7 concludes the paper.

2. Related Work

Recently, some works have studied energy problem about SWIPT system from the aspects of optimizing time, power, power splitting ratio, and channel resource [4–12]. The coupled time and power allocation problem of user-centric energy efficiency maximization problem considering time switching protocol for wireless powered communication network was solved by the proposed iterative resource allocation scheme in [4]. In [5], the authors presented optimal parameter design for the harvested energy maximization problem with the constraint of a minimum information rate requirement for SWIPT system, which included both channel assignment and power allocation. Reference [6] aimed to maximize the sum harvested energy considering constraints of rate, transmit power, and subchannel assignment firstly. Then, a scheme for harvested energy maximization of worst case individual link was proposed to ensure fairness among different links. In [7, 8], the authors studied SWIPT system in fog-computing networks. In [7], authors aimed to minimize energy cost of ultralow power devices through optimizing time slots and power allocation. Moreover, the conclusion that harvested energy would decrease when the number of computing operations became larger and the distance between access point and ultralow power devices increased was obtained in [7]. In [8], a quantum particle swarm optimization algorithm was introduced to minimize the total energy consumption at the source node through a power, time, and data allocation scheme while the latency requirement was maintained. Reference [9] considered a decode-and-forward relaying network based on SWIPT, where the optimal dynamic power splitting ratio and time allocation ratio for minimizing the outage probability were obtained through split-step iterative method. Moreover, the problem of maximizing the instantaneous channel capacity was solved by an alternate convex optimization method. A dynamic algorithm with a control parameter to jointly allocate the transmission power and time switching factor

was proposed in [10]. Authors in [11] proposed a unified framework to optimize the influence of SWIPT on the system throughput and energy efficiency through both time splitting and power splitting schemes. In [12], the authors established an iterative suboptimal resource allocation algorithm for multiuser to minimize total transmit power of the network. Besides, authors in [13, 14] derived exact closed-form expressions for the outage probability to evaluate the impact of power allocation on outage probability. However, SWIPT system with caching capability is not considered in [4–14].

Additionally, a number of literature works have concentrated on caching problems [15–21]. Authors in [15] employed physical caching scheme that brought both cache-induced cooperation and the cache-assisted multihopping gains. In [16], the authors considered density of SBSs, memory, and backhaul optimization problem considering wireless QoS constraint, where most popular contents prior caching scheme were adopted. In [17], the authors proposed a resource allocation optimization problem to minimize the blocking probability considering caching capacity and backhaul limitation, where multidimensional Markov chains were employed to evaluate the performance of network. Authors in [18] discussed cooperative random and uniform caching scheme between base stations (BSs) and devices to maximize the successful transmission probability, and the equivalently transformed biconvex problem was solved by block coordinate descent algorithm. In [19], the authors analyzed the probability that mobile users could successfully download their requested files from the SBSs based on partitioned file groups, random and uniform caching strategy, where impact of LoS and NLoS, transmit power, and density of SBSs were considered. In [20], the authors proposed three algorithms of power allocation to achieve different objectives, i.e., sum transmission rate maximization, average outage probability minimization, and average satisfaction maximization, to promote the performance of cache-aided small cell networks with limited backhaul capacity, where a fix ratio of requested contents was assumed to exist in local caches of SBSs, and other contents should be fetched from core networks. In [21], the authors proposed a power control method for energy harvesting SBSs and revealed that the energy and sum-throughput performances of these SBSs were influenced by energy harvesting and caching abilities. However, energy harvesting of SWIPT system and caching of contents are not considered simultaneously in [15–21].

The main contributions of this paper are summarized as follows:

- (i) Our proposed SWIPT system with popularity cache scheme has the advantages of improving harvested energy of UTs, saving backhaul resources and energy.
- (ii) We formulate the harvested energy maximization problem of SWIPT system in dense small cell networks considering the maximum transmit power of SBSs, minimum rate requirement, i.e., QoS of UTs, and power splitting ratio.

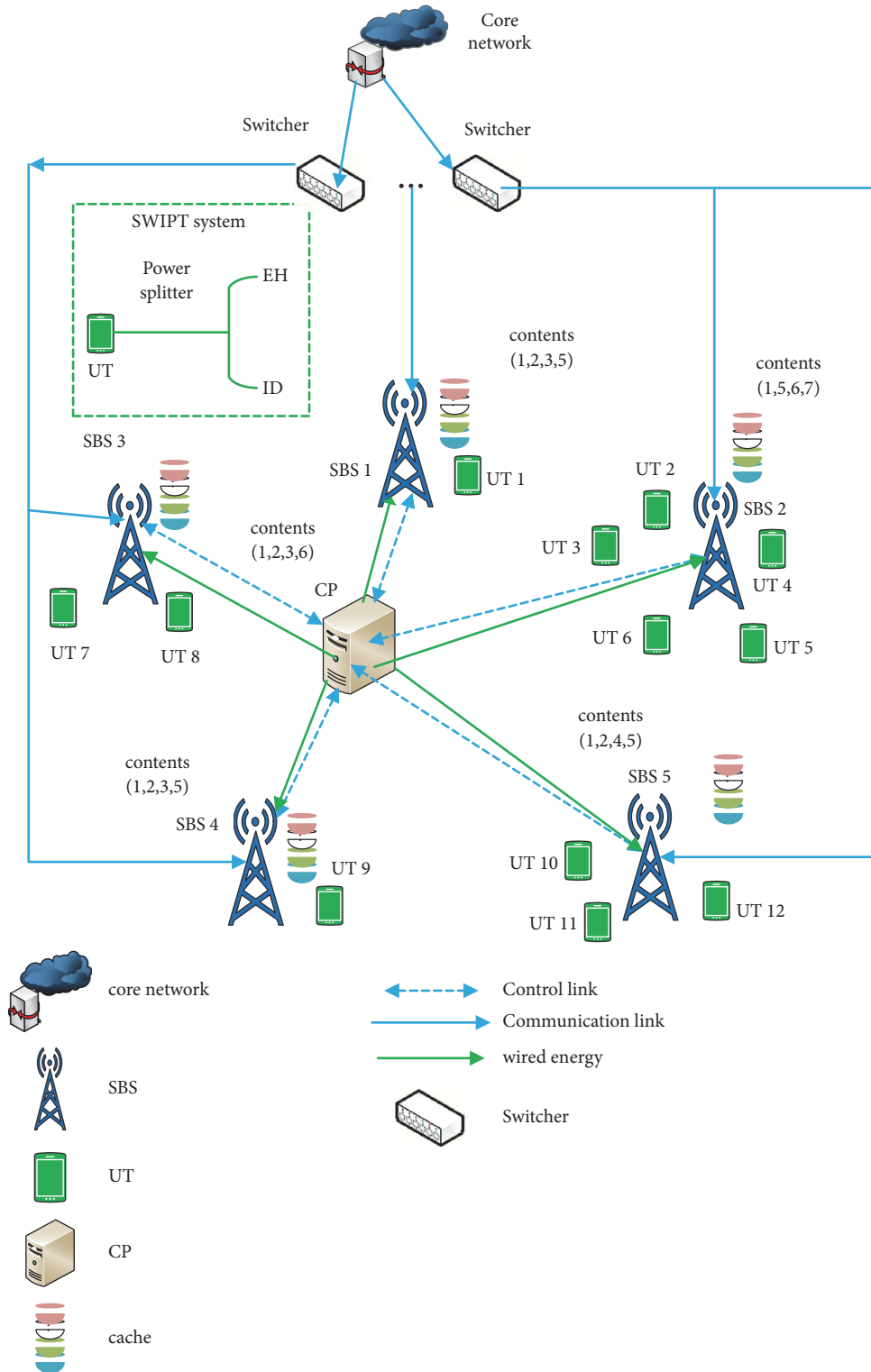


FIGURE 1: Network model.

- (iii) An IPSPA algorithm is proposed to solve the formulated harvested energy maximization problem.
- (iv) The influence of different parameters on the network performance is evaluated in the simulation.

3. System Model

3.1. Network Model. As shown in Figure 1, we consider a SWIPT system with popularity cache scheme in dense small networks. All UTs are uniformly and randomly distributed

TABLE 1: A simplified example of popularity cache-based user association scheme.

Requested content	whether requested content cached in the nearest SBS	Association scheme
content1 (UT1)	Yes (SBS1)	<i>case1</i>
content2 (UT2)	No (SBS2)	<i>case2</i>
content3 (UT3)	No (SBS2)	<i>case2</i>
content6 (UT4)	Yes (SBS2)	<i>case1</i>
content1 (UT5)	Yes (SBS2)	<i>case1</i>
content7 (UT6)	Yes (SBS2)	<i>case1</i>
content3 (UT7)	Yes (SBS3)	<i>case1</i>
content6 (UT8)	Yes (SBS3)	<i>case1</i>
content2 (UT9)	Yes (SBS4)	<i>case1</i>
content4 (UT10)	Yes (SBS5)	<i>case1</i>
content5 (UT11)	Yes (SBS5)	<i>case1</i>
content7 (UT12)	No (SBS5)	<i>case2</i>

in the coverage range of SBSs, and all SBSs are deployed in the same spectrum with the bandwidth BW and N_{BW} orthogonal frequency division multiple access (OFDMA) resource blocks (RBs). Let $\mathcal{S} = \{1, 2, \dots, j, \dots, S\}$ and $\mathcal{K} = \{1, 2, \dots, i, \dots, K\}$ denote the set of SBSs and UTs, respectively. Moreover, we let $\mathbf{x} = \{x_1, x_2, \dots, x_j, \dots, x_K\}$ denote information symbols sent by corresponding SBSs 1 to S , where $E(x_j^2) = 1$ is the energy of symbol x_j . A central processor (CP) is responsible for providing energy to the SBSs that provide service to their associated UTs, and switches are used to connect the core network and SBSs. Optical fiber is used as the medium of backhaul links. Moreover, a power splitter is configured in each user terminal (UT) forming a SWIPT system to sense the radio frequency energy of the surrounding SBSs and split the received signal into two parts, which are used for ID and EH.

3.2. Content Request and Popularity Cache Schemes. According to [17, 18], the request probability mass function of all contents can be modeled as a Zipf distribution. The probability of the f -ranked popularity content requested by UT i can be expressed as follows:

$$pp_{i,f} = \frac{1/f^\alpha}{\sum_{f=1}^F 1/f^\alpha} \quad (f \in \mathcal{F}), \quad (1)$$

where α is the parameter of the model reflecting the popularity distribution of content f . The larger α represents the fewer popular contents undertaking the majority of the requests.

For the contents caching problem, we assume that F popular contents with the same size constitute a content library, which can be denoted as $\mathcal{F} = \{1, 2, \dots, f, \dots, F\}$. Let C denote the cache size of a small cell base station (SBS). Different from current caching models [16–20], we assume that all contents are precached in each cache space of an SBS

according to Zipf distribution, and the cache spaces of an SBS are independent of each other. Therefore, the contents cached in all the spaces of SBS j obey binomial distribution $B(C, pp_{i,j,f})$, where C is the cache size of SBS j and $pp_{i,j,f} = pp_{i,f}$ is the probability that a cache space of SBS j caches content f that user i requests.

4. Problem Formulation and Solution

We study the harvested energy maximization problem of SWIPT system with popularity cache scheme through three processes, which are popularity cache-based user association scheme, resource allocation, and iterative power splitting ratio and power allocation optimization.

4.1. Popularity Cache-Based User Association Scheme. There are two cases for the popularity cache-based user association scheme. *Case1*: a number of UTs can obtain the required contents from their nearest local SBSs that cache the required contents without consuming backhaul resources. *Case2*: some UTs cannot access the contents directly from their nearest (minimum path loss) SBSs. Therefore, these UTs will fetch the required contents from the core network and choose the SBSs nearest them as their serving SBSs. We would like to use a simplified example of a snapshot shown in Figure 1 to illustrate the proposed user association scheme. In Table 1, the required contents of UT1, UT4, UT5, UT6, UT7, UT8, UT9, UT10, and UT11 are cached in their nearest SBSs, so they can obtain their required contents from local SBSs. However, the required contents of UT2, UT3, and UT12 are not cached in their nearest SBSs; they have to fetch their required contents from the core network and then be served by their nearest SBSs. Let \mathcal{B}_i denote the set of SBS that UT i is associated with, which is determined by the proposed popularity cache-based user association scheme and can be expressed as follows.

$$B_i = \begin{cases} \text{local nearest SBS} & (\text{case1}) \\ \text{nearest SBS that fetched contents by backhaul link} & (\text{case2}). \end{cases} \quad (2)$$

Then, we can derive the probability that at least one cache space of SBS j caches content f that UT i requests as follows:

$$pp_{i,j,f}^A = 1 - (1 - pp_{i,j,f})^C. \quad (3)$$

Further, we can derive the association probability that UT i associated with its nearest SBS belongs to B_i when it requests content f , i.e., hit ratio, as follows:

$$A_{i,j,f}^{hit} = pp_{i,j,f} \times (pp_{i,j,f}^A)^{|B_i|}, \quad (4)$$

$$\forall j \in \mathcal{S}, i \in \mathcal{K}, \text{ and } f \in \mathcal{F}.$$

Therefore, we can derive the probability that UT i obtains content f from local SBS and backhaul link as follows:

$$\zeta_{i,j,f} = \begin{cases} A_{i,j,f}^{hit}, & \text{local nearest SBS (case1)} \\ 1 - A_{i,j,f}^{hit}, & \text{backhaul link (case2)}. \end{cases} \quad (5)$$

Depending on practical network measurement described in [22, 23], UTs fetch contents through backhaul link will introduce delay. We denote by η_{BH} the energy harvesting impact factor, which represents energy harvesting efficiency affected backhaul link. Here, $\eta_{BH} = 1/m$ and $T_{BH} = mT$, where T_{BH} is the time of UTs obtaining contents from the core network, T is the time of UTs obtaining contents from local SBSs caching required contents, and $m > 1$ is the energy harvesting delay impact factor that denotes the relationship between the time of UTs obtaining desired contents from backhaul link and local SBSs. The illustration of energy harvesting delay impact factor m is shown in Figure 2. We set η_{BH} and m on the basis of [22, 23] in our simulation.

Consequently, we can derive the energy harvesting coefficient $\ell_{i,j,f}$ as follows:

$$\ell_{i,j,f} = \begin{cases} A_{i,j,f}^{hit}, & \text{local nearest SBS (case1)} \\ (1 - A_{i,j,f}^{hit}) \times \eta_{BH}, & \text{backhaul link (case2)}, \end{cases} \quad (6)$$

where energy harvesting coefficient $\ell_{i,j,f}$ represents energy harvesting efficiency of UTs obtaining contents from local SBSs (case 1) and backhaul link (case 2), and energy harvesting impact factor η_{BH} indicates the energy harvesting efficiency affected by backhaul link.

4.2. Resource Allocation. After the aforementioned analysis of popularity cache-based user association scheme, we will determine the RBs assigned to each UT. Assume that N_{BW} OFDMA RBs of the system are equally allocated to the UTs associated with each SBS. Each RB has the bandwidth of 0.18 MHz. Therefore, there is no intracell interference, while there exists intercell interference since all the RBs of the system are shared among different SBSs. Let $\mathcal{N} = \{1, 2, \dots, n, \dots, N\}$ denote the set of subbands allocated to the UTs deployed in the network, where the

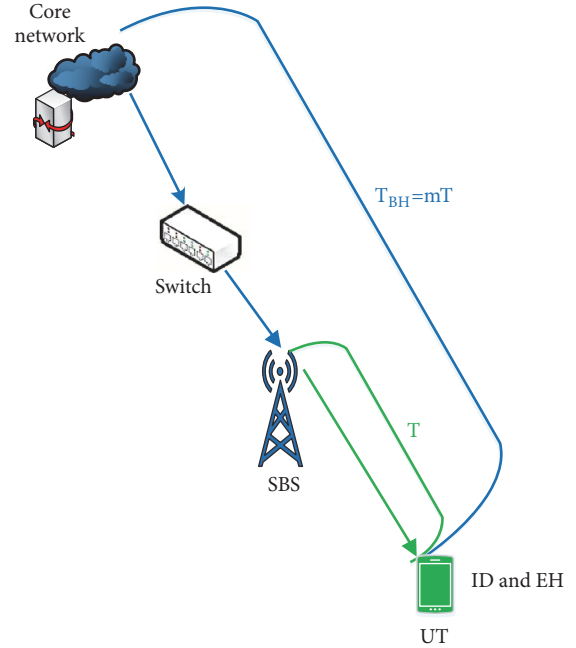


FIGURE 2: Illustration of energy harvesting delay impact factor m .

resource blocks allocated to a UT are defined as a subband. Besides, let \mathcal{K}_j denote the set of UTs that SBS j associated with. Then, the subbandwidth of UT i associated with SBS j can be denoted as $BW_i = 0.18 \times \lfloor N_{BW} / |\mathcal{K}_j| \rfloor$ MHz, where $\lfloor N_{BW} / |\mathcal{K}_j| \rfloor$ represents the maximum integer not larger than $\lfloor N_{BW} / |\mathcal{K}_j| \rfloor$.

4.3. Iterative Power Splitting Ratio and Power Allocation Optimization. After the analytical processes of popularity cache-based user association and resource allocation schemes, we can determine the set of SBS that each UT is associated with, energy harvesting coefficient of each content requested by UTs, and the subbandwidths allocated to the UTs. In this phase, we maximize the harvested energy of the SWIPT system considering the minimum rate requirement, i.e., QoS of UTs, by optimizing power splitting ratio and power allocation from SBSs to UTs. Let $\mathbf{p} = (p_{i,j,n})_{K \times S \times N}$ denote the transmit power of SBSs, where $p_{i,j,n}$ represents the transmit power from SBS j to UT i on subband n . Then, the received signal of UT i on subband n from SBS j can be written as

$$y_i = \sqrt{p_{i,j,n}} h_{i,j,n} x_j + \sum_{j \notin \mathcal{S}_i} \sqrt{p_{i,j,n}} h_{i,j,n} x_j + n_i, \quad (7)$$

where $x_j \in \mathbf{x}$ and $n_i \sim \mathcal{CN}(0, \sigma^2)$. We specify ρ as the power splitting ratio, which denotes the ratio of signal strength that the ID module occupied in the total received signal. Then, we can obtain the received signal of UT i for ID module as

$$y_i^{ID} = \sqrt{\rho} \left(\sqrt{p_{i,j,n}} h_{i,j,n} x_j + \sum_{j \notin \mathcal{S}_i} \sqrt{p_{i,j,n}} h_{i,j,n} x_j + n_i \right) + n_i^{ID}, \quad (8)$$

and the signal of UT i for energy harvesting as

$$\begin{aligned} \mathcal{Y}_i^{\text{EH}} &= \sqrt{1-\rho} \left(\sqrt{P_{i,j,n}} h_{i,j,n} x_j + \sum_{j \notin \mathcal{S}_i} \sqrt{P_{i,j,n}} h_{i,j,n} x_j + n_i \right), \end{aligned} \quad (9)$$

respectively, where $n_i^{\text{ID}} \sim \mathcal{CN}(0, (\sigma_i^{\text{ID}})^2)$ is the additive white Gaussian noise introduced by the ID module. It can be observed that the signals used to harvest energy come from the serving SBS and the interfering SBSs. We can derive the achievable SINR of UT i when it requests content f as follows:

$$\text{SINR}_{i,f} = \frac{\rho \left| \sqrt{P_{i,j,n}} h_{i,j,n} \right|^2}{\rho \sum_{j \notin \mathcal{S}_i} \left| \sqrt{P_{i,j,n}} h_{i,j,n} \right|^2 + \rho \sigma^2 + (\sigma_i^{\text{ID}})^2}. \quad (10)$$

Since the power of n_i is too low, so we can obtain the average harvested energy of UT i when it requests content f from SBS j on subband n by ignoring the power of noise n_i as follows:

$$\begin{aligned} \text{EH}_{i,f} &= (1-\rho) \\ &\times \ell_{i,j,f} \left(\left| \sqrt{P_{i,j,n}} h_{i,j,n} \right|^2 + \sum_{j \notin \mathcal{S}_i} \left| \sqrt{P_{i,j,n}} h_{i,j,n} \right|^2 \right), \end{aligned} \quad (11)$$

where we assume that the EH module has the perfect energy conversion efficiency 1. Further, we can obtain the rate of UT i when it requests content f as follows:

$$R_{i,f} = \text{BW}_i \times \log_2 (1 + \text{SINR}_{i,f}), \quad (12)$$

where BW_i is the bandwidth of UT i determined in the process of resource allocation. Eventually, we can construct harvested energy maximization problem of the network as follows:

$$\begin{aligned} \max_{(\rho, \mathbf{p})} \quad & \sum_{i \in \mathcal{K}, f \in \mathcal{F}} \text{EH}_{i,f} \\ \text{s.t.} \quad & (13a) \quad 0 \leq \sum_{n \in \mathcal{N}, i \in \mathcal{K}} P_{i,j,n} \leq P_{\max}, \quad \forall j \in \mathcal{S} \\ & (13b) \quad R_{i,f} \geq \gamma_i, \quad \forall i \in \mathcal{K} \\ & (13c) \quad 0 < \rho < 1, \end{aligned} \quad (13)$$

where (13a) is the maximum transmit power constraint of SBSs, (13b) specifies minimum rate requirement, i.e., QoS of UTs, and (13c) is the constraint of power splitting ratio. Since the formulated problem is not convex, to solve the established problem, we firstly convert nonconvex constraint (13b) into an equivalent form as follows:

$$\begin{aligned} (13b') : \quad & \rho \times P_{i,j,n} h_{i,j,n}^2 \\ & - \left(\rho \sum_{j \notin \mathcal{S}_i} P_{i,j,n} h_{i,j,n}^2 + \rho \sigma^2 + (\sigma_i^{\text{ID}})^2 \right) \\ & \times 2^{(\gamma_i/\text{BW}_i-1)} \geq 0. \end{aligned} \quad (14)$$

Then, problem (13) can be reformulated as follows:

$$\begin{aligned} \max_{(\rho, \mathbf{p})} \quad & \sum_{i \in \mathcal{K}, f \in \mathcal{F}} \text{EH}_{i,f} \\ \text{s.t.} \quad & (13a), (13b'), (13c). \end{aligned} \quad (15)$$

Since ρ and $\mathbf{p} = (p_{i,j,n})_{K \times S \times N}$ are coupled in the objective of (15) and the condition (13b'). Therefore, we propose an IPSPA algorithm to solve problem (15) by decoupling ρ and \mathbf{p} . We fix ρ firstly, and then (15) is converted from a nonconvex optimization problem into a convex one. Further, interior point method can be adopted to solve (15) [24]. Finally, the maximum harvested energy value can be obtained through alternately iterating ρ and \mathbf{p} . The detail description of the proposed IPSPA algorithm to maximize the harvested energy of all UTs deployed in the SWIPT system with popularity cache scheme in dense small cell networks is shown in Algorithm 1. Energy harvesting coefficient, associated SBS, and subbandwidth for each UT are firstly determined in Algorithm 1. Then, optimal power allocation \mathbf{p}^* and corresponding harvested energy for each ρ are obtained by solving problem (15). Finally, the maximum value of harvested energy can be gained from all the cases of harvested energy.

5. Complexity Analysis

In Algorithm 1, the computational complexity of step (2) is $\mathcal{O}(\text{FKS})$. Step (3) and step (4) have the computational complexity $\mathcal{O}(((\rho_{\max} - \rho_{\min}) \times V_{\max})/\rho_{in})$, where $\mathcal{O}(V_{\max})$ is the complexity of interior point method. Both step (5) and step (8) have the computational complexity $\mathcal{O}(\text{FK})$. Thus, the total computational complexity of Algorithm 1 is $\mathcal{O}(((\rho_{\max} - \rho_{\min}) \times V_{\max} \times F^2 K^2 S)/\rho_{in} + \text{FK}) \approx \mathcal{O}(((\rho_{\max} - \rho_{\min}) \times V_{\max} \times F^2 K^2 S)/\rho_{in})$, which increases linearly with F^2, K^2 , and S . Nevertheless, for the algorithm of joint user association, resource assignment, power splitting ratio, and power optimization given in [25], the computational complexity of user association and resource assignment is $\mathcal{O}(\text{FS}^K)$. Thus, the total computational complexity is $\mathcal{O}(((\rho_{\max} - \rho_{\min}) \times V_{\max} \times F^2 K S^K)/\rho_{in})$ when the algorithm runs to step (5), where the computational complexity of step (5) is $\mathcal{O}(\text{FK})$. Moreover, the complexity of step (8) is $\mathcal{O}(\text{FK})$. Therefore, the total complexity of joint user association, resource assignment, power splitting ratio, and power optimization is $\mathcal{O}(((\rho_{\max} - \rho_{\min}) \times V_{\max} \times F^2 K S^K)/\rho_{in} + \text{FK}) \approx \mathcal{O}(((\rho_{\max} - \rho_{\min}) \times V_{\max} \times F^2 K S^K)/\rho_{in})$, which increases exponentially with the number of deployed UTs. Therefore, the proposed algorithm has a significantly reduced computational complexity.

6. Simulation Results

In our simulation, all the UTs and SBSs are randomly and uniformly distributed in the circular region with a radius of 20 m. We consider the channel model with path loss, Rayleigh fading, and shadowing fading. The path loss from

- (1) **Initialization** $d = 0$, \mathcal{S} , \mathcal{F} , \mathcal{K} , \mathcal{C} , $\rho_{min} = 0.001$, $\rho_{max} = 1$, and $\rho_{in} = 0.001$.
- (2) **Calculate** $\ell_{i,j,f}$, \mathcal{B}_i and BW_i .
- (3) **for** $\rho = \rho_{min} : \rho_{in} : \rho_{max}$ **do**
- (4) **Obtain** \mathbf{p}^* through solving (15) by using interior point method given in [24].
- (5) **Substitute** $\mathbf{p}^d = \mathbf{p}^*$ into the objective function of (15), and calculate corresponding harvested energy.

$$HE(\mathbf{p}^d) = \sum_{i \in \mathcal{K}, f \in \mathcal{F}} EH_{i,f}$$
- (6) **Update** $\rho^d = \rho$, $d = d + 1$.
- (7) **end for**
- (8) **Calculate** the maximum harvested energy $HE_{max} = \max(HE(\mathbf{p}^d))$.
- (9) **Output** HE_{max} , and corresponding $\mathbf{p}^* = \mathbf{p}^l$ and $\rho^* = \rho^l$.

ALGORITHM 1: IPSPA algorithm.

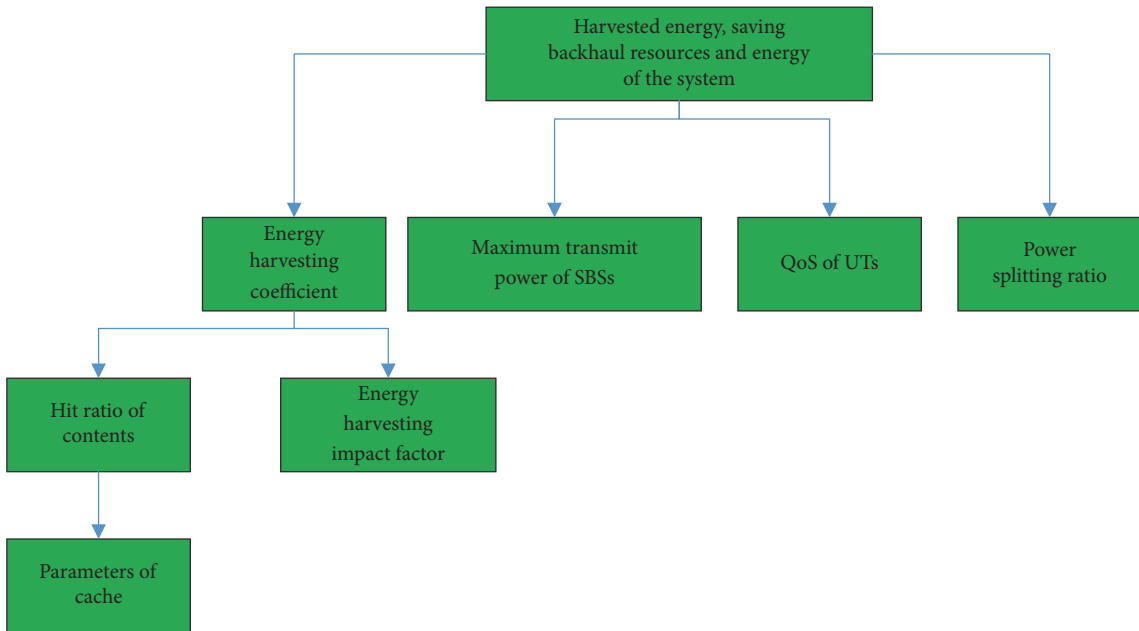


FIGURE 3: Relationship of different system parameters.

SBS s to UT u is set as $PL_{su} = 38.46 + 20 * \log_{10}(d_{su})$, where d_{su} is the distance between SBS s and UT u , with the unit m. Besides, Rayleigh fading follows exponential distribution with parameter 1. The standard deviation of the shadowing fading is 8dB for the link between SBS and the UT [26]. Therefore, $h(i, j, n) = \text{Rayleigh}(i, j, n) * 10^{((-PL_{su}(i,j) - \text{shadowing}(i,j,n))/10 - 3)}$ denotes the channel gain from SBS j to UT i on subband n . Besides, we set $\sigma^2 = -50\text{dBm}$ and $(\sigma_i^{\text{ID}})^2 = -30\text{dBm}$, respectively. Assume that each UT randomly requests a content in 1s, and the size of each content is 20 kbit. Moreover, we set $\eta_{BH} = 0.68$, i.e., $m = 1.47$, $p_{max} = 1\text{w}$, and the number of OFDMA RBs as 50, respectively.

Our proposed SWIPT system with popularity cache scheme has the advantages of improving harvested energy of UTs and saving backhaul resources and energy. The performance of the system is influenced by different system parameters given in Figure 3. Therefore, we carry out the simulation from the aspects given in Figures 4, 5, 6, 7, 8, 9, 10,

and 11. Additionally, we compare our proposed scheme with the following schemes.

- (i) Uniform cache scheme is given in [18, 19] applied in our proposed SWIPT system.
- (ii) No caching scheme (nocache) of SWIPT system is given in [6].

Firstly, we simulate the hit ratio of our proposed popularity cache scheme and uniform cache scheme given in [18, 19].

Figure 4 shows the hit ratio with respect to the content index. We set the total number of contents as 10, $\alpha = 0.5$ for blue and black curves, and $\mathcal{C} = 6$ for green and red curves. We can observe that for a content under the same popularity distribution parameter α , hit ratio of the content increases with cache size. Moreover, for a content under the same cache size of SBSs, hit ratio of the content becomes larger when popularity distribution parameter α increases. Besides, hit ratio for a content with high popularity of our

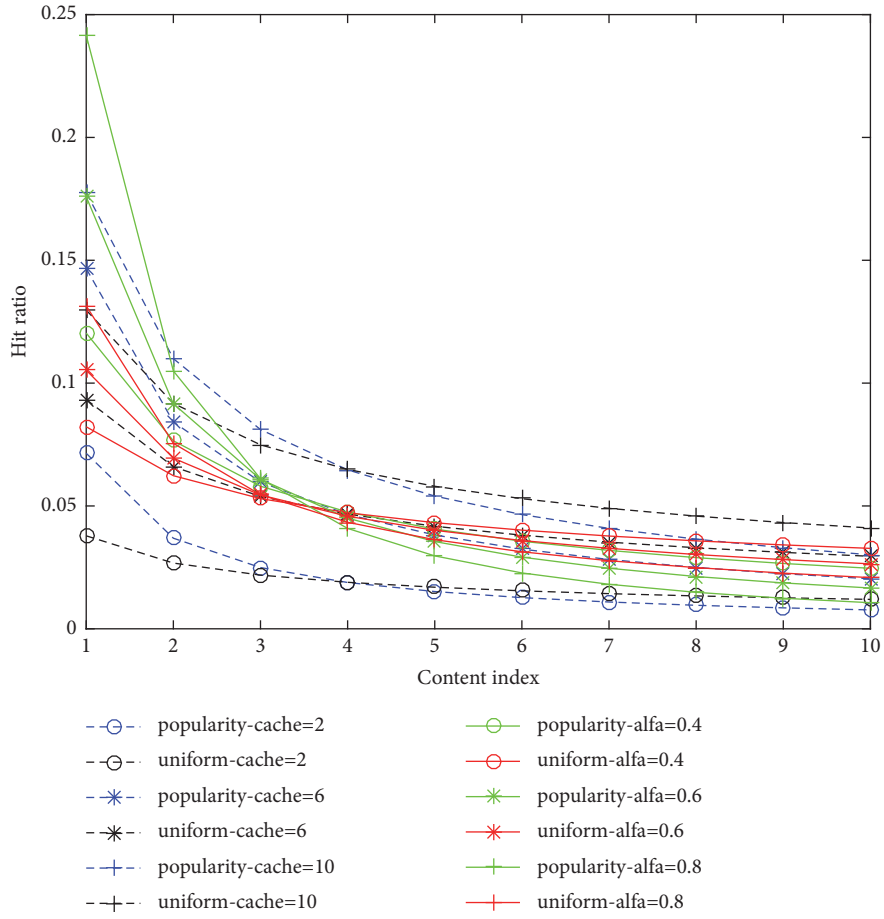


FIGURE 4: Hit ratio varies with content index.

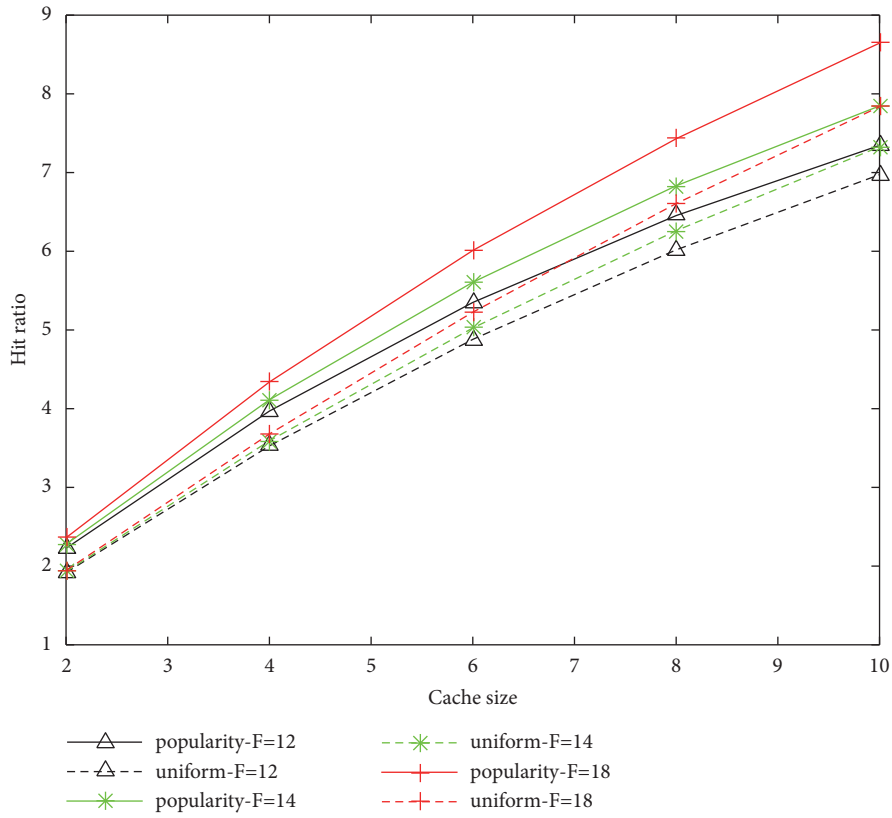


FIGURE 5: Hit ratio varies with cache size C.

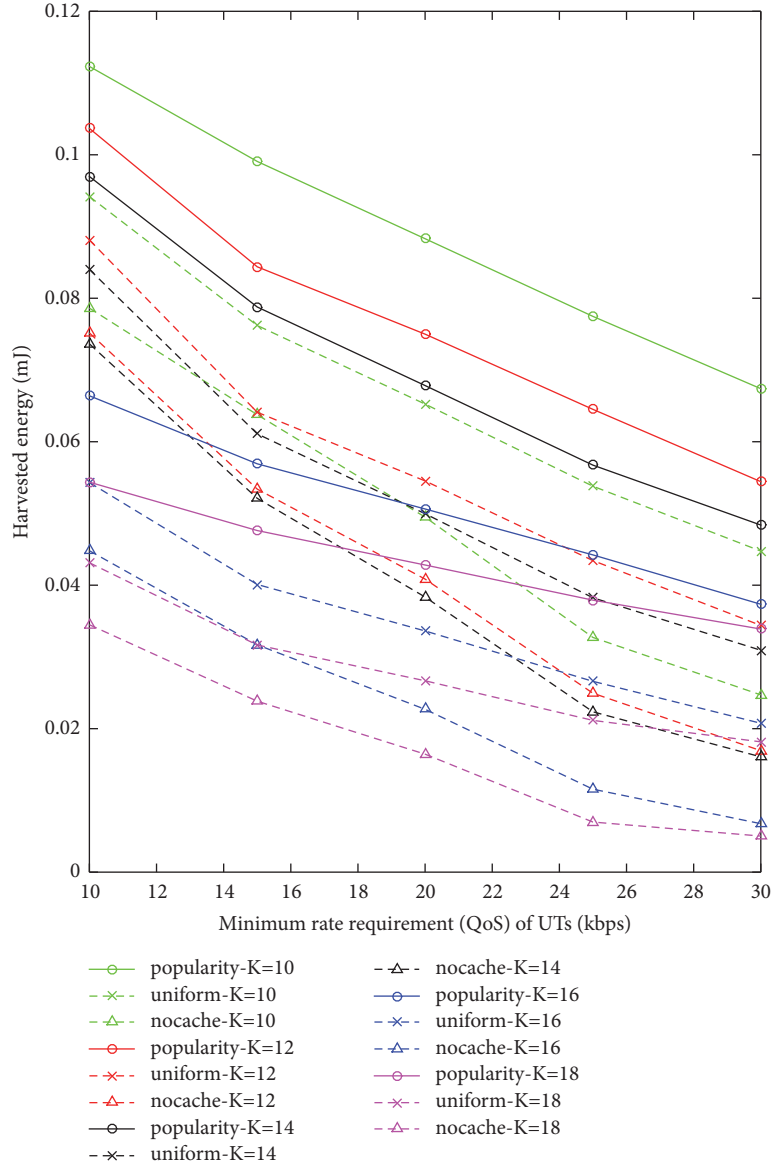


FIGURE 6: Harvested energy varies with QoS of UTs under different K.

proposed popularity cache scheme is larger than uniform cache scheme when cache size of SBSs and popularity distribution parameter α are the same.

Figure 5 shows hit ratio with respect to C . We set $\alpha = 0.5$. We can observe that our proposed popularity cache scheme has better hit ratio than uniform scheme. Moreover, the hit ratio of our proposed and uniform schemes increases with the increasing of C under the same number of contents F . The reason is that the probability of contents being cached increases with the increasing of C . Additionally, the hit ratio of our proposed and uniform schemes increases with the total number of contents under the same C . Then, we compare the energy harvesting property of our proposed popularity cache scheme with the uniform cache scheme given in [18, 19] and the no caching scheme (nocache) given in [6].

Figure 6 shows that harvested energy of the system with respect to minimum rate requirement, i.e., QoS of UTs under

different number of UTs K , where $C=6$ and $S=8$. We can observe that harvested energy decreases with the number of deployed UTs K . The reason is that more power is used to provide service for UTs. Moreover, we can see that our proposed scheme has better performance than uniform cache scheme and no caching scheme. The reason is that our proposed scheme has larger energy harvesting coefficients through improving the probability of obtaining contents from local SBSs.

Figure 7 shows that harvested energy of the system varies with the minimum rate requirement, i.e., QoS of UTs under different C , where $K=14$ and $S=8$. We can intuitively observe that harvested energy increases with C . The reason is that energy harvesting ability of our proposed scheme increases with C . Besides, we can see that our proposed popularity cache scheme has better performance than the uniform cache scheme and the no caching scheme because the proposed

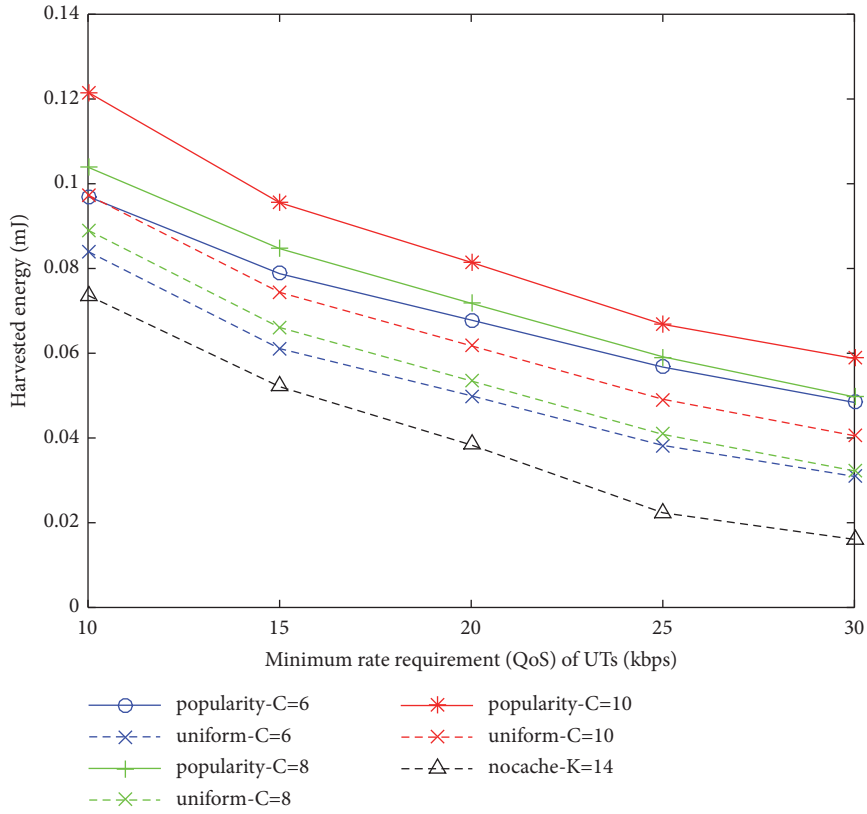


FIGURE 7: Harvested energy varies with QoS of UTs under different C.

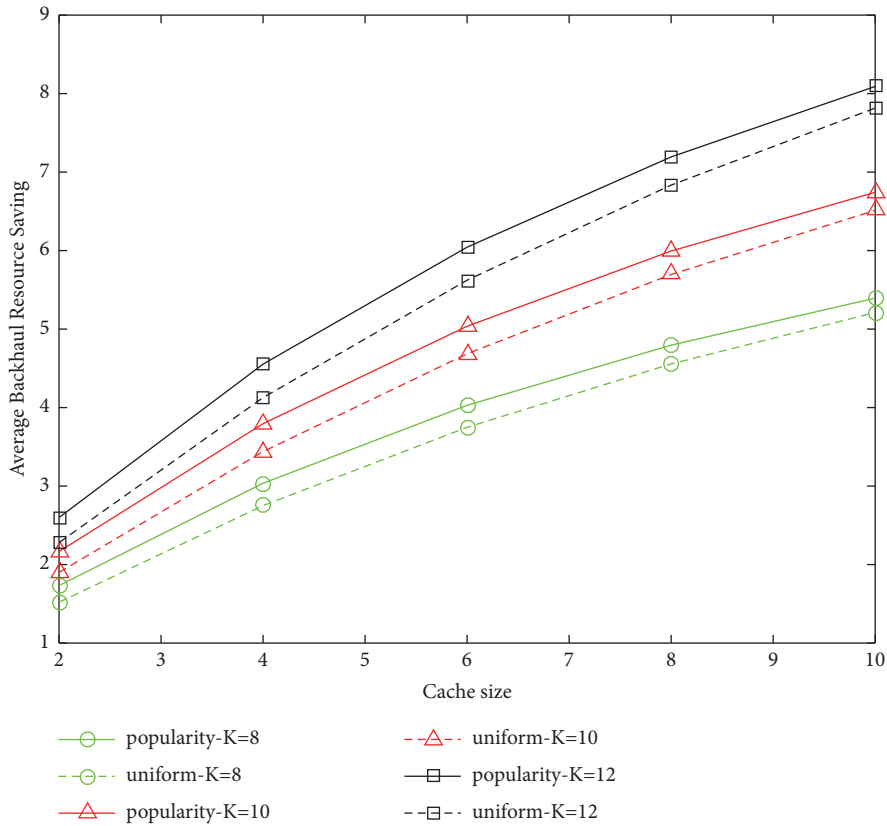


FIGURE 8: Average backhaul resource saving varies with cache size.

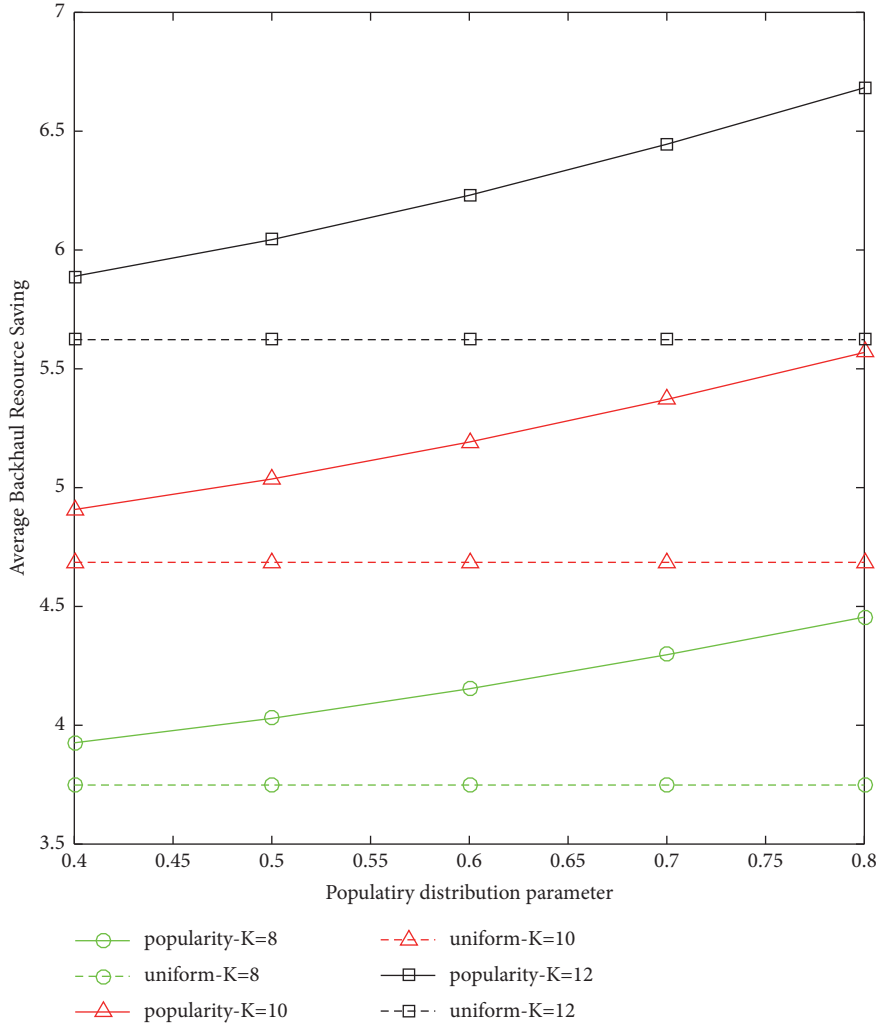


FIGURE 9: Average backhaul resource saving varies with popularity distribution parameter α .

scheme can achieve higher hit ratio for the content with high popularity.

Finally, we compare our proposed cache scheme with the uniform cache scheme given in [18, 19] in terms of the ability of saving backhaul resources and energy. Average saving backhaul resource is depicted in Figures 8 and 9. We assume that each content consumes 1 unit backhaul resource when it is fetched through the backhaul link.

Figure 8 shows the average backhaul resource saving with respect to the size of cache C . We can observe that our proposed popularity cache scheme has better performance than uniform cache scheme. Moreover, our proposed popularity cache scheme can save more backhaul resources when cache size C becomes larger. Additionally, our proposed popularity cache scheme has better performance than uniform cache scheme when the number of deployed UTs K in dense small cell networks increases. The reason is that our proposed scheme has higher hit ratio and energy harvesting coefficient.

Figure 9 shows the average backhaul resource saving with respect to popularity distribution parameter α . We can observe that the performance of uniform cache scheme is not

influenced by the parameter α , while our proposed popularity cache scheme can save more backhaul resources with the increasing of parameter α . Moreover, our proposed popularity cache scheme has better performance than uniform cache scheme as α increases. The reason is that our proposed scheme guarantees more contents obtained from local SBSs. As given in [27, 28], the average saving energy of backhaul link can be calculated as follows:

$$\begin{aligned}
 P_{\text{BH}}^{\text{save}} &= \overline{p_{\text{hit}}} \times \left(\frac{S}{\max_{dl}} \times P_s + S \times P_{dl} \right) \\
 &= \sum_{j \in \mathcal{S}, f \in \mathcal{F}} A_{i,j,f}^{\text{hit}} \times K \times \left(\frac{S}{\max_{dl}} \times P_s + S \times P_{dl} \right)
 \end{aligned} \tag{16}$$

where $\overline{p_{\text{hit}}}$ is the average hit probability of all contents when the number of UTs is K , \max_{dl} is the maximum number of downlink available aggregation switch interfaces, and P_{dl} is the power consumption of one downlink interface in the aggregation switch for receiving the backhauled traffic. Moreover, $P_s = \delta \times P_{\text{max}} + (1 - \delta) \times U_{\text{total}} / U_{\text{max}} \times P_{\text{max}}$ denotes

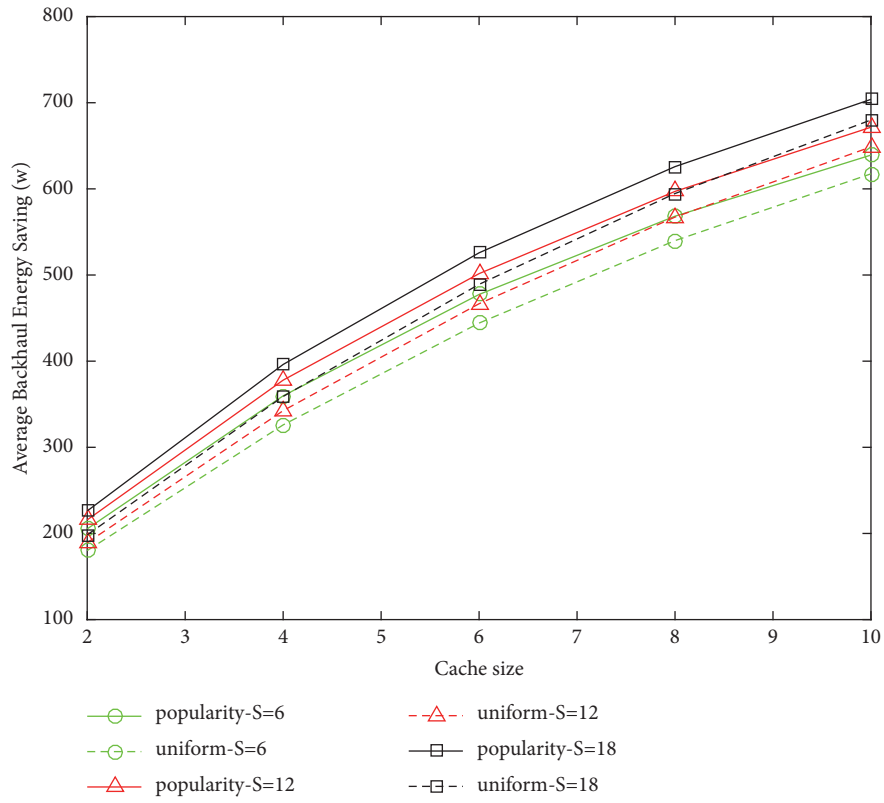
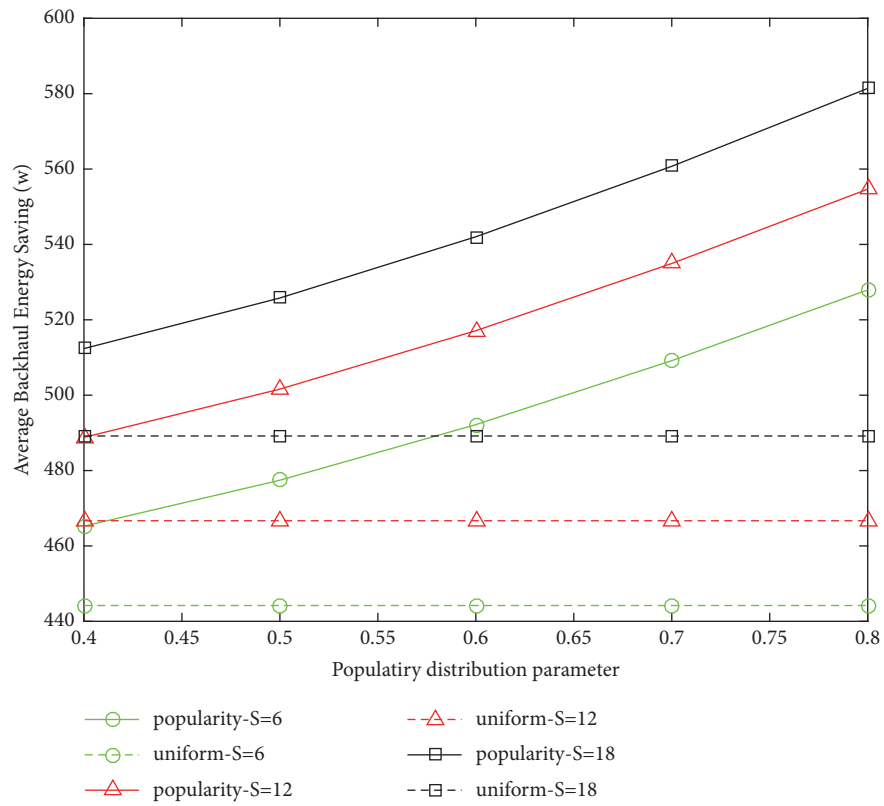


FIGURE 10: Average backhaul energy saving varies with cache size.

FIGURE 11: Average backhaul energy saving varies with popularity distribution parameter α .

the power consumed by a switch, where P_{\max} represents the maximum power consumption of the switch, U_{\max} is the maximum amount of traffic a switch can deal with, and U_{total} represents the amount of traffic that is traversing the switch that is influenced by the parameter $\delta \in (0, 1)$. We set $K = 8$, $F = 10$, $max_{dl} = 24$, $p_{dl} = 1$ w, $\delta = 0.9$, $P_{\max} = 300$ w, $U_{\max} = 36$ Gbps, and $\gamma_i = 20$ kbps.

Figure 10 shows average backhaul saving energy with respect to the cache size C , where $\alpha = 0.5$. We can see that our proposed popularity cache scheme has better performance than uniform cache scheme. Moreover, our proposed popularity cache scheme can save more backhaul resources when cache size C becomes larger. The reason is that hit ratio of our proposed scheme increases with the increasing of cache size C , which improves energy harvesting coefficient. Besides, our proposed scheme has better performance than uniform cache scheme with the increasing number of deployed SBSs S since it ensures more UTs get requested contents from local SBSs.

Figure 11 illustrates average backhaul saving energy with respect to popularity distribution parameter α , where $C = 6$. We can observe that the performance of uniform cache scheme is not affected by the parameter α . However, our proposed popularity cache scheme can save more backhaul resources when α increases. The reason is that hit ratio and energy harvesting coefficient increase with the increasing of α . Moreover, our proposed popularity cache scheme has better performance than uniform cache scheme with the increasing of parameters α and S because it ensures more contents requested by UTs obtained through local SBSs without adding burden on backhaul link.

7. Conclusion

In this paper, the harvested energy maximization problem of SWIPT system with popularity cache scheme in dense small cell networks has been studied. Firstly, system model consisting of the network model, content request, and popularity cache scheme was provided. Then, a harvested energy maximization problem of SWIPT system with popularity cache scheme was established. Further, an IPSPA algorithm was given to solve the formulated problem. Finally, we demonstrated that the proposed SWIPT system with popularity cache scheme can improve harvested energy of UTs and save backhaul resources and energy through a number of simulations.

Data Availability

The data used to support the findings of this study are included within the article.

Disclosure

Jiandong Li serves as a Senior Member of IEEE.

Conflicts of Interest

The authors declare that there are no conflicts of interest regarding the publication of this paper.

Acknowledgments

This paper is supported in part by the National Natural Science Foundation of China [nos. 91638202, 61231008, and 61571351].

References

- [1] J. Huang, C. Xing, and C. Wang, "Simultaneous wireless information and power transfer: technologies, applications, and research challenges," *IEEE Communications Magazine*, vol. 55, no. 11, pp. 26–32, 2017.
- [2] F. Jameel, M. A. A. Haider, A. A. Butt et al., "A technical review of simultaneous wireless information and power transfer (SWIPT)," in *Proceedings of the IEEE International Symposium on Recent Advances in Electrical Engineering*, pp. 1–6, 2017.
- [3] T. D. P. Perera, D. N. K. Jayakody, S. K. Sharma, S. Chatzinothas, and J. Li, "Simultaneous wireless information and power transfer (SWIPT): recent advances and future challenges," *IEEE Communications Surveys and Tutorials*, vol. 20, no. 1, pp. 264–302, 2018.
- [4] J. Ding, L. Jiang, and C. He, "User-centric energy-efficient resource management for time switching wireless powered communications," *IEEE Communications Letters*, vol. 22, no. 1, pp. 165–168, 2018.
- [5] D. Mishra and G. C. Alexandropoulos, "Jointly optimal spatial channel assignment and power allocation for MIMO SWIPT systems," *IEEE Wireless Communications Letters*, vol. 7, no. 2, pp. 214–217, 2018.
- [6] Z. Hu, N. Wei, and Z. Zhang, "Optimal resource allocation for harvested energy maximization in wideband cognitive radio network with SWIPT," *IEEE Access*, vol. 5, pp. 23 383–23 394, 2017.
- [7] N. Janatian, I. Stupia, and L. Vandendorpe, "Optimal resource allocation in ultra-low power fog-computing SWIPT-based networks," in *Proceedings of the IEEE Wireless Communications and Networking Conference*, pp. 1–6, IEEE, 2018.
- [8] H. Chai, S. Leng, J. Hu, and K. Yang, "Resources allocation in SWIPT aided fog computing networks," in *Proceedings of the 9th International Conference on Advanced Infocomm Technology, ICAIT '17*, pp. 239–244, November 2017.
- [9] Y. Ye, Y. Li, D. Wang, F. Zhou, R. Q. Hu, and H. Zhang, "Optimal transmission schemes for df relaying networks using SWIPT," *IEEE Transactions on Vehicular Technology*, vol. 67, no. 8, pp. 7062–7072, 2018.
- [10] Y. Dong, M. J. Hossain, and J. Cheng, "Joint power control and time switching for SWIPT systems with heterogeneous QoS requirements," *IEEE Communications Letters*, vol. 20, no. 2, pp. 328–331, 2016.
- [11] G. Pan, H. Lei, Y. Yuan, and Z. Ding, "Performance analysis and optimization for SWIPT wireless sensor networks," *IEEE Transactions on Communications*, vol. 65, no. 5, pp. 2291–2302, 2017.
- [12] D. W. K. Ng and R. Schober, "Resource allocation for coordinated multipoint networks with wireless information and power transfer," in *Proceedings of the Global Communications*

- Conference, GLOBECOM '14*, pp. 4281–4287, IEEE, December 2014.
- [13] L. Xu, J. Wang, H. Zhang, and T. A. Gulliver, “Performance analysis of IAF relaying mobile D2D cooperative networks,” *Journal of The Franklin Institute*, vol. 354, no. 2, pp. 902–916, 2017.
- [14] L. Xu, J. Wang, Y. Liu, J. Yang, W. Shi, and T. A. Gulliver, “Outage performance for IDF relaying mobile cooperative networks,” in *Proceedings of the International Conference on 5G for Future Wireless Networks*, pp. 395–402, 2017.
- [15] A. Liu and V. K. N. Lau, “Capacity gain of physical layer caching in backhaul-limited dense wireless networks,” in *Proceedings of the Computer Communications Conference*, pp. 64–72, IEEE, April 2015.
- [16] J. Song and W. Choi, “Minimum cache size and backhaul capacity for cache-enabled small cell networks,” *IEEE Wireless Communications Letters*, vol. 7, no. 4, pp. 490–493, 2018.
- [17] R. Hou, Y. Cheng, L. X. Cai, and H. Zhuang, “Performance evaluation for caching-based content distribution in backhaul-limited small cell networks,” in *Proceedings of the International Conference on Wireless Communications and Signal Processing (WCSP '15)*, pp. 1–5, October 2015.
- [18] Y. Wang, X. Tao, X. Zhang, and Y. Gu, “Cooperative caching placement in cache-enabled D2D underlaid cellular network,” *IEEE Communications Letters*, vol. 21, no. 5, pp. 1151–1154, 2017.
- [19] J. Li, Y. Chen, M. Ding, F. Shu, B. Vucetic, and X. You, “A small-cell caching system in mobile cellular networks with LoS and NLoS channels,” *IEEE Access*, vol. 5, pp. 1296–1305, 2017.
- [20] F. Cheng, Y. Yu, Z. Zhao, N. Zhao, Y. Chen, and H. Lin, “Power allocation for cache-aided small-cell networks with limited backhaul,” *IEEE Access*, vol. 5, pp. 1272–1283, 2017.
- [21] A. Kumar and W. Saad, “On the tradeoff between energy harvesting and caching in wireless networks,” in *Proceedings of the IEEE International Conference on Communication Workshop, ICCW '15*, pp. 1976–1981, June 2015.
- [22] X. Peng, J. Shen, J. Zhang, and K. B. Letaief, “Backhaul-aware caching placement for wireless networks,” in *Proceedings of the Global Communications Conference*, pp. 1–6, IEEE, December 2015.
- [23] H. Ahleghagh and S. Dey, “Video-aware scheduling and caching in the radio access network,” *IEEE/ACM Transactions on Networking*, vol. 22, no. 5, pp. 1444–1462, 2014.
- [24] S. Boyd and L. Vandenberghe, *Convex Optimization*, Cambridge University Press, 2004.
- [25] M. Ali, Q. Rabbani, M. Naeem, S. Qaisar, and F. Qamar, “Joint user association, power allocation, and throughput maximization in 5G H-CRAN networks,” *IEEE Transactions on Vehicular Technology*, vol. 66, no. 10, pp. 9254–9262, 2017.
- [26] E. U. T. R. Access, “Further advancements for E-UTRA physical layer aspects,” Tech. Rep. 3GPP TR 36.814, 2010.
- [27] S. Tombaz, P. Monti, K. Wang, A. Västberg, M. Forzati, and J. Zander, “Impact of backhauling power consumption on the deployment of heterogeneous mobile networks,” in *Proceedings of the Global Telecommunications Conference*, pp. 1–5, IEEE, December 2011.
- [28] K. M. S. Huq, S. Mumtaz, J. Bachmatiuk, J. Rodriguez, X. Wang, and R. L. Aguiar, “Green HetNet CoMP: energy efficiency analysis and optimization,” *IEEE Transactions on Vehicular Technology*, vol. 64, no. 10, pp. 4670–4683, 2015.

Research Article

Robust Power Allocation for Cooperative Localization in Jammed Wireless Sensor Networks

Mingxing Ke, Shiwei Tian , Lu Lu, and Chuang Wang

College of Communications Engineering, PLA Army Engineering University, Nanjing 210007, China

Correspondence should be addressed to Shiwei Tian; tianxwell@163.com

Received 18 February 2019; Revised 16 April 2019; Accepted 12 May 2019; Published 10 June 2019

Guest Editor: Zoran Stamenkovic

Copyright © 2019 Mingxing Ke et al. This is an open access article distributed under the Creative Commons Attribution License, which permits unrestricted use, distribution, and reproduction in any medium, provided the original work is properly cited.

In this paper, we propose robust power allocation strategies to improve the localization performance in cooperative wireless sensor localization systems when suffering interference of jammer nodes. In wireless sensor localization systems, transmitting power strategies will affect the localization accuracy and determine the lifetime of wireless sensor networks. At the same time, the power allocation problem will be evolution to a new challenge when there are jammed nodes. So in this paper, we first present the optimization framework in jammed cooperative localization systems. Moreover, the imperfect parameter estimations of agent and jammer nodes are considered to develop robust power allocation strategies. In particular, this problem can be transformed into second-order cone programs (SOCPs) to obtain the end solution. Numerical results show the proposed power allocation strategies can achieve better performance than uniform power allocation and the robust schemes can ensure lower localization error than nonrobust power control when systems are subject to uncertainty.

1. Introduction

HIGH precious localization information is essential in many location-based applications and services, such as intelligent robot, logistics tracking, equipment management, and so on [1]. Traditional localization techniques, e.g., the global positioning system (GPS), may not provide satisfied localization accuracy in some harsh environments [2]. So the wireless sensor localization systems are motivated to provide necessary supplements.

In a wireless sensor localization system, there are always three types of nodes, i.e., agent nodes which are devices with unknown positions, anchor nodes which are infrastructures with known positions, and jammer nodes which are designedly or unintentional distributed in some places. Conventionally, the agent nodes can infer their positions by range measurements from anchor to agent nodes. Besides, the cooperation between agent nodes can improve localization accuracy through information sharing and additional measurements between agent nodes [3]. However, the jammer nodes will bring interference to degrade the localization performance of agent nodes. In other words, the localization accuracy of agent nodes is depended on the network topology

and the measurement errors [4]. The measurement errors are related to the transmit power, signal waveform, channel condition, and interference condition. Consequently, power allocation strategies are critical to reduce the localization error and improve the lifetime of wireless sensor networks.

Existing studies have been worked on power allocation problems. In study [5], the author established an optimization framework to allocate robust power for anchor nodes and designed a distributed power allocation algorithm via conic programming. In [6], the power allocation strategies in both active and passive localization networks were researched. For network navigation, literature [7] developed efficient navigation algorithms to obtain optimized energy allocation strategies. Then for the cooperative localization, literature [4] built a general framework for wide-band cooperative localization networks and established the fundamental limits. In [7], the author proposed a distributed robust power allocation algorithm by infrastructure and cooperation phases. In [8], the power management problem was solved by game approach under the knowledge of local and global information. In [9], a hierarchical game was developed to obtain optimal power allocation strategies for different kinds of nodes simultaneously. What is more, when the jammer nodes are

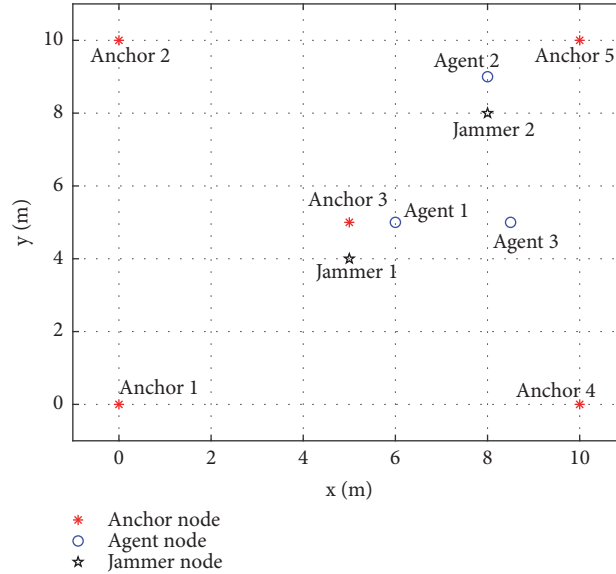


FIGURE 1: Illustration of a jammed wireless sensor localization system.

considered, two schemes were proposed to optimize power management for jammer nodes in [10, 11]. However, existing works in [10, 11] focus on jamming techniques to degrade the localization performance. So the author in [12] proposed an optimal power allocation approach based on semidefinite programs (SDP) to minimize the maximum Cramer-Rao lower bound (CRLB) or average CRLB in jammed wireless sensor localization systems.

While for above researches, there are some new challenges to be considered. First, the authors did not consider the effect of jammer nodes in [5–9]. If there are jammer nodes in localization systems, their positions and transmit power will affect the power allocation strategies of different nodes. Second, in [10, 11], the authors have investigated the analogous power allocation problems, but they focused on jamming techniques. The antijamming techniques through optimizing the power allocation strategies of anchor and agent nodes are still challenging tasks. Moreover, though the jammer nodes were introduced, the cooperative technique and the parameter uncertainty did not consider in study [12]. For cooperative localization, it will be more complicated due to additional measurements. At the same time, the parameter uncertainty of different nodes should be tackled to guarantee the localization requirement. So the main contributions of this paper can be concluded as follows:

- (i) We propose optimal power allocation strategies for cooperation in jammed wireless sensor localization system, aiming to guarantee the localization requirement.
- (ii) We develop a robust optimization method to combat the uncertainty parameters of agent nodes and jammer nodes.
- (iii) We exploit that the problem can be transformed into second-order cone programs (SOCPs) due to the functional properties of squared position error

bound (SPEB) when considering the cooperative agent nodes as pseudo anchor nodes.

The rest of this paper is organized as follows. In Section 2, the system model is described, and the problem to optimize is formulated. Section 3 studies the uncertainty model and robust formulation. The robust power allocation strategies are presented in Section 4. The simulation results are presented in Section 5. Conclusions are given in Section 6.

Notation. $\mathbf{1}_n$ denotes a column vector with all 1's. The operation \otimes denotes the Kronecker product. \mathbf{e}_k denotes a unit vector and the k -th element is 1 while the others are 0's. $\|\cdot\|$ represents the Euclidean norm of its argument.

2. System Models and Problem Formulation

2.1. System Model. For a two-dimensional jammed wireless sensor localization system, there are three types of nodes illustrated in Figure 1. This network includes N_a agent nodes, N_b anchor nodes, and N_j jammer nodes (the jammer nodes may be designedly or unintentionally distribute in some interested areas and they will degrade the localization accuracy of agent nodes in this network. If the jammer nodes are unintentional introduced into localization systems, they may be caused by different equipment. Then if the jammer nodes are designed, they may be employed by enemies), denoted by $\mathcal{N}_a = \{1, 2, \dots, N_a\}$, $\mathcal{N}_b = \{1, 2, \dots, N_b\}$, and $\mathcal{N}_j = \{1, 2, \dots, N_j\}$, respectively. The position of node k is denoted by \mathbf{p}_k for $k \in \mathcal{N}_a \cup \mathcal{N}_b \cup \mathcal{N}_j$. For arbitrary nodes k and j , the distance and angle from k to j are denoted by φ_{kj} and d_{kj} , respectively. In addition, it is assumed that jammer nodes transmit zero-mean Gaussian noise [10].

In this paper, each agent node can cooperate with its neighbors to increase localization accuracy. So each agent node not only receives signals from anchor nodes but also from neighbor agent nodes. The connectivity sets can

be denoted as $\mathcal{A}_k = \{\{j \in \mathcal{N}_a \cup \mathcal{N}_b\} \mid \text{node } j \text{ is connect with agent } k\}$ for $k \in \mathcal{N}_a$. Then the received waveform at agent node k from node j can be represented as [10]

$$r_{kj}(t) = \sum_{i=1}^{L_{kj}} \sqrt{x_j} \alpha_{kj}^i s(t - \tau_{kj}^i) + \sum_{\ell=1}^{N_j} \gamma_{k\ell} \sqrt{P_\ell^j} \nu_{k\ell}(t) + n_{kj}(t), \quad (1)$$

where $t \in [0, T_{obs}]$ and T_{obs} represents the observation interval, x_j denotes the transmit power of node j , $s(t)$ represents known transmit signal waveform with Fourier transform $S(f)$, α_{kj}^i and τ_{kj}^i denote the amplitude and time delay of the k -th path, and L_{kj} denotes the number of multipath between agent node i and agent node j . Here the influence of jammer nodes is considered as jamming noise with a transmit power P_ℓ^j , $P_\ell^j \nu_{k\ell}(t)$ is assumed as independent zero-mean white Gaussian random Process, and $\gamma_{k\ell}$ denotes the channel coefficient between agent node k and the ℓ -th jammer node. Moreover, the different noises are modeled as independent zero-mean white Gaussian processes with the spectral density level $N_0/2$ and that of $\nu_{k\ell}(t)$ are equal to one. Then the time delay τ_{kj}^i can be expressed by

$$\tau_{kj}^i = \frac{\|\mathbf{p}_j - \mathbf{p}_k\| + b_{kj}^i}{c}, \quad (2)$$

where \mathbf{p}_j and \mathbf{p}_k represent the different positions of nodes, c is the propagation speed of signal, and b_{kj}^i is a range bias for non-line-of-sight (NLOS), denoting those NLOS anchor nodes as set \mathcal{A}_k^{NL} . If the i -th path is line-of-sight (LOS), such that $b_{kj}^i = 0$, denote those nodes as set \mathcal{A}_k^L . Here we consider the cooperative agent node j as a pseudo anchor node when it provides localization information to agent node k .

2.2. Performance Metric. For agent node k , the unknown parameters can be introduced as

$$\theta_k \triangleq [\boldsymbol{\kappa}_k^T \boldsymbol{\kappa}_{k1}^T \cdots \boldsymbol{\kappa}_{k|\mathcal{A}_k|}^T], \quad (3)$$

where $\mathcal{A}_i = \mathcal{A}_i^{NL} \cup \mathcal{A}_i^L$ and $|\mathcal{A}_i|$ is the number of elements in \mathcal{A}_i ; the vector of multipath parameters $\boldsymbol{\kappa}$ can be associated with $r_{kj}(t)$ [4], expressed as

$$\boldsymbol{\kappa}_{kj} = \begin{cases} [\alpha_{kj}^1 & \alpha_{kj}^2 & b_{kj}^2 & \cdots & \alpha_{kj}^{L_{kj}} & b_{kj}^{L_{kj}}]^T, & j \in \mathcal{A}_k^L, \\ [\alpha_{kj}^1 & b_{kj}^1 & \alpha_{kj}^2 & b_{kj}^2 & \cdots & \alpha_{kj}^{L_{kj}} & b_{kj}^{L_{kj}}]^T, & j \in \mathcal{A}_k^{NL}. \end{cases} \quad (4)$$

Then let $\tilde{\theta}$ denote the estimation of unknown parameter vector θ ; the mean squared error (MSE) matrix for $\tilde{\theta}$ will satisfy the following inequality [4]:

$$\mathbb{E} \{(\tilde{\theta} - \theta)(\tilde{\theta} - \theta)^T\} \geq \mathbf{J}_\theta^{-1}, \quad (5)$$

where \mathbf{J}_θ is the Fisher information matrix (FIM). Let $\tilde{\mathbf{p}}_k$ be the unbiased position estimation of individual agent node i , then (4) implies that

$$\mathbb{E} \{(\tilde{\mathbf{p}}_k - \mathbf{p}_k)(\tilde{\mathbf{p}}_k - \mathbf{p}_k)^T\} \geq [\mathbf{J}_\theta^{-1}]_{2 \times 2, k}, \quad (6)$$

For cooperative localization in jammed wireless sensor systems, the mean squared error (MSE) of position estimation for agent k is satisfied the following inequality [4]:

$$E \{ \|\tilde{\mathbf{p}}_k - \mathbf{p}_k\|^2 \} \geq \text{tr} \{ \mathbf{J}_k^{-1}(\mathbf{p}_k) \}, \quad (7)$$

where $\mathbf{J}_k(\mathbf{p}_k)$ denotes the Fisher information matrix (FIM). $\text{tr}[\cdot]$ denotes the trace operator and $\mathcal{P}(\mathbf{p}_k) = \text{tr}\{\mathbf{J}_k^{-1}(\mathbf{p}_k)\}$ is the individual squared position error bound (SPEB) for agent node k , which provides a lower bounded for unbiased estimate.

In addition, the network EFIM $\mathbf{J}(\mathbf{p})$ is given in [7]

$$\mathbf{J}(\mathbf{p}) = \sum_{k \in \mathcal{N}_a} \sum_{j \in \mathcal{N}_a \cup \mathcal{N}_b \setminus \{k\}} x_j \xi_{kj} \mathbf{u}_{kj} \mathbf{u}_{kj}^T, \quad (8)$$

with

$$x_j \xi_{kj} = \frac{4\pi^2 W^2}{c^2} (1 - \chi_{kj}) \text{SINR}_{kj}^l, \quad (9)$$

$$\mathbf{u}_{kj} = \begin{cases} \mathbf{e}_k \otimes [\cos \varphi_{kj} & \sin \varphi_{kj}]^T & \text{if } j \in \mathcal{N}_b, \\ (\mathbf{e}_k - \mathbf{e}_j) \otimes [\cos \varphi_{kj} & \sin \varphi_{kj}]^T & \text{if } j \in \mathcal{N}_a, \end{cases} \quad (10)$$

where x_j is the transmit power of node j and ξ_{kj} is called equivalent ranging coefficient (ERC), W denotes the effective bandwidth of node j , $\chi_{kj} \in [0, 1]$ is the path-overlap coefficient characterizing the effect of multipath propagation for localization, and \mathbf{e}_k and \mathbf{e}_j are N_a -dimensional vectors [7]. Moreover, the SINR_{kj}^l denotes the energy ratio between the l -th component and the noise (here we only consider the line-of-sight connection between nodes, so $l = 1$), given by

$$\text{SINR}_{kj}^l = \frac{|\alpha_{kj}^l|^2 \int_{-\infty}^{+\infty} |S(f)|^2 df}{N_0/2 + \sum_{n=1}^{N_j} |\gamma_{kn}|^2 P_n^j}, \quad (11)$$

in which α_{kj}^l is the amplitude of the l -th path, $S(f)$ is the Fourier transform of transmit signal waveform $s(t)$, γ_{kn} is the channel coefficient between agent node k and jammer node n , and P_n^j is the transmit power of jammer node n . Without loss of generality, the ERC can be transformed as [10]

$$\xi_{kj} = \frac{\zeta_{kj}/d_{kj}^\rho}{\left(N_0/2 + \sum_{n=1}^{N_j} \zeta_{kn} (P_n^j/d_{kn}^\rho)\right)}, \quad (12)$$

where ζ_{kj} is a positive coefficient determined by the channel properties and effective bandwidth; ρ is the pathloss coefficient during transmission. Here we simply recognize the cooperative agent nodes as pseudo anchor nodes. So the

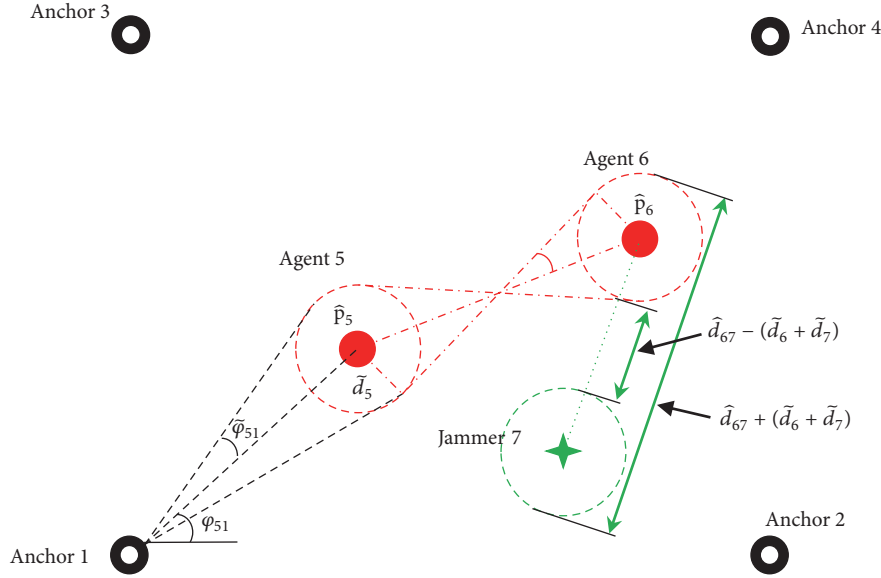


FIGURE 2: An example of uncertainty model for cooperation in a jammed wireless sensor localization system.

individual SPEB can be also obtained by (2). If the agent nodes k and j are not connected, the parameter can be set as $\xi_{kj} = \xi_{jk} = 0$.

In this paper, it is assumed that jammer nodes transmit zero-mean Gaussian noise. In practice, this assumption may be inappropriate for some situations. However, this assumption is used in our work for following purposes: First, to best of our knowledge, it is the first time to develop an antijamming approach through optimizing power allocation strategies for anchor and agent nodes. Those initial results can provide a fundamental feasibility for further studies on this problem. Second, the prior information of jammer nodes may not be reached for some situations, so we simplify the transmission of each jammer node as zero-mean Gaussian noise, which is commonly employed in [10, 11].

2.3. Power Allocation Formulation. The SPEB is adopted to be the performance matrix, so it is reasonable to minimize the total transmit power when each agent node requires the localization accuracy [6]. Thus, we can formulate the power allocation problem as

$$\begin{aligned}
 P_A : \min_{\{\mathbf{x}_a, \mathbf{x}_b\}} & \mathbf{1}^T \mathbf{x}_a + \mathbf{1}^T \mathbf{x}_b \\
 \text{s.t.} & \mathcal{P}(p_k; \mathbf{x}_a, \mathbf{x}_b) \leq \tau_k, \quad \forall k \in \mathcal{N}_a \\
 & c_q(\mathbf{x}_a, \mathbf{x}_b) \leq 0, \quad q = 1, 2, \dots, Q
 \end{aligned} \quad (13)$$

where \mathbf{x}_a and \mathbf{x}_b are transmit power strategies of agent nodes and anchor nodes, τ_k is the localization accuracy requirement for agent node k , and $\{c_q(\cdot)\}$ represents the linear constraints of each power allocation strategy, such as the individual power constraints $0 \leq x_k \leq x_k^{\max}$, $\forall k \in \mathcal{N}_a \cup \mathcal{N}_b$. Note that the optimization objective and the optimization variables in our paper are different from the references [10, 11]. Moreover, it is

impracticable to obtain the solution for the proposed problem through the approaches in [10, 11].

3. Uncertainty Model and Robust Formulation

Due to the imperfect estimates of network parameters, the robust formulation is necessary for the proposed power allocation problem. Figure 2 shows an example of uncertainty model. For any agent node k , its position can be defined in an area with center \mathbf{p}_k and radius \tilde{d}_k . Let $\hat{\varphi}_{kj}$, $\hat{\xi}_{kj}$, and \hat{d}_{kj} be the nominal value of angle φ_{kj} , channel coefficient ξ_{kj} , and distance d_{kj} . For any agent node k , the actual network parameters with anchor node j can be represented by

$$\varphi_{kj} \in [\hat{\varphi}_{kj} - \tilde{\varphi}_{kj}, \hat{\varphi}_{kj} + \tilde{\varphi}_{kj}] =: \mathcal{F}_{kj}, \quad (14)$$

$$d_{kj} \in [\hat{d}_{kj} - \tilde{d}_k, \hat{d}_{kj} + \tilde{d}_k] =: \mathcal{D}_{kj}, \quad (15)$$

From Figure 2, we can find the angular uncertainty $\tilde{\varphi}_{kj}$ fits $\sin \tilde{\varphi}_{kj} = \tilde{d}_k / \hat{d}_{kj}$ (it is assumed that the radius is larger than the minimum distance between nodes). Similarly, the actual network parameters with anchor nodes k with agent node i can be also represented by

$$\varphi_{ki} \in [\hat{\varphi}_{ki} - \tilde{\varphi}_{ki}, \hat{\varphi}_{ki} + \tilde{\varphi}_{ki}] =: \mathcal{F}_{ki}, \quad (16)$$

$$d_{ki} \in [\hat{d}_{ki} - \tilde{d}_k - \tilde{d}_i, \hat{d}_{ki} + \tilde{d}_k + \tilde{d}_i] =: \mathcal{D}_{ki}. \quad (17)$$

Here we can find from Figure 3 that the angular uncertainty $\tilde{\varphi}_{ki}$ fits $\sin \tilde{\varphi}_{ki} = (\tilde{d}_k + \tilde{d}_i) / \hat{d}_{ki}$. Then for the jammer node n , the angular uncertainty will not affect the result, so the network parameters are given by

$$d_{kn} \in [\hat{d}_{kn} - \tilde{d}_k - \tilde{d}_n, \hat{d}_{kn} + \tilde{d}_k + \tilde{d}_n] =: \mathcal{D}_{kn}. \quad (18)$$

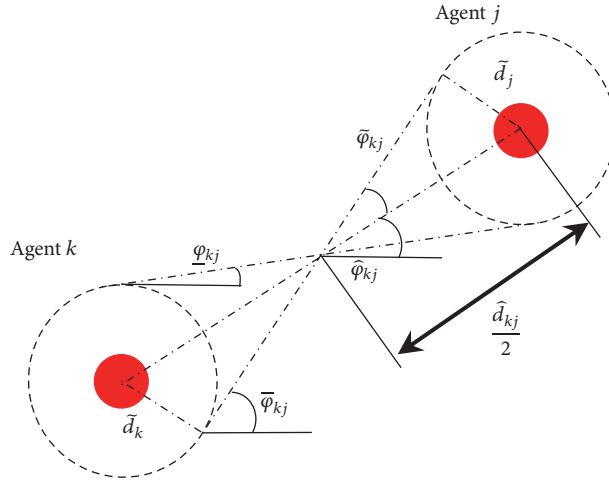


FIGURE 3: A detailed example of uncertainty model for two cooperative nodes.

From (6), we can find that the channel coefficient ξ_{kj} is a monotonically nonincreasing function of d_{kj} , $j \in \mathcal{A}_k$ and a monotonically increasing function of d_{kn} , $n \in \mathcal{N}_j$. Thus, the ERC ξ_{kj} is bounded by

$$\underline{\xi}_{kj} = \frac{\zeta_{kj} \bar{d}_{kj}^p}{N_0/2 + \sum_{n=1}^{N_j} \zeta_{kn} (P_n^J / \bar{d}_{kn}^p)}, \quad (19)$$

$$\bar{\xi}_{kj} = \frac{\zeta_{kj} \underline{d}_{kj}^p}{N_0/2 + \sum_{n=1}^{N_j} \zeta_{kn} (P_n^J / \underline{d}_{kn}^p)}, \quad (20)$$

$$\xi_{kj} \in [\underline{\xi}_{kj}, \bar{\xi}_{kj}] =: \mathcal{C}_{kj}. \quad (21)$$

In summary, we have the set of actual network parameters as

$$\{\varphi_{kj}, \xi_{kj}\}_{k \in \mathcal{N}_a, j \in \mathcal{A}_k} \in \prod_{k \in \mathcal{N}_a, j \in \mathcal{A}_k} \mathcal{F}_{kj} \times \mathcal{C}_{kj}. \quad (22)$$

To ensure the localization accuracy, the worst-case should be considered with parameter uncertainty. Then the worst-case SPBE is given by

$$\mathcal{P}_R(\mathbf{p}_k) = \max_{\{\{\varphi_{kj}, \xi_{kj}\} \in \mathcal{F}_{kj} \times \mathcal{C}_{kj}\}} \text{tr} \{ \mathbf{J}_k^{-1}(\mathbf{p}_k) \}. \quad (23)$$

4. Robust Power Allocation Strategies

To solve the proposed problem, we introduce following proposition.

Proposition 1. *The SPEB of each agent node is convex about $\mathbf{x} = [x_1, x_2, \dots, x_{N_a+N_b}]$. At the same time, it can be formulated as*

$$\mathcal{P}(\mathbf{p}_k; \mathbf{x}) = \frac{4 \cdot \mathbf{1}^T \mathbf{R}_k \mathbf{x}}{\mathbf{x}^T \mathbf{R}_k^T \mathbf{\Lambda}_k \mathbf{R}_k \mathbf{x}}, \quad (24)$$

where $\mathbf{R}_k = \text{diag}\{\xi_{k1}, \xi_{k2}, \dots, \xi_{k(N_a+N_b)}\}$ and $\mathbf{\Lambda}_k$ is the symmetric matrix to reflect the topology, given by

$$\mathbf{\Lambda}_k = \mathbf{1}\mathbf{1}^T - \mathbf{c}(2\varphi_k) \mathbf{c}(2\varphi_k) - \mathbf{s}(2\varphi_k) \mathbf{s}(2\varphi_k), \quad (25)$$

where

$$\varphi_k = [\varphi_{k1} \ \varphi_{k2} \ \dots \ \varphi_{k(N_a+N_b)}]^T, \quad (26)$$

$$\mathbf{c}(2\varphi_k) = [\cos(2\varphi_{k1}) \ \cos(2\varphi_{k2}) \ \dots \ \cos(2\varphi_{k(N_a+N_b)})]^T \quad (27)$$

$$\mathbf{s}(2\varphi_k) = [\sin(2\varphi_{k1}) \ \sin(2\varphi_{k2}) \ \dots \ \sin(2\varphi_{k(N_a+N_b)})]^T. \quad (28)$$

Proposition 2. *According to the result in Proposition 1, the proposed power allocation problem can be transformed into the SOCP, given as*

$$\begin{aligned} P_A^{\text{SOCP}} : \quad & \mathbf{1}^T \mathbf{x}_a + \mathbf{1}^T \mathbf{x}_b \\ \text{s.t.} \quad & \|\mathbf{A}^T \mathbf{R}_k \mathbf{x} + \mathbf{b}_k\| \leq \mathbf{1}^T \mathbf{R}_k \mathbf{x} - 2 \cdot \tau_k^{-1}, \\ & \forall k \in \mathcal{N}_a \end{aligned} \quad (29)$$

$$c_l(\mathbf{x}_a, \mathbf{x}_b) \leq 0, \quad l = 1, 2, \dots, L$$

where $\mathbf{A}_k = [\mathbf{c}(2\varphi_k) \ \mathbf{s}(2\varphi_k) \ \mathbf{0}]^T$ and $\mathbf{b}_k = [0 \ 0 \ 2\tau_k^{-1}]^T$. Note that the proofs of Propositions 1 and 2 are similar to Appendix B and proposition 3 in [6], so here we omit the details for brevity. The next task is to address the uncertainty parameters about angel and ERC.

Form Proposition 1, we can conclude that the SPEB is a monotonically nonincreasing function of ERC. So it will be the worst-case for SPEB when the ERC $\xi_{kj} = \underline{\xi}_{kj}$ for all $j \in \mathcal{A}_k$. In other words, when $\mathbf{R}_k = \text{diag}\{\underline{\xi}_{k1}, \underline{\xi}_{k2}, \dots, \underline{\xi}_{k(N_a+N_b)}\}$, the maximization of SPEB over ERC ξ can be reached.

Moreover, because the SPEB over angel φ_{kj} is not an explicit expression, it will be more complicated to address the angular uncertainty.

From (18), we can find that only the denominator includes the angel φ_{kj} . Then the angular uncertainty problem can be transformed to find the lower bound of the denominator.

Proposition 3. *In the (18), the denominator can be expressed by*

$$\mathbf{x}^T \mathbf{R}_k^T \Lambda_k \mathbf{R}_k \mathbf{x} = (\mathbf{1}^T \mathbf{R}_k \mathbf{x})^2 - \left\| [\mathbf{c}_k \ \mathbf{s}_k]^T \mathbf{R}_k \mathbf{x} \right\|^2. \quad (30)$$

Then let

$$\sin \check{\varphi}_{kj} = \max_{|\varepsilon| \leq \bar{\varphi}_{kj}} \left| 2 \sin(2\bar{\varphi}_{kj} + \varepsilon) \sin \varepsilon \right|, \quad (31)$$

$$\cos \check{\varphi}_{kj} = \max_{|\varepsilon| \leq \bar{\varphi}_{kj}} \left| 2 \cos(2\bar{\varphi}_{kj} + \varepsilon) \cos \varepsilon \right|, \quad (32)$$

and

$$\begin{aligned} \check{\mathbf{c}}(\varphi_k) &= \left[\cos(\check{\varphi}_{k1}) \ \cos(\check{\varphi}_{k2}) \ \cdots \ \cos(\check{\varphi}_{k(N_a+N_b)}) \right]^T, \quad (33) \\ \check{\mathbf{s}}(\varphi_k) &= \left[\sin(\check{\varphi}_{k1}) \ \sin(\check{\varphi}_{k2}) \ \cdots \ \sin(\check{\varphi}_{k(N_a+N_b)}) \right]^T, \quad (34) \end{aligned}$$

We can get

$$\mathcal{P}_R(\mathbf{p}_k, \mathbf{x}) \leq \mathcal{P}_U(\mathbf{p}_k, \mathbf{x}), \quad (35)$$

$$\begin{aligned} \mathcal{P}_U(\mathbf{p}_k, \mathbf{x}) &= \max_{e_1, e_2 = \pm 1} \frac{4 \cdot \mathbf{1}^T \mathbf{R}_k \mathbf{x}}{(\mathbf{1}^T \mathbf{R}_k \mathbf{x})^2 - \left\| \left([\hat{\mathbf{c}}_k \ \hat{\mathbf{s}}_k \ \mathbf{0}]^T + [e_1 \check{\mathbf{c}}_k \ e_2 \check{\mathbf{s}}_k \ \mathbf{0}]^T \right) \mathbf{R}_k \mathbf{x} \right\|^2}. \quad (36) \end{aligned}$$

Proof. One has

$$\mathbf{c}_k^T \mathbf{R}_k \mathbf{x} = \hat{\mathbf{c}}_k^T \mathbf{R}_k \mathbf{x} + (\mathbf{c}_k - \hat{\mathbf{c}}_k)^T \mathbf{R}_k \mathbf{x}, \quad (37)$$

and

$$\begin{aligned} & \max_{\varphi_{kj} \in \mathcal{F}_{kj}} \left| (\mathbf{c}_k - \hat{\mathbf{c}}_k)^T \mathbf{R}_k \mathbf{x} \right| \\ &= \max_{\max_{|\varepsilon| \leq \bar{\varphi}_{kj}}} \left| \sum \left\{ \cos(2\bar{\varphi}_{kj}) - \cos[2(\bar{\varphi}_{kj} + \varepsilon)] \right\} \right. \\ & \quad \cdot \left. \xi_{kj} x_j \right| \\ &\leq \sum (\xi_{kj} x_j) \max_{|\varepsilon| \leq \bar{\varphi}_{kj}} \left| \cos(2\bar{\varphi}_{kj}) - \cos[2(\bar{\varphi}_{kj} + \varepsilon)] \right| \\ &= \sum (\xi_{kj} x_j) \sin \check{\varphi}_{kj} = \check{\mathbf{s}}(\varphi_k)^T \\ & \quad \cdot \mathbf{R}_k \mathbf{x}. \end{aligned} \quad (38)$$

So

$$\begin{aligned} \max_{\varphi_{kj} \in \mathcal{F}_{kj}} \left| \mathbf{c}_k^T \mathbf{R}_k \mathbf{x} \right| &\leq \left| \hat{\mathbf{c}}_k^T \mathbf{R}_k \mathbf{x} \right| + \max_{\varphi_{kj} \in \mathcal{F}_{kj}} \left| (\mathbf{c}_k - \hat{\mathbf{c}}_k)^T \mathbf{R}_k \mathbf{x} \right| \\ &\leq \left| \hat{\mathbf{c}}_k^T \mathbf{R}_k \mathbf{x} \right| + \check{\mathbf{s}}(\varphi_k)^T \mathbf{R}_k \mathbf{x} \\ &\leq \max_{e_1 = \pm 1} \left| [\hat{\mathbf{c}}_k + e_1 \check{\mathbf{s}}(\varphi_k)]^T \mathbf{R}_k \mathbf{x} \right|. \quad (39) \end{aligned}$$

Consequently, we have

$$\max_{\varphi_{kj} \in \mathcal{F}_{kj}} \left| \mathbf{s}_k^T \mathbf{R}_k \mathbf{x} \right| \leq \max_{e_1 = \pm 1} \left| [\hat{\mathbf{c}}_k + e_1 \check{\mathbf{c}}(\varphi_k)]^T \mathbf{R}_k \mathbf{x} \right|. \quad (40)$$

Thus,

$$\begin{aligned} & \max_{\varphi_{kj} \in \mathcal{F}_{kj}} \left\{ (\mathbf{c}_k^T \mathbf{R}_k \mathbf{x})^2 + (\mathbf{s}_k^T \mathbf{R}_k \mathbf{x})^2 \right\} \\ &\leq \max_{e_1, e_2 = \pm 1} \left\{ \left[[\hat{\mathbf{c}}_k + e_1 \check{\mathbf{c}}(\varphi_k)]^T \mathbf{R}_k \mathbf{x} \right]^2 \right. \\ & \quad \left. + \left[[\hat{\mathbf{s}}_k + e_2 \check{\mathbf{s}}(\varphi_k)]^T \mathbf{R}_k \mathbf{x} \right]^2 \right\}. \quad (41) \end{aligned}$$

Therefore, Proposition 3 is proved. \square

In summary, combining the uncertainty parameters about angel and ERC, the upper bound for the worst-case SPEB can be expressed by

$$\begin{aligned} & \mathcal{P}'_U(\mathbf{p}_k, \mathbf{x}) \\ &= \max_{e_1, e_2 = \pm 1} \frac{4 \cdot \mathbf{1}^T \mathbf{R}_k \mathbf{x}}{(\mathbf{1}^T \mathbf{R}_k \mathbf{x})^2 - \left\| \left([\hat{\mathbf{c}}_k \ \hat{\mathbf{s}}_k \ \mathbf{0}]^T + [e_1 \check{\mathbf{c}}_k \ e_2 \check{\mathbf{s}}_k \ \mathbf{0}]^T \right) \mathbf{R}_k \mathbf{x} \right\|^2}. \quad (42) \end{aligned}$$

Then the constraint in (29) can be relaxed and the proposed problem becomes

$$\begin{aligned} & P_{R-A}^{SOCP} : \min_{\{x_a, x_b\}} \mathbf{1}^T \mathbf{x}_a + \mathbf{1}^T \mathbf{x}_b \\ & \text{s.t.} \quad \left\| \overline{\mathbf{A}}_k \mathbf{R}_k \mathbf{x} + \mathbf{b}_k \right\| \leq \mathbf{1}^T \mathbf{x} - 2 \cdot \tau_k^{-1}, \quad (43) \\ & \quad \quad \quad \forall k \in \mathcal{N}_a \end{aligned}$$

$$c_l(\mathbf{x}_a, \mathbf{x}_b) \leq 0, \quad l = 1, 2, \dots, L$$

where

$$\begin{aligned} \overline{\mathbf{A}}_k &= [(\hat{\mathbf{c}}(2\varphi_k) + e_1 \check{\mathbf{s}}(\varphi_k)) \ (\hat{\mathbf{s}}(2\varphi_k) + e_2 \check{\mathbf{c}}(\varphi_k)) \ \mathbf{0}]^T \\ & \quad e_1, e_2 = \pm 1 \end{aligned} \quad (44)$$

and $\mathbf{b}_k = [0 \ 0 \ 2\tau_k^{-1}]^T$.

Successively, the power allocation strategies can be described in Algorithm 1.

5. Simulation Result

To evaluate the proposed robust power allocation method, the simulation scenario is illustrated in Figure 1. Here we compare the proposed algorithm with the uniform power management scheme and the nonrobust power allocation strategy. In this paper, the normalized power is considered as $x_k^{\max} = 10$, $k \in \mathcal{N}_a \cup \mathcal{N}_b$ and $P_n^J = 5$, $\forall n \in \mathcal{N}_j$. The channel parameter is given as $\varsigma_{kj} = 100N_0/2$ for different nodes and $N_0 = 2$. Moreover, the standard optimization solver CVX is used to address the proposed problem [13].

Figure 4 illustrates the average and worst SPEBs respect to different normalized total power. First, the cooperative

Input $\{\tilde{d}_k, x_k^{\max}\}, k \in \mathcal{N}_a \cup \mathcal{N}_b, \{\tilde{d}_n, P_n^J\}, n \in \mathcal{N}_j.$

Output $\{x_k\}, k \in \mathcal{N}_a \cup \mathcal{N}_b.$

(Step 1) Estimate the positions of each agent nodes with each anchor node power strategy $x_j = x_j^{\max}, j \in \mathcal{N}_b.$

(Step 2) For $k \in \mathcal{N}_a \cup \mathcal{N}_b,$ solve the P_{R-A}^{SOCP} problem in (43).

(Step 3) Output $\{x_k\}, k \in \mathcal{N}_a \cup \mathcal{N}_b.$

ALGORITHM 1: Robust power allocation strategies via SOCP.

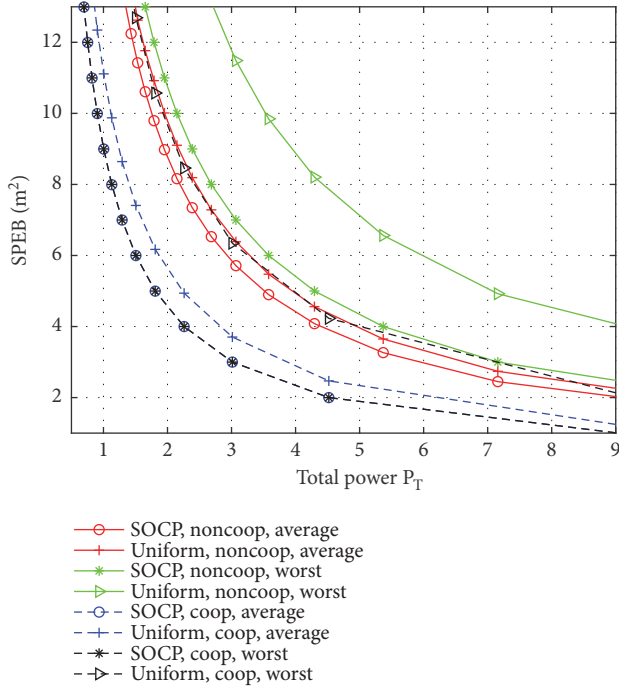


FIGURE 4: Different SPEBs with respect to total power consumption.

localization can obtain lower SPEB than the noncooperative localization in all cases. Second, when consuming the same power, the proposed method via SOCP can reach a better performance than the uniform allocation strategy in both average SPEB and worst SPEB.

Figure 5 shows the average SPEB in different methods with respect to the total power consumption. In both non-cooperative and cooperative localization systems, the robust power allocation strategies have better localization accuracy than the nonrobust approaches. When the uncertainty size $\tilde{d} = 0,$ the problem P_{R-A}^{SOCP} will be equal to P_A^{SOCP} and they have the same performance for nonrobust and robust approaches.

For the same localization accuracy requirement $\tau_k = 4, \forall k \in \mathcal{N}_a,$ the total power consumption and the worst-case SPEB with respect to the uncertainty size are demonstrated in Figures 6 and 7. It can be seen that the cooperative localization consumes less power to achieve the same localization of noncooperative localization. When the parameter uncertainty size increases, the power consumption

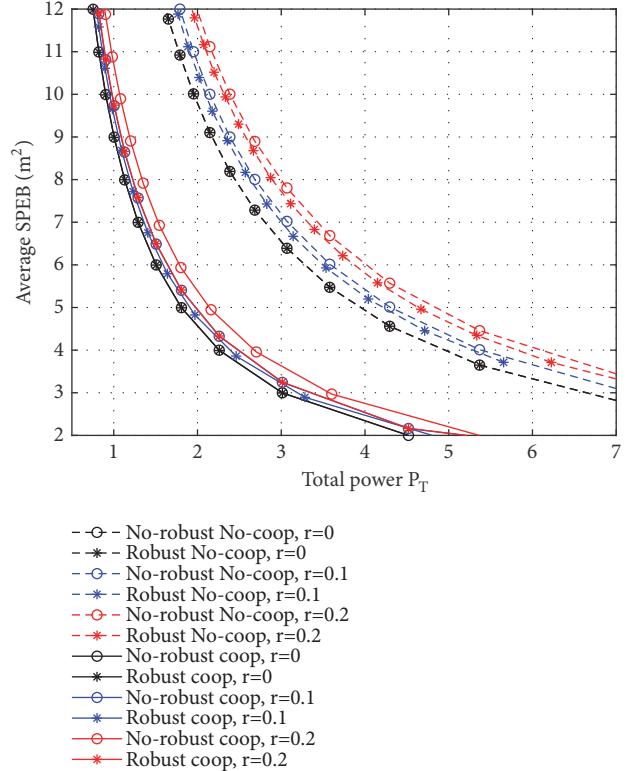


FIGURE 5: Different average SPEBs with respect to total power consumption.

will also increase to ensure the localization requirement in robust cases. At the same time, the worst-case SPEB will decrease due to the robust formulation. But in the nonrobust cases, the worst-case SPEB increase with the uncertainty size, significantly violating the localization accuracy requirement.

6. Conclusion

In this paper, we investigated the robust power allocation strategies for cooperation in jammed wireless sensor localization systems. First, the optimization framework is presented in jammed cooperative localization systems. Then, the robust power allocation strategies are developed to address the parameter uncertainty problem. Moreover, the problem can be transformed into SOCP and obtained the end solution

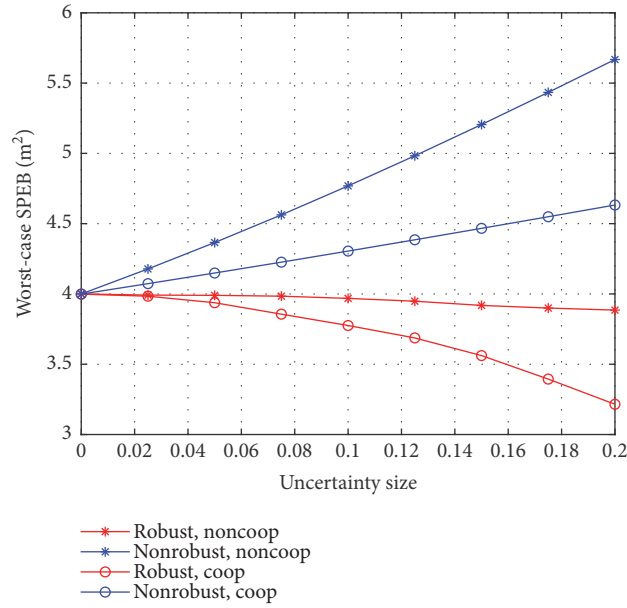


FIGURE 6: The total power consumption with respect to the uncertainty size.

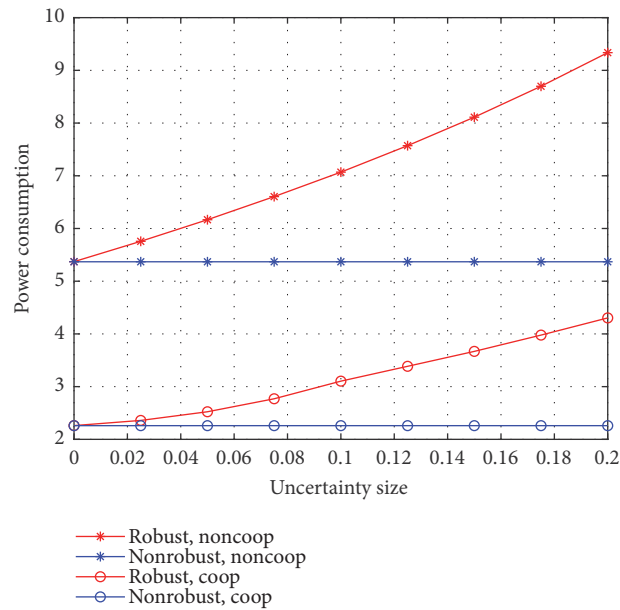


FIGURE 7: The worst-case SPEB with respect to the uncertainty size.

via conic programming. The simulation results demonstrated that the cooperative localization can reach better localization accuracy than noncooperative localization, the power allocation scheme via SOCP outperforms the uniform scheme, and the robust formulation approach outperforms the nonrobust approach.

Data Availability

The data in this paper is generated from the simulation in Matlab, and the detail simulation settings can refer to

Section 5. Therefore, the data used to support the findings of this study are included within the article.

Conflicts of Interest

The authors declare that they have no conflicts of interest.

Acknowledgments

This work was supported by the National Science Foundation of China under Grant 61601511.

References

- [1] G. Han, J. Jiang, C. Zhang, T. Q. Duong, M. Guizani, and G. K. Karagiannidis, "A survey on mobile anchor node assisted localization in wireless sensor networks," *IEEE Communications Surveys & Tutorials*, vol. 18, no. 3, pp. 2220–2243, 2016.
- [2] M. Ke, Y. Wang, M. Li, F. Gao, and Z. Du, "Distributed power allocation for cooperative localization: A potential game approach," in *Proceedings of the 3rd IEEE International Conference on Computer and Communications, ICC3 2017*, pp. 616–621, Chengdu, China, December 2017.
- [3] Y. Shen, H. Wymeersch, and M. Z. Win, "Fundamental limits of wideband localization—part II: cooperative networks," *IEEE Transactions on Information Theory*, vol. 56, no. 10, pp. 4981–5000, 2010.
- [4] Y. Shen and M. Z. Win, "Fundamental limits of wideband localization—part I: a general framework," *IEEE Transactions on Information Theory*, vol. 56, no. 10, pp. 4956–4980, 2010.
- [5] W. W.-L. Li, Y. Shen, Y. J. Zhang, and M. Z. Win, "Robust power allocation for energy-efficient location-aware networks," *IEEE/ACM Transactions on Networking*, vol. 21, no. 6, pp. 1918–1930, 2013.
- [6] Y. Shen, W. Dai, and M. Z. Win, "Power optimization for network localization," *IEEE/ACM Transactions on Networking*, vol. 22, no. 4, pp. 1337–1350, 2014.
- [7] W. Dai, Y. Shen, and M. Z. Win, "Distributed power allocation for cooperative wireless network localization," *IEEE Journal on Selected Areas in Communications*, vol. 33, no. 1, pp. 28–40, 2015.
- [8] J. Chen, W. Dai, Y. Shen, V. Lau, and M. Z. Win, "Power management for cooperative localization: a game theoretical approach," *IEEE Transactions on Signal Processing*, vol. 64, no. 24, pp. 6517–6532, 2016.
- [9] M. Ke, Y. Sun, M. Wang, S. Tian, and L. Lu, "Distributed power optimization for cooperative localization: a hierarchical game approach," *IEEE Wireless Communications Letters*, In press.
- [10] S. Gezici, M. R. Gholami, S. Bayram, and M. Jansson, "Jamming of wireless localization systems," *IEEE Transactions on Communications*, vol. 64, no. 6, pp. 2660–2676, 2016.
- [11] S. Bayram, M. F. Keskin, S. Gezici, and O. Arikan, "Optimal power allocation for jammer nodes in wireless localization systems," *IEEE Transactions on Signal Processing*, vol. 65, no. 24, pp. 6489–6504, 2017.
- [12] M. Ke, G. Zhao, S. Tian, C. Wang, and Y. Liu, "Optimal power allocation for anchor nodes in jammed wireless localization systems," *IEEE Wireless Communications Letters*, In press.
- [13] M. Grant and S. Boyd, "CVX: MATLAB software for disciplined convex programming," *Version 1.21*, 2010, <http://cvxr.com/cvx>.

Research Article

A Self-Powered PMFC-Based Wireless Sensor Node for Smart City Applications

**Daniel Ayala-Ruiz,¹ Alejandro Castillo Atoche,² Erica Ruiz-Ibarra ¹,
Edith Osorio de la Rosa,³ and Javier Vázquez Castillo ⁴**

¹Department of Electronics Engineering, Technology Institute of Sonora, Ciudad Obregon Sonora, Mexico

²Embedded System Department, Autonomous University of Yucatan, Merida Yucatan, Mexico

³Catedras CONACYT and Division of Sciences and Engineering, University of Quintana Roo, Chetumal Quintana Roo, Mexico

⁴Division of Sciences and Engineering, University of Quintana Roo, Chetumal Quintana Roo, Mexico

Correspondence should be addressed to Javier Vázquez Castillo; jvazquez@uqroo.edu.mx

Received 23 March 2019; Revised 2 May 2019; Accepted 19 May 2019; Published 3 June 2019

Guest Editor: Zoran Stamenkovic

Copyright © 2019 Daniel Ayala-Ruiz et al. This is an open access article distributed under the Creative Commons Attribution License, which permits unrestricted use, distribution, and reproduction in any medium, provided the original work is properly cited.

Long power wide area networks (LPWAN) systems play an important role in monitoring environmental conditions for smart cities applications. With the development of Internet of Things (IoT), wireless sensor networks (WSN), and energy harvesting devices, ultra-low power sensor nodes (SNs) are able to collect and monitor the information for environmental protection, urban planning, and risk prevention. This paper presents a WSN of self-powered IoT SNs energetically autonomous using Plant Microbial Fuel Cells (PMFCs). An energy harvesting device has been adapted with the PMFC to enable a batteryless operation of the SN providing power supply to the sensor network. The low-power communication feature of the SN network is used to monitor the environmental data with a dynamic power management strategy successfully designed for the PMFC-based LoRa sensor node. Environmental data of ozone (O₃) and carbon dioxide (CO₂) are monitored in real time through a web application providing IoT cloud services with security and privacy protocols.

1. Introduction

The concept of smart cities and Urban Internet of Things (IoT) is an important research field with the aim to make a better use of the public resources and increase the quality of the services offered to the citizens, while operational costs of the public administration are reduced [1]. In this scenario, the interconnection of sensor nodes (SNs) within a wireless sensor network (WSN) can be used to monitor environmental parameters. At the same time, the integration of an IoT-WSN enables the interconnection of the SNs with the Internet, opening a wide opportunity of end-user applications and Web services. Even though the technology advances in embedded systems with many low-power sensors, microcontroller, and transceivers for digital communications, there is still a great challenge in the power supply of these SNs. In general, these devices are usually powered by batteries; this

constrains the lifetime of the network since they need to be replaced or recharged after a certain period of time.

Currently, several approaches have been developed to prolong the lifetime of SNs, e.g., covering routing protocols, sensing techniques, low-power WSN standards, among others [2–5]. Energy harvesting (EH) is one of the most promising techniques for this purpose, allowing SNs to operate autonomously by collecting and storing energy from the environment. Energy harvesting systems are typically composed of three components: energy source, energy harvesting module, and load (e.g., microcontroller, sensors, wireless transceivers, among others). In this sense, energy plays a leading role in smart cities as in most of our everyday activities, where an advantage of natural resources can be taken. These energy sources can be typically classified as mechanical, radiant, thermal, fluid flow, electromagnetic, and hybrid [5–9]. In this regard, new types of energy sources

have emerged and are still under development, such as the case of Plant Microbial Fuel Cells (PMFCs). PMFC is a green technology that generates energy through an electrochemical process based on the degradation of plant roots via active bacteria [10–12]. A PMFC is able to provide a continuous time-variant power that is managed by the energy harvesting module and stored in a supercapacitor, which can handle a large number of recharge cycles with a high charge-discharge efficiency, and without the need of a complex charge circuitry, albeit at the cost of higher self-discharge rate and lower weight-to-energy density compared with batteries [5, 6].

In this context, a WSN with PMFC-EH is suitable for smart cities, where real-time data acquisition is required in order to improve the collection, aggregation, and use of data using low-cost sensors and low-power communication systems. Authors in [13] designed a self-powered wearable IoT sensor network to monitor environmental conditions. The system incorporates a solar cell, supercapacitors as a storage device, and a LoRa-based wireless transmission module. Even though photovoltaic cells are powerful devices, they provide intermittent energy and depend on environmental conditions (i.e., sun light). Pietrelli et al. [12] reported a Terrestrial Microbial Fuel Cell (TMFC) able to produce a maximum power of $310 \mu\text{W}$ on a soil characterized by a pH of 7.6 and a controlled temperature. The TMFC provided energy to a WSN where IEEE 802.15.4 (Zigbee protocol) based transceivers were tested transmitting a single bit. The experiments showed that it is possible to power a sensor node with a TMFC; however, a more realistic load needs to be tested. This is because the energy consumption of the sensor and microcontroller are not considered in the experiments which would result in a transmission cost increase. Finally, authors in [14] reported a PMFC-EH system for an IoT-based WSN based on *Cordyline fruticosa* plant. The designed PMFC was able to provide 3.5 mW/cm^2 with 0.7 V and 5 mA. The sensor node senses temperature and humidity with a dynamic power management strategy, and data is transmitted using Zigbee. However, several new wireless technologies (e.g., LoRa, Sigfox, and NB-IoT) promise better performance than Zigbee for applications where low-power and long-range are required [15].

The objective of this paper is to propose an IoT-based sensor network design with self-powered PMFC-EH architecture aiming to prolong the lifetime of the network for continuous environmental analysis. The PMFC, based on a *Sansevieria asparagaceae* plant, is able to produce a stable output voltage, allowing the energy harvesting circuit to harvest energy from the PMFC enabling a continuous DC energy supply for the SN. The mean power consumption of the SN is approximately 2.92 mW, considering the sensor measurements, microcontroller processing tasks, and wireless transmission. In addition, experimental results demonstrate a batteryless operation of the PMFC-based LoRa sensor network for environmental monitoring of smart cities.

The rest of the paper is organized as follows: Section 2 describes the PMFC, energy harvesting circuit, and sensor node data acquisition. In Section 3, the performance analysis

of the self-powered PMFC-based LoRa sensor network is showed and discussed. Finally, Section 4 presents the conclusions.

2. IoT-Energy Harvesting System Design

The sensor node energy consumption must be adequate to accomplish an autonomous operation of the IoT WSN; this includes the SN processing tasks and LoRa wireless transmission. The energy harvesting circuit is adapted to PMFC as a power supply, providing a regulated voltage to the microcontroller, ozone (O_3) and carbon dioxide (CO_2) sensors, and LoRa-based transceiver. Figure 1 shows the conceptual architecture of a PMFC-EH system for the proposed sensor node. The following subsections describe the components of the system architecture.

2.1. Plant Microbial Fuel Cell (PMFC). PMFC is a power source that generates energy through the anaerobic degradation of organic matter via rhizosphere bacteria in a sustainable way, having a potential application in supplying electricity to devices. The use of PMFCs can be found in applications for monitoring environmental parameters, maturity of plants, bioremediation, and heavy metal recovering of contaminated environments [10, 11, 16–18].

According to the plant classification in [19], C3 and C4 type of plants achieve a high photosynthetic efficiency by converting the carbon dioxide (CO_2) into a four-carbon sugar compound [20]. Also, these types of plant have a high-rate of solar energy conversion into electrical energy with an increase of rhizosphere surface area for microbiome proliferation. Most microorganisms tend to transfer electrons produced from the metabolism of organic debris. On one hand, the plant root zone provides substrate in the form of root exudates to microbes, and on the other hand, microbes simplify the elemental form of nutrients to an ionic form amenable to the plant [21].

The electrodes are usually separated by a proton exchange membrane, which can be of Na ion [22] or a salt bridge [23]. However, membrane-less PMFC configurations have been reported, where the PMFC-cathode is placed in an oxygen-rich environment [24, 25]. Thus, the PMFC electricity is driven by rhizodeposition of the living plants [19].

The rhizodeposition contains a wide variety of carbon sources that can be used as electrodes, which represent a unique feature of PMFCs. In PMFC designs, the distance between anode and cathode, the dimensions of the electrodes, and the type of plant should be considered as shown in Figure 2.

As illustrated in Figure 2, the plant was placed above the anode and the separation between anode and cathode is 5 cm. The substrate availability per square meter can be improved by increasing the distance among the anode and the plant. Thus, the more roots are between the anode and plant, and the higher rhizodeposition would result. Moreover, studies report that increasing the depth of the anode with a factor of 3 results in more substrate, and consequently, a higher current density and output power can be harvested [23].

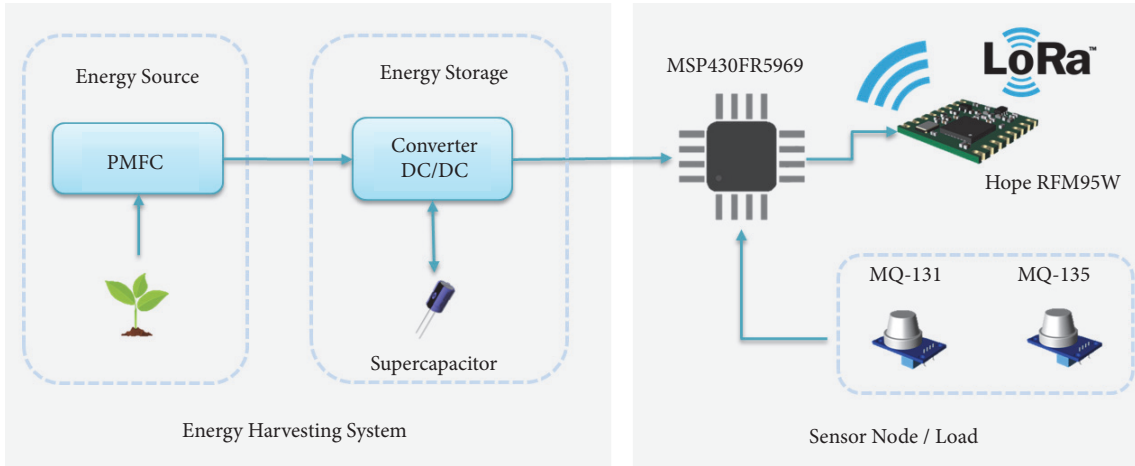


FIGURE 1: Conceptual self-powered sensor node architecture.

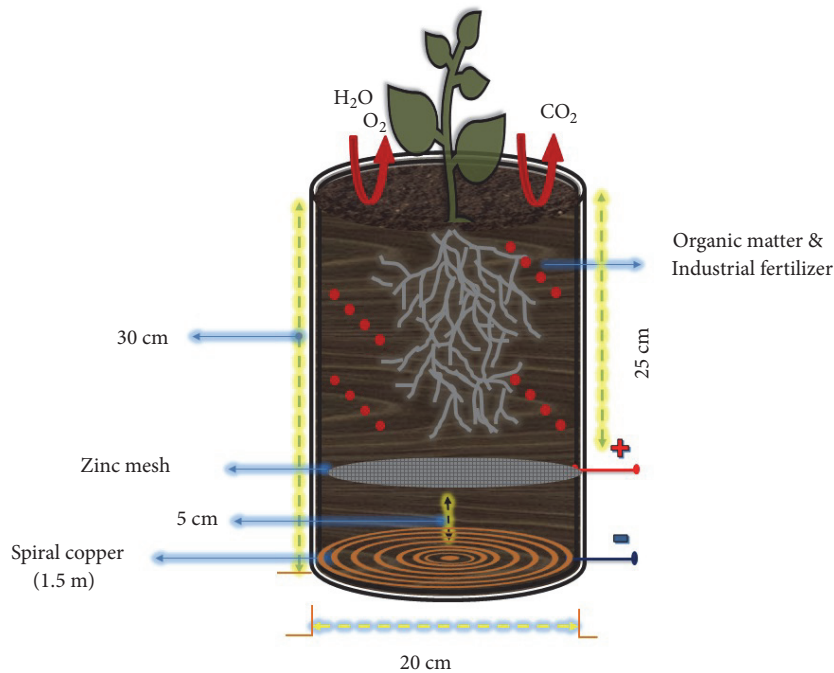


FIGURE 2: Schematic design of the PMFC used as IoT WSN power source.

2.2. Energy Harvesting Circuit. In order to extract the maximum power from the proposed PMFC, it is necessary to use an energy harvesting circuit with the aim of storing power in an external device such as supercapacitors. However, this kind of power sources (e.g., photovoltaic, piezoelectric, among others) is prone to voltage variations due to physical environmental changes, which results in dynamic power charges. Thus, it is necessary to use an efficient energy harvester management module.

The BQ25570 is a nano-power boost charger and buck converter for energy harvester powered applications that manages energy from an input voltage as low as 100 mV, which allows to use this device in thermoelectric generators,

small solar cells, piezoelectric generators, among others. Also, this device was specifically designed to efficiently acquire and manage microwatts (μW) to milliwatts (mW) of power generated from a variety of high output impedances.

The used energy harvester management module can be observed in Figure 3. For our application, the voltage provided by the PMFC is enough to guaranty the BQ25570 operation. The boost converter is powered from output V_{Stor} . Once the V_{Stor} voltage is above $V_{\text{Stor_Chgen}}$ (1.8 V typically), the boost converter can effectively extract power from the PMFC. The V_{Out} voltage is externally programmed to slightly less than the V_{Stor} voltage [26]. Likewise, it implements a programmable maximum power point tracking (MPPT)

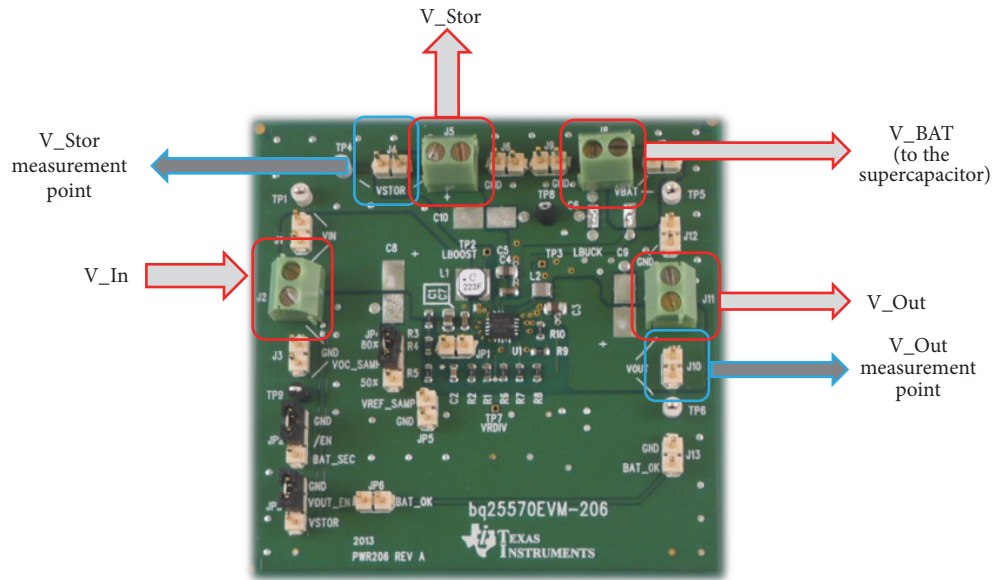


FIGURE 3: Energy harvester subsystem based on BQ25570 power management module.

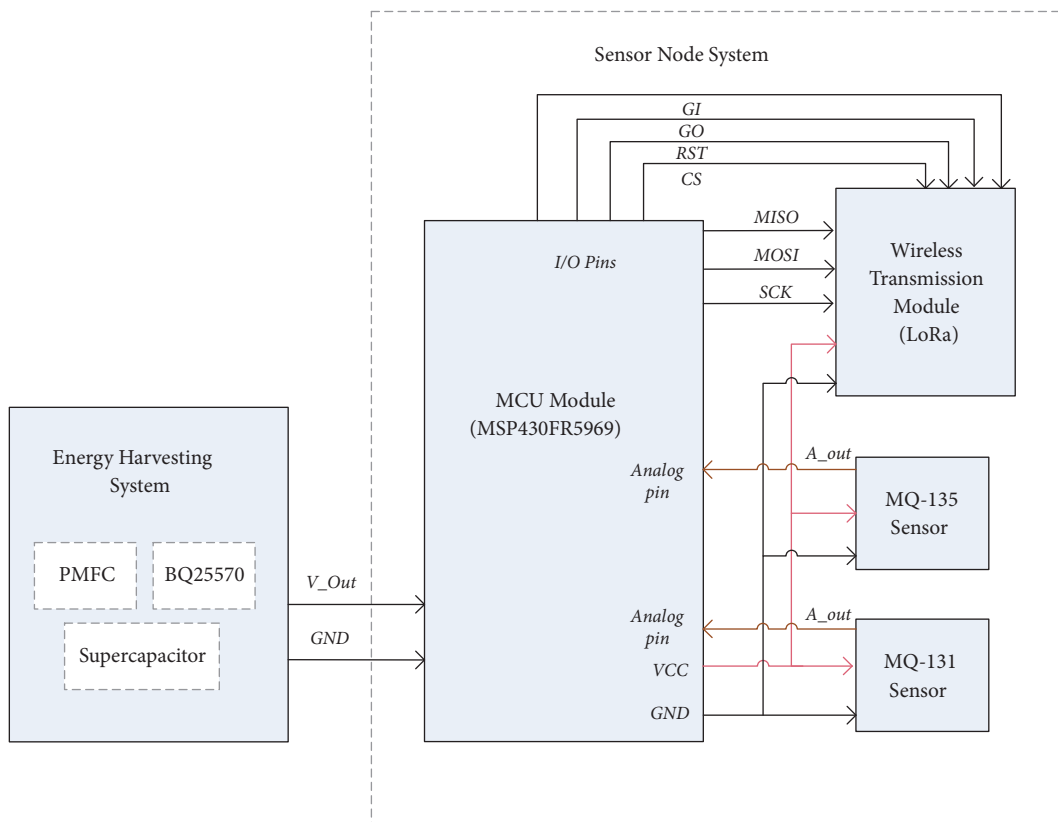


FIGURE 4: Schematic diagram of the sensor node.

sampling network to optimize the transfer of power within the device. Finally, the BQ25570 was designed with the flexibility to support a variety of energy storage elements.

2.3. *Sensor Node Design.* The sensor node is composed of three components: microcontroller, sensors, and LoRa

transceiver radio. Figure 4 illustrates the schematic circuit of the sensor node. The characteristics of the components are described in the following subsections.

2.3.1. *Sensor Module.* The data acquisition of the ozone and carbon dioxide is performed using the MQ-131 and MQ-135

sensors, respectively [27], [28]. The main features of the sensors are fast response, high sensitivity, and wide detecting range and do not need a complex drive circuit. Both sensors are composed by a micro Al_2O_3 ceramic tube, a sensitive layer, measuring electrode, and heater fixed into a crust. Standard condition operation is power and heating voltages of $5V \pm 0.1$, the heater resistance is $33 \Omega \pm 5\%$, and sensing resistance is $50 \text{ k}\Omega - 500 \text{ k}\Omega$. Also, detection range for CO_2 is $10 \text{ ppm} - 1000 \text{ ppm}$ and 10 ppb to 2000 ppb for O_3 gas.

2.3.2. Digital Signal Processing Module. The MSP430FR5969 is an ultra-low power microcontroller unit (MCU) from Texas Instruments with up to 64 KB of non-volatile Ferroelectric Random Access Memory (FRAM). The MCU also supports optimized ultra-low power modes, such as standby (LPM3) and real-time clock (LPM3.5) with a typically power consumption of $0.4 \mu A$ and $0.25 \mu A$, respectively. Moreover, its architecture consists of a 16-bit RISC with up to 16 MHz clock supporting a supply voltage range from 1.8 V to 3.6 V [29]. The Code Composer Studio IDE with EnergyTrace™ tool is used to measure and display the energy consumption of MCU and peripherals.

2.3.3. Wireless Transmission Module. The LoRa transceiver device is the RFM95W, which operates in 868.1 MHz unlicensed band and it is based on the SX1276 LoRa module with SPI interface. This radio can transmit as far as 2 km in line of sight or up to 20 km with directional antennas according to the standard. The output power can be tuned in software from +5 to +20 dBm, with a $\sim 100 \text{ mA}$ peak current within maximum power output and $\sim 30 \text{ mA}$ during active radio listening [19]. Also, an OMNI-directional and 5 dBi gain antenna is coupled to the radio transceiver. In addition, LoRaWAN-Class A is used as a Medium Access Control (MAC) protocol. The Class A MAC protocol opens a transmission window followed by two downlink windows allowing a bidirectional communication with the gateway.

2.4. WSN Architecture. The WSN is composed of three elements: (i) the SNs, (ii) the gateway module, and (iii) an IoT SW application to analyze and manage data coming from SNs. The gateway receives the data and upload the information to a cloud server via WiFi. The network topology is the star configuration. Figure 5 shows the SNs deployment on the Chetumal campus of the University of Quintana Roo, Mexico as a proof of concept of a smart city application.

3. Experimental Results and Discussion

In this section, the PMFC-based LoRa sensor network is evaluated. An experiment with the PMFC, SN, network topology, and power management strategy is presented.

3.1. PMFC. The experiment setup is the following: the PMFC consists of a *Sansevieria asparagaceae* plant in a plastic container with a volume of $V = 9500 \text{ cm}^3$ ($h = 30 \text{ cm}$ and $d = 20 \text{ cm}$), filled with 5 kg of a mixed nutrient-rich soil and 125 gr of industrial fertilizer as a salt bridge. A zinc



FIGURE 5: PMFC-based LoRa WSN architecture.

(Zn) mesh and copper (Cu) wire were used as anode and cathode, respectively (see Figure 2 for details). The PMFC considers a realistic soil sample gathered in University of Quintana Roo, Mexico. It is important to remark that C3 and C4 types of plants are rich for microbiome proliferation, which means that if the organic matter area (or plant root zone) is increased, it will impact in the generation of electrical energy. Thus, the microbial population at the rhizosphere (roots area over the cathode) acts as a biocatalyst for the uptake of root exudates as a substrate and releases redox equivalents (electrons and protons) during its metabolic activity generating energy as voltage/power [19].

To ensure the presence of the electrochemically active bacteria, a mix of organic matter at 100% humidity with diammonium phosphate industrial fertilizer FERTIQUIM [30] is applied into the PMFC. FERTIQUIM composition is 18% of nitrogen (N), 18% of ammonium (NH_4), 46% of phosphorous pentoxide (P_2O_5), 2.20% of soluble sulfur (S), and PH in solution (level 6-7) at 10%. The electrical performance of PMFC was measured using Metrohm Autolab model potentiostat.

In the experiment, the PMFC was stressed along 30 cycles for one week, in order to observe its polarization curve. Figure 6(a) illustrates the polarization and power density curves showing that PMFC voltage is inversely proportional to the output current; also Figure 6(b) shows a voltage and current ranging from 0.8 to 1.25 mW/cm^2 per electrode area that delivers the maximum power density to each cycle. Likewise, it can be seen that a hysteresis effect (i.e., dynamic behavior) is produced and accentuated on the maximum power level, which is related to the initial stabilization of the electron and proton production generated by the bacteria. Figure 6(b) also presents the maximum power density value reached in the polarization curve.

The current density and voltage generated by the PMFC using a load resistance of $1 \text{ k}\Omega$ considering a constant

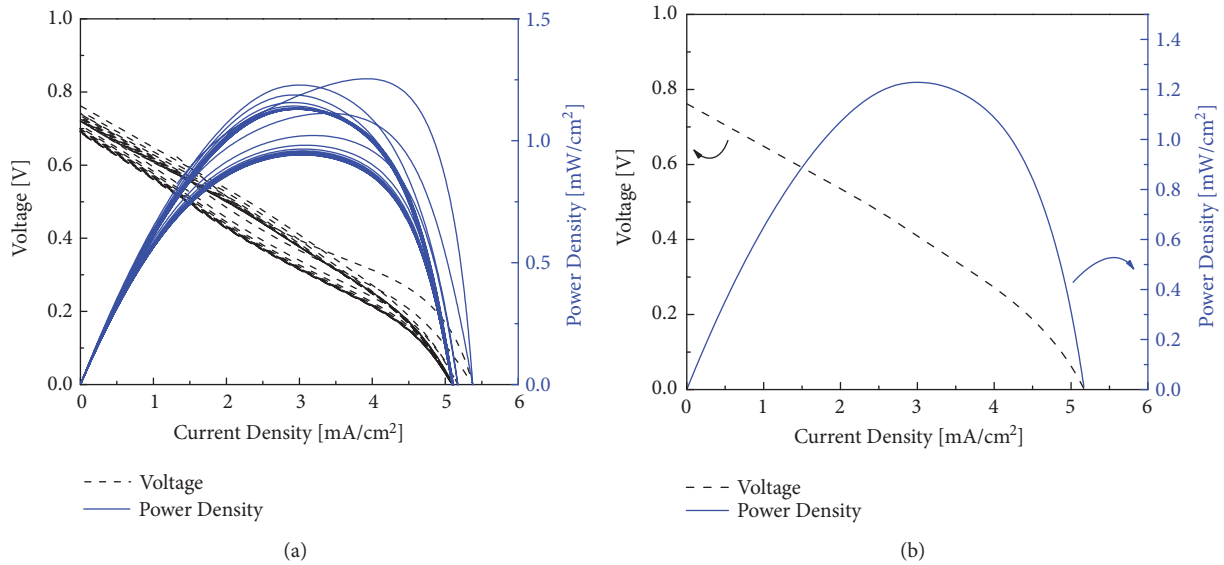


FIGURE 6: Polarization curve and power density of the designed PMFC. (a) PMFC behavior for 30 cycles and (b) PMFC behavior for the maximum power density reached (1.25 mW/cm²).

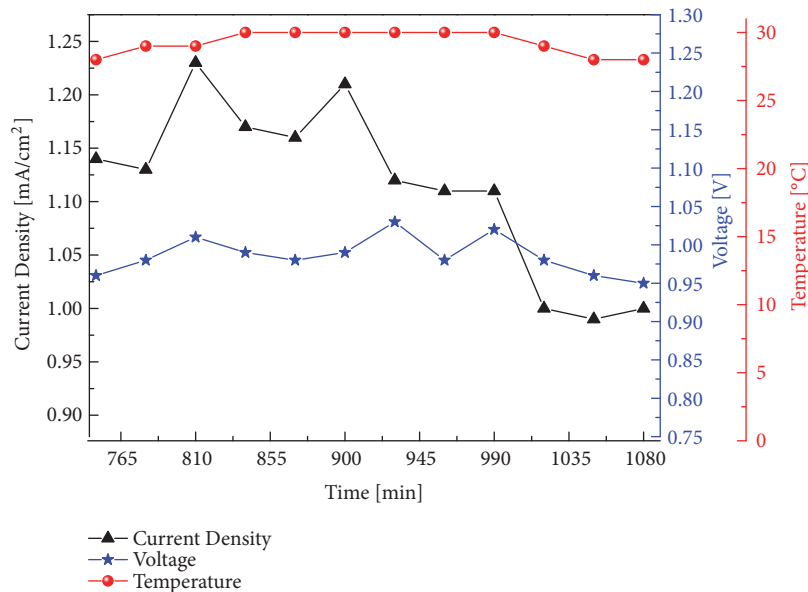


FIGURE 7: Measured electrical parameters of PMFC versus time.

outdoor temperature of 30°C are shown in Figure 7. The measurements were carried out every 50 min, from 12:00 h to 18:00 h. The average values measured of voltage and current density were 1.00 V and 1.125 mA/cm² with a variation of 0.1 V and 0.225 mA/cm², respectively, and the maximum current density was produced at 810 minutes (13:50 h).

The stability of the PMFC as power source is one of the main issues in this study. The analysis of the power density for different charging values and its dynamic behavior depend on the number of cycles in time. Figure 8 shows the voltage and power density, when the PMFC provides a constant current of 2.35 mA. Both voltage and power density decreased down

to 0.4 V and 1 mW/cm² in average, respectively. Also it can be seen that the electrical parameters were recovered after 5 min.

Figure 9 shows another experiment for 45 min, in which the PMFC did not receive water (or fertilizer) along the first 15 min (see the black continuous line in the figure), then the PMFC was irrigated with water. In the experiment, the PMFC was continuously stressed with the Metrolab equipment demanding a constant output voltage of 0.3 V. It can be notice that after the first 15 min the current density of the PMFC was recovered (see the dashed red line in the figure).

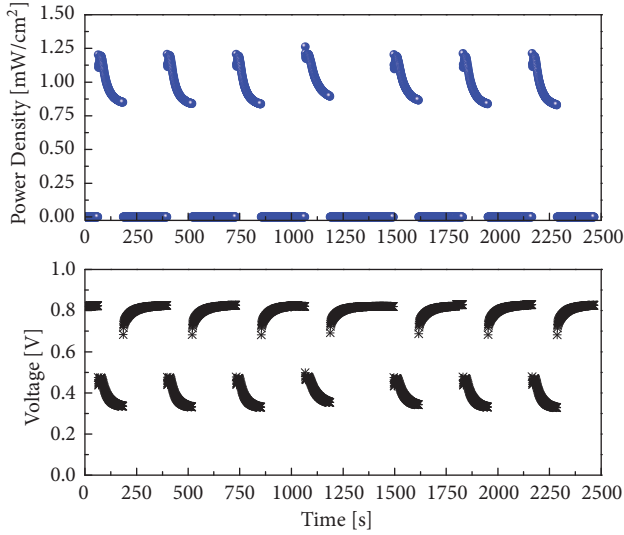


FIGURE 8: PMFC behavior under discharge and recovery stages of its voltage and power density providing a constant current of 2.35 mA.

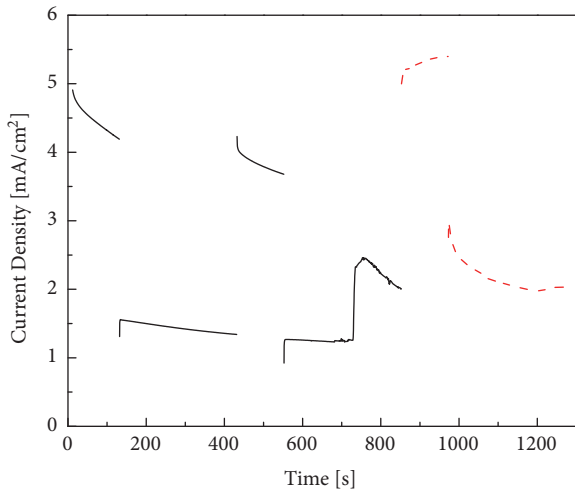


FIGURE 9: Current density versus time of the PMFC with a recovery stage.

3.2. Energy Harvesting Circuit. The BQ25570 circuit is a nano-power energy harvester solution for ultra-low power application. This power management circuit was connected to an external supercapacitor of 0.1 F to storage the energy. In this process, the boost charger output, V_{Stor} , is configured to deliver up to 4.2 V. This voltage is applied to the supercapacitor as long as V_{BAT} is below to the programmed maximum voltage $V_{\text{BAT_LOV}}$. The $V_{\text{BAT_LOK}}$ indicator toggles high when V_{Stor} increases up to 3.3 V and toggles down when V_{Stor} goes below to 2.8 V.

3.3. Sensor Node Design. The dynamic power management strategy considers five processing stages of the sensor nodes. Figure 10 presents the processing flow diagram of the sensor node. The first stage requires 47 ms and setups the sensor

TABLE 1: LoRa configuration parameter selection.

SF	Frequency Channel (Mhz)	BW (Mhz)	CR	Transmission Power (dBm)
7	868.1	125	4/5	14

TABLE 2: Duty cycling schemes.

Transmission intervals (min)	Power (mW) (Max / Mean)	Current (mA) (Max / Mean)
5	166.25 / 3.47	46.36 / 0.96
10	158.98 / 3.09	44.34 / 0.86
20	164.37 / 2.92	45.85 / 0.81

node configuration such as the spreading factor (SF), frequency channel, channel bandwidth (BW), coding rate (CR), and transmission power. In the configuration, short periods of 8 ms are used to achieve the gas concentration. These fast responses in the sensor read measurements are related to stable temperature and humidity environment and to a reduced sensors resistance ratio between the target gas concentration and the resistance of the sensor. The `sense_interval` and `tx_interval` can be adjusted according to the application. In this study, time periods of 5, 10, and 20 min were considered. Both `sense` and `Tx` intervals are configured in LPM3 low-power mode, which means an average power consumption down to 2.92 mW for a time period of 20 min. After the `sense_interval`, the MCU wakes up to read during 8 ms the ozone and carbon dioxide sensors with a bit rate of 12500 bps, then the SN returns to sleep mode and remains a `tx_interval` before the uplink transmission is executed. The transmission stage requires 63 ms, and finally two response windows are opened (i.e., RX1 and RX2 in Figure 10) of 10 ms and 30 ms, respectively, in order to establish bidirectional communication with the application server. Table 1 shows the LoRa radio parameters selection used for the experiment.

Figure 11 shows the real-time behavior of the SN power consumption, and Table 2 summarizes the measured values for different transmission periods. In order to estimate the power and current consumption of the SN, the EnergyTrace software is used for real-time energy-power measurements designed specifically for ultra-low power applications. EnergyTrace technology is included in Code Composed Studio version 6.0 and newer [31]. The resulting maximum and mean power consumption values, with transmission period of 20 min, are equal to 164.37 mW and 2.92 mW, respectively. EnergyTrace software also provides the maximum and mean current consumption of the SN with resulting values of 45.85 mA and 0.81 mA, respectively, for the same transmission interval experiment.

3.4. IoT Monitoring System. A web-server monitoring system was developed for online data visualization and analysis. Figure 12 shows the visual interface of the software application for the measured data in the test field. The interface was implemented using Apache and PHP web design tools. Likewise, in order to comply with security matters, all data is encrypted and transmitted to a cloud platform through a

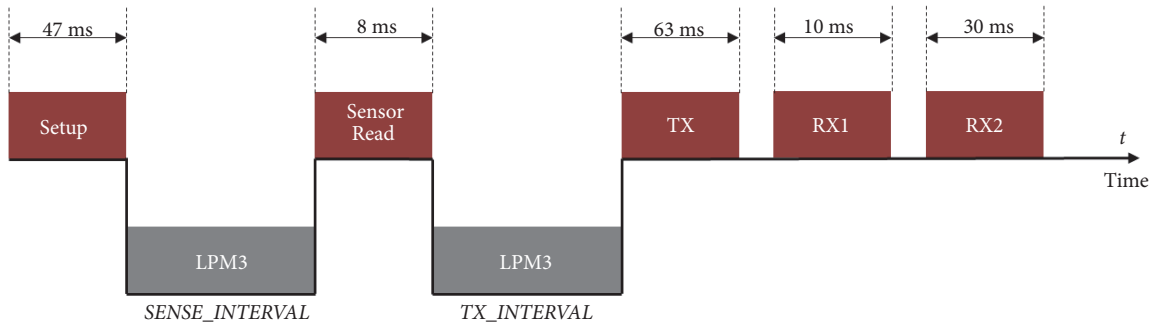


FIGURE 10: Duty cycle of the sensor node.

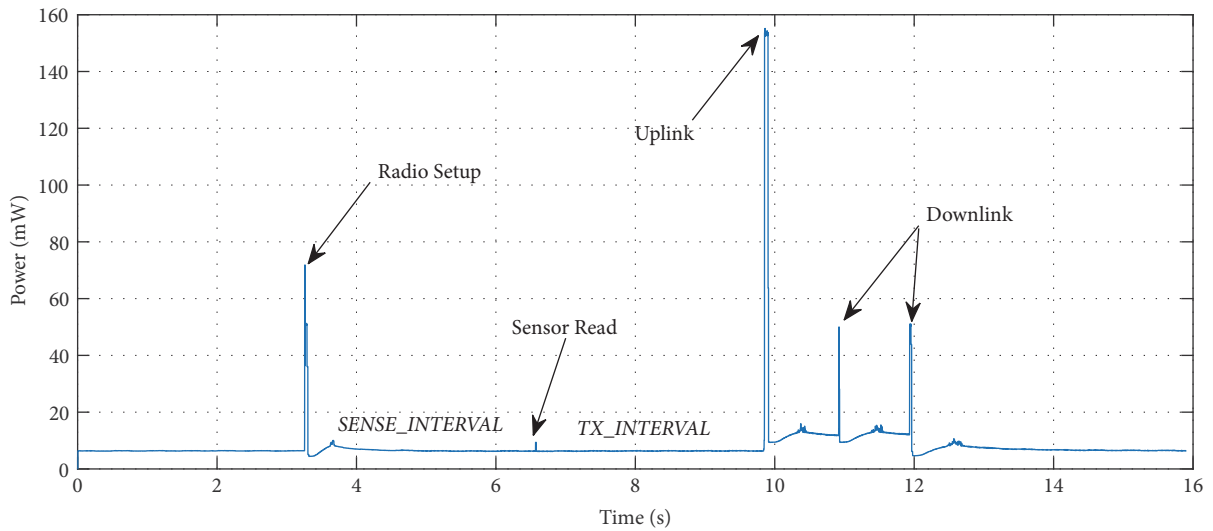


FIGURE 11: Sensor node power consumption.

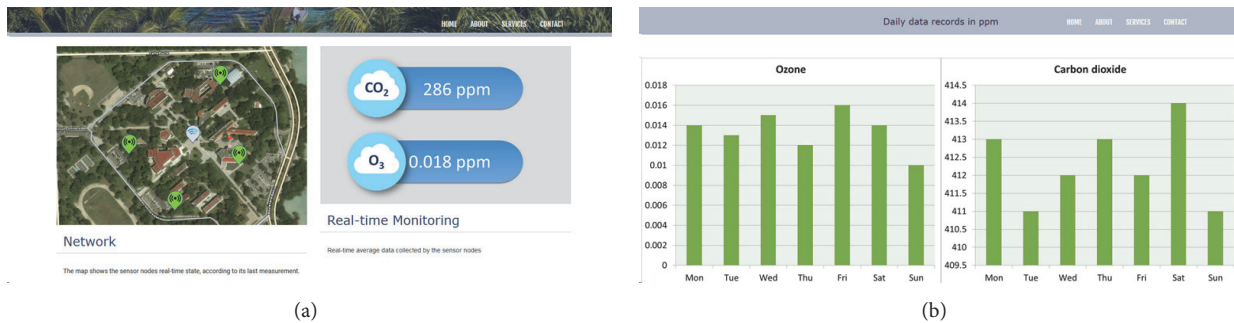


FIGURE 12: IoT monitoring system for the self-powered PMFC-based LoRa sensor network for environmental analysis in smart cities: (a) sensor node network and (b) visualization of averaged data per day.

LoRa single-channel gateway. The encryption is performed following the activation-by-personalization method defined by the LoRaWAN standard [32]. Also, the sensor data is retrieved from the cloud platform and stored on a local server employing MySQL.

3.5. Discussion. A self-powered IoT system is a power-aware solution for the design of wireless sensor nodes with a batteryless feature. In this sense, the integration of energy

conservation and harvesting techniques is demanded for applications in smart cities.

In this study, a PMFC based on the *Sansevieria asparagaceae* plant is adapted to an energy harvester circuit as a power cell source. PMFC implementation results show that providing a constant current of 2.35 mA to an external device the voltage goes from 0.8 V to 0.5 V. After 2 min, the voltage decreases to 0.33 V, which represents a loss of 42% of the open circuit voltage (0.8 V). Once the load is removed, the

PMFC suddenly recovers 85% of the open circuit voltage and the 100% of its open circuit voltage is recovered after ~4 min. Regarding the power density, it decays to 30% of its initial value (1.25 mW/cm^2) considering the time of discharge and recovery voltage as showed in Figure 8.

In this sense, we can conclude that the PMFC is able to provide a power density of 1.25 mW/cm^2 to the energy harvester BQ25570 circuit, which provides a regulated output of 3.3 V, and stores the energy in a supercapacitor. As illustrated in Figure 11 and Table 2, the mean power consumption of the SN is 3.47, 3.09, and 2.92 mW for transmission intervals of 5, 10, and 20 min, respectively. The test case scenario results reported in Figures 6, 7, 8, 9, and 11 indicate an autonomous operation of the PMFC-based LoRa sensor node.

4. Conclusions

This paper proposes a WSN of self-powered PMFC-based LoRa sensor nodes (SNs) for environmental analysis in smart cities. The system was implemented in the Campus of the University of Quintana Roo in Chetumal, Mexico, as a proof of concept of a smart city, monitoring the surrounding environmental data of ozone (O_3) and carbon dioxide (CO_2) in real time. In the design, a PMFC power cell, based on the *Sansevieria asparagaceae* plant, was implemented and adapted with an energy harvester circuit to supply a DC output power to the SN. To demonstrate a stable operation, the PMFC was stressed with the Metrohm Autolab potentiostat equipment achieving an adequate performance of 1.25 mW/cm^2 with 0.8 V in open circuit. The used energy harvesting circuit is able to collect the energy from the PMFC regardless of the variations in the charging rates and low input voltages (namely, 100mV). The BQ25570 energy harvester module with nano-power boost charger and buck converter was implemented to manage and store the energy in a supercapacitor. In combination with the PMFC-EH, a dynamic power management strategy was also proposed for ultra-low power consumption of the LoRa-based wireless SN. Experimental results presented in Section 3 showed a SN mean power consumption of 2.92 mW, which is well supported by the proposed PMFC, achieving an autonomous operation of the self-powered PMFC-based LoRa SNs.

Data Availability

The data used to support the findings of this study are available from the corresponding author upon request.

Conflicts of Interest

The authors declare that there are no conflicts of interest regarding the publication of this article.

Acknowledgments

This work was supported by the Programa para el Desarrollo Profesional Docente (PRODEP) 2019, Mexico.

References

- [1] A. Zanella, N. Bui, A. P. Castellani, L. Vangelista, and M. Zorzi, "Internet of things for smart cities," *IEEE Internet of Things Journal*, vol. 1, no. 1, pp. 22–32, 2014.
- [2] N. A. Pantazis, S. A. Nikolidakis, and D. D. Vergados, "Energy-efficient routing protocols in wireless sensor networks: a survey," *IEEE Communications Surveys & Tutorials*, vol. 15, no. 2, pp. 551–591, 2013.
- [3] T. Rault, A. Bouabdallah, and Y. Challal, "Energy efficiency in wireless sensor networks: a top-down survey," *Computer Networks*, vol. 67, pp. 104–122, 2014.
- [4] S. Sendra, J. Lloret, M. García, and J. F. Toledo, "Power saving and energy optimization techniques for wireless sensor networks," *Journal of Communications*, vol. 6, no. 6, pp. 439–459, 2011.
- [5] F. Engmann, F. A. Katsriku, J.-D. Abdulai, K. S. Adu-Manu, and F. K. Banaseka, "Prolonging the lifetime of wireless sensor networks: a review of current techniques," *Wireless Communications and Mobile Computing*, vol. 2018, Article ID 8035065, 23 pages, 2018.
- [6] S. Sudevalayam and P. Kulkarni, "Energy harvesting sensor nodes: survey and implications," *IEEE Communications Surveys & Tutorials*, vol. 13, no. 3, pp. 443–461, 2011.
- [7] G. Zhou, L. Huang, W. Li, and Z. Zhu, "Harvesting ambient environmental energy for wireless sensor networks: a survey," *Journal of Sensors*, vol. 2014, Article ID 815467, 20 pages, 2014.
- [8] K. Z. Panatik, K. Kamardin, S. A. Shariff et al., "Energy harvesting in wireless sensor networks: a survey," in *Proceedings of the 3rd IEEE International Symposium on Telecommunication Technologies (ISTT)*, pp. 53–58, IEEE, 2016.
- [9] X. Lu, P. Wang, D. Niyato, D. I. Kim, and Z. Han, "Wireless networks with RF energy harvesting: a contemporary survey," *IEEE Communications Surveys & Tutorials*, vol. 17, no. 2, pp. 757–789, 2015.
- [10] H. Deng, Z. Chen, and F. Zhao, "Energy from plants and microorganisms: progress in plant-microbial fuel cells," *ChemSusChem*, vol. 5, no. 6, pp. 1006–1011, 2012.
- [11] D. Brunelli, P. Tosato, and M. Rossi, "Flora health wireless monitoring with plant-microbial fuel cell," *Procedia Engineering*, vol. 168, pp. 1646–1650, 2016.
- [12] A. Pietrelli, A. Micangeli, V. Ferrara, and A. Raffi, "Wireless sensor network powered by a terrestrial microbial fuel cell as a sustainable land monitoring energy system," *Sustainability*, vol. 6, no. 10, pp. 7263–7275, 2014.
- [13] F. Wu, J. Redouté, M. R. Yuçe, and J. Redouté, "WE-Safe: a self-powered wearable iot sensor network for safety applications based on LoRa," *IEEE Access*, vol. 6, no. 40, pp. 846–853, 2018.
- [14] E. Osorio de la Rosa, J. Vázquez Castillo, M. Carmona Campos et al., "Plant microbial fuel cells-based energy harvester system for self-powered IoT applications," *Sensors*, vol. 19, no. 6, p. 1378, 2019.
- [15] K. Mekki, E. Bajic, F. Chaxel, and F. Meyer, "A comparative study of LPWAN technologies for large-scale IoT deployment," *ICT Express*, 2018.
- [16] N. Habibul, Y. Hu, Y.-K. Wang, W. Chen, H.-Q. Yu, and G.-P. Sheng, "Bioelectrochemical chromium(VI) removal in plant-microbial fuel cells," *Environmental Science & Technology*, vol. 50, no. 7, pp. 3882–3889, 2016.
- [17] R. Nitisravut and R. Regmi, "Plant microbial fuel cells: a promising biosystems engineering," *Renewable & Sustainable Energy Reviews*, vol. 76, pp. 81–89, 2017.

- [18] N. Tapia, C. Rojas, C. Bonilla, and I. Vargas, "A new method for sensing soil water content in green roofs using plant microbial fuel cells," *Sensors*, vol. 18, no. 2, p. 71, 2018.
- [19] P. Chiranjeevi, D. K. Yeruva, K. A. Kumar, V. S. Mohan, and S. Varjani, "Plant-microbial fuel cells technology," *Microbial Electrochemical Technology*, pp. 549–561, 2019.
- [20] S. Enríquez, C. M. Duarte, and K. Sand-Jensen, "Patterns in decomposition rates among photosynthetic organisms: the importance of detritus C:N:P content," *Oecologia*, vol. 94, no. 4, pp. 457–471, 1993.
- [21] L. Moulin, A. Munive, B. Dreyfus, and C. Boivin-Masson, "Nodulation of legumes by members of the β -subclass of Proteobacteria," *Nature*, vol. 411, no. 6840, pp. 948–950, 2001.
- [22] R. Regmi, R. Nitorisavut, and J. Ketchaimongkol, "A decade of plant-assisted microbial fuel cells: looking back and moving forward," *Biofuels*, vol. 9, no. 5, pp. 605–612, 2018.
- [23] K. Wetser, E. Sudirjo, C. J. N. Buisman, and D. P. B. T. B. Strik, "Electricity generation by a plant microbial fuel cell with an integrated oxygen reducing biocathode," *Applied Energy*, vol. 137, pp. 151–157, 2015.
- [24] M. M. Ghangrekar and V. B. Shinde, "Performance of membrane-less microbial fuel cell treating wastewater and effect of electrode distance and area on electricity production," *Bioresource Technology*, vol. 98, no. 15, pp. 2879–2885, 2007.
- [25] S. R. Gilani, A. Yaseen, S. R. A. Zaidi, M. Zahra, and Z. Mahmood, "Photocurrent generation through plant microbial fuel cell by varying electrode materials," *Journal of the Chemical Society of Pakistan*, vol. 38, no. 1, pp. 17–27, 2016.
- [26] TI, "Ultra low power management IC, boost charger nanopowered buck converter evaluation module, 2019," <http://www.ti.com/tool/BQ25570EVM-206>.
- [27] Sainsmart, "MQ131 gas sensor ozone module, 2019," <https://www.sainsmart.com/>.
- [28] HiLetgo, "MQ135 air quality sensor hazardous gas detection module, 2019," <http://www.hiletgo.com/>.
- [29] TI, "MSP430FR5969 launchpad development kit, 2019," <http://www.ti.com/tool/MSP-EXP430FR5969>.
- [30] Fertiquim, "Diammonium phosphate, 2019," <http://fertiquim.com.mx/wp-content/uploads/2016/06/fosfatodiamonico.pdf>.
- [31] TI, "Code composer studio (CCS) integrated development environment (IDE), 2019," <http://www.ti.com/tool/CCSTUDIO>.
- [32] N. Sornin, M. Luis, T. Eirich, T. Kramp, and O. Hersent, "LoRaWAN Specification, LoRa Alliance Std, 2016".

Research Article

Novel Energy-Efficient Data Gathering Scheme Exploiting Spatial-Temporal Correlation for Wireless Sensor Networks

Ying Zhou , Lihua Yang , Longxiang Yang, and Meng Ni

Jiangsu Key Laboratory of Wireless Communication, Nanjing University of Posts and Telecommunications, Nanjing, Jiangsu 210003, China

Correspondence should be addressed to Lihua Yang; yanglh@njupt.edu.cn

Received 14 March 2019; Accepted 8 May 2019; Published 19 May 2019

Guest Editor: Bojan Dimitrijevic

Copyright © 2019 Ying Zhou et al. This is an open access article distributed under the Creative Commons Attribution License, which permits unrestricted use, distribution, and reproduction in any medium, provided the original work is properly cited.

A novel energy-efficient data gathering scheme that exploits spatial-temporal correlation is proposed for clustered wireless sensor networks in this paper. In the proposed method, dual prediction is used in the intracluster transmission to reduce the temporal redundancy, and hybrid compressed sensing is employed in the intercluster transmission to reduce the spatial redundancy. Moreover, an error threshold selection scheme is presented for the prediction model by optimizing the relationship between the energy consumption and the recovery accuracy, which makes the proposed method well suitable for different application environments. In addition, the transmission energy consumption is derived to verify the efficiency of the proposed method. Simulation results show that the proposed method has higher energy efficiency compared with the existing schemes, and the sink can recover measurements with reasonable accuracy by using the proposed method.

1. Introduction

Wireless sensor networks (WSNs), typically consisting of a vast number of densely deployed and collaborative battery-powered sensors, have been widely used in various application fields, such as the environment, industry, and the military [1]. However, the energy constraints are one of the main performance-limiting challenges for the WSNs. In the WSNs, most energy is consumed in three stages: sensing, data processing, and data delivery, and the energy consumed by the data delivery dominates the energy budget. Therefore, the data gathering approach with high energy efficiency is the key to prolong network lifetime.

There are two main types of data gathering methods for WSNs: the mobile sink based data gathering methods [2] and the stationary sink based data gathering methods [3]. In the mobile sink scenario, the long delay is an inevitable problem [4], so both the movement speed and the traveling path for the sink are the difficulties in designing. However, the stationary sink can avoid the above problems. In the stationary sink scenario, since the observed data should be transmitted to the sink by multihop forwarding transmission, the high transmission energy consumption by the sensors is

a problem that must be considered, which depends on the routing model and the data reduction technique. Therefore, the high energy efficient data collection with efficient routing is the key in the stationary sink scenario.

Because of the overlap among the observation regions of the different sensors and the gradual variation of the data observed at a sensor over time, the measurements from a WSN are either spatially or temporally correlated [5], which leads to the existing of much redundant information among the observed data. Therefore, data gathering approaches that exploited the inherent correlation have been widely studied to improve the energy efficiency of the WSNs [6]. In [7–11], data reduction methods that utilized temporal correlation or spatial correlation are presented to reduce the transmission energy consumption. Moreover, many data compression algorithms are employed in these data gathering methods to obtain data reduction, where the network coding (NC) and compressed sensing (CS) techniques are applied in the data gathering methods in [7, 8], which utilize the spatial correlation to reduce the data transmissions. In [9–11], the principal component analysis (PCA) methods or different prediction models are applied to reduce the temporal redundancy. However, the redundant information is still excessive

after using the above methods [7–11], which will cause low energy efficiency.

To further improve the energy efficiency, data gathering schemes exploring both temporal and spatial correlations [12–15] are presented. In [12], a collective prediction scheme exploiting spatial-temporal correlation (CoPeST) is given for the energy efficient WSNs. In the CoPeST method, the temporal redundancy and spatial redundancy of data are, respectively, reduced by the prediction approach and similarity based subcluster method. However, the energy cost by the frequent updating of cluster and subcluster topology is large in this case. A framework with dedicated combination of data prediction and compression is discussed for clustered WSNs in [13] (which is called as DPPCA method for convenience). In the framework, the Least Mean Square (LMS) dual prediction algorithm is used to reduce the temporal redundancy, and a centralized PCA technique is utilized to eliminate the spatial redundancy of the sensed data. However, these schemes in [12, 13] are not practical in different monitoring environments due to the employed fixed error threshold in the prediction algorithms. By the spatial and temporal compressions, the multiresolution compression and query (MRCQ) framework is given in [14], which organizes sensor nodes hierarchically and establishes multiresolution summaries of sensing data inside the network. In [15], a neighbor-aided Kronecker compressed sensing scheme is provided for the WSNs. However, the delay of the methods in [13–15] cannot be ignored, because the operation of reducing the temporal redundancy can only be executed after collecting enough data from continuous time intervals. Therefore, these schemes in [13–15] are not suited for the WSNs with the requirement of high real-time transmission.

To solve the above problems and further improve the energy efficiency, we propose an energy efficient data gathering scheme exploiting spatial-temporal correlation for the WSNs. With distinctions to the above approaches, dual prediction and hybrid compressed sensing techniques are jointed to eliminate the redundancy to improve the energy efficiency in the proposed method. Specifically, dual prediction is utilized during the intracluster transmission, and a new error threshold selection method is designed for the prediction stage, which is obtained by optimizing the relationship between the energy consumption and the recovery accuracy. Moreover, hybrid compressed sensing is employed during intercluster transmission, and the cluster heads (CHs) aggregate all the obtained values only when the number of values is no less than the required number of projections for CS reconstruction. Therefore, the proposed method has high energy efficiency and the reasonable quality.

The rest of this paper is organized as follows. The background and system model are discussed in Section 2. In Section 3, we introduce our proposed protocol in detail. Section 4 discusses the simulation results and conclusions are given in Section 5.

2. Background and System Model

2.1. Hybrid Compressed Sensing. Compressed sensing [16], as an advanced sampling theory, provides a new data

compression solution, and it indicates that only a small fraction of data projections is needed to reconstruct all of the raw data, which contains many zero entries. Assume a data vector \mathbf{x} has a K -sparse representation under a $N \times N$ transform basis, i.e., Ψ :

$$\mathbf{x} = \Psi\boldsymbol{\theta} \quad (1)$$

where $\mathbf{x} = [x_1, x_2, \dots, x_N]^T$, $\boldsymbol{\theta} = [\theta_1, \theta_2, \dots, \theta_N]^T$, and it has K ($K \ll N$) nonzero entries. Under this premise, the projection transformation is applied \mathbf{x} ; that is,

$$\mathbf{z} = \Phi\mathbf{x} = [\phi_1, \phi_2, \dots, \phi_N] \mathbf{x} \quad (2)$$

where Φ is a $M \times N$ ($M \ll N$) measurement matrix, and it satisfies the restricted isometry principle (RIP) [17]. ϕ_i is the corresponding coefficient vector of x_i , and $\phi_i = [\phi_{1i}, \phi_{2i}, \dots, \phi_{Mi}]^T$. Then the M -dimension vector \mathbf{z} can be used to recover the raw data \mathbf{x} by solving a l_1 -norm minimization.

According to the theory, only a few measurements are enough to reconstruct all original data for sink by CS in WSNs. Figure 1(a) shows the process of data gathering with pure CS, where each node i codes its data x_i with its corresponding coefficient vector ϕ_i in measurement matrix Φ and then sends out M -dimension vector $\sum_{k=1}^a x_k \phi_k$ which is aggregated by its encoded vector $x_k \phi_k$ and the $(a-1)$ achieved data vectors. In this case, every node needs to send out M data. However, the number of original data that needs to be transmitted may be smaller than M in the front nodes of links, and it is not the best choice to directly applying the CS coding on every node.

To avoid this problem, a modified hybrid compressed sensing method is discussed in [18]. In the hybrid CS method, each node i is initially set to transmit its raw data directly at first. Then, once an intermediate node j receives more than $(M-1)$ raw readings or any encoded readings, the intermediate node switches to the CS aggregation mode. In this case, the unnecessary transmissions are avoided in the data gathering by the hybrid CS. Figure 1(b) shows the process of data gathering with hybrid CS, where each node sends out original readings directly if the number of readings is smaller than M . Otherwise, the node codes the data with corresponding coefficient vectors and sends out M -dimension coded vector later. Obviously, the hybrid CS has a higher energy efficiency.

2.2. System Model. As seen in Figure 2, a cluster-based wireless sensor network with N sensor nodes is considered in this paper. The whole network is divided into p clusters. Both cluster members (CMs) and cluster heads (CHs) continuously generate a set of data that need to be collected by the sink. Let $\mathbf{x}(t) = [x_1(t), x_2(t), \dots, x_N(t)]^T$ denote the observed data from the network at the time instant t and the data vector can also be written as

$$\mathbf{x}(t) = [\mathbf{x}_1^T(t), \mathbf{x}_2^T(t), \dots, \mathbf{x}_p^T(t)]^T \quad (3)$$

where $\mathbf{x}_k(t)$ is the raw data vector of the k -th cluster. The member nodes in a cluster selectively send their data to the

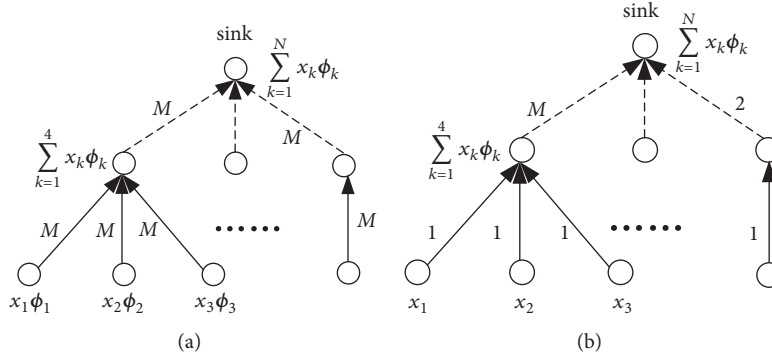


FIGURE 1: Example of $M=3$ for difference between pure CS and hybrid CS. (a) Data gathering with pure CS. (b) Data gathering with hybrid CS.

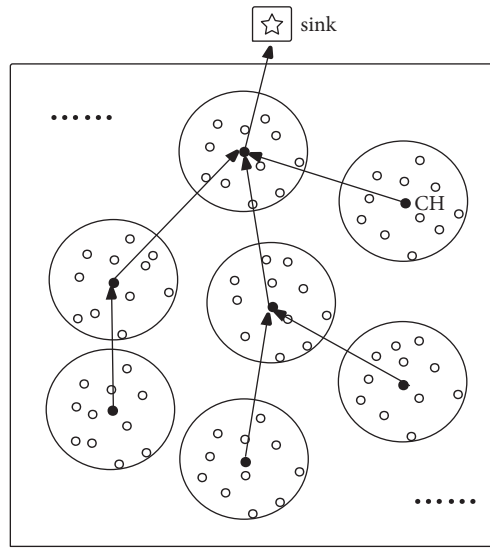


FIGURE 2: A cluster-based wireless sensor network.

CH with prediction model, and the data vector obtained in all CHs is

$$\begin{aligned} \mathbf{y}(t) &= [y_1(t), y_2(t), \dots, y_N(t)]^T \\ &= [\mathbf{y}_1^T(t), \mathbf{y}_2^T(t), \dots, \mathbf{y}_p^T(t)]^T \end{aligned} \quad (4)$$

where $\mathbf{y}_k(t)$ is the obtained data vector by the k -th CH. Then the CHs forward all the data to the sink with hybrid compressed sensing via multihop communication. Assume that each CH knows the CS projection vectors of all nodes within the cluster. The M -dimension measurement vector obtained in the sink is $\mathbf{z}(t) = \Phi \mathbf{y}(t)$ where Φ is a constant $M \times N$ measurement matrix which meets the RIP condition. The sink reconstructs the data vector from $\mathbf{z}(t)$ with the CS recovery algorithm, such as basis pursuit (BP) and orthogonal matching pursuit (OMP).

3. Proposed Method

3.1. Overall Description of the Proposed Method. In the proposed method, dual prediction [17] and hybrid compressed

sensing are jointed to reduce the energy consumption of data gathering in the clustered WSNs. Moreover, an error threshold selection principle is designed to make the proposed method well suitable for a myriad of environments.

Figure 3 shows the diagram of the proposed method for the cluster-based WSN. In the scheme, dual prediction technique is firstly applied in the intracluster transmission to eliminate the temporal redundancy of measurements. With the prediction method, the cluster members selectively transmit their measurements to the CHs, and the CHs use the forecasted values instead of the actual ones which are not received. Next, the hybrid CS is used in intercluster transmission to reduce the spatial redundancy. With the hybrid CS, the CHs aggregate the obtained data or not and then send the coded/uncoded vectors to the sink via multihop communication. Finally, the sink reconstructs the original data with a CS recovery algorithm. The details of the proposed scheme are given in the following.

Stage 1 (intracluster transmission). At every sampling time t , each node i obtains an observed value $x_i(t)$ from the surrounding environment, and then it forecasts $\hat{x}_i(t)$ using

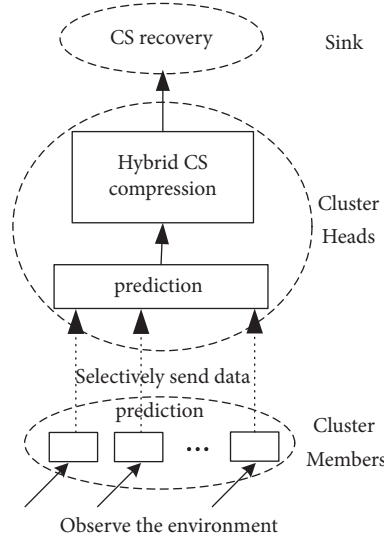


FIGURE 3: The diagram of the proposed method for the cluster-based WSN.

the preconstructed prediction model. There are two cases that should be considered for the node i as follows:

Case 1. If the error between the forecasted and observed values is over the threshold ε_i , which is prespecified based on the error threshold selection principle (it will be discussed in the Section 3.2), i.e.,

$$|\widehat{x}_i(t) - x_i(t)| > \varepsilon_i \quad (5)$$

the node i transfers the actual value $x_i(t)$ to its CH.

Case 2. If the forecasted value is acceptable, i.e.,

$$|\widehat{x}_i(t) - x_i(t)| \leq \varepsilon_i \quad (6)$$

the cluster head calculates $\widehat{x}_i(t)$ with the same prediction model to approximate the actual data. In this case, unnecessary transmissions are avoided.

Stage 2 (intercluster transmission). Let $\mathbf{y}_j(t) = [y_j^1(t), y_j^2(t), \dots, y_j^{N_j}(t)]^T$ denote the data vector of the cluster head j obtained from the cluster, where N_j is the number of nodes in the cluster j , and $y_j^k(t)$ is an actual value obtained directly or a prediction value calculated by the CH for the k -th node in cluster j . Assume $\mathbf{J} = \{j_1, j_2, \dots, j_h\}$ is the set of cluster heads which transfer their data to the cluster head j . There are two cases that need to be considered for the cluster head j as follows:

Case 1. If $\sum_{k=1}^h N_{j_k} + N_j < M$, the cluster head j sends out the data vector $\mathbf{y}_j^*(t)$ without aggregation, where

$$\mathbf{y}_j^*(t) = [\mathbf{y}_{j_1}^T(t), \mathbf{y}_{j_2}^T(t), \dots, \mathbf{y}_{j_h}^T(t), \mathbf{y}_j^T(t)]^T \quad (7)$$

and the number of elements in $\mathbf{y}_j^*(t)$ is

$$q_j = \sum_{k=1}^h N_{j_k} + N_j \quad (8)$$

Case 2. If $\sum_{k=1}^h N_{j_k} + N_j \geq M$,

$$\mathbf{y}_j^*(t) = \sum_{k=1}^h \Phi^{j_k} \mathbf{y}_{j_k}(t) + \Phi^j \mathbf{y}_j(t) \quad (9)$$

and

$$q_j = M \quad (10)$$

Stage 3. The sink obtains the data vector

$$\begin{aligned} \mathbf{z}(t) &= \Phi \mathbf{y}(t) \\ &= \sum_{k=1}^p \Phi^k \mathbf{y}_k(t) \end{aligned} \quad (11)$$

and reconstructs the original data with the CS recovery algorithm, such as basis pursuit (BP) and orthogonal matching pursuit (OMP).

3.2. Error Threshold Selection Principle. As illustrated in Section 3.1, a node i will send its observed value to the CH if $|\widehat{x}_i(t) - x_i(t)| > \varepsilon_i$ where ε_i is a user given error threshold. It means that the value ε_i determines the number of transmissions in every time instant, and it influences the accuracy of data recovery in the sink. Therefore, it is important to select an appropriate error threshold ε_i for the data gathering scheme with prediction.

According to the Central Limit Theorem, we assume unbiased predictions and errors normally distributed. In this paper, we select a simple autoregressive (AR) model to

predict in the proposed method, which is only an example for understanding easily. Moreover, the proposed error selection principle is universal for different prediction methods when prediction error distribution models of these methods can be estimated.

A l -order AR predictor can be denoted as

$$\widehat{x}_i(t) = \sum_{k=1}^l \xi_k x_i(t-k) \quad (12)$$

where $\xi_1, \xi_2, \dots, \xi_l$ are the parameters of the prediction model, which can be constructed by the Yule-Walker equations or the least square method. Assume the observed value can be written as

$$x_i(t) = \sum_{k=1}^l \xi_k x_i(t-k) + e_i(t) \quad (13)$$

where $e_i(t)$ is the prediction error with zero mean and variance σ_i^2 , i.e., $e_i(t) \sim N(0, \sigma_i^2)$. To a fixed error threshold ε_i , the probability of a node to send its observed data out is

$$\alpha = 2 - 2\Phi\left(\frac{\varepsilon_i}{\sigma_i}\right) \quad (14)$$

where $\Phi(\cdot)$ is the CDF of Gaussian white noise. Clearly, to make sure that the scheme with dual prediction is more energy efficient, the additional computation power must be much less than the reduced energy of transmission; that is,

$$(2 - \alpha)E_p < (1 - \alpha)E_s \quad (15)$$

where E_p and E_s are the energy costs of a single prediction and sending a value to the CH, respectively. In general, E_s is larger than E_p , and suppose $E_s = kE_p$. Thus, the error threshold needs to satisfy

$$\Phi\left(\frac{\varepsilon_i}{\sigma_i}\right) > \frac{k}{2k-2} \quad (16)$$

In practice, the value σ_i is unknown. Authors in [10] use $\sigma_{x_i} \sqrt{1 - \sum_{j=1}^p \phi_j \rho_{x_i}(j)}$ instead of the unknown value σ_i , where σ_{x_i} and $\rho_{x_i}(j)$ are the standard deviation and correlation coefficient of a stationary time series \mathbf{x}_i , respectively.

Combining (14) and (16), it is obvious that a bigger ε_i leads to lower energy consumption but decreases the recovery accuracy. Therefore, the choice of ε_i must be weighed between the energy consumption and the recovery accuracy.

The energy consumption for one node sending T data to its CH in the proposed method is

$$\begin{aligned} E_T &= (2 - \alpha)TE_p + \alpha TE_s \\ &= 2\Phi\left(\frac{\varepsilon_i}{\sigma_i}\right)TE_p + \left[2 - 2\Phi\left(\frac{\varepsilon_i}{\sigma_i}\right)\right]TE_s \end{aligned} \quad (17)$$

The mean square error (MSE) of the process is

$$\text{MSE} = \frac{1}{T} \sum_{j=1}^T \eta(j) \times e_i^2(j) \quad (18)$$

where $e_i(j) \leq \varepsilon_i$ and

$$\eta(j) = \begin{cases} 0, & \text{send out } x_i(j) \\ 1, & \text{not send out } x_i(j) \end{cases} \quad (19)$$

Thus, one can obtain the following:

$$\text{MSE} \leq (1 - \alpha) \varepsilon_i^2 \quad (20)$$

Formulate the optimization as

$$\begin{aligned} \min \quad & 2\Phi\left(\frac{\varepsilon_i}{\sigma_i}\right)E_p + \left[2 - 2\Phi\left(\frac{\varepsilon_i}{\sigma_i}\right)\right]E_s \\ \text{s.t.} \quad & \Phi\left(\frac{\varepsilon_i}{\sigma_i}\right) > \frac{k}{2k-2} \\ & \left[2\Phi\left(\frac{\varepsilon_i}{\sigma_i}\right) - 1\right] \varepsilon_i^2 \leq \lambda \varepsilon_i^2 \end{aligned} \quad (21)$$

where λ is a user given parameter which indicates the acceptable maximum recovery accuracy. In practice, the value of λ is between 0 and 1, and it reflects the ratio of expected prediction error to the maximum error. A larger λ means less energy cost (i.e., high energy efficiency) and lower recovery accuracy. The users can determine an appropriate λ depending on the tradeoff between energy efficiency and recovery accuracy for different applications; that is because different applications have different requirements for energy efficiency and recovery accuracy. For example, some applications require high energy efficiency and low recovery accuracy, while others require low energy efficiency and high recovery accuracy. Therefore, the value of λ needs to be determined according to the specific application requirements, and we only give the performance of proposed method under a given value in the simulation.

To solve the above optimization problem in Equation (21), $\Phi(\varepsilon_i/\sigma_i)$ is treated as a variable. In this case, the above optimization is translated into a simple linear programming problem, which can be solved by the existing algorithms [19]. Once $\Phi(\varepsilon_i/\sigma_i)$ is calculated, ε_i can be obtained according to the corresponding σ_i and Gaussian distribution table.

Specifically, to ensure the energy efficiency of the system, a small transmit probability is required. In the meanwhile, the accuracy of intracluster transmission should be guarantee to a certain extent. In this case, a prediction model with higher estimated accuracy (but higher computation complexity in general) should be considered.

3.3. Procedures of the Proposed Method. Algorithm 1 illustrates the proposed threshold selection-based data collection algorithm. As discussed in Section 3.1, the procedure of the proposed method is as the following 4 paragraphs:

Firstly, each cluster member calculates its error threshold according to the error threshold selection principle which is discussed in Section 3.2.

Then, intracluster transmission begins. The cluster member predicts the current value and compares the predicted value with the actual observed one. If the error between them

```

1: Each cluster member obtains its error threshold  $\varepsilon_i$  using (21)
   Stage 1: Intra-cluster Transmission
2: for each cluster member  $i$ 
3:   forecasts  $\widehat{x}_i(t)$  for the current sampling time  $t$  using the preconstructed prediction
   model;
4:   calculates the error between  $\widehat{x}_i(t)$  and the observed value  $x_i(t)$ ;
5:   if  $|\widehat{x}_i(t) - x_i(t)| > \varepsilon_i$ 
6:     the node  $i$  transfers the actual value to its cluster heads
7:   else
8:     the corresponding cluster head calculates  $\widehat{x}_i(t)$  with the same prediction model;
9:   end
10: end
   Stage 2. Inter-cluster Transmission
11: After stage 1, each cluster head  $j$  obtains the values of its members
       $\mathbf{y}_j^*(t) = [\mathbf{y}_{j_1}^T(t), \mathbf{y}_{j_2}^T(t), \dots, \mathbf{y}_{j_h}^T(t), \mathbf{y}_j^T(t)]^T$ .
12: for each cluster head  $j$  in the multi-hop link
13:   calculates the number of values which have been obtained by the node  $j$  from all front
      cluster heads  $\mathbf{J} = \{j_1, j_2, \dots, j_h\}$  in the link and its own members;
14:   if  $\sum_{k=1}^h N_{j_k} + N_j \geq M$ 
15:      $\mathbf{y}_j^*(t) = \sum_{k=1}^h \Phi^{j_k} \mathbf{y}_{j_k}(t) + \Phi^j \mathbf{y}_j(t)$ 
16:   else
17:      $\mathbf{y}_j^*(t) = [\mathbf{y}_{j_1}^T(t), \mathbf{y}_{j_2}^T(t), \dots, \mathbf{y}_{j_h}^T(t), \mathbf{y}_j^T(t)]^T$ 
18:   end
19:   sends out  $\mathbf{y}_j^*(t)$ ;
20: end
   Stage 3. Reconstruction
21: The sink obtains the data vector
       $\mathbf{z}(t) = \Phi \mathbf{y}(t) = \sum_{k=1}^p \Phi^k \mathbf{y}_k(t)$ 
      and reconstructs the original data with the CS recovery algorithm.

```

ALGORITHM 1: Threshold selection-based data collection algorithm.

is larger than the error threshold, the cluster member sends the observed reading to its corresponding cluster head. Else, the cluster head predicts the current value with the same prediction model.

Next, once the cluster heads collect all data of their members, the intercluster transmission begins. If the number of data that needs to be transmitted for one cluster head is less than M , the cluster head sent these data out directly. Else, the cluster head aggregates these data to M dimension with compressed sensing which is discussed in Section 2.1 and sends the coded data out after.

Finally, the sink reconstructs the original data according to the obtained data vector and some CS recovery algorithms.

Ignore the computation complexity of the reconstruction process. Assume the complexity of the applied prediction model is O_{pred} , and the computation complexity of stage 1 is $(N - p)[(2 - \alpha)O_{pred} + 2]$. The computation complexity of stage 2 is about $O(MN)$ which depends on the complexity of the matrix multiplication $\Phi \mathbf{y}(t)$. Thus, the total computation complexity of Algorithm 1 is about $(N - p)[(2 - \alpha)O_{pred} + 2] + O(MN)$.

3.4. Transmission Energy Cost Analysis. In this paper, the reduction of the communication cost means the energy saving while guaranteeing the user-defined data accuracy. As

shown in Figure 3, the scheme concludes two communication stages: intracuster transmission with prediction and inter-cluster transmission with compressed sensing.

Assume that there are N nodes in network (p of them are cluster heads), and each node has T data for gathering. In intracuster transmission, each node costs E_p energy to forecast the current value, and then the node sends its observed data to its cluster with probability α ; otherwise, the cluster head needs to predict the data with probability $(1 - \alpha)$. The expected energy cost of each cluster member for this process is $\alpha E_s + (1 - \alpha)E_p$. Therefore, the energy cost of intracuster transmission is

$$E_1 = T \left[(2 - \alpha)(N - p)E_p + \alpha(N - p)E_s \right] \quad (22)$$

In intercluster transmission, the energy cost of each cluster head k for each time is $q_k E_t$, where q_k is the number of data that CH k needs to send out (which is defined in Section 3.1), and E_t is the energy cost for a cluster head sending out data. Therefore, the transmission energy cost of intercluster transmission is

$$E_2 = T \sum_{k=1}^p (q_k E_t) \quad (23)$$

where p is the number of clusters in network.

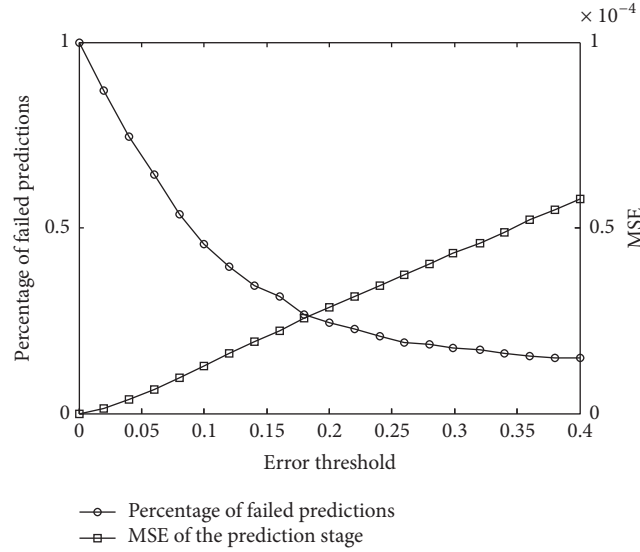


FIGURE 4: Percentage of transmission nodes and MSE performance under the different error thresholds.

Combining (22) and (23), the total transmission energy cost is

$$E_{total} = T \left[(2 - \alpha)(N - p)E_p + \alpha(N - p)E_s + \sum_{k=1}^p (q_k E_t) \right] \quad (24)$$

4. Results and Discussion

To evaluate the performance of the proposed method, the cluster-based WSNs with fixed area are considered. For simplicity, the LEACH [20] is used for the clustering approach in the simulation, and the probability for each node to become a cluster head is set to 0.1. In the simulation, the number of nodes N of the synthetic network takes value from 500 to 1500, and each node in the network has $T=1000$ values that need to be gathered. The parameter λ of the proposed method ranges from 0.01 to 0.95. A simple AR predictor is used in the simulation, and ten history data values can be cached by each node for constructing the parameters of the prediction model. The energy cost model of MICAZ [21] is used for energy estimation of our work. In MICAZ model, the transmission cost of one bit is 600 nJ and the computation energy per clock cycle is 3.5 nJ. Assume that data is with 16 bits. In comparison with the proposed method, the available schemes, i.e., DPPCA [13] and CHCS [18], are also simulated, specifically, the fixed threshold of the DPPCA method which with prediction program is set to 0.1 according to the reference. All simulations are run in the MATLAB software.

Figure 4 shows the percentage of failed predictions and MSE curves versus the different error threshold at one node for the first stage of the proposed method. In Figure 4, MSE is the mean square error of the prediction stage of the proposed method. Clearly, if the prediction fails in a time

instant, the node will need to send the raw data to its CH. As the error threshold increases, the percentage of failed predictions decreases and the MSE performance is degraded. When the error threshold is larger than 0.2, the percentage of failed predictions tends to decrease slightly, while the MSE performance is still degraded rapidly, because the prediction error obeys an approximate Gaussian distribution in general.

Figure 5 gives the error threshold curve versus the different for the proposed method λ . In Figure 5, λ is a user given parameter, and a larger λ means a larger MSE performance for the first stage of the proposed method. In the simulation, $k=30$ is considered for determining the error threshold. From Figure 5, the error threshold increases rapidly when λ is larger than 0.8. According to the MSE performance in Figure 4, the MSE performance will be too poor in this case. Therefore, a reasonable λ should be chosen in practical application.

Figure 6 gives the number of transmissions curves versus the number of clusters in network for the proposed method. From Figure 6, one can see that the total number of transmissions increases as the number of clusters increases in network, because more clusters in network mean more intercluster transmissions, and while prediction model is applied in intracluster transmission, the number of intercluster transmissions is larger. In addition, as the number of clusters increases, the total numbers of transmissions with different λ tend to be the same. It is because the number of intracluster transmissions will be reduced (note that its limit value will tend to zero) as the number of clusters increases, and the value of λ only affects the intracluster transmission, so the gaps between the numbers of intracluster transmissions with different λ become smaller as the number of clusters increases.

Figure 7 shows the total number of transmissions curves versus the number of nodes in the network for different methods. In Figure 7, “normal method” is one without any compression operation during the transmission. From Figure 7, one can see that the transmission energy consumption of the proposed method is smaller than those of the available

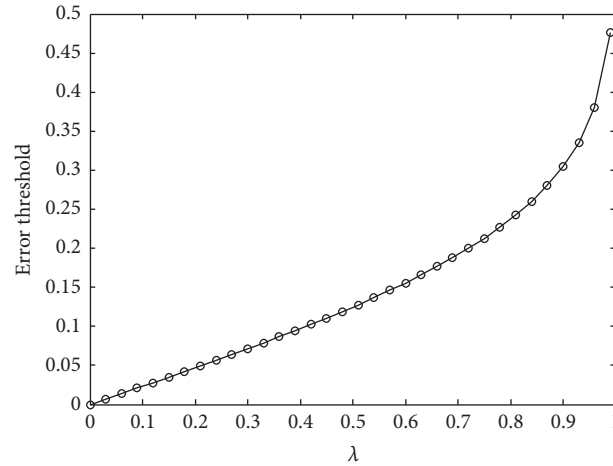


FIGURE 5: Error threshold against different λ for the proposed method ($N=1000$).

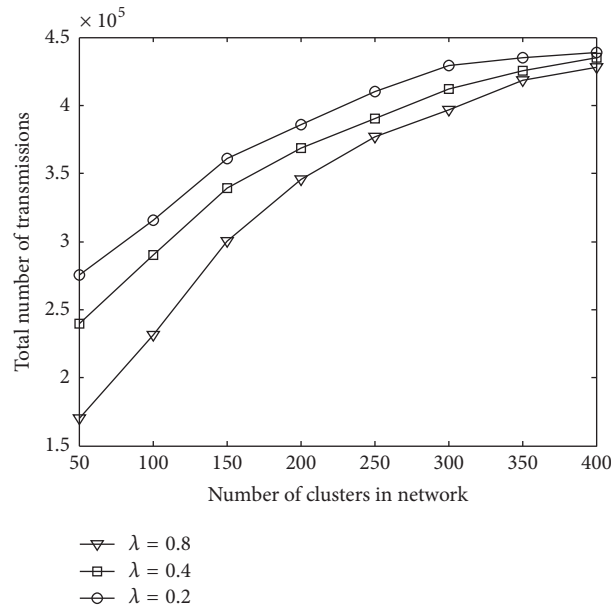


FIGURE 6: Total number of transmissions against the number of clusters in network for the proposed method ($N=1000$).

methods. Compared with the normal method, the proposed method reduces the transmission energy consumption by 50%. Moreover, the proposed method can reduce the transmission energy cost about 40% and 20% when compared with the CHCS and DPPCA methods, respectively; that is because the proposed method uses dual prediction with adaptive error threshold and hybrid compressed sensing. In addition, as the number of nodes increases, the proposed method will have better energy efficiency, which also shows that the proposed method is suitable for the large-scale networks.

Figure 8 gives the MSE performance against the number of nodes for different methods. In Figure 8, the CHCS in [18] and the DPPCA in [13] are compared with the proposed method. From Figure 8, one can see that the MSE performance improves as the number of nodes increases. It is because the distribution area for all nodes of the network is assumed to be fixed, and the node density increases

with the increase of total number of nodes. In this case, the overlap degree of observed area for nodes is higher, which means that the spatial correlation of observed data increases. Therefore, the MSE performance improves when the compressed sensing with fixed compression ratio is applied in intertransmission stage. Moreover, one can see that the MSE performance of the CHCS method is the best due to its only having the intercluster compression, but it costs the most energy in transmission stage which can be seen from Figure 7. The MSE performance of the DPPCA method is a little better while $\lambda = 0.8$, but the advantage gradually diminished as the network size increases, and the DPPCA method always costs much more energy than the proposed method which can be seen from Figure 7. When λ is smaller than 0.4, the MSE performance of the proposed is better, and meanwhile the proposed method still has a higher energy efficiency. Therefore, taking into consideration the

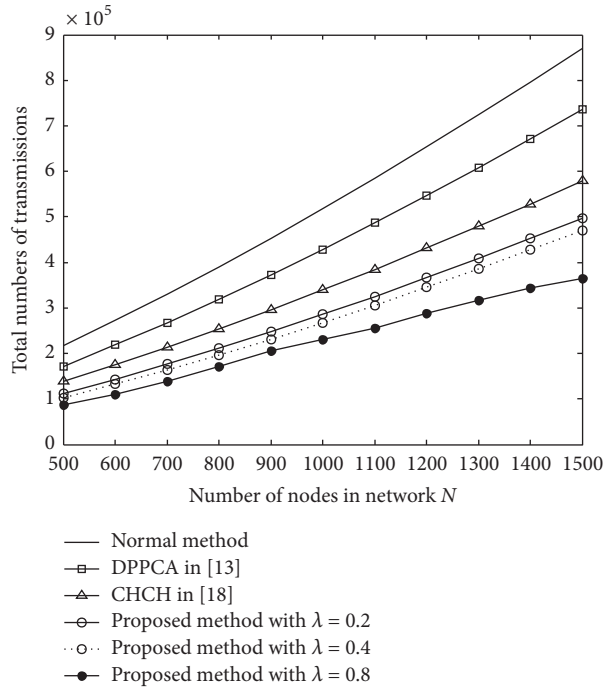


FIGURE 7: Total number of transmissions against the number of nodes in network for different methods.

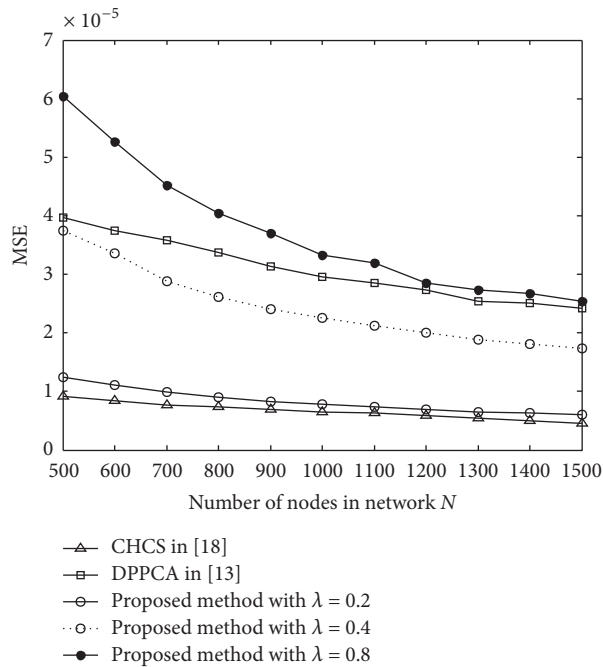


FIGURE 8: MSE performance of different methods against the number of nodes in network.

energy cost and the MSE performance, the proposed method with adaptive threshold has a distinct advantage in practical applications.

5. Conclusions

In this paper, a novel energy-efficient data gathering scheme exploiting both spatial and temporal correlations is proposed

for clustered WSNs. The method uses dual prediction to reduce the temporal redundancy during the intracluster transmission, and the hybrid CS technique is utilized to reduce the spatial redundancy during the intercluster transmission. In this way, the transmission energy cost is decreased greatly. To enhance the availability of the proposed method for different environments, an error threshold selection principle based on the tradeoff between the MSE and the

energy cost is designed. Compared with the CHCS and DPPCA methods, the proposed scheme can greatly reduce the transmission energy cost. In addition, the proposed method offers adequate data recovery accuracy, and it can perform well in large-scale and dense WSNs.

Data Availability

The data used to support the findings of this study are available from the corresponding author upon request.

Conflicts of Interest

The authors declare that there are no conflicts of interest regarding the publication of this paper.

Acknowledgments

This work was supported in part by the National Key Research and Development Program of China under Grant 2018YFC1314903, in part by the National Natural Science Foundation of China under Grant 61372124 and Grant 61427801, the Natural Science Foundation of the Jiangsu Higher Education Institutions of China (No. 18KJ13510034), and the 11th Batch of China Postdoctoral Science Fund Special Funding (No. 2018T110530).

References

- [1] I. F. Akyildiz, W. Su, Y. Sankarasubramaniam, and E. Cayirci, "A survey on sensor networks," *IEEE Communications Magazine*, vol. 40, no. 8, pp. 102–105, 2002.
- [2] Y. Gu, F. Ren, Y. Ji, and J. Li, "The evolution of sink mobility management in wireless sensor networks: A survey," *IEEE Communications Surveys & Tutorials*, vol. 18, no. 1, pp. 507–524, 2016.
- [3] M. Dong, K. Ota, and A. Liu, "RMER: reliable and energy-efficient data collection for large-scale wireless sensor networks," *IEEE Internet of Things Journal*, vol. 3, no. 4, pp. 511–519, 2016.
- [4] C.-F. Cheng and C.-F. Yu, "Data gathering in wireless sensor networks: a combine-TSP-reduce approach," *IEEE Transactions on Vehicular Technology*, vol. 65, no. 4, pp. 2309–2324, 2016.
- [5] M. Duarte, S. Sarvotham, D. Baron, M. Wakin, and R. Baraniuk, "Distributed compressed sensing of jointly sparse signals," in *Proceedings of the Conference Record of the Thirty-Ninth Asilomar Conference on Signals, Systems and Computers, 2005.*, pp. 1537–1541, Pacific Grove, California.
- [6] G. Anastasi, M. Conti, M. Di Francesco, and A. Passarella, "Energy conservation in wireless sensor networks: a survey," *Ad Hoc Networks*, vol. 7, no. 3, pp. 537–568, 2009.
- [7] N. Nguyen, D. L. Jones, and S. Krishnamurthy, "Netcompress: Coupling network coding and compressed sensing for efficient data communication in wireless sensor networks," in *Proceedings of the 2010 IEEE Workshop on Signal Processing Systems, SiPS 2010*, pp. 356–361, USA, October 2010.
- [8] Y. Zhou, L. H. Yang, and L. X. Yang, "Improved compressed network coding scheme for energy-efficient data communication in wireless sensor networks," *Ksii Transactions on Internet Information Systems*, vol. 9, no. 7, pp. 2488–2511, 2017.
- [9] N. A. Alduais, J. Abdullah, A. Jamil, and H. Heidari, "Performance evaluation of real-time multivariate data reduction models for adaptive-threshold in wireless sensor networks," *IEEE Sensors Letters*, vol. 1, no. 6, pp. 1–4, 2017.
- [10] H. Jiang, S. Jin, and C. Wang, "Prediction or not? an energy-efficient framework for clustering-based data collection in wireless sensor networks," *IEEE Transactions on Parallel Distributed Systems*, vol. 22, no. 6, pp. 1064–1071, 2010.
- [11] U. Raza, A. Camerra, A. L. Murphy, T. Palpanas, and G. P. Picco, "Practical data prediction for real-world wireless sensor networks," *IEEE Transactions on Knowledge and Data Engineering*, vol. 27, no. 8, pp. 2231–2244, 2015.
- [12] M. Arunraja and V. Malathi, "Collective prediction exploiting spatio temporal correlation (CoPeST) for energy efficient wireless sensor networks," *Ksii Transactions on Internet and Information Systems*, vol. 9, no. 7, pp. 2488–2511, 2015.
- [13] M. Wu, L. Tan, and N. Xiong, "Data prediction, compression, and recovery in clustered wireless sensor networks for environmental monitoring applications," *Information Sciences*, vol. 329, pp. 800–818, 2016.
- [14] Y.-C. Wang, Y.-Y. Hsieh, and Y.-C. Tseng, "Multiresolution spatial and temporal coding in a wireless sensor network for long-term monitoring applications," *Institute of Electrical and Electronics Engineers. Transactions on Computers*, vol. 58, no. 6, pp. 827–838, 2009.
- [15] L. Quan, S. Xiao, X. Xue, and C. Lu, "Neighbor-aided spatial-temporal compressive data gathering in wireless sensor networks," *IEEE Communications Letters*, vol. 20, no. 3, pp. 578–581, 2016.
- [16] D. L. Donoho, "Compressed sensing," *IEEE Transactions on Information Theory*, vol. 52, no. 4, pp. 1289–1306, 2006.
- [17] G. M. Dias, B. Bellalta, and S. Oechsner, "A survey about prediction-based data reduction in wireless sensor networks," *ACM Computing Surveys*, vol. 49, no. 3, 2016.
- [18] R. Xie and X. Jia, "Transmission-efficient clustering method for wireless sensor networks using compressive sensing," *IEEE Transactions on Parallel and Distributed Systems*, vol. 25, no. 3, pp. 806–815, 2014.
- [19] V. Chvatal, *Linear Programming*, vol. 5, no. 1, W. H. Freeman and Company, New York, NY, USA, 1983.
- [20] W. R. Heinzelman, A. Chandrakasan, and H. Balakrishnan, "Energy-efficient communication protocol for wireless micro-sensor networks," in *Proceedings of the 33rd Annual Hawaii International Conference on System Sciences (HICSS '00)*, vol. 2, p. 8020, IEEE, January 2000.
- [21] B. Gedik, L. Liu, and P. S. Yu, "ASAP: an adaptive sampling approach to data collection in sensor networks," *IEEE Transactions on Parallel and Distributed Systems*, vol. 18, no. 12, pp. 1766–1783, 2007.

Research Article

Priority-Based Pipelined-Forwarding MAC Protocol for EH-WSNs

Kyuwook Shim and Hyung-Kun Park 

School of Electrical, Electronics & Communication Engineering, KOREATECH, Cheonan 31253, Republic of Korea

Correspondence should be addressed to Hyung-Kun Park; hkpark@koreatech.ac.kr

Received 23 March 2019; Accepted 7 May 2019; Published 14 May 2019

Guest Editor: Bojan Dimitrijevic

Copyright © 2019 Kyuwook Shim and Hyung-Kun Park. This is an open access article distributed under the Creative Commons Attribution License, which permits unrestricted use, distribution, and reproduction in any medium, provided the original work is properly cited.

To reduce the end-to-end delay in EH-WSNs (energy-harvesting wireless sensor networks), medium access control protocols using pipelined-forwarding have been introduced and studied. In real-life applications, there are several situations where it is difficult to harvest more energy than the energy consumed. Therefore, it is crucial to design a MAC protocol that allows nodes to efficiently relay data without exhausting the power in pipelined-forwarding multihop transmission. In this paper, we propose a PP-MAC (priority-based pipelined-forwarding MAC) protocol that determines the priority of relay nodes based on the residual power and energy-harvesting rate. The proposed protocol determines the probability of a node becoming a relay node based on the priority of the node and attempts to access the channel in a distributed manner. Furthermore, the PP-MAC protocol controls the sleep interval based on the power conditions of the nodes. It also minimizes the power exhaustion problem by controlling the sleep interval based on the priority of the nodes. The performance of the proposed PP-MAC was evaluated via computer simulation, and the results indicated that PP-MAC could improve the network lifetime by mitigating the power imbalance of nodes.

1. Introduction

In recent times, the development of various wireless applications has led to a remarkable increase in the importance of wireless sensor networks. It is well known that, in the wireless sensor network, the fact that the sensor node is battery powered (because of size limitations and cost) and has limited energy and lifetime is a challenge. Several kinds of research have been carried out to handle the energy shortage problem. One such attempt was the introduction of EH-WSNs (energy-harvesting wireless sensor networks), which use energy-harvesting sensor nodes that can collect energy from external energy sources such as light, heat, and wind [1, 2]. In EH-WSNs, sensor nodes have a relatively long lifetime, and the networks are comparably more stable.

In the design of EH-WSNs, the MAC protocol plays a vital role in determining network performances such as throughput, delay, and energy consumption [3, 4]. When designing the MAC protocol to increase the power efficiency in EH-WSNs, the residual power of the node is considered as the most critical factor. Duty cycling has been proposed

to balance the node power [5]. However, even with the same residual power, the variation in the value of the residual power depends on the energy-harvesting rate. For example, if the charging rate is faster than the data transmission period, data transmission will be possible instantaneously regardless of the residual power. However, if the charging rate is slower than the data generation rate, then the data transmission has to be adjusted by considering the remaining power of the battery as well as the charging rate.

Most existing MAC protocols are designed without considering the routing protocols. Notwithstanding, MAC protocols that do not support routing can increase the network overhead and decrease the network lifetime. Therefore, considerable research attention has been devoted to the improvement of network performance through the cross-layer designed MAC protocol by considering the routing protocol [6]. To reduce the end-to-end delay caused by multihop routing, pipelined-forwarding MAC protocols such as R-MAC (Routing-enhanced duty-cycle MAC) [7] and PRI-MAC (Pipelined-forwarding, Routing-integrated, and effectively Identifying MAC) [8] were proposed. Furthermore,

to achieve efficient utilization of node energy, RP-MAC (Reduced Pipelined-forwarding MAC) [9] was introduced.

In the design of routing and MAC protocols in an energy-harvesting wireless sensor network, the remaining power and energy-harvesting rate are considered as vital design factors. For the EH-WSN, an important design criterion is maintenance of the ENO (Energy Neutral Operation) state [3]; that is, the harvested energy must always be greater than or equal to the energy consumed. In the ENO state, a node can operate without a battery problem. However, in real-life applications, there are several situations where it is incredibly challenging to harvest enough energy for data transmission. If the harvested energy is not sufficient, the transmission delay will be significant. Therefore, the relay node should be selected based on the residual power and energy-harvesting rate. Nodes with low energy-harvesting rates should adaptively increase the sleep interval so that sufficient charging time can be obtained. Even if each node does not satisfy the ENO state, the node group can satisfy the ENO state as a whole by adaptively selecting the relay node.

In this paper, we propose a priority-based pipelined-forwarding MAC (PP-MAC) protocol. The PP-MAC protocol relays data through pipelined forwarding for multihop transmission. To select a relay node in an ad hoc network that has no central station, each node in the same grade accesses the channel with different access probabilities based on its priority (which is determined by the residual power and energy-harvesting rate). Besides, each node adaptively determines the sleep period. If a node has a low residual power and harvesting rate, then it will have a longer sleep interval. However, if a node has a high residual power and harvesting rate, it can perform more frequently as a relay node: this ensures that the relay nodes do not run out of power, thus enabling stable and low-latency data transmission.

The rest of this paper is organized as follows. Section 2 introduces pipelined forwarding and describes the framework of the proposed PP-MAC protocol. Simulation results are provided and discussed in Section 3, and the conclusions are presented in Section 4.

2. Pipelined-Forwarding MAC

In a sensor network, data are transmitted to the destination node by multihop transmission. In this paper, as shown in Figure 1, all the nodes of the network are grouped based on their distance from the destination node; moreover, the data packet is transmitted to the destination node from a higher grade to a lower grade in a multihop manner. To accomplish this, the network initially performs a procedure for grade division [8, 10]. Nodes at the same grade compete with each other for media access, whereas nodes at different grades relay data to transmit a packet to the destination node. Therefore, the path from the source to the destination node is established based on which of the nodes at the same grade are selected as relay nodes. It is evident that the routing path is established through the MAC protocol.

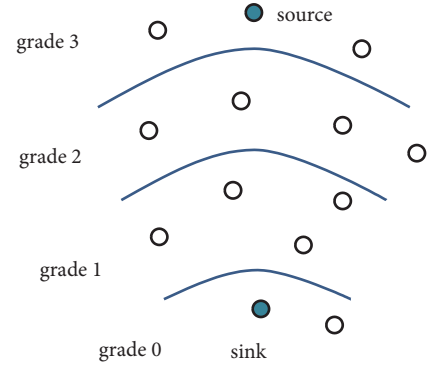


FIGURE 1: Example of network topology after the procedure of grade division.

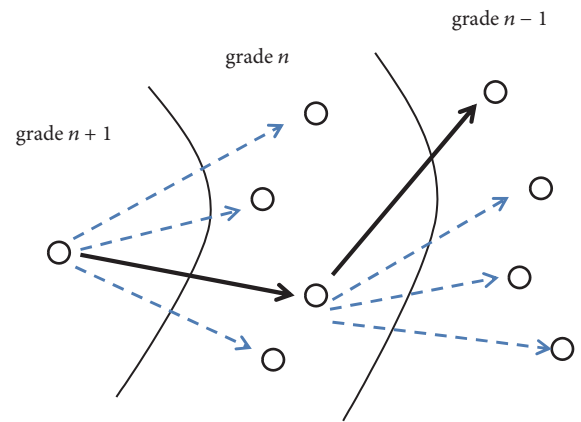


FIGURE 2: Relay node selection and data relating to a node in a lower grade.

As shown in Figure 2, when transmitting data with the simplest flooding method, the nodes in grade n receive data from a higher grade node and serve as a relay node to relay the data to a lower grade node. Each node follows a pipelined-forwarding scheme with a staggered sleep-wake-up schedule. Therefore, it is not necessary that all the nodes will serve as relay nodes. Besides, data relay by specific nodes may be performed based on the energy state of the node. Therefore, in the MAC stage, access to the medium is appropriately limited and the sleep period is controlled based on the energy state of the node while minimizing the transmission delay.

3. PP-MAC Design

3.1. PP-MAC Overview. In PP-MAC, a node receives data from a higher grade node. As demonstrated in Figure 3, after receiving the data, the node transmits an ACK packet to the $n+1$ grade node. The ACK packet is also transmitted to the $n-1$ grade nodes, and the $n-1$ nodes receiving the ACK packet indicate that they are ready to receive data by transmitting a beacon. At this time, there are several nodes in the $n-1$ grade, and they must compete to receive data. Each node in the $n-1$ grade computes its priority P_i , where the priority depends on its residual power and energy-harvesting rate and tries to

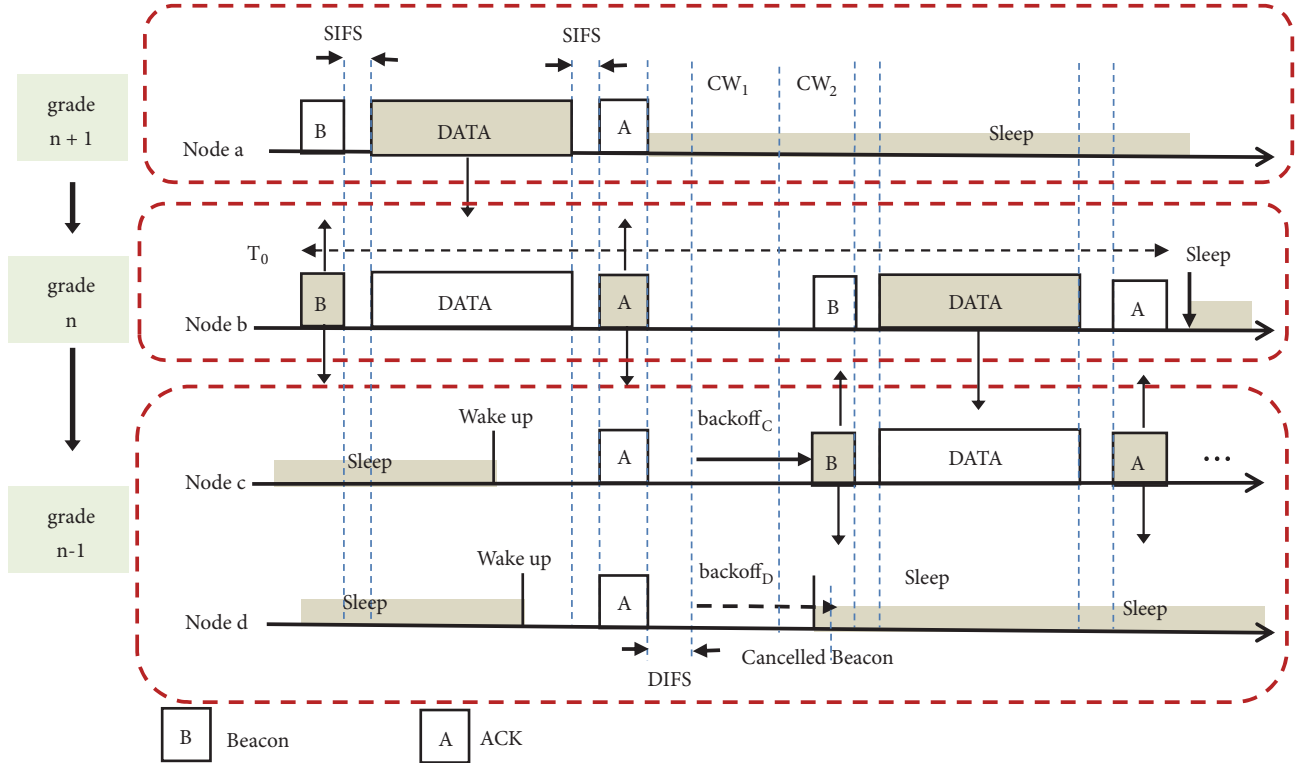


FIGURE 3: Illustration of the PP-MAC procedure.

transmit the beacon by setting a backoff value based on the P_i value. The higher the priority, the smaller the backoff value, which increases the probability of a node operating as a relay node. The calculation of the priority value and the method of setting the backoff value will be described in detail in the next section.

One of the nodes at the $n-1$ grade transmits the beacon and receives the data. After receiving the data, when a node transmits the ACK packet, it transmits alongside the ACK the next time information to be awakened. Based on this time information, lower grade nodes are scheduled to serve as relay nodes before the ACK is delivered in the next period. The relay node, which has received the data, transmits the data to the lower grade nodes in the same manner as before. The relay node transmits the data and receives the ACK, and then enters the sleep mode. Thus, a pipeline-forwarding structure to sequentially transmit data with the sequential sleep-wake-up schedule is provided.

3.2. Priority by Residual Power and Energy-Harvesting Rate.

The nodes determine the priority P by taking both the residual power and the energy-harvesting rate into account. Even if there is a large amount of residual power, if the energy-harvesting rate is small, the residual power can be used more conservatively. In this case, if priority is given to a node having a substantial residual power but a low energy-harvesting rate, the power of the battery is quickly consumed, and the node can be stopped. In contrast, even if the residual power is very small, if the energy collection rate is high,

a sufficient amount of energy will be charged in each data transmission period so that the node can be selected as a relay node in preference to other nodes. T_0 determine the priority considering both the residual power and the energy-harvesting rate; the expected residual power after the unit sleep interval T_0 is set as the priority of the node, as shown in (1):

$$P_i = E_{r,i} + R_{h,i}T_0 \quad (1)$$

where P_i is the priority, $E_{r,i}$ is the residual power, and $R_{h,i}$ is the energy-harvesting rate for the i -th node. The priority P_i represents the expected residual power of the node after the sleep interval at the next transmission time. Nodes having residual power below the minimum power do not have enough energy for data transmission even if the nodes gain access to the channel through contention, so that the sleep state is maintained until the power is charged above the minimum power.

3.3. *Backoff by Priority.* Even though a priority value is given to each node, in an ad hoc network, the priority of neighboring nodes cannot be known because there is no central base station. Therefore, a distributed MAC protocol is needed that can reduce collisions and allow access to channels based on priority. In this paper, we designed a MAC protocol to reflect the priority of a node and minimize the collision of packets by differentiating the channel access probability and the backoff value based on the priority of the node. Besides,

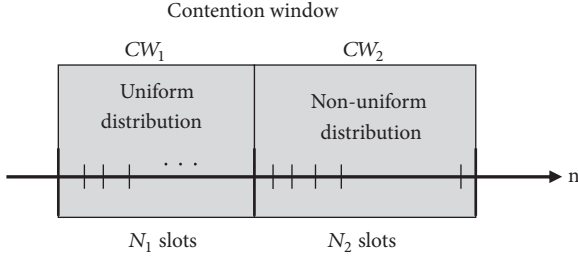


FIGURE 4: Two types of contention windows based on priority.

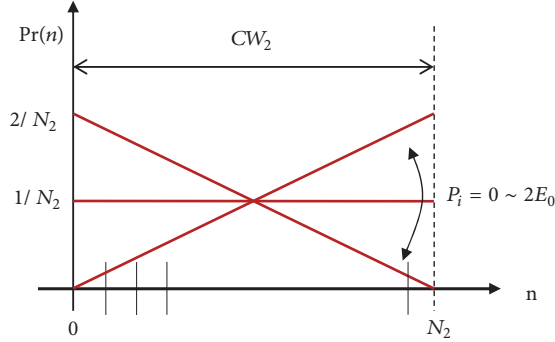


FIGURE 5: Asymmetry access probability in contention window 2.

it is necessary to adaptively adjust the node's sleep interval based on the energy collection rate and the residual power.

In this paper, we divide the contention window into two periods: CW_1 and CW_2 . CW_1 is the interval in which nodes satisfy the condition $\eta \leq P_i$, where η denoting the threshold is set to $2E_0$ throughout this paper, and E_0 denotes the energy required to receive and transmit a packet in the interval T_0 . This implies that the node in CW_1 has sufficient energy for packet transmission in the next period after transmitting the packet in the current slot. If $\eta > P_i$, it means that the node does not have sufficient energy and harvesting rate and hence competes in CW_2 .

Nodes whose energy consumption in the current slot does not affect the next packet transmission compete to access the channel in the CW_1 period. This is so that the nodes of CW_1 are given priority to access the channel. However, nodes that do not satisfy (2) below do not have enough power after T_0 and compete to access the channel in CW_2 . The nodes in CW_2 have lower priority than those in CW_1 . If there are nodes in CW_1 , the nodes of CW_2 check the existence of nodes having enough energy in the CW_1 interval and go to the sleep state.

As shown in Figure 4, the access probabilities of CW_1 and CW_2 are distinguished. In CW_1 , all nodes have enough energy to transmit packets in the next cycle, so they attempt to access the channel with uniform probability. However, in CW_2 , it is difficult to secure sufficient energy for packet transmission in the next cycle. Therefore, the channel is accessed with a different probability distribution based on the priority value P_i . For the backoff setting in CW_2 , we defined the probability $\Pr(n)$ of having the n th backoff among the total CW_2 length, N_2 , as shown in (2) below. Figure 5

TABLE 1: Networking parameters for simulation.

Parameter	Value
Data packet	128 byte
Bandwidth	250 kbps
Energy of the fully charged battery	10 J
Tx power	31.2 mW
Rx power	22.2 mW
Power in idle listening	13.5 mW
SIFS	192 μ s
DIFS	640 μ s
Beacon	12 byte
ACK	14 byte
Slot time	320 μ s

shows the probability distribution of backoff based on the priority value P_i in CW_2 . The PP-MAC algorithm is shown in Algorithm 1.

$$\Pr(n) = m_i \left(n - \frac{N_2}{2} \right) + \frac{1}{N_2}, \quad m_i = 2 \left(\frac{P_i}{E_0} - 1 \right) \quad (2)$$

3.4. Sleep Duration. If there is no beacon signal or no competition in CW_1 , then it means that there is no node in CW_1 . Consequently, all the nodes join the competition for channel connection in CW_2 , and the nodes that fail to access the channel will enter the sleep mode immediately. At this time, it is necessary to wake up before time T_0 for the next data reception and transmission. If there are nodes in CW_1 , it means that there exists a relay node having enough power in the next cycle. Therefore, nodes in CW_2 have to enter the sleep mode for the time duration $2T_0$. In contrast, nodes in CW_1 must wake up before the time interval T_0 . In this manner, the contention window is divided into two, and the nodes can recognize the existence of nodes having higher priority so that the length of the sleep period for a node in CW_2 can be adjusted without exchanging additional information.

4. Simulation and Performance Evaluation

In this paper, the performance of the proposed PP-MAC is analyzed via simulation analysis. For the simulation, the nodes are arranged uniformly at three grades, and the energy-harvesting rate of the nodes is set to be uniformly distributed between 0.28 and 7.3 mW. In this study, we set the initial value of the backoff exponent of each of the competing windows CW_1 and CW_2 to 3, increasing it by 1 each time a collision occurred, and to a maximum of 7 so that each of the contending windows is in the range of 0–127. To achieve fast simulation, we assumed a battery capacity of 5 mJ. Table 1 shows the parameters for the simulation [6, 11].

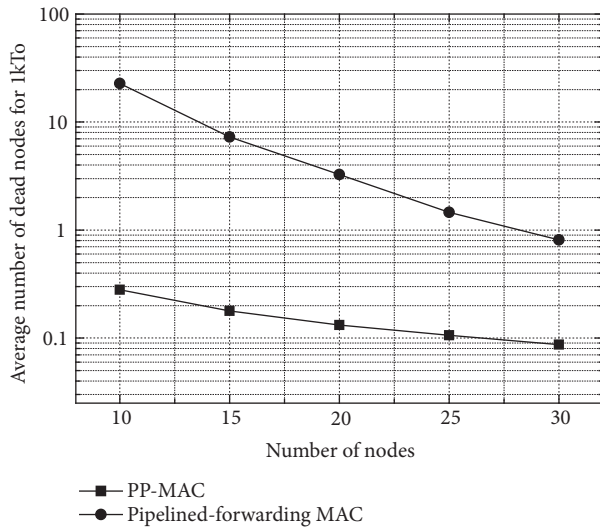
Figures 6 and 7 show the average number of dead nodes and the standard deviation of the residual energy based on the number of nodes for $1000T_0$ sec in the case of average $R_h = 50$ –100 mW. As the number of nodes increases, the imbalance of the residual power among nodes is relaxed, and the lifetime

```

Node Wakeup and CCA(Clear Channel Assessment);
if (node receive ACK packet)
     $P_i = E_{r,i} + R_{h,i}T_0$ 
if ( $P_i > \eta$ )
     $\Pr(n) = 1/N_1$  generate random backoff  $n$  having  $\Pr(n)$ 
else  $m_i = 2(P_i/E_0 - 1)$ 
     $\Pr(n) = m_i(n - N_2/2) + 1/N_2$  generate random backoff  $n$  having  $\Pr(n)$ 
    Delay for backoff period  $n$  slots;
    Perform CCA;
if (channel is idle)
    send beacon packet;
    receive data packet;
elseif (packet in  $CW_1$ )
    sleep for  $2T_0$ 
else sleep for  $T_0$ 

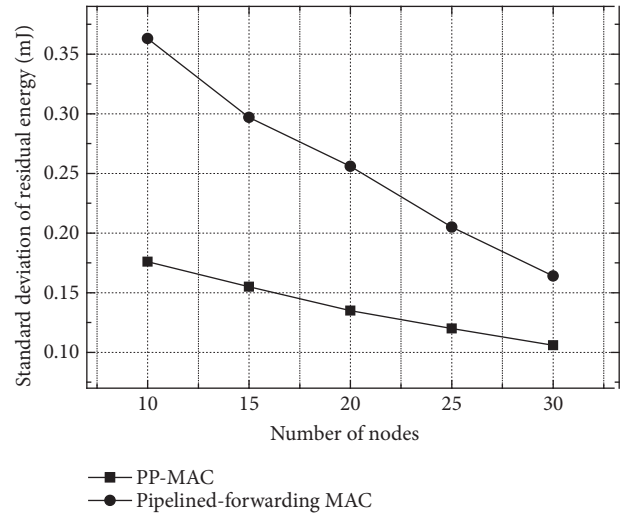
```

ALGORITHM 1: Channel access procedure in PP-MAC.

FIGURE 6: Average number of dead nodes based on the number of nodes for $1000T_0$ in the case of average $R_h = 50-100$.

of the node is increased. Besides, as the number of nodes increases, the number of nodes that can operate as relay nodes also increases, leading to an increase in the overall lifetime. In particular, in the case of PP-MAC, the standard deviation of the residual power between nodes is significantly reduced and the lifetime of the node is longer than that of the conventional pipelined-forwarding MAC. Therefore, the overall network lifetime is prolonged.

Figures 8 and 9 show the average number of dead nodes and the standard deviation of the residual energy based on the energy-harvesting rate for $1000T_0$, where the number of nodes is 15. As the average energy collection rate increases, the lifetime of the node increases. Overall, in comparison to the pipelined-forwarding MAC, the lifetime and power balance in PP-MAC are better. It is observed that, as the average energy collection rate increases, the difference in the lifetime of the conventional pipelined-forwarding MAC node

FIGURE 7: Standard deviation of residual energy based on the number of nodes for $1000 T_0$ in the case of $R_h = 50-100$ mW.

and the lifetime of the PP-MAC node is reduced. However, if the energy situation improves more than a particular grade, then the network performance improves beyond the required grade; hence, the network performance becomes more significant when the energy-harvesting rate is low. Based on the simulation results, PP-MAC demonstrates better performance than the conventional pipelined-forwarding MAC with a worse energy situation.

5. Conclusions

In this paper, we proposed a priority-based pipelined-forwarding MAC (PP-MAC) protocol to select relay nodes for multihop transmission in EH-WSNs. In the distributed ad hoc network environment where the power status of other nodes is unknown, each node independently calculates its priority in a probabilistic manner, which can reduce the excessive probing overhead required to gather power-related

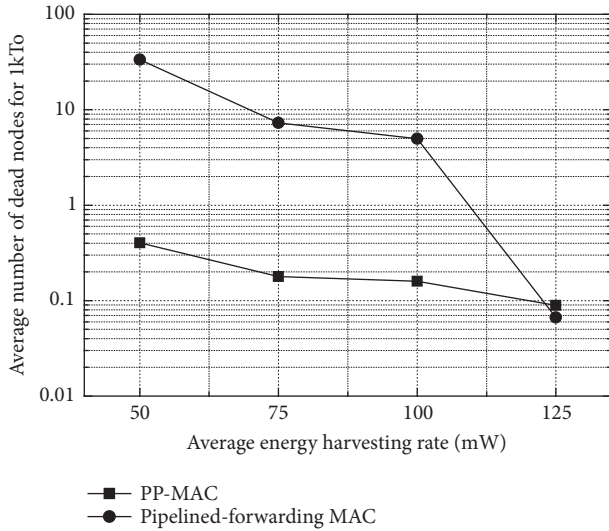


FIGURE 8: Average number of dead nodes based on the energy-harvesting rate for $1000 T_0$, where the number of nodes is 15.

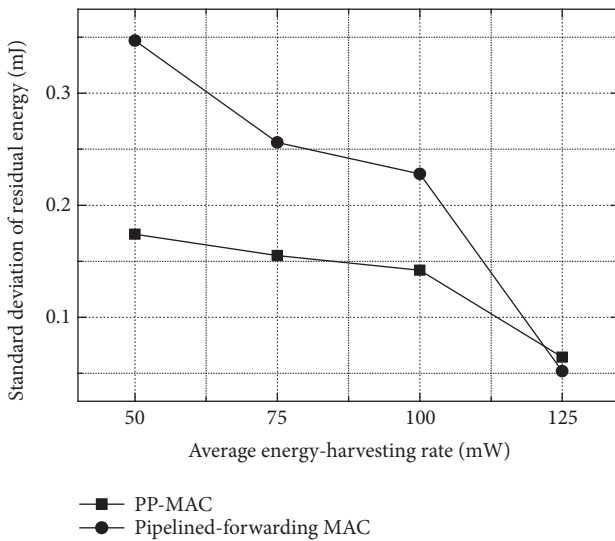


FIGURE 9: Standard deviation of residual energy based on the energy-harvesting rate for $1000 T_0$, where the number of nodes is 15.

information of all the nodes. Furthermore, the proposed MAC protocol classifies the competition window into two sections to give priority to channel access based on the residual power and energy-harvesting rate. A high-priority node has more residual power and energy-harvesting capability than a low-priority node. For a high-priority node, the probability of channel access increases, so that the power imbalance among relay nodes is mitigated and the overall performance of network lifetime is improved. Simulation results show that the proposed PP-MAC achieves higher power balance among nodes and increases the lifetime of nodes compared with the conventional pipelined-forwarding MAC protocol, particularly under poor energy conditions.

Data Availability

The data used to support the findings of this study are available from the corresponding author upon request.

Conflicts of Interest

The authors declare that there are no conflicts of interest regarding the publication of this article.

Acknowledgments

This research was supported by Basic Science Research Program through the National Research Foundation of Korea (NRF) funded by the Ministry of Education, Science and Technology (NRF-2017R1D1A3B03034202).

References

- [1] M. Ku, W. Li, Y. Chen, and K. J. Ray Liu, "Advances in energy harvesting communications: past, present, and future challenges," *IEEE Communications Surveys & Tutorials*, vol. 18, no. 2, pp. 1384–1412, 2016.
- [2] J. M. Yi, M. J. Kang, and D. K. Noh, "Solar energy harvesting wireless sensor network simulator," *Journal of the Korea Institute of Information and Communication Engineering*, vol. 19, no. 2, pp. 477–485, 2015.
- [3] P. Ramezani and M. R. Pakravan, "Overview of MAC protocols for energy harvesting wireless sensor networks," in *Proceedings of the 26th IEEE Annual International Symposium on Personal, Indoor, and Mobile Radio Communications (PIMRC '15)*, pp. 2032–2037, August 2015.
- [4] S. Kosunalp, "MAC protocols for energy harvesting wireless sensor networks: survey," *ETRI Journal*, vol. 37, no. 4, pp. 804–812, 2015.
- [5] J. S. Karthi, S. V. Rao, and S. S. Pillai, "Duty cycle adapted MAC for wireless sensor networks with energy harvesting," in *Proceedings of the International Conference on Control, Communication & Computing*, pp. 685–689, November 2015.
- [6] M. Hefeida, T. Canli, and A. Khokhar, "Supporting multi-hop and multi-packet transmission in asynchronous WSNs," in *Proceedings of the IFIP Wireless Days (WD '11)*, pp. 1–6, October 2011.
- [7] S. Du, A. K. Saha, and D. B. Johnson, "RMAC: a routing-enhanced duty-cycle MAC protocol for wireless sensor networks," in *Proceedings of the 26th IEEE International Conference on Computer Communications (INFOCOM '07)*, pp. 1478–1486, IEEE, May 2007.
- [8] F. Tong, M. Ni, L. Shu, and J. Pan, "A pipelined-forwarding, routing-integrated and effectively-identifying MAC for large-scale WSN," in *Proceedings of the IEEE Global Communications Conference (GLOBECOM '13)*, pp. 225–230, December 2013.
- [9] N. M. Nguyen and M. K. Kim, "Reduced-pipelined duty cycle MAC protocol (RP-MAC) for wireless sensor network," *KSII Transactions on Internet and Information Systems*, vol. 11, no. 5, pp. 2433–2452, 2017.
- [10] H.-I. Liu, W.-J. He, and W. K. G. Seah, "LEB-MAC: load and energy balancing MAC protocol for energy harvesting powered wireless sensor networks," in *Proceedings of the 20th IEEE International Conference on Parallel and Distributed Systems (ICPADS '14)*, pp. 584–591, December 2014.

- [11] K. Shim and B. An, "A RF energy based protocol in mobile ad-hoc wireless sensor networks," *Journal of the Institute of Electronics and Information Engineers*, vol. 53, no. 4, pp. 567-557, 2016.

Research Article

Relaying Communications in Energy Scavenging Cognitive Networks: Secrecy Outage Probability Analysis

Khuong Ho-Van ¹ and Thiem Do-Dac ^{1,2}

¹Ho Chi Minh City University of Technology, VNU-HCM, 268 Ly Thuong Kiet Street, District 10, Ho Chi Minh City, Vietnam

²Thu Dau Mot University, 6 Tran Van On Street, Phu Hoa Ward, Thu Dau Mot City, Binh Duong Province, Vietnam

Correspondence should be addressed to Khuong Ho-Van; khuong.hovan@yahoo.ca

Received 1 March 2019; Revised 9 April 2019; Accepted 16 April 2019; Published 6 May 2019

Guest Editor: Zoran Stamenkovic

Copyright © 2019 Khuong Ho-Van and Thiem Do-Dac. This is an open access article distributed under the Creative Commons Attribution License, which permits unrestricted use, distribution, and reproduction in any medium, provided the original work is properly cited.

This paper exploits a self-powered secondary relay to not only maintain but also secure communications between a secondary source and a secondary destination in cognitive radio networks when source-destination channel is unavailable. The relay scavenges energy from radio frequency (RF) signals of the primary transmitter and the secondary source and consumes the scavenged energy for its relaying activity. Under the maximum transmit power constraint, Rayleigh fading, the primary outage constraint, and the interference from the primary transmitter, this paper suggests an accurate closed-form expression of the secrecy outage probability to promptly assess the security performance of relaying communications in energy scavenging cognitive networks. The validity of the proposed expression is verified by computer simulations. Numerous results demonstrate the security performance saturation in the range of large maximum transmit power or high required outage probability of primary users. Moreover, the security performance is a function of several system parameters among which the relay's position, the power splitting factor, and the time splitting factor can be optimized to achieve the minimum secrecy outage probability.

1. Introduction

Currently low spectrum utilization efficiency is a great motivation for the application of the cognitive radio technology which enables secondary/unlicensed users to access the allocated spectrum of primary/licensed users in order to better exploit the available spectrum [1]. Cognitive radios operate on three (overlay, underlay, and interweave) mechanisms amidst which the underlay one is more preferable owing to its low system design complexity [2]. According to the underlay mechanism, the transmit power of secondary users (SUs) must be adaptively limited to obey the maximum transmit power constraint imposed by hardware design and the primary outage constraint imposed by communication reliability of primary users (PUs) [3]. These power constraints set the upper-bound on the power of secondary transmitters, inflicting unreliable communication through the direct channel between a secondary source and a secondary destination. Another reason for unreliable communication through the direct channel is the blockage

of this channel owing to heavy path-loss, severe fading, and strong shadowing. A secondary relay between the source and the destination should be exploited to reduce the path-loss for hop-to-hop communication, mitigate severe fading and strong shadowing, and relax the requirement of high transmit power for long distance communication. Therefore, the relay can bridge the source with the destination in order to maintain reliable connection between them [4]. Nevertheless, as a helper, the relay may be unenthusiastic to utilize its private energy for assistance activity. Currently modern technologies make feasible for self-powered terminals that can scavenge energy with high energy conversion efficiency from green energy sources (e.g., radio frequency signals [5, 6]). Consequently, the relay can utilize its scavenged energy to lengthen the transmission range of the source, better remaining the continuous connection between the source and the destination. However, the scavenged energy may be insufficient, and, hence, the problem is whether the relay can guarantee reliable and secure communication between the source and the destination under the threat

of eavesdroppers in the information-theoretic aspect. This aspect confirms that wireless communication is secured when the capacity difference between the desired channel and the wiretap channel is positive [7]. This paper finds the solution to such a problem.

1.1. Literature Review. This subsection merely surveys published works related to security performance analysis for relaying communications in energy scavenging cognitive networks. Therefore, published works which did not reflect a complete set of specifications such as power constraints for SUs, security performance analysis, relaying communications, and energy scavenging should not be surveyed (e.g., [8–13] merely dealt with the security performance analysis for direct communications (i.e., without relaying) in energy scavenging cognitive networks). Through this survey, contributions of the current paper will be summarized in the next subsection.

The authors in [14] exploited the secondary relay between the secondary source and the secondary destination to not only expand the transmission range of the source but also secure its communication. The system model in [14] considered the decode-and-forward relay, the power splitting based energy scavenging mechanism which allows the relay to scavenge energy from the signals of both the secondary source and the primary transmitter, the maximum transmit power constraint, the interference power constraint, and the interference from the primary transmitter to the relay. Nevertheless, [14] neglected the interference from the primary transmitter to the secondary destination and the eavesdropper. The authors in [15] studied the same problem as [14] but with three different points: (i) the amplify-and-forward relay is used; (ii) the time splitting based energy scavenging mechanism allows the relay to scavenge energy from only the signal of the secondary source; (iii) the interference from the primary transmitter is ignored. To improve the security performance, [16] extended [15] with allowing both the source and the relay to jam the eavesdropper. The authors in [17] continued to expand the work in [16] with relay selection for more secure information transmission. As an alternative approach to enhance the security performance, [18] proposed a path selection scheme where the path with the highest end-to-end channel capacity is selected. The system model in [18] ignored interference from PUs and allowed the relays to scavenge the energy from the signals of dedicated beacons based on the time splitting mechanism. Nevertheless, [18] merely analyzed the connection outage probabilities (the connection outage probability is the probability that the received signal-to-noise ratio is below a threshold) at the destination and the eavesdropper.

In summary, [14–18] considered relaying communications in energy scavenging cognitive networks. However, they neglected the secrecy outage analysis (i.e., only simulation results are provided in [14–18]), the primary outage constraint, and the interference from the primary transmitter to all secondary receivers. This paper will complement their shortcomings to complete the framework of the secrecy outage analysis for relaying communications in energy scavenging cognitive networks.

1.2. Contributions. This paper extends the system model in [14–18] with noticeable differences as follows:

- (i) The decode-and-forward relay is activated merely when it can exactly restore the source information. This limits the error propagation (e.g., [14])
- (ii) The relay exploits the interference from the primary transmitter for energy scavenging. This is helpful in turning unwanted signals to useful energy source and differs from [15–18] where the interference from the primary transmitter is not exploited for energy scavenging
- (iii) Periods of two (energy scavenging and information processing) stages are unequal. This facilitates optimizing these periods for minimum secrecy outage probability (SOP). Also, this makes our work distinguished from [14–16] where these stages are of equal times
- (iv) This paper proposes the accurate closed-form SOP analysis, which differs from [14–18] in which only simulation results are presented

The contributions of the paper are highlighted as follows:

- (i) Exploit a secondary relay to guarantee secure communications between the secondary source and the secondary destination in case that their direct communication is in outage. The relay is capable of scavenging the energy from both signals of the secondary source and the primary transmitter. Also, it must be successful in restoring the source information before taking part in the relaying activity
- (ii) Suggest accurate closed-form expressions for crucial security performance metrics such as the SOP, the probability of strictly positive secrecy capacity (PSPSC), the intercept probability (IP) under both maximum transmit power constraint and primary outage constraint, and interference from the primary transmitters to promptly evaluate the security performance of relaying communications in energy scavenging cognitive networks without time-consuming computer simulations
- (iii) Employ the suggested expressions to optimize important system parameters
- (iv) Provide numerous results to obtain helpful insights into security performance such as the security performance saturation in the range of large maximum transmit power or high required outage probability of PUs and the minimum secrecy outage probability achievable with appropriate selection of the relay's position, the time splitting factor, and the power splitting factor

1.3. Structure of Paper. The paper continues as follows. System model, signal model, secrecy capacity, and secondary power allocation are described in the next section. Section 3 details the derivation of important performance metrics such as the SOP, the PSPSC, and the IP. Section 4 presents

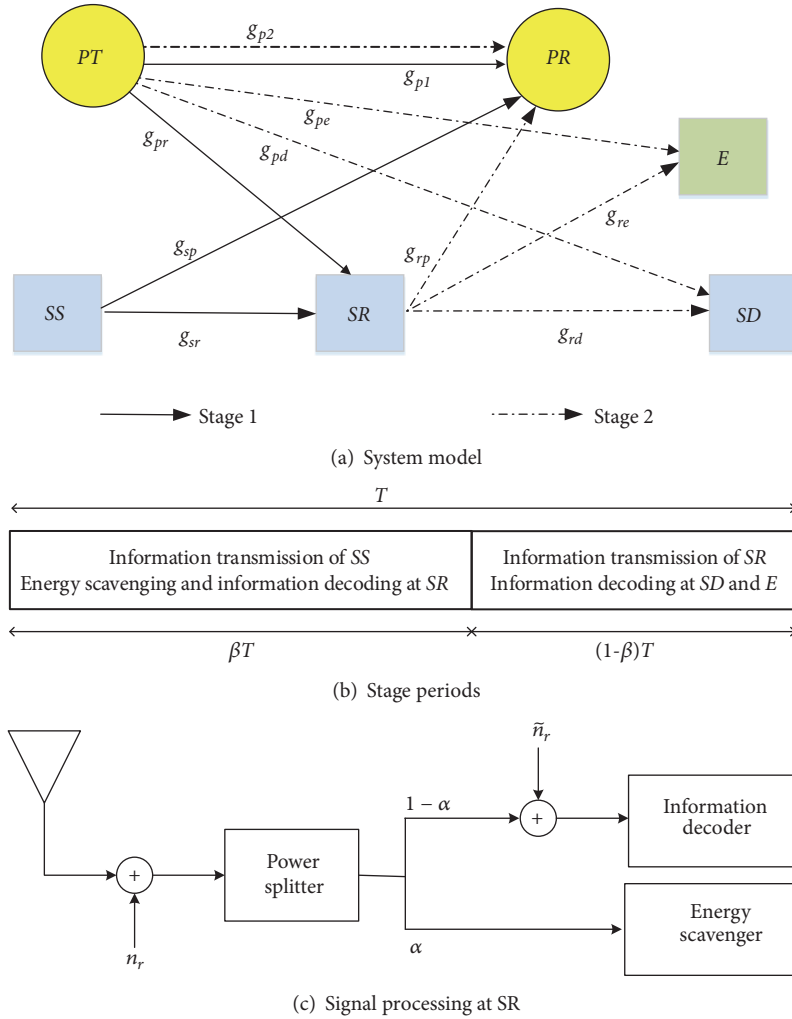


FIGURE 1: System model.

simulated/numerical results and Section 5 concludes the paper.

2. System Model, Signal Model, Secrecy Capacity, and Secondary Power Allocation

2.1. System Model. Figure 1(a) illustrates relaying communications in energy scavenging cognitive networks. Relaying communications experience two stages as shown in Figure 1(b).

In stage 1, both the secondary source SS and the primary transmitter PT simultaneously broadcast their own information to the secondary destination SD and the primary receiver PR , respectively, causing mutual interference signals between the secondary network and the primary network. The interference signals from the secondary network to the primary network are considered in most published works while those from the primary network to the secondary network are usually neglected (e.g., [19–21] and references therein). Therefore, by considering these mutual interference signals, our work is apparently more general than the existing

ones but the secrecy outage probability analysis is more sophisticated. The eavesdropper E intends to wire-tap the secondary source's information. Owing to heavy path-loss, severe fading, and large shadowing, the secondary source's signals cannot reach SD and E . As such, it is supposed that the secondary relay SR is in the radio coverage of SS and eager to assist SS by forwarding SS 's information to SD according to the decode-and-forward principle. SR is a self-powered terminal for its relaying operation which is capable of scavenging the energy from the received signals according to the power splitting method (e.g., [22, 23]) as observed in Figure 1(c). More specifically, SR scavenges the energy from the RF signals of both SS and PT . This means that SR takes advantage of the interference signal (from PT) for useful purpose of energy scavenging. The power splitting method divides the received signal at SR into two parts: one part for recovering the source information (it is supposed that the information decoder consumes the negligible amount of the energy, which is commonly assumed in most existing publications (e.g., [8–14] and references therein)) and the other for scavenging the energy.

In stage 2, *SR* is idle if it fails to restore the source information. Otherwise, it forwards the restored source information to *SD* in parallel to the information transmission of *PT*. At the end of stage 2, *SD* tries to recover while *E* eavesdrops the source information from *SR*'s transmit signal.

2.2. Signal Model. In Figure 1(a), $g_{ab} \in \{g_{p1}, g_{p2}, g_{pe}, g_{pd}, g_{pr}, g_{sp}, g_{sr}, g_{rp}, g_{re}, g_{rd}\}$ denotes the channel coefficient between a corresponding pair of the transmitter and the receiver. Although Figure 1(a) only shows one primary transmitter-receiver pair, the realistic scenario may have two pairs communicating in two stages. To reflect such a scenario, two different channel coefficients, g_{p1} and g_{p2} , are used to represent two different channels for two primary transmitter-receiver pairs in two stages. All frequency nonselective independent Rayleigh fading channels are supposed, producing the zero-mean κ_{ab} -variance circular symmetric complex Gaussian distribution for g_{ab} , i.e., $g_{ab} \sim \mathcal{CN}(0, \kappa_{ab})$. When the path-loss is accounted, κ_{ab} can be represented as $\kappa_{ab} = l_{ab}^{-\nu}$, with l_{ab} denoting the transmitter a-receiver b distance, and ν denoting the path-loss exponent. As such, it is implicit in the sequel that the probability density function (pdf) and the cumulative distribution function (cdf) of the channel gain $|g_{ab}|^2$ are, respectively, given by

$$f_{|g_{ab}|^2}(x) = \frac{e^{-x/\kappa_{ab}}}{\kappa_{ab}}, \quad (1)$$

$$F_{|g_{ab}|^2}(x) = 1 - e^{-x/\kappa_{ab}}, \quad (2)$$

where $x \geq 0$.

In Figure 1(b), β with $\beta \in (0, 1)$ and T correspondingly denote the time splitting factor and the total transmission time from *SS* to *SD* through *SR*. In Figure 1(c), α with $\alpha \in (0, 1)$ denotes the power splitting factor. With the notations in Figure 1 in mind, the signals are modelled as follows.

By denoting u_s and u_{p1} as the unity-power transmit symbols of *SS* and *PT* in stage 1, correspondingly, the received signals at *SR* and *PR* can be, respectively, represented as

$$v_r = g_{sr} \sqrt{P_s} u_s + g_{pr} \sqrt{P_{p1}} u_{p1} + n_r, \quad (3)$$

$$v_{p1} = g_{sp} \sqrt{P_s} u_s + g_{p1} \sqrt{P_{p1}} u_{p1} + n_{p1}, \quad (4)$$

where $n_r \sim \mathcal{CN}(0, \sigma_r^2)$ and $n_{p1} \sim \mathcal{CN}(0, \sigma_{p1}^2)$ are the additive white Gaussian noises (AWGN) produced by the receive antennas at *SR* and *PR*, respectively; P_s and P_{p1} are the transmit powers of *SS* and *PT* in stage 1, respectively.

Based on the operation principle in Figure 1(c), the relay *SR* partitions the received signal v_r into two parts: the first part of $\sqrt{\alpha} v_r$ input to the energy scavenger and the second part of $\sqrt{1-\alpha} v_r$ input to the information decoder. Given the energy conversion efficiency of the energy scavenger as μ with $\mu \in (0, 1)$, the average amount of the energy which *SR* can scavenge in stage 1 is given by

$$\begin{aligned} W_{rm} &= \mu E \left\{ |\sqrt{\alpha} v_r|^2 \right\} \beta T \\ &= \mu \alpha (P_s \kappa_{sr} + P_{p1} \kappa_{pr} + \sigma_r^2) \beta T, \end{aligned} \quad (5)$$

where $E\{\cdot\}$ denotes the statistical average.

The maximum transmit power which *SR* can use for information transmission in stage 2 is given by

$$P_{rm} = \frac{W_{rm}}{(1-\beta)T} = \frac{\beta \mu \alpha}{1-\beta} (P_s \kappa_{sr} + P_{p1} \kappa_{pr} + \sigma_r^2). \quad (6)$$

The signal input to the information decoder in Figure 1(c) can be expressed as

$$\tilde{v}_r = \sqrt{1-\alpha} v_r + \tilde{n}_r, \quad (7)$$

where $\tilde{n}_r \sim \mathcal{CN}(0, \tilde{\sigma}_r^2)$ is the noise produced by the passband-to-baseband signal converter.

Plugging (3) into (7) results in $\tilde{v}_r = \sqrt{(1-\alpha)P_s} g_{sr} u_s + \sqrt{(1-\alpha)P_{p1}} g_{pr} u_{p1} + \sqrt{1-\alpha} n_r + \tilde{n}_r$ from which the SINR (Signal-to-Interference plus Noise Ratio) at the input of the information decoder can be represented as

$$\begin{aligned} \varphi_{sr} &= \frac{(1-\alpha) P_s |g_{sr}|^2}{(1-\alpha) P_{p1} |g_{pr}|^2 + (1-\alpha) \sigma_r^2 + \tilde{\sigma}_r^2} \\ &= \frac{P_s |g_{sr}|^2}{P_{p1} |g_{pr}|^2 + \tilde{\sigma}_r^2}, \end{aligned} \quad (8)$$

where

$$\tilde{\sigma}_r^2 = \sigma_r^2 + \frac{\sigma_r^2}{1-\alpha}. \quad (9)$$

Then, the channel capacity which *SR* achieves in stage 1 is $C_{sr} = \beta \log_2(1 + \varphi_{sr})$ bps/Hz where the prelog factor of β is because the period of stage 1 is βT . According to the communication theory, *SR* can restore the source information when its channel capacity is higher than the required spectral efficiency of *SUs*, C_1 , i.e., $C_{sr} \geq C_1$. In order words, u_s is successfully recovered at *SR* if $\varphi_{sr} \geq \varphi_1$ where $\varphi_1 = 2^{C_1/\beta} - 1$.

In stage 2, *SR* transmits the recovered source symbol u_r with the transmit power P_r if it can successfully restore the source information (i.e., $\varphi_{sr} \geq \varphi_1$ and $u_r = u_s$). Otherwise, it keeps idle. The information transmission of *SR* is in parallel to that of *PT*. As such, *SD*, *E*, and *PR* correspondingly receive the following signals:

$$v_{rd} = \begin{cases} g_{rd} \sqrt{P_r} u_r + g_{pd} \sqrt{P_{p2}} u_{p2} + n_d, & \varphi_{sr} \geq \varphi_1 \\ g_{pd} \sqrt{P_{p2}} u_{p2} + n_d, & \varphi_{sr} < \varphi_1, \end{cases} \quad (10)$$

$$v_{re} = \begin{cases} g_{re} \sqrt{P_r} u_r + g_{pe} \sqrt{P_{p2}} u_{p2} + n_e, & \varphi_{sr} \geq \varphi_1 \\ g_{pe} \sqrt{P_{p2}} u_{p2} + n_e, & \varphi_{sr} < \varphi_1, \end{cases} \quad (11)$$

$$v_{rp} = \begin{cases} g_{rp} \sqrt{P_r} u_r + g_{p2} \sqrt{P_{p2}} u_{p2} + n_{p2}, & \varphi_{sr} \geq \varphi_1 \\ g_{p2} \sqrt{P_{p2}} u_{p2} + n_{p2}, & \varphi_{sr} < \varphi_1, \end{cases} \quad (12)$$

where $n_d \sim \mathcal{CN}(0, \sigma_d^2)$, $n_e \sim \mathcal{CN}(0, \sigma_e^2)$, and $n_{p2} \sim \mathcal{CN}(0, \sigma_{p2}^2)$ are the noises produced by the receive antennas at

SD , E , and PR , correspondingly; P_{p2} and u_{p2} are, respectively, the transmit power and the unity-power transmit symbol of PT in stage 2. That (P_{p1}, u_{p1}) differs from (P_{p2}, u_{p2}) reflects the realistic scenario where two different primary transmitter-receiver pairs may communicate in two stages.

2.3. Secrecy Capacity. The SINRs at SD and E can be achieved from (10) and (11) as

$$\varphi_{rd} = \begin{cases} \frac{P_r |g_{rd}|^2}{P_{p2} |g_{pd}|^2 + \varrho_d^2}, & \varphi_{sr} \geq \varphi_1 \\ 0, & \varphi_{sr} < \varphi_1, \end{cases} \quad (13)$$

$$\varphi_{re} = \begin{cases} \frac{P_r |g_{re}|^2}{P_{p2} |g_{pe}|^2 + \varrho_e^2}, & \varphi_{sr} \geq \varphi_1 \\ 0, & \varphi_{sr} < \varphi_1. \end{cases} \quad (14)$$

Then, SD and E obtain channel capacities correspondingly as [24]

$$C_{rd} = (1 - \beta) \log_2 (1 + \varphi_{rd}), \quad (15)$$

$$C_{re} = (1 - \beta) \log_2 (1 + \varphi_{re}), \quad (16)$$

where the prelog factor of $1 - \beta$ is because the time of stage 2 is $(1 - \beta)T$.

The secrecy capacity of relaying communications in energy scavenging cognitive networks, which is the difference between the channel capacities of the trusted channel (from SR to SD) and the wiretap channel (from SR to E), is expressed as [7]

$$\begin{aligned} \mathcal{C}_{sec} &= [C_{rd} - C_{re}]^+ \\ &= \begin{cases} (1 - \beta) \left[\log_2 \frac{1 + \varphi_{rd}}{1 + \varphi_{re}} \right]^+, & \varphi_{sr} \geq \varphi_1 \\ 0, & \varphi_{sr} < \varphi_1, \end{cases} \end{aligned} \quad (17)$$

where $[x]^+$ denotes $\max(x, 0)$.

2.4. Secondary Power Allocation. The SINR at PR in stage 1 is computed from (4) as

$$\varphi_{p1} = \frac{P_{p1} |g_{p1}|^2}{P_s |g_{sp}|^2 + \varrho_{p1}^2}. \quad (18)$$

Then, the channel capacity that PR achieves in stage 1 is

$$C_{p1} = \beta \log_2 (1 + \varphi_{p1}). \quad (19)$$

Similarly, the SINR at PR in stage 2 is computed from (12) as

$$\varphi_{p2} = \begin{cases} \frac{P_{p2} |g_{p2}|^2}{P_r |g_{rp}|^2 + \varrho_{p2}^2}, & \varphi_{sr} \geq \varphi_1 \\ \frac{P_{p2} |g_{p2}|^2}{\varrho_{p2}^2}, & \varphi_{sr} < \varphi_1 \end{cases} \quad (20)$$

and the channel capacity that PR achieves in stage 2 is

$$C_{p2} = (1 - \beta) \log_2 (1 + \varphi_{p2}). \quad (21)$$

Because the secondary transmitters (SS and SR) opportunistically access the spectrum of the primary users, their transmit powers must be limited such that the outage probability of the primary receiver is below a certain threshold λ . More specifically, P_s and P_r must be constrained by

$$\Pr \{C_{p1} \leq C_2\} \leq \lambda, \quad (22)$$

$$\Pr \{C_{p2} \leq C_2\} \leq \lambda, \quad (23)$$

where C_2 is the required spectral efficiency of PR .

Constraints in (22) and (23) are, namely, the primary outage constraints.

The transmit powers of SS and SR must be also limited by their maximum transmit powers, P_{sm} and P_{rm} , respectively, which are determined by the hardware implementation and the energy scavenger, correspondingly. Therefore, P_s and P_r are upper-bounded by

$$P_s \leq P_{sm}, \quad (24)$$

$$P_r \leq P_{rm}. \quad (25)$$

Constraints in (24) and (25) are, namely, the maximum transmit power constraints.

Transmit power constraints for P_s in (22) and (24) result in

$$P_s = \min \left(\frac{P_{p1} \kappa_{p1}}{\varphi_{21} \kappa_{sp}} \left[\frac{1}{1 - \lambda} e^{-\varphi_{21} \varrho_{p1}^2 / P_{p1} \kappa_{p1}} - 1 \right]^+, P_{sm} \right), \quad (26)$$

where $\varphi_{21} = 2^{C_2/\beta} - 1$.

Similarly, transmit power constraints for P_r in (23) and (25) result in

$$P_r = \min \left(\frac{P_{p2} \kappa_{p2}}{\varphi_{22} \kappa_{rp}} \left[\frac{1}{1 - \lambda} e^{-\varphi_{22} \varrho_{p2}^2 / P_{p2} \kappa_{p2}} - 1 \right]^+, P_{rm} \right), \quad (27)$$

where $\varphi_{22} = 2^{C_2/(1-\beta)} - 1$.

In (26) and (27), κ_{p1} and κ_{p2} represent the fading powers of the channels between the primary transmitter and the primary receiver in stage 1 and stage 2, respectively.

The derivation of (26) follows [25, eq. (18)] while the derivation of (27) follows [25, eq. (20)] with a note that (27) is obtained with φ_{p2} in the case that SR is active (i.e., $\varphi_{sr} \geq \varphi_1$). The case that SR is idle is of no interest because the source information cannot reach the secondary destination.

3. SOP Analysis

The SOP is a crucial performance metric in assessing information security of wireless communications in the information-theoretic aspect. It is defined as the probability that the secrecy capacity \mathcal{C}_{sec} does not reach a required security degree \bar{C}_3 . As such, the smaller the SOP is, the more

secure the wireless communication is. In this section, the SOP of relaying communications in energy scavenging cognitive networks is derived in closed form, which facilitates not only evaluating security performance without exhaustive simulations but also inferring other crucial security performance metrics such as the IP and the PSPSC.

The SOP of relaying communications in energy scavenging cognitive networks is given by

$$Y(\bar{C}_3) = \Pr\{\mathcal{E}_{\text{sec}} < \bar{C}_3\}, \quad (28)$$

where $\Pr\{\mathcal{V}\}$ is the probability of the event \mathcal{V} .

Since \mathcal{E}_{sec} is nonnegative when $\varphi_{sr} \geq \varphi_1$ as seen in (17), one can decompose (28) into two cases as

$$\begin{aligned} Y(\bar{C}_3) &= \Pr\left\{(1-\beta)\left[\log_2\left(\frac{1+\varphi_{rd}}{1+\varphi_{re}}\right)\right]^+ < \bar{C}_3 \mid \varphi_{sr}\right. \\ &\geq \varphi_1\left.\right\} \Pr\{\varphi_{sr} \geq \varphi_1\} + \Pr\{0 < \bar{C}_3 \mid \varphi_{sr} < \varphi_1\} \\ &\cdot \Pr\{\varphi_{sr} < \varphi_1\}. \end{aligned} \quad (29)$$

Because the required security degree \bar{C}_3 is positive, (29) is rewritten as

$$\begin{aligned} Y(\bar{C}_3) &= \Pr\left\{\left[\log_2\left(\frac{1+\varphi_{rd}}{1+\varphi_{re}}\right)\right]^+ < \frac{\bar{C}_3}{1-\beta} \mid \varphi_{sr} \geq \varphi_1\right\} \underbrace{\Pr\{\varphi_{sr} \geq \varphi_1\}}_{\mathcal{F}_1} \\ &+ \underbrace{\Pr\{\varphi_{sr} < \varphi_1\}}_{\mathcal{F}_2}. \end{aligned} \quad (30)$$

Theorem 1. *The accurate closed-form representation of \mathcal{F}_1 is given by*

$$\begin{aligned} \mathcal{F}_1 &= CD\Psi(D, C) + C\Phi(D, C) + \frac{e^{(1-2^{C_3})B}AC}{2^{C_3}(C-G)} \\ &\cdot \Phi(2^{C_3}B + D, C) \\ &+ \frac{e^{(1-2^{C_3})B}AC}{2^{C_3}(C-G)} \left(D + \frac{1}{C-G}\right) \\ &\cdot \left[\Psi(2^{C_3}B + D, C) - \Psi(2^{C_3}B + D, G)\right], \end{aligned} \quad (31)$$

where

$$A = \frac{\kappa_{rd}P_r}{\kappa_{pd}P_{p2}}, \quad (32)$$

$$B = \frac{\varrho_d^2}{\kappa_{rd}P_r}, \quad (33)$$

$$C = \frac{\kappa_{re}P_r}{\kappa_{pe}P_{p2}}, \quad (34)$$

$$D = \frac{\varrho_e^2}{\kappa_{re}P_r}, \quad (35)$$

$$G = 1 + 2^{-C_3}(A-1), \quad (36)$$

$$\Psi(a, b) = -e^{ab}Ei(-ab), \quad (37)$$

$$\Phi(a, b) = \frac{1}{b} + ae^{ab}Ei(-ab), \quad (38)$$

$$C_3 = \frac{\bar{C}_3}{1-\beta}, \quad (39)$$

with $Ei(\cdot)$ being the exponential integral in [26].

Proof. Please refer to Appendix. \square

Theorem 2. *The accurate closed-form representation of \mathcal{F}_2 is given by*

$$\mathcal{F}_2 = 1 - U \frac{e^{-V\varphi_1}}{\varphi_1 + U}, \quad (40)$$

where

$$U = \frac{\kappa_{sr}P_s}{\kappa_{pr}P_{p1}}, \quad (41)$$

$$V = \frac{\varrho_r^2}{\kappa_{sr}P_s}. \quad (42)$$

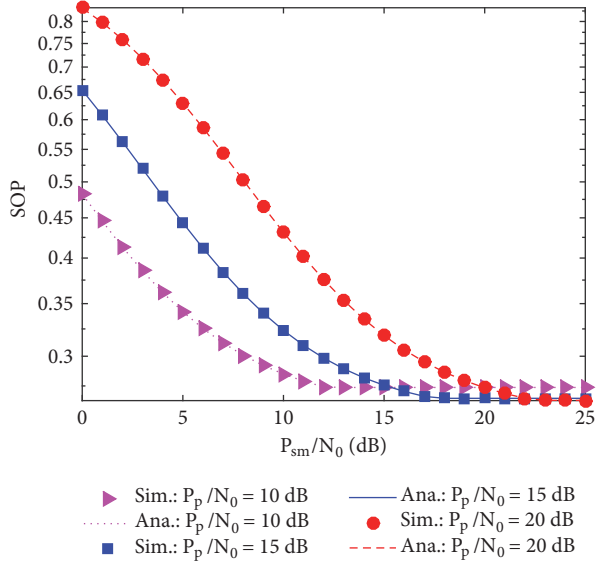
Proof. By imitating the derivation of (A.5) in the Appendix, it is easy to see that \mathcal{F}_2 is the cdf of φ_{sr} evaluated at φ_1 . Therefore, \mathcal{F}_2 can be represented as (40), completing the proof. \square

Plugging (31) and (40) into (30), one obtains the accurate closed-form expression of the SOP for relaying communications in energy scavenging cognitive networks as $Y(\bar{C}_3) = \mathcal{F}_1(1-\mathcal{F}_2) + \mathcal{F}_2$. This expression is useful to quickly evaluate the security performance without exhaustive simulations. To the best of the authors' understanding, this expression is newly reported. Moreover, some crucial security performance metrics (e.g., the IP or the PSPSC) can be easily derived from this expression. More specifically, the IP refers to the probability that the secrecy capacity is negative [27], i.e.,

$$\Theta = \Pr\{\mathcal{E}_{\text{sec}} < 0\} = Y(0). \quad (43)$$

TABLE I: Simulation parameters.

PARAMETER	VALUE
Path-loss exponent	$\nu = 4$
Energy conversion efficiency	$\mu = 0.9$
Coordinate of SS	SS at (0.0, 0.0)
Coordinate of SD	SD at (1.0, 0.0)
Coordinate of PT	PT at (0.2, 0.8)
Coordinate of PR	PR at (0.9, 0.7)
Coordinate of E	E at (1.0, 0.4)
Coordinate of SR	SR at (d , 0.0)

FIGURE 2: SOP versus P_{sm}/N_0 . “Sim.” and “Ana.” represent “Simulation” and “Analysis,” respectively.

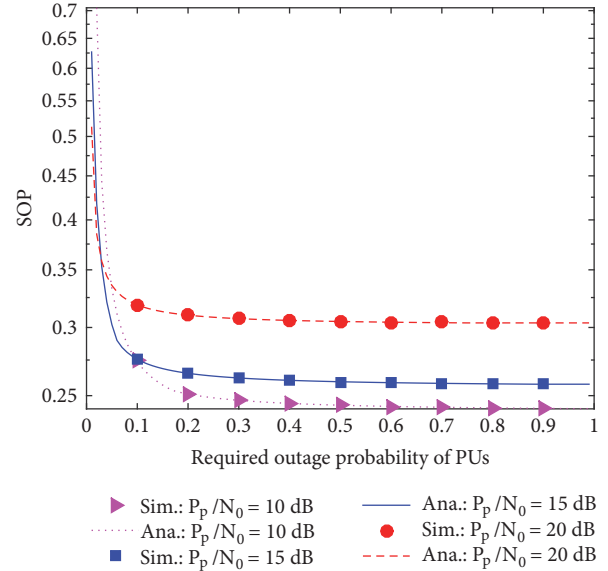
Additionally, the PSPSC refers to the probability that the secrecy capacity is strictly positive, i.e.,

$$\Omega = \Pr \{ \mathcal{C}_{sec} > 0 \} = 1 - \Pr \{ \mathcal{C}_{sec} < 0 \} = 1 - \Upsilon(0). \quad (44)$$

4. Results and Discussions

Simulated/numerical results in this section are collected to assess the security performance of relaying communications in energy scavenging cognitive networks in terms of the SOP through typical parameters. Numerical results are produced by (30) while simulated ones are generated by Monte-Carlo simulation with 10^7 channel realizations. Without loss of generality, equal noise variances are supposed (i.e., $\varrho_{p1}^2 = \varrho_{p2}^2 = \varrho_d^2 = \varrho_e^2 = \varrho_r^2 = \tilde{\varrho}_r^2 = N_0$) and only one primary transmitter-receiver pair is considered (i.e., $\kappa_{p1} = \kappa_{p2} = \kappa_{pp}$ and $P_{p1} = P_{p2} = P_p$). Simulation parameters under investigation are specified in Table 1.

Figure 2 shows the SOP versus the maximum transmit power-to-noise variance ratio P_{sm}/N_0 for $d = 0.5$, $\lambda = 0.1$, $C_1 = 0.2$ bps/Hz, $C_2 = 0.3$ bps/Hz, $\bar{C}_3 = 0.1$ bps/Hz, $\alpha = 0.8$, $\beta = 0.6$, and $P_p/N_0 = 10, 15, 20$ dB. This figure

FIGURE 3: SOP versus λ .

verifies the accuracy of (30) due to the exact agreement between the analysis and the simulation. Additionally, the SOP decreases with increasing P_{sm}/N_0 . This is attributed to the fact that increasing P_{sm}/N_0 offers SR more opportunities to correctly recover the source information and to scavenge more energy from the RF signals of SS, eventually decreasing the outage probability in stage 2. Nevertheless, the SOP suffers the error floor in the range of high P_{sm}/N_0 . This error floor originates from the power allocation mechanism for SS and SR (please recall (26) and (27)) where SS and SR transmit signals with powers independent of P_{sm}/N_0 in the range of large P_{sm}/N_0 (i.e., the maximum transmit power constraint is ignored when P_{sm}/N_0 is large), resulting in the constant SOP. Furthermore, the SOP increases with increasing P_p/N_0 . This is because increasing the power of the primary transmitter inflicts more interference to secondary receivers which cannot be compensated by the increase in the energy of SR scavenged from the transmit signals of PT. However, when P_{sm}/N_0 is greater than a certain value, the SOP decreases with increasing P_p/N_0 . For example, when P_{sm}/N_0 is greater than 15.5 dB, the SOP with $P_p/N_0 = 10$ dB is larger than the SOP with $P_p/N_0 = 15$ dB. This can be explained as follows. When P_{sm}/N_0 is greater than a certain value, the transmit power of SS is large according to (26). Therefore, the relay can scavenge more energy from the transmit signal of SS according to (6). This increases the transmit power of the relay according to (27), which can better compensate for more interference from the primary transmitter due to larger value of P_p/N_0 , ultimately reducing the SOP.

Figure 3 demonstrates the SOP versus the required outage probability of PUs, λ , for $P_{sm}/N_0 = 15$ dB, $d = 0.5$, $\alpha = 0.8$, $\beta = 0.6$, $C_1 = 0.2$ bps/Hz, $C_2 = 0.3$ bps/Hz, $\bar{C}_3 = 0.1$ bps/Hz, and $P_p/N_0 = 10, 15, 20$ dB. This figure validates (30) due to the match between the simulation and the analysis. Moreover, increasing the required outage probability of PUs

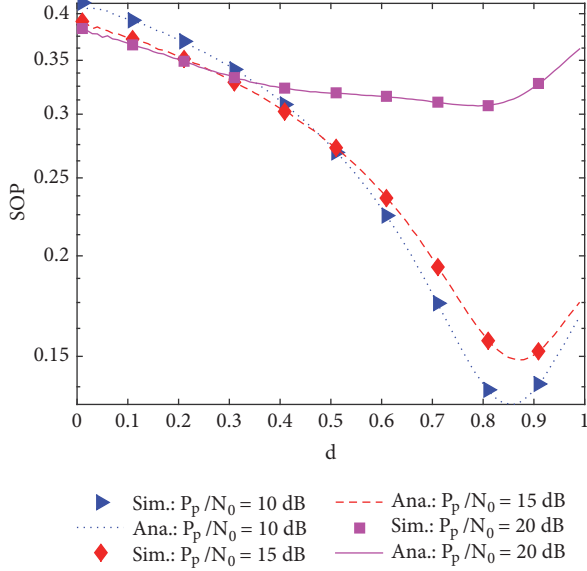


FIGURE 4: SOP versus the relay's position.

decreases the SOP. This is because such an increase allows PUs to tolerate more interference from SUs. Therefore, SUs can transmit signals with higher powers, eventually reducing the outage in stage 2. Nevertheless, the SOP is saturated in the range of large λ (e.g., $\lambda > 0.5$). Such a SOP saturation is because of the power allocation mechanism in (26) and (27) where the second term in P_s (or P_r) is independent of λ . Therefore, P_s (or P_r) is constant for large values of λ at which the first term dominates the second term in P_s (or P_r), causing the error floor in the SOP. Furthermore, the SOP saturation level increases with increasing P_p/N_0 . This can be comprehended from increasing the interference on SUs when P_p/N_0 increases.

Figure 4 shows the SOP versus the relay's position (i.e., d) for $P_{sm}/N_0 = 15$ dB, $\beta = 0.6$, $\lambda = 0.1$, $\alpha = 0.8$, $C_1 = 0.2$ bps/Hz, $C_2 = 0.3$ bps/Hz, $\bar{C}_3 = 0.1$ bps/Hz, and $P_p/N_0 = 10, 15, 20$ dB. This figure confirms the validity of (30) due to the exact agreement between the simulation and the analysis. We are reminded that the secrecy outage event occurs as R cannot successfully recover the source information (i.e., SS is distant from SR) or SR cannot reliably send the decoded source information to SD (i.e., SD is distant from SR). As such, it is obvious that there is always an existence of the relay's optimum position, which optimally trades off the probability that SR can correctly restore the source information with the probability that SR can reliably send the decoded source information to SD to minimize the SOP. Figure 4 confirms this fact which achieves the minimum SOP as SR is $d_{opt} = 0.86, 0.87, 0.79$ distant from SS for $P_p/N_0 = 10, 15, 20$ dB, respectively. Moreover, the minimum SOP corresponding to the relay's optimum position increases with increasing the interference from PUs (i.e., increasing P_p/N_0) as expected. However, when d is smaller than a certain value, the SOP decreases with increasing P_p/N_0 . For instance, when d is smaller than 0.48, the SOP with $P_p/N_0 =$

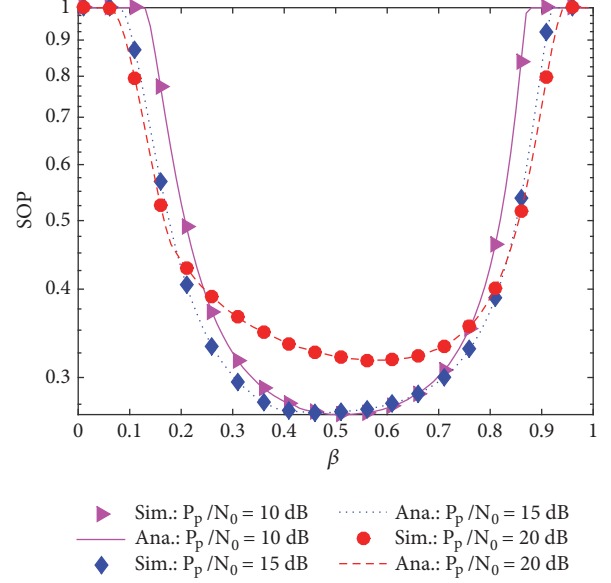


FIGURE 5: SOP versus the time splitting factor.

10 dB is larger than the SOP with $P_p/N_0 = 15$ dB. This can be interpreted as follows. When d is smaller than a certain value (i.e., SR is nearer to SS), SR can correctly decode the source information with a higher probability and scavenge more energy from the transmit signal of SS . This increases the transmit power of the relay, which can better compensate for more interference from the primary transmitter due to larger value of P_p/N_0 , ultimately reducing the SOP.

Figure 5 illustrates the SOP versus β for $d = 0.5$, $P_{sm}/N_0 = 15$ dB, $\lambda = 0.1$, $\alpha = 0.5$, $C_1 = 0.2$ bps/Hz, $C_2 = 0.3$ bps/Hz, $\bar{C}_3 = 0.1$ bps/Hz, and $P_p/N_0 = 10, 15, 20$ dB. This figure validates (30) because the simulation perfectly matches the analysis. In addition, there exist optimum values of β (e.g., $\beta_{opt} = 0.51, 0.46, 0.56$ for $P_p/N_0 = 10, 15, 20$ dB, correspondingly as shown in Figure 5) for the minimum SOPs. The existence of β_{opt} can be interpreted as follows. Increasing β prolongs the period of stage 1, and thus, SR can scavenge more energy and correctly restore the source information with a higher probability. Nevertheless, increasing β can also mitigate the secrecy capacity in stage 2, and thus, the SOP increases. Consequently, β should be selected to optimally compromise the periods of two stages for the minimum SOP. Furthermore, the minimum SOP corresponding to the optimum value of β increases with P_p/N_0 as expected. However, when β is outside a certain range, the SOP decreases with increasing P_p/N_0 . For instance, when β is outside $[0.47, 0.66]$, the SOP with $P_p/N_0 = 10$ dB is larger than the SOP with $P_p/N_0 = 15$ dB. This can be interpreted as follows. The value of β affects the required SINRs of PR (i.e., $\varphi_{21} = 2^{C_2/\beta} - 1$ and $\varphi_{22} = 2^{C_2/(1-\beta)} - 1$ as seen in (26) and (27)). Therefore, the primary receiver has more chances to obtain the required SINRs when P_p/N_0 increases. Accordingly, it can be more tolerable with the interference from the secondary transmitters. Furthermore, the relay has more chances to scavenge more energy from the transmit

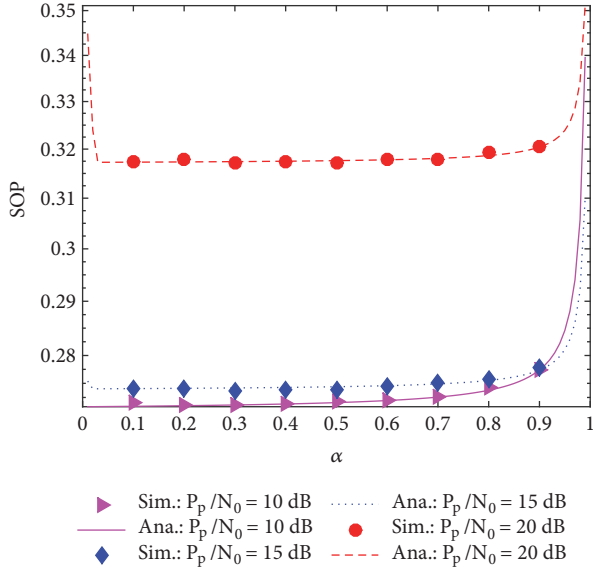


FIGURE 6: SOP versus the power splitting factor.

signal of PT when P_p/N_0 increases. As such, the relay transmits signals with higher power, which can better compensate for more interference from the primary transmitter due to larger value of P_p/N_0 , eventually mitigating the SOP.

Figure 6 demonstrates the SOP versus α for $P_{sm}/N_0 = 15$ dB, $\lambda = 0.1$, $d = 0.5$, $\beta = 0.6$, $C_1 = 0.2$ bps/Hz, $C_2 = 0.3$ bps/Hz, $\bar{C}_3 = 0.1$ bps/Hz, and $P_p/N_0 = 10, 15, 20$ dB. This figure exposes an exact agreement between the simulation and the analysis, validating (30). Moreover, the SOP can be minimized by optimally selecting α . The existence of the optimal value of α for the minimum SOP can be explained as follows. Increasing α permits SR to scavenge more energy, and thus, SR can enhance its transmission reliability in stage 2, ultimately decreasing the SOP. Nevertheless, increasing α also decreases the energy for the information decoder, decreasing the probability that SR can correctly restore the source information in stage 1 and inflicting more secrecy outage in stage 2. Consequently, α should be optimally adopted to compromise transmission reliability of SS and SR in both stages. Furthermore, the minimum SOP corresponding to the optimum value of α increases with P_p/N_0 as expected.

Figure 7 illustrates the SOP versus the required spectral efficiency of SUs, C_1 , for $P_{sm}/N_0 = 15$ dB, $\beta = 0.6$, $\lambda = 0.1$, $d = 0.5$, $\alpha = 0.8$, $C_2 = 0.3$ bps/Hz, $\bar{C}_3 = 0.1$ bps/Hz, and $P_p/N_0 = 10, 15, 20$ dB. This figure verifies a perfect match between the simulation and the analysis, confirming the precision of (30). In addition, the SOP increases with increasing C_1 . This is apparent because the higher the required spectral efficiency of SUs, the lower the probability for the relay to correctly restore the source information, and, hence, the higher the probability for the system to be outage in stage 2. Moreover, the SOP is higher for larger values of P_p/N_0 as expected.

Figure 8 demonstrates the SOP versus the required spectral efficiency of PUs, C_2 , for $P_{sm}/N_0 = 15$ dB, $\beta = 0.6$, $\lambda = 0.1$, $d = 0.5$, $\alpha = 0.8$, $C_1 = 0.2$ bps/Hz,

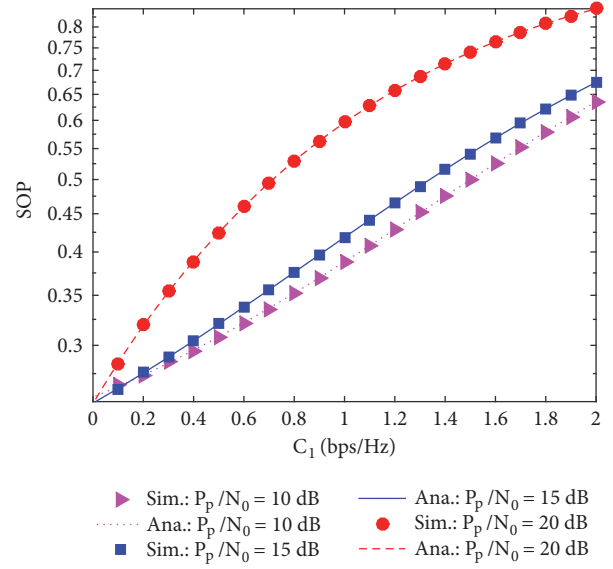


FIGURE 7: SOP versus the required spectral efficiency of SUs.

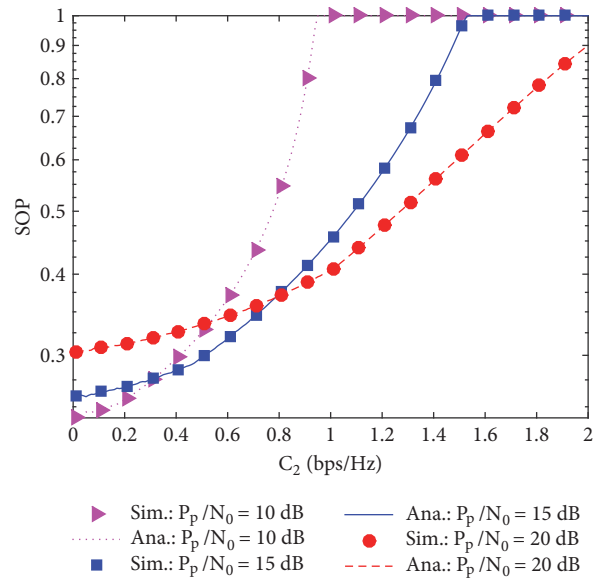


FIGURE 8: SOP versus the required spectral efficiency of PUs.

$\bar{C}_3 = 0.1$ bps/Hz, and $P_p/N_0 = 10, 15, 20$ dB. This figure confirms an exact agreement between the analysis and the simulation, validating (30). Additionally, the SOP increases with increasing C_2 . This is because for the fixed value of λ (please see (22) and (23)) the higher the required spectral efficiency of PUs is, the lower the interference at PUs caused by SUs must be, and, hence, the lower the transmit power of SUs must be, leading to the higher SOP. Nevertheless, the system is always in outage at large values of C_2 . This is because according to (26) and (27), the terms inside $[\cdot]^+$ are inversely proportional to φ_{21} and φ_{22} (or C_2). As such, increasing C_2 up to a certain value (e.g., 1.53 bps/Hz for $P_p/N_0 = 15$ dB) incurs $[\cdot]^+ = 0$ and, hence, P_s and P_r are always zero when C_2 exceeds a threshold, causing the system outage all the

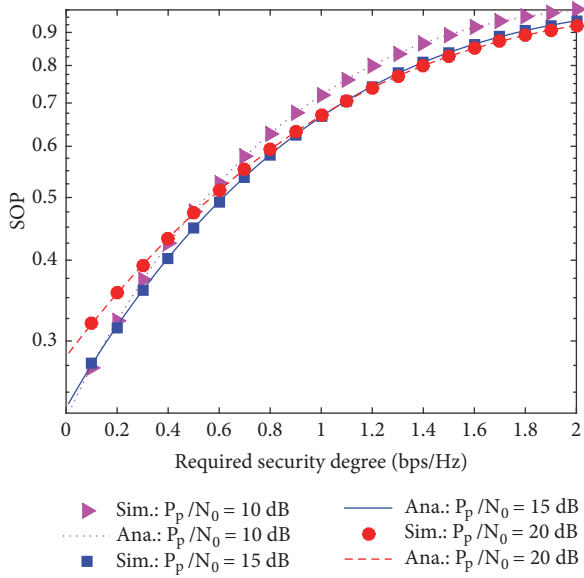


FIGURE 9: SOP versus the required security degree.

time. Furthermore, the SOP is affected by P_p/N_0 as expected. More noticeably, when C_2 is greater than a certain value, the SOP decreases with increasing P_p/N_0 . For example, when C_2 is greater than 0.31 bps/Hz, the SOP with $P_p/N_0 = 10$ dB is larger than the SOP with $P_p/N_0 = 15$ dB. This can be interpreted as follows. The primary receiver has more chances to obtain the required spectral efficiency C_2 when P_p/N_0 increases. As such, it can be more tolerable with the interference from the secondary transmitters. Moreover, the relay has more chances to scavenge more energy from the transmit signal of PT when P_p/N_0 increases. Accordingly, the relay transmits signals with higher power, which can better compensate for more interference from the primary transmitter due to larger value of P_p/N_0 , eventually reducing the SOP.

Figure 9 shows the SOP versus the required security degree \bar{C}_3 for $P_{sm}/N_0 = 15$ dB, $\beta = 0.6$, $\lambda = 0.1$, $d = 0.5$, $\alpha = 0.8$, $C_1 = 0.2$ bps/Hz, $C_2 = 0.1$ bps/Hz, and $P_p/N_0 = 10, 15, 20$ dB. This figure validates (30) because of the match between the analysis and the simulation. Additionally, the SOP increases with increasing \bar{C}_3 . This is because, given system parameters, the higher the required security degree, the higher the SOP. Moreover, the SOP is influenced by P_p/N_0 as expected.

5. Conclusion

This paper evaluated the security performance of relaying communications in energy scavenging cognitive networks in terms of the SOP. For quick performance assessment, the accurate closed-form expression of the SOP was derived under consideration of Rayleigh fading, the primary outage constraint, the interference from PUs, and the maximum transmit power constraint. The validity of the proposed expression was verified by computer simulations. Various

results exposed that the self-powered relay considerably enhances the security performance even when the source-destination channel is unavailable owing to deep fading, severe path-loss, and strong shadowing. Moreover, the security performance suffered the error floor in the range of large maximum transmit power or high required outage probability of PUs. Furthermore, the security performance of relaying communications in energy scavenging cognitive networks depends on several system parameters among which the time splitting factor, the relay's position, and the power splitting factor should be optimally selected to minimize the SOP.

Appendix

Proof of Theorem 1. Decompose \mathcal{F}_1 into two cases, $\log_2((1 + \varphi_{rd})/(1 + \varphi_{re})) > 0$ and $\log_2((1 + \varphi_{rd})/(1 + \varphi_{re})) < 0$; one can simplify it as

$$\begin{aligned} \mathcal{F}_1 &= \Pr \left\{ \log_2 \left(\frac{1 + \varphi_{rd}}{1 + \varphi_{re}} \right) < C_3 \mid \log_2 \left(\frac{1 + \varphi_{rd}}{1 + \varphi_{re}} \right) \right. \\ &\geq 0, \varphi_{sr} \geq \varphi_1 \left. \right\} \times \Pr \left\{ \log_2 \left(\frac{1 + \varphi_{rd}}{1 + \varphi_{re}} \right) \geq 0 \mid \varphi_{sr} \right. \\ &\geq \varphi_1 \left. \right\} + \Pr \left\{ 0 < C_3 \mid \log_2 \left(\frac{1 + \varphi_{rd}}{1 + \varphi_{re}} \right) < 0, \varphi_{sr} \right. \\ &\geq \varphi_1 \left. \right\} \Pr \left\{ \log_2 \left(\frac{1 + \varphi_{rd}}{1 + \varphi_{re}} \right) < 0 \mid \varphi_{sr} \geq \varphi_1 \right\}, \end{aligned} \quad (\text{A.1})$$

where C_3 is defined in (39).

Because the required security degree is positive (i.e., $\bar{C}_3 > 0$), (A.1) is further shortened as

$$\begin{aligned} \mathcal{F}_1 &= \Pr \left\{ \frac{1 + \varphi_{rd}}{1 + \varphi_{re}} < 2^{C_3} \mid \varphi_{sr} \geq \varphi_1 \right\} \\ &= \Pr \left\{ \varphi_{rd} < 2^{C_3} (1 + \varphi_{re}) - 1 \mid \varphi_{sr} \geq \varphi_1 \right\} \\ &= \int_0^\infty \int_0^{2^{C_3}(1+x)-1} f_{\varphi_{re}, \varphi_{rd}}(x, y \mid \varphi_{sr} \geq \varphi_1) dy dx. \end{aligned} \quad (\text{A.2})$$

Because φ_{rd} and φ_{re} are statistically independent, their joint pdf can be represented as a product of their marginal pdfs, i.e., $f_{\varphi_{re}, \varphi_{rd}}(x, y \mid \varphi_{sr} \geq \varphi_1) = f_{\varphi_{re}}(x \mid \varphi_{sr} \geq \varphi_1) f_{\varphi_{rd}}(y \mid \varphi_{sr} \geq \varphi_1)$. Then, (A.2) is rewritten as

$$\begin{aligned} \mathcal{F}_1 &= \int_0^\infty \left[\int_0^{2^{C_3}(1+x)-1} f_{\varphi_{rd}}(y \mid \varphi_{sr} \geq \varphi_1) dy \right] \\ &\cdot f_{\varphi_{re}}(x \mid \varphi_{sr} \geq \varphi_1) dx \\ &= \int_0^\infty F_{\varphi_{rd}}(2^{C_3}[1+x] - 1 \mid \varphi_{sr} \geq \varphi_1) \\ &\cdot f_{\varphi_{re}}(x \mid \varphi_{sr} \geq \varphi_1) dx. \end{aligned} \quad (\text{A.3})$$

To numerically evaluate (A.3), the cdf of φ_{rd} , $F_{\varphi_{rd}}(z \mid \varphi_{sr} \geq \varphi_1)$, and the pdf of φ_{re} , $f_{\varphi_{re}}(z \mid \varphi_{sr} \geq \varphi_1)$, must be derived first.

The cdf of φ_{rd} is computed from its definition as

$$\begin{aligned}
F_{\varphi_{rd}}(z | \varphi_{sr} \geq \varphi_1) &= \Pr \{ \varphi_{rd} \leq z | \varphi_{sr} \geq \varphi_1 \} \\
&= \Pr \left\{ \frac{P_r |g_{rd}|^2}{P_{p2} |g_{pd}|^2 + \varrho_d^2} \leq z \right\} \\
&= \Pr \left\{ |g_{rd}|^2 \leq \frac{z}{P_r} (P_{p2} |g_{pd}|^2 + \varrho_d^2) \right\} \quad (\text{A.4}) \\
&= \int_0^\infty F_{|g_{rd}|^2} \left(\frac{z}{P_r} [P_{p2} |g_{pd}|^2 + \varrho_d^2] \right) f_{|g_{pd}|^2}(x) dx \\
&= \int_0^\infty \left(1 - e^{-(z/\kappa_{rd} P_r)(P_{p2} x + \varrho_d^2)} \right) \frac{1}{\kappa_{pd}} e^{-x/\kappa_{pd}} dx.
\end{aligned}$$

The last integral in (A.4) is straightforwardly computed, resulting in

$$F_{\varphi_{rd}}(z | \varphi_{sr} \geq \varphi_1) = 1 - A \frac{e^{-Bz}}{z + A}, \quad (\text{A.5})$$

where A and B are given by (32) and (33), respectively.

Similarly, the cdf of φ_{re} has the same form as that of φ_{rd} :

$$F_{\varphi_{re}}(z | \varphi_{sr} \geq \varphi_1) = 1 - C \frac{e^{-Dz}}{z + C}, \quad (\text{A.6})$$

where C and D are given by (34) and (35), respectively.

Taking the derivative of $F_{\varphi_{re}}(z | \varphi_{sr} \geq \varphi_1)$ with respect to z arrives at

$$f_{\varphi_{re}}(z | \varphi_{sr} \geq \varphi_1) = CD \frac{e^{-Dz}}{z + C} + C \frac{e^{-Dz}}{(z + C)^2}. \quad (\text{A.7})$$

Plugging (A.5) and (A.7) with reasonable variable substitutions into (A.3), one obtains

$$\begin{aligned}
\mathcal{J}_1 &= \int_0^\infty \left[1 - A \frac{e^{-B(2^{C_3} x + 2^{C_3} - 1)}}{2^{C_3} x + 2^{C_3} - 1 + A} \right] \left[CD \frac{e^{-Dx}}{x + C} + C \frac{e^{-Dx}}{(x + C)^2} \right] dx \\
&= CD \int_0^\infty \frac{e^{-Dx}}{x + C} dx + C \int_0^\infty \frac{e^{-Dx}}{(x + C)^2} dx \\
&\quad - 2^{-C_3} e^{-B(2^{C_3} - 1)} ACD \int_0^\infty \frac{e^{-2^{C_3} Bx}}{x + 1 + 2^{-C_3} (A - 1)} \frac{e^{-Dx}}{x + C} dx \\
&\quad - 2^{-C_3} e^{-B(2^{C_3} - 1)} AC \int_0^\infty \frac{e^{-2^{C_3} Bx}}{x + 1 + 2^{-C_3} (A - 1)} \frac{e^{-Dx}}{(x + C)^2} dx.
\end{aligned} \quad (\text{A.8})$$

By letting $G = 1 + 2^{-C_3}(A - 1)$ as in (36) and applying the partial fraction decomposition to $1/(x + G)(x + C)$ and $1/(x + G)(x + C)^2$, one can transform (A.8) to

$$\begin{aligned}
\mathcal{J}_1 &= CD \int_0^\infty \frac{e^{-Dx}}{x + C} dx + C \int_0^\infty \frac{e^{-Dx}}{(x + C)^2} dx \\
&\quad - 2^{-C_3} e^{-B(2^{C_3} - 1)} ACD \int_0^\infty \frac{e^{-(2^{C_3} B + D)x}}{(x + G)(x + C)} dx \\
&\quad - 2^{-C_3} e^{-B(2^{C_3} - 1)} AC \int_0^\infty \frac{e^{-(2^{C_3} B + D)x}}{(x + G)(x + C)^2} dx \\
&= CD \int_0^\infty \frac{e^{-Dx}}{x + C} dx + C \int_0^\infty \frac{e^{-Dx}}{(x + C)^2} dx \\
&\quad - 2^{-C_3} e^{-B(2^{C_3} - 1)} \frac{ACD}{C - G} \left[\int_0^\infty \frac{e^{-(2^{C_3} B + D)x}}{x + G} dx \right. \\
&\quad \left. - \int_0^\infty \frac{e^{-(2^{C_3} B + D)x}}{x + C} dx \right] - 2^{-C_3} e^{-B(2^{C_3} - 1)} \\
&\quad \cdot \frac{AC}{C - G} \left[\frac{1}{C - G} \int_0^\infty \frac{e^{-(2^{C_3} B + D)x}}{x + G} dx \right. \\
&\quad \left. - \frac{1}{C - G} \int_0^\infty \frac{e^{-(2^{C_3} B + D)x}}{x + C} dx \right. \\
&\quad \left. - \int_0^\infty \frac{e^{-(2^{C_3} B + D)x}}{(x + C)^2} dx \right].
\end{aligned} \quad (\text{A.9})$$

It is obvious that the integrals in the last equality of (A.9) have the two following forms:

$$\Psi(a, b) = \int_0^\infty \frac{e^{-ax}}{x + b} dx, \quad (\text{A.10})$$

$$\Phi(a, b) = \int_0^\infty \frac{e^{-ax}}{(x + b)^2} dx. \quad (\text{A.11})$$

The accurate closed form of (A.10) is presented as (37) by changing the variable $y = x + b$ and applying the definition of the exponential integral in [26].

To obtain the accurate closed form of (A.11) as presented in (38), partial integration is firstly implemented in the integral in (A.11) as $\Phi(a, b) = 1/b - a \int_0^\infty e^{-ax}/(x + b) dx$ and, then, one applies (A.10) to transform (A.11) to (38).

By representing the integrals in the last equality of (A.9) in terms of $\Psi(a, b)$ and $\Phi(a, b)$, one can reduce (A.9) to (31). This completes the proof. \square

Data Availability

We declare that all data used to support the findings of this study are included within the article.

Conflicts of Interest

The authors declare that they have no conflicts of interest.

Acknowledgments

This research is funded by Vietnam National University Ho Chi Minh City (VNU-HCM) under grant number B2019-20-01.

References

- [1] Y. Zhang, R. Lu, B. Cao, and Q. Zhang, "Cooperative jamming-based physical-layer security of cooperative cognitive radio networks: system model and enabling techniques," *IET Communications*, vol. 13, no. 5, pp. 539–544, 2019.
- [2] K. Ho-Van and T. Do-Dac, "Impact of primary interference on secrecy performance of physical layer security in cognitive radio networks," *Wireless Personal Communications*, vol. 100, no. 3, pp. 1099–1127, 2018.
- [3] H. Tran, T. X. Quach, H.-V. Tran, and E. Uhlemann, "Optimal energy harvesting time and power allocation policy in crn under security constraints from eavesdroppers," in *Proceedings of the 28th Annual IEEE International Symposium on Personal, Indoor and Mobile Radio Communications, PIMRC 2017*, pp. 1–8, Canada, October 2017.
- [4] B. R. Manoj, R. K. Mallik, M. R. Bhatnagar, and S. Gautam, "Virtual full-duplex relaying in multi-hop DF cooperative networks using half-duplex relays with buffers," *IET Communications*, vol. 13, no. 5, pp. 489–495, 2019.
- [5] L. Ni, X. Da, H. Hu, Y. Huang, R. Xu, and M. Zhang, "Outage constrained robust transmit design for secure cognitive radio with practical energy harvesting," *IEEE Access*, vol. 6, pp. 71444–71454, 2018.
- [6] C. Li, J. Wang, and M. Li, "Spatiotemporal compression-transmission strategies for energy-harvesting wireless sensor networks," *IET Communications*, vol. 13, no. 5, pp. 630–636, 2019.
- [7] A. D. Wyner, "The wire-tap channel," *Bell Labs Technical Journal*, vol. 54, no. 8, pp. 1355–1387, 1975.
- [8] F. Zhou, Z. Chu, H. Sun, R. Q. Hu, and L. Hanzo, "Artificial noise aided secure cognitive beamforming for cooperative MISO-NOMA using SWIPT," *IEEE Journal on Selected Areas in Communications*, vol. 36, no. 4, pp. 918–931, 2018.
- [9] J. Qiao, H. Zhang, F. Zhao, and D. Yuan, "Secure transmission and self-energy recycling with partial eavesdropper CSI," *IEEE Journal on Selected Areas in Communications*, vol. 36, no. 7, pp. 1531–1543, 2018.
- [10] K. Khalil and M. S. Khan, "Futiling eavesdropping in harvested energy powered cognitive radio networks under secrecy constraints and multi slot spectrum sensing schedule," in *Proceedings of the 2018 International Conference on Computing, Mathematics and Engineering Technologies (iCoMET)*, pp. 1–6, Sukkur, Pakistan, March 2018.
- [11] R. Su, Y. Wang, and R. Sun, "Destination-assisted jamming for physical-layer security in SWIPT cognitive radio systems," in *Proceedings of the 2018 IEEE Wireless Communications and Networking Conference (WCNC)*, pp. 1–6, Barcelona, Spain, April 2018.
- [12] X. Chen, L. Guo, X. Li, C. Dong, J. Lin, and P. T. Mathiopoulos, "Secrecy rate optimization for cooperative cognitive radio networks aided by a wireless energy harvesting jammer," *IEEE Access*, vol. 6, pp. 34127–34134, 2018.
- [13] F. Zhou, Z. Chu, H. Sun, and V. C. Leung, "Resource allocation for secure MISO-NOMA cognitive radios relying on SWIPT," in *Proceedings of the 2018 IEEE International Conference on Communications (ICC 2018)*, pp. 1–6, Kansas City, MO, USA, May 2018.
- [14] S. Raghuvanshi, P. Maji, S. D. Roy, and S. Kundu, "Secrecy performance of a dual hop cognitive relay network with an energy harvesting relay," in *Proceedings of the 2016 International Conference on Advances in Computing, Communications and Informatics (ICACCI)*, pp. 1622–1627, Jaipur, India, September 2016.
- [15] F. P. Benedict, P. Maji, S. D. Roy, and S. Kundu, "Secrecy analysis of a Cognitive Radio Network with an energy harvesting AF relay," in *Proceedings of the 2017 International Conference on Wireless Communications, Signal Processing and Networking (WiSPNET)*, pp. 1358–1363, Chennai, India, March 2017.
- [16] P. Maji, S. D. Roy, and S. Kundu, "Physical layer security in cognitive radio network with energy harvesting relay and jamming in the presence of direct link," *IET Communications*, vol. 12, no. 11, pp. 1389–1395, 2018.
- [17] P. Maji, B. Prasad, S. D. Roy, and S. Kundu, "Secrecy outage of a cognitive radio network with selection of energy harvesting relay and imperfect CSI," *Wireless Personal Communications*, vol. 100, no. 2, pp. 571–586, 2018.
- [18] T. D. Hieu, T. T. Duy, and S. G. Choi, "Performance enhancement for harvest-to-transmit cognitive multi-hop networks with best path selection method under presence of eavesdropper," in *Proceedings of the 2018 20th International Conference on Advanced Communications Technology (ICACT)*, pp. 323–328, Chuncheon-si Gangwon-do, South Korea, February 2018.
- [19] X. Zhang, J. Xing, Z. Yan, Y. Gao, and W. Wang, "Outage performance study of cognitive relay networks with imperfect channel knowledge," *IEEE Communications Letters*, vol. 17, no. 1, pp. 27–30, 2013.
- [20] M. Seyfi, S. Muhaidat, and J. Liang, "Relay selection in cognitive radio networks with interference constraints," *IET Communications*, vol. 7, no. 10, pp. 922–930, 2013.
- [21] K. Ho-Van, "Influence of channel information imperfection on outage probability of cooperative cognitive networks with partial relay selection," *Wireless Personal Communications*, vol. 94, no. 4, pp. 3285–3302, 2017.
- [22] X. Zhou, R. Zhang, and C. K. Ho, "Wireless information and power transfer: architecture design and rate-energy tradeoff," *IEEE Transactions on Communications*, vol. 61, no. 11, pp. 4754–4761, 2013.
- [23] A. A. Nasir, X. Zhou, S. Durrani, and R. A. Kennedy, "Relaying protocols for wireless energy harvesting and information processing," *IEEE Transactions on Wireless Communications*, vol. 12, no. 7, pp. 3622–3636, 2013.
- [24] E. Biglieri, J. Proakis, and S. Shamai, "Fading channels: information-theoretic and communications aspects," *Institute of Electrical and Electronics Engineers Transactions on Information Theory*, vol. 44, no. 6, pp. 2619–2692, 1998.

- [25] K. Ho-Van, "Outage analysis of opportunistic relay selection in underlay cooperative cognitive networks under general operation conditions," *IEEE Transactions on Vehicular Technology*, vol. 65, no. 10, pp. 8145–8154, 2016.
- [26] I. S. Gradshteyn and I. M. Ryzhik, *Table of Integrals, Series and Products*, Academic Press, San Diego, Calif, USA, 6 edition, 2000.
- [27] Y. Zou, X. Wang, and W. Shen, "Physical-layer security with multiuser scheduling in cognitive radio networks," *IEEE Transactions on Communications*, vol. 61, no. 12, pp. 5103–5113, 2013.

Research Article

EEHRT: Energy Efficient Technique for Handling Redundant Traffic in Zone-Based Routing for Wireless Sensor Networks

Rab Nawaz Jadoon ^{1,2}, WuYang Zhou ¹, Iftikhar Ahmed Khan,²
Muhammad Amir Khan ³, and Waqas Jadoon²

¹School of Information Science and Technology, University of Science and Technology of China, Hefei 230000, China

²Department of Computer Science, COMSATS University, Islamabad-Abbottabad Campus 22060, Pakistan

³Department of Electrical Engineering, COMSATS University, Islamabad-Abbottabad Campus 22060, Pakistan

Correspondence should be addressed to WuYang Zhou; wyzhou@ustc.edu.cn

Received 11 February 2019; Accepted 9 April 2019; Published 6 May 2019

Guest Editor: Bojan Dimitrijevic

Copyright © 2019 Rab Nawaz Jadoon et al. This is an open access article distributed under the Creative Commons Attribution License, which permits unrestricted use, distribution, and reproduction in any medium, provided the original work is properly cited.

This paper presents an energy-efficient technique to handle redundant traffic (EEHRT) in the zone-based routing for wireless sensor networks. In this technique, multihop routing is performed based on the remaining energy of the nodes. Afterwards, it performs position-based routing without the need for the nodes to know their respective position. The main objective of this paper is to handle the redundant packets generated in zone-based routing using short beacon messages. Nodes of lower zones route the data of the higher zone to base station (BS) with a minimum number of hops and utilize only those nodes on the path which are energy efficient and located closer to BS. Moreover, the source node is acknowledged by the relaying node using a wireless broadcast advantage (WBA) without sending any special ACK packet to the sender, which reduces the control overhead in the routing process. The EEHRT technique improves the routing against RARZ by ensuring only one copy of the packet is propagated at each hop along the routing path to BS. Simulation results show that EEHRT achieved 28% improvement in energy efficiency, 10% and 25% improvements in data throughput against total and distinct packet reception at BS respectively, 35% increase in overall network lifetime, and 100% reduction in redundant packets generation and propagation in the network against RARZ routing.

1. Introduction

Wireless sensor networks are used to monitor the terrain either reachable or unreachable to human beings. A sensor node in the network can sense, process, and deliver data to its neighboring nodes or to the base station (BS), i.e., sink node either directly or in multihop fashion [1–4], etc. These types of networks are resource constraint in terms of memory, processing, bandwidth, and node residual battery (energy). After deployment, it is almost impossible in some cases in certain environments to charge or replace the battery upon depletion.

For physically remote and hostile environments, this is now a possibility through new emerging concept of sensor technology which monitors the physical phenomenon of

interest. Sensor nodes are able to gather, manipulate, and transmit data to an ultimate destination with energy efficient data delivery techniques [5]. To extend the overall network lifetime of the nodes, the network should consume less energy for sensing, processing, and transceiving. Currently, researchers are working to develop efficient protocols which are lightweight, scalable, and energy efficient and does position-based routing without using any location service or GPS assumption.

In this paper, we have proposed a new protocol called EEHRT which handles the redundant packets generated especially when the next hop relaying node is not reachable to its neighboring node. The implementation condition is that this node is also contending to become the next hope node [6]. The next hop node is selected based on a timer which is a

function of node residual energy and its closest location, i.e., zoneID.

According to RARZ, if a node has outstanding data to send, it first senses the channel. If the channel is available, then it broadcasts its data with its network ID (zoneID). All the nodes located in the same zone share the same zoneID, i.e., the network address. Nodes having lower zoneID will receive and schedule the packet for further relaying. Higher energy nodes having lower zoneID will become the potential next hop nodes. When the next hop node further relays the data, the nodes that hear that packet will kill their timer and drop the scheduled packet. The nodes that are not in the range of the relaying node will send the same packet again upon expiry of their timer, so multiple copies of the same packet are routed to BS, which ultimately degrade the overall network lifetime and throughput. This work aims to remove the probability of redundant packets generated in RARZ routing [6] and to enhance the overall throughput and network lifetime.

EEHRT is different from RARZ with the following points:

- (i) EEHRT controls the redundant packets by introducing short beacon message in the routing algorithm.
- (ii) EEHRT ensures distinct packet delivery at every hop on the path to BS.
- (iii) The acknowledgment is handled in the EEHRT using WBA (wireless broadcast advantage) without considering a separate special ACK packet to the sender at each hop along the routing path.

When a node in the lower zone further relays this message, the same copy of the message is also received by the sender node using the benefit of a wireless broadcast. This technique is also called a wireless broadcast advantage (WBA). Once this message is correctly received by the source node, a short beacon message is exchanged to the next hop nodes by the sender node. The short message should have the following properties: (1) it should have message type 3 and (2) should have the same packet sequence number and zoneID. The short beacon message is targeted for those nodes who could not hear the relaying node packet. This packet is the same for which they are still waiting to transmit it, i.e., their timer not elapsed yet. Upon receiving this small beacon message, the nodes will delete the schedule packet and kill their timer. In this way only one copy of the data will be routed to the BS and sender is also acknowledged that its packet is relayed further.

The rest of the paper is organized as follows: related work and problem statement are described in Section 2 and Section 3, respectively. EEHRT technique is presented in detail in Section 4 and simulation results are presented in Section 5. The paper is concluded in Section 6.

2. Related Work

The researcher has contributed a lot to energy efficiency especially in sensor networks. Every routing protocol developed in the sensor networks considered energy efficiency because it overall affects the lifespan of the network. A lot of energy efficient routing techniques have been developed in the past

for wireless sensor networks longevity. Despite all the routing categories in WSN, hierarchical routing techniques are considered more energy efficient and scalable as compared to rest of the techniques because only the aggregated data is transmitted through high-level energy nodes to BS [7] with few numbers of transmissions.

Hierarchical protocols are also called cluster-based protocols. In cluster-based routing, the sensing region is divided into different regions called cluster, and each region has one designated cluster head (CH). CH gathers data from all its associated nodes and transmits the aggregated data to BS [8]. CH selection is an important mechanism which may be either distributed or centralized. In the centralized method, BS has the responsibility to setup clusters and CHs selection based on nodes remaining energy and location information [9–11] whereas, in distributed techniques, nodes organized themselves to form clusters without the control of a central authority. There are three types of clustering, static, dynamic, and hybrid.

In static clustering, once the clusters are formed, they will never be changed till the end of the network. In the case of dynamic clustering, there are two phases, setup, and steady-state phase. In the setup phase, each node sends its energy and location information to the BS. After getting this information from all the nodes in the network, BS will select the optimal number of clusters and CHs and intimate this information to all the nodes in the sensing region. At the end of the setup phase, the steady-state phase begins which is also called a data communication phase. In this phase, nodes send their data sensed data to designated CH and then CH is responsible for onward transmission to BS [5–8]. Hybrid techniques utilized both the mechanism of static and dynamic clustering at the same time.

A lot of energy efficient routing protocols have been developed in the recent past. LEACH (Low Energy Adaptive Clustering Hierarchy) [1] is a hierarchical protocol which sets a benchmark for the researchers to develop energy efficient techniques in cluster-based routing to prolong the network lifetime.

The work described in [12] is Power-Efficient Gathering in Sensor Information Systems (PEGASIS) called a chain-based protocol in which a chain of nodes having one leader is elected to send the data to BS. It outperforms LEACH in terms of an overall network lifetime.

Work described in [13] implemented a hybrid approach by incorporating data aggregation [7], energy awareness, and clustering into one algorithm. It greatly enhances the overall longevity of the network. After each round of communication new CHs is selected. Data is aggregated to achieve energy efficiency and long distances are handled using optimal multihop routing.

An energy and context-aware routing-based technique on clustering is presented in [10, 14] for the sensor networks. Based on routing protocols, a comprehensive comparison of sensor networks and MANET (mobile ad hoc networks) is presented in [15]. This qualitative comparison exposes new areas of research for developing new energy efficient routing protocols, especially for WSNs.

In normal clustering techniques, the arrangement of the nodes is fixed [7]. The new research implemented the clustering in an ad hoc fashion in [6, 11]. Work presented in [10] is a connected cluster architecture, where all nodes are like sensor nodes; CHs and gateways are treated in the same node of the network. The CH worked as a central control node, while the gateway node acts as a backbone to transmit the data to different users.

A similar network setup scheme is adopted as done in [6, 16], in which nodes are organized in a sensing region into equal size clusters. Cluster-based routing is used for prolonging the network lifetime. Authors claim that the network lifetime is extended by balancing the energy consumption among all the cluster heads in the network.

As sensor nodes are equipped built-in battery-powered and hence their lifespans are short, the researcher gave keen attention to these issues in almost every protocol developed at every layer of the protocol stack. To further enhance the network lifetime and conserve energy, a data query dissemination and gathering scheme is presented in [2]. In this work, the authors gave the concept of the parameterized query based on the user's profile to get the required data from the sensor nodes. The scheme is proven to be the most energy efficient as compared to the rest of the techniques of a similar domain.

A novel zone-based scheme is implemented in [16], which is energy-efficient and edge-based network apportioning technique, that organizes nodes into equal size clusters. It also proposed a cluster-based routing algorithm, called zone-based routing protocol (ZBRP), for prolonging network lifetime. BS divided the whole network into different equal size zones around the BS. Authors proved through simulation results that they equally balance the energy consumption among all the CHs in the network, hence extended the overall network lifetime.

A lot of work has also been investigated on energy-aware routing. A similar sort of work is done in [17], in which they utilize an energy-aware technique with static clustering called centralized control clustering (EACCC) to achieve energy efficiency and greater lifespan of the network along with network scalability as well. The performance of the EACCC is accessed through extensive analytical proofs and simulation and showed that EACCC is highly efficient in terms of balancing the energy consumption and prolonging network lifetime.

The work in [11] is based on hybrid clustering. According to this scheme, clusters are static and never changed up to 10 rounds. BS is responsible for the selection of next phase CHs. If the round number is less than 10, the current CH selects the new utmost energy level node as a CH and intimates its status to BS. After round number 10, all the nodes send their energy status and location information to the BS and BS will setup new clusters for the next time.

There are cases in which the environment is monitored periodically. In periodic monitoring applications, building protocols of such type are a challenging task. A handsome work to cater to such issues is done in [3], in which the authors worked in the two domains. The first is to make the protocol energy efficient and then provide a comprehensive

mechanism for energy load balancing using distributed antenna theory.

An energy saving architecture for wireless sensor networks is presented in [18], in which biography-based optimization (BBO) is adapted which is a new paradigm to optimized complex problems. Optimal cluster head selection and routing are considered more complex problems in wireless sensor networks. Authors proposed BBO based cluster head selection algorithm having an efficient encoding scheme based on residual energy and distance as its metrics. Simulation results show that BERA (BBO based routing architecture) outperforms the existing routing architecture in terms of energy efficiency and communication overhead.

Along with energy efficiency, secure data communication is also needed during transmission either transmission from node to node or from node to BS. A virtual backbone is created for energy efficient intercluster routing. Signcryption technique is used for secure data transmission in the network. Energy efficient secure cluster-based routing is performed in [4] and compared with LEACH and hence showed that the proposed scheme can save 2720nJ/bit/m² energy in one round of communication along with security than LEACH protocol.

For reliable data delivery of the packets to BS, authors handle the reliability issue by incorporating trust model in Cluster Algorithm for Sink Selection (CASS) scheme [19] to assure the reliability with the minimum overhead of maintenance to extend the overall network lifetime. Simulations results show that CASS with trust model greatly reduces the packet loss in the presence of unreliable nodes while extending the network lifetime by deploying multiple sinks.

Routing is considered the most energy consumptive process in sensor networks. Improving the routing in sensor networks researcher has contributed a lot to minimize the overhead of unwanted packets in the network. In [20], state free geographic forwarding protocol is proposed which is a cross-layer designed for minimizing the energy consumption. All the protocols developed in the past under SGF utilized Distributed Coordination Function MAC protocol of 802.11 for routing because it deals well with the hidden terminal problem using four-way handshaking. This creates an overhead in terms of end to end delay and energy consumption in the network. To handle these issues, a directional compact Geographic Forwarding (DCGF) protocol [20] is proposed which mitigated the overhead incurred in four-way handshaking in multihop networks. It uses a smart antenna and QoS aware data aggregation approach to handle the broadcast data received and multiple unicast traffic, respectively.

Despite all these efforts, there is still the requirement in contributing to energy efficiency and to increase the overall network lifetime of the sensor networks. All the protocols discussed above use a lot of control information along with actual data sensing and transmission, but our focus is to develop a protocol which has low control overhead to make the routing energy efficient, lightweight, and reliable [6]. Moreover controlling the unwanted traffic in the network increases the network lifetime.

2.1. A Brief Overview of RARZ Routing. In our early study presented in [6], the routing strategy is more energy efficient but, in some specific scenario, it generated redundant packets in the network which ultimately waste some scarce resources and affect the overall throughput and network lifetime. The routing strategies that were used in [6] is as follows.

RARZ works in three phases: network setup and configuration phase, the next hop node selection phase, and data communication phase. The network configuration or setup phase splits the whole sensing region into different concentric static rings around the BS. For ring formation, the BS broadcasts messages with various transmission powers to the sensing field. Each message from the BS contains a ring ID and each node, upon first time receiving the message, will set its ring ID to the one contained in the message received. For covering the whole sensing field, the BS progressively broadcasts messages with various communication ranges comprising different ring IDs. Each node, upon receiving a ring i message from BS, recognizes that the latter belongs to ring i unless they have already set a ring with lower ring ID. All the nodes in a particular ring have the same ring ID (i.e., network address). At the end of this phase, the route discovery process is formulated that nodes belonging to the smallest ring will relay the packet to the BS and any other node in the same ring and nodes located in the higher ring will discard the packets.

The main work done in RARZ protocol is the next hope selection phase. According to RARZ, the next hop node is also called a relaying node that is selected on the fly without considering any prior information available in the network. Selection is purely done based on its residual energy and the zone in which it is located. A node having high energy and lower zone ID has the highest probability to become the next ultimate relaying node. Only the lower zone nodes can carry the data of the higher zones to BS. Same and higher zone nodes will delete the packet after receiving at the MAC layer. The node whose timer expired first will become the potential next hope node. Once the relaying node sends the data further, the nodes located in its radio range will cancel their timer and delete the packet for which they have already running timer. In RARZ the timer is a function of node residual energy and node current location Z_ID , i.e., zoneID,

$$Timer = \alpha * Z_ID + \beta \left[\frac{\eta}{\mu} \right] \quad (1)$$

α and β are weighted values against node current location and its residual energy, respectively. The values of α and β are the tuning parameters set in simulations according to Table 1 for efficient and normalized setup of data routing. The parameter η is the initial energy level and μ is the current energy level of a node at any particular time. As residual energy appears in the denominator, the higher the node current energy level is, the lower the time value will be and vice versa. The timer returns values in a millisecond. In (1) Z_ID (zoneID) played an important role in routing because some of the nodes are immediate to next ring, so that node should be selected as a next hop node. This is because one hop will be reduced and the average energy consumption in the system will also be minimized.

Figure 1 shows the graphical demonstration of the RARZ routing scheme. Three nodes (B, C, and D) are in zone 3 and are directly in the radio range of A. Once the node A broadcast its data, nodes in zone 3 will setup their timer as per (1). Node B's timer expired first because its energy level is high as compared to node D and C. When node B further relays the packet, neighboring node of B (i.e., C, D, E, and F) will also receive that message and nodes C and D will kill their timer and delete the packet for which they have currently running timer for the same packet sent by B.

Node E and F from zone 2 will now start their timer after getting the message from node B as they both are located in zone 2. Node F will become the next potential hop node due to its high energy as compared to E, so it further relays the packet. Through this way, the packet is routed to BS without any reactive mechanism in the routing procedure. On the path, only those nodes are selected which are energy efficient and located near to BS.

3. Problem Statement

In [6], whenever a node acts as a relaying node, there are some nodes that could not hear the data of the relaying node. The nodes that could not hear the relaying node packet will also relay the same packet further upon their timer expiration. This will create redundant packets in the network, i.e., multiple copies of the same packet are transmitted in the network, hence degrading the network resources and affecting overall network lifetime.

Figure 2 shows how the duplicate packets are generated in the network in RARZ routing [6]. Upon receiving the data from node A in zone 4, node B and C in zone 3 schedule their timer according to (1) and become the next potential hope node to route the received packet to BS. According to the scenario presented, the timer of node B will be expired first. When node B further relays the packet, node C could not hear that packet, so upon timer expiration of node C, it will also relay the same packet that is already sent by node B. In this way the duplicate packet is routed to BS resulting in degrading network lifetime.

4. EEHRT (Energy Efficient Technique for Handling Redundant Traffic) in Zone-Based Routing

EEHRT tackles the above scenario as follows. When node A sends its data, it adds the packet ID and zone ID in its buffer called "sent queue". When node B becomes the next hop node and relays the received packet after updating its zoneID to 3, node A will also get the packet sent by node B with zoneID 3. Afterward, A will compare the received packet ID and its zone ID to its sent queue values. This is an intimation for node A that the packet is successfully sent by a node from the lower zone. After that, it will send a small beacon message immediately in its vicinity so that the nodes with active timers who could not hear the packet sent by B due to out of the radio range of B could kill their timers and drop the scheduled packet. After sending the short beacon

TABLE I: Simulation setup.

Serial #	Type	Parameters	Values
1	Network	Sensing region	$600 \times 600 \text{ m}^2$
		Node initial energy	3000 mJ/battery (Random $2.8J \sim 3J$)
		Deployment	Random
		Number of Zones	10
		Node Transmission Range	100m
		Distance between zones	50m
2	Application	Data Packet	100 bytes
		Broadcast packet	25 bytes
		Packet header	25 bytes
		Beacon packet	15 bytes
		Carrier frequency	$2.4 \text{ e}^+ 9$
		NAV	8 bits
		Zone ID	4 bits
		Node ID	4 bits
3	Timer values	MAC protocol	CSMA/CA (DCF)
		t_g (Guard time)	$50 \mu\text{s}$
		t_l (Listening time)	$500 \mu\text{s}$
		t_b (Back-off time)	$500 \mu\text{s}$
		(α, β)	(0.003, 0.001)

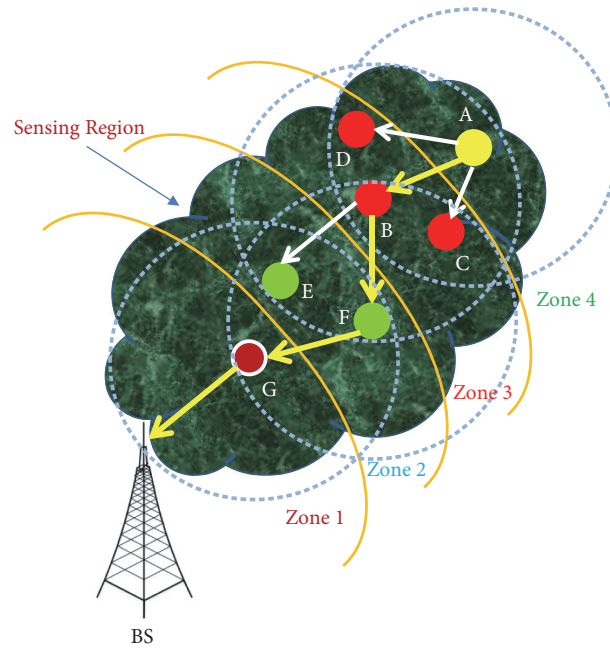


FIGURE 1: The selection of next hop node.

message by node A, it then clears its buffer. In this way, the sent packet acknowledgment is also received. Furthermore, confirmation is sent to those nodes that are located outside the radio range of the relaying node to kill their timers and delete the packets for further relaying. Through this way, the RARZ routing is improved by eliminating the probability of the duplicate packets generated in the network.

4.1. Network Model. We have assumed the same network configuration as used in [6, 9] with the following assumptions:

- (1) All nodes are static w.r.t their position, i.e., immobile.
- (2) BS position is flexible and can be setup either inside or outside the sensing region.

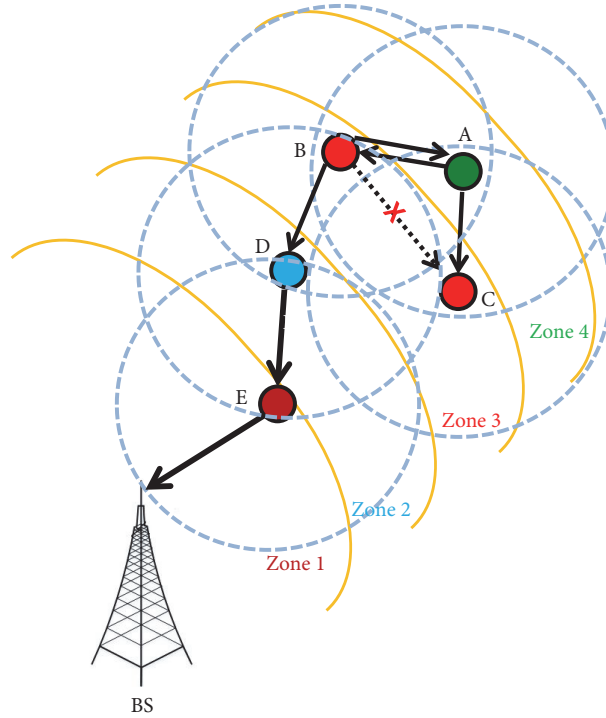


FIGURE 2: Redundant packet generation scenario.

- (3) In a specified timeslot, each node can send its data to BS.
- (4) All the nodes in the network are homogenous in nature with limited battery.
- (5) The data sampling rate is fixed.

4.2. *EEHRT Algorithmic Description.* See Algorithm 1.

4.3. *Message Types.* We have defined different type of messages in our protocol. Detail and parameter value's description is presented in Figure 3.

4.4. *How EEHRT Works?* In EEHRT a node may not always be in listening state. A node may listen till it detects an event or has data of other nodes to relay it to BS. Moreover, for power saving, NAV (Network Allocation Vector) based virtual channel sensing technique is used for medium sensing and channel reservation for the current duration of the data transmission. The virtual carrier-sensing is a logical concept which does not let nodes sense the channel physically at the air interface to conserve node battery. The NAV field specifies the transmission time required for the frame, in which time the medium will be busy.

In EEHRT the receiver node is not predetermined, which contrasts with 802.11 standards. Hence, there is an additional random backoff time t_b required to ensure that potential relaying nodes in the lower zone will not collide upon their timer expiration.

In EEHRT, we give a random ID to each node in the network. Every time a node sends or relays the data, it will

choose a newly generated ID as an originator ID, but the message sequence number remains the same. This greatly reduces the chance of sensor nodes in the locality choosing same identifiers and then steadily colliding.

Whenever a node has outstanding data to transmit, the node attempts to find an ultimate next hop node located in the lower zone or immediate to next zone having high energy, which could relay its data. This is in contrast with IEEE 802.11 where a node attempts to transmit to a node as decided beforehand by the routing algorithm. In EEHRT source node does not need to discover the neighbors for data transmission. Among the ultimate neighbors of the sender, one node is selected on the fly as a next hop node that is energy efficient and located closer to BS as compared to rest of the neighbors without any prior routing, energy and location information. We used the same routing strategy as used in [6] except some changes to handle the duplicate message created in RARZ routing. This is the main change done in our protocol to make the routing lightweight (i.e., less routing control overhead). This is done based on location and energy efficiency routing in which nodes do not need to know their respective position as well as any prior information for neighbor or route discovery mechanism.

The node that has data to send or relay the received packet on its timer expiration waits for a guard time t_g before attempting to transmit its data. Upon t_g expiration or freeing event of the channel, the node further waits for time t_l (listening time) before transmitting. The guard time t_g is used to ensure that the channel status should be either busy or idle. The additional random listening time t_l is to ensure that nodes do not transmit at the same time to avoid a collision

```

Begin
Set MsgSeqNo  $\leftarrow$  0
Set SzoneID  $\leftarrow$  -1
Set SMsgType  $\leftarrow$  -1
For each node's Schedule MSG
Set MsgType  $\leftarrow$  0
  If Msg  $\leftarrow$  OwnMsg then
    Set MsgType  $\leftarrow$  1
    Waits for a guard time  $t_g$  // After the guard time expires or when the channel becomes free, then
    Waits for a random listening time  $t_l$  // Wait for time  $t_l$  before the actual transmission
    BroadCast Msg
    Add zoneID, MsgSeqNo and MsgType into buffer
  End if
  If MsgType  $\leftarrow$  1 or 2 and Node  $\leftarrow$  BS then
    Set RecvPCKT  $\leftarrow$  RecvPCKT + 1
    Drop Msg
  Else
    If MsgScheduled == RcvMsgSeqNo then
      If Recv_zoneID < SzoneID and MsgType > = SMsgtype //SMsgType is the buffered value of MsgType
      and SzoneID is buffered/stored zoneID
      Set SeqNo  $\leftarrow$  MsgRcvSeqNo
      Set zoneID  $\leftarrow$  SzoneID
      Set MsgType  $\leftarrow$  3
      BroadCast Beacon //Broadcast Beacon message
      CANCEL Event
      Drop Msg
      Reset buffer to initial value
    Else
      If RcvPCKT_zoneID < = ZoneID then
        Drop Msg
      Else
        Schedule Msg for relaying by adding its own zoneID
        Set MsgType  $\leftarrow$  2
      End if
    End if
  If zoneID==RecvZoneID and SeqNo==MsgRcvSeqNo and MsgType == 3
  Kill timer
  Drop Msg
  Reset the buffer
  End if
End while
End

```

ALGORITHM 1: Pseudocode for EEHRT routing strategy.

which increases the data losses and greatly affects the network throughput.

The next hop node avoids contention with other potential next hop nodes in its vicinity by immediately choosing a random backoff time t_b and listening to the channel for sending a packet with the same sequence number. After that, it relays the received packet further with its own zoneID and with a message type 2. This again is in contrast with 802.11 where there is only one receiver node determined by the routing algorithm. This does not need any contention between potential receiver nodes. However, in EEHRT multiple receivers in the lower zones contend to become the ultimate potential next hop node. The EEHRT mechanism is based on random access and based closely to 802.11. In waiting period t_l , if next hop node hears the same packet

with the same sequence number with the correct zoneID and message type from another next hop node or beacon from the source node, it will immediately kill its timer, delete the schedule packet, and immediately go back into the listener state.

If the message is received successfully by another node with a lower zoneID (which we call the next hop nodes), then one of the receiving nodes in the lower zone relays the received packet once its timer expired. The source node will also hear that packet because it is in the vicinity of the relaying node. The source node upon receiving the message with the same sequence number and lower zoneID will know that a node in the lower zone has relayed its data further. This is an acknowledgment (ACK) for the sender node. This is not a special ACK message but a copy of the lower zone

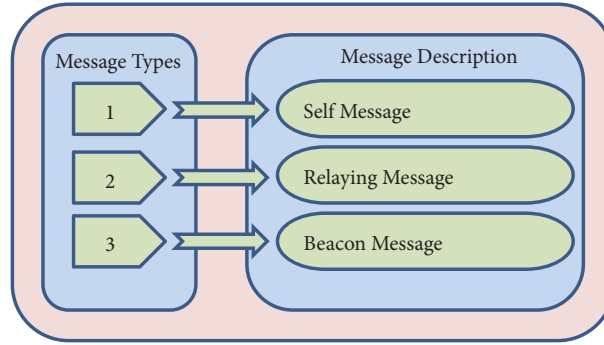


FIGURE 3: Messages types defined in the simulation.

node relayed message which is received by the sender node using the benefit of the wireless broadcast. This technique is also called wireless broadcast advantage (WBA). Once this message is correctly received by the source node, a short beacon message with message type 3 with the same packet sequence number and zoneID is quickly exchanged among the next hop nodes by the sender node. This message is for those nodes who could not hear the relaying node packet. This is the same packet for which they are still waiting to transmit it, i.e., their timer not elapsed yet. Upon receiving this small beacon message, they will kill their timer and delete the schedule packet and again go back to the listening state. In this way, the only one copy of the data at each hop along the routing path will be transmitted to the BS.

In EEHRT, once the sender node could not receive or hear its packet from the lower zone node, this means that there is no node in its vicinity (i.e., in lower zone) to further relays its data. If it could not hear an ACK from the lower zone, it will no more participate in the communication process and will be considered dead. In our simulation setup, we have not observed any situation where there is an isolation of a region in the network at the time of node deployment, i.e., the network topology is assumed completely dense in the proposed technique. There is no need of the rebroadcast packets as per the routing scheme used in EEHRT. When the sender did not receive the same packet from the lower zone node, this situation may happen especially when the network is almost near to depletion stage, i.e., when most of the nodes may deplete their energy, create holes, and make the network sparse. This may occur only once when the last rounds of communications in the network are in progress.

4.5. EEHRT Routing Illustration. The EEHRT routing process is illustrated graphically in Figure 4.

- (a) Node S broadcasts its packet once the channel becomes free. Nodes in zone 2 will receive the packet and schedule it according to (1).
- (b) Nodes in zone 2 will receive the packet and scheduled it according to (1).
- (c) Node A will become the potential next hop node according to (1). When node A further relays the packet, node S will receive the packet, but node B will

not receive it because it is out of the radio range of node A.

- (d) After getting the packet from node A, node S will immediately broadcast a short beacon message with same packet ID and its own zone ID with MsgType 3.
- (e) As node B is in the radio range of S, once it hears the beacon from the node S, it will cancel its timer and remove the packet from its buffer

Through this way, the redundant packets generated in the network are handled and only one copy of each packet is routed to BS. This technique totally removes the redundant packets from the network and ensures reliable data delivery in the network without any extra control overhead using WBA technique.

5. Simulation and Results

5.1. Energy Model. We have used the same energy consumption model in EEHRT as used in [1, 6, 7, 9, 14].

5.2. Simulation Setup. EEHRT scheme is implemented and evaluated in OMNET++, INET simulation Framework. Simulation parameters and their values are defined in Table 1.

Following parameters are defined in the simulation to assess the performance of the EEHRT routing scheme:

- (a) Measuring duplicate packets reception at BS.
- (b) Measuring unique packets reception at BS.
- (c) Calculating network lifetime (i.e., no. of nodes alive over time).
- (d) Average energy consumption in the system over time.
- (e) Throughput (no. of messages successfully received at BS)

Figure 5 shows a total number of packets successfully received at BS in both RARZ and EEHRT. It is clearly depicted from the results that EEHRT outperforms RARZ in terms of the total number of messages received at BS and also it removes the probability of the duplicated packets creation in the network.

As EEHRT completely removed the redundant packets generation in the network, only a single copy of each packet is

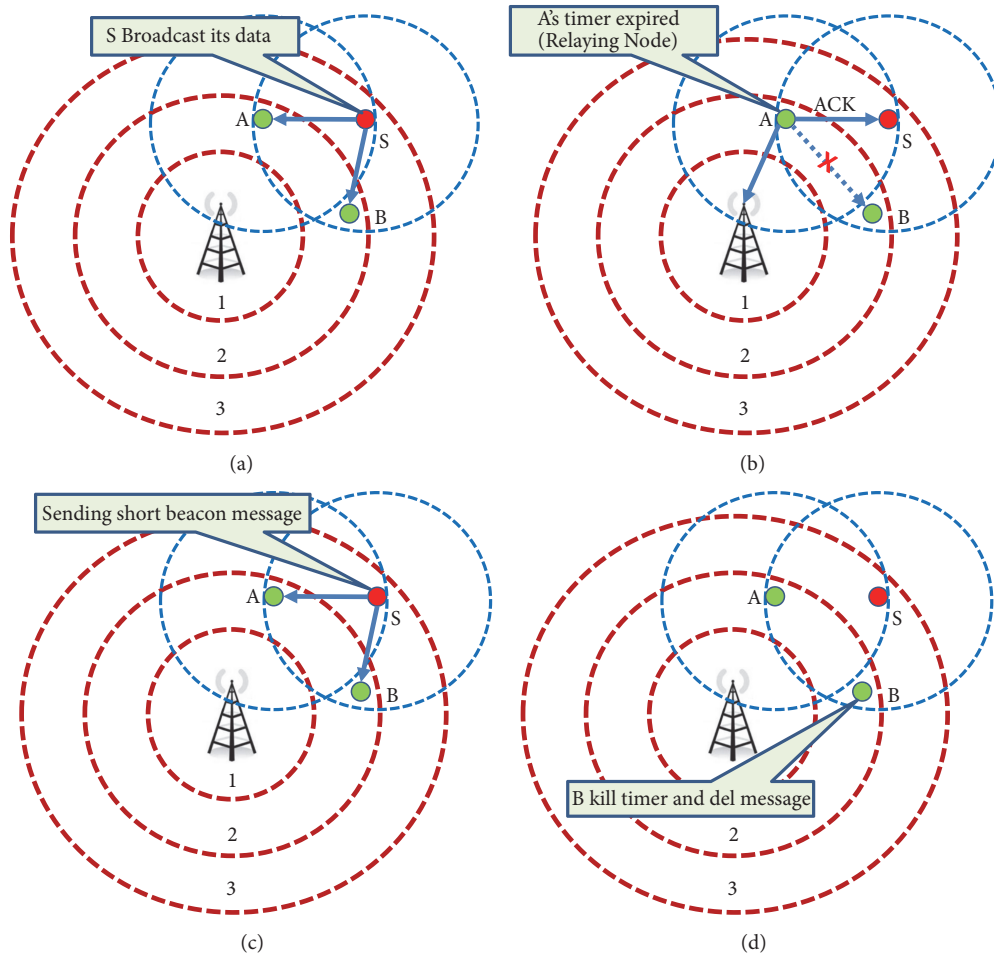


FIGURE 4: EEHRT working mechanism.

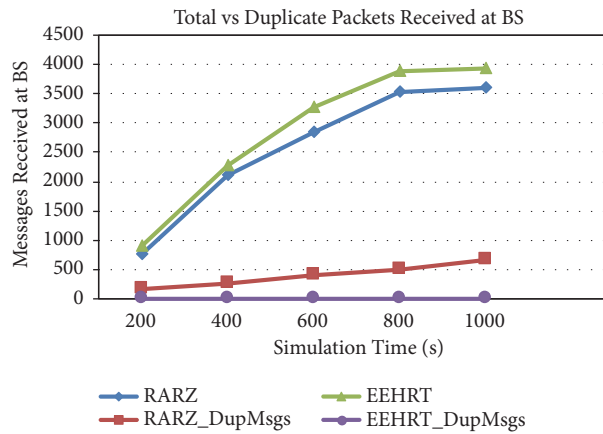


FIGURE 5: Total versus duplicate packet reception at BS.

received at BS. As shown in Figure 6, it is clearly seen that the total number of successfully received packets at BS is equal against the unique packets' reception at BS over time; hence, EEHRT outperforms RARZ in terms of distinct messages received at BS.

As in EEHRT, one short beacon message is introduced in the RARZ algorithm which eliminated the chance of duplicate packets creation in the network. All the redundant packets are removed in the proposed technique which greatly increases the overall network lifetime. Figure 7 shows a

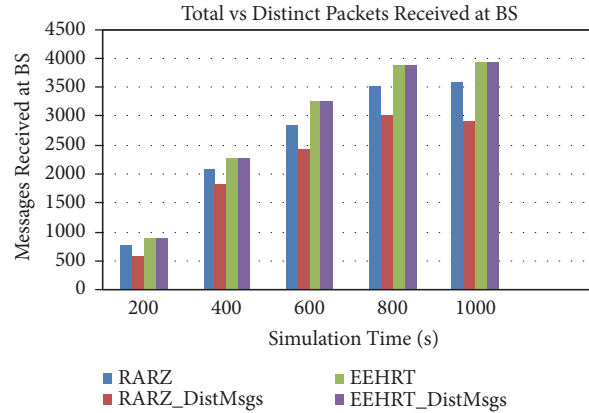


FIGURE 6: Total versus distinct/unique packet reception at BS.

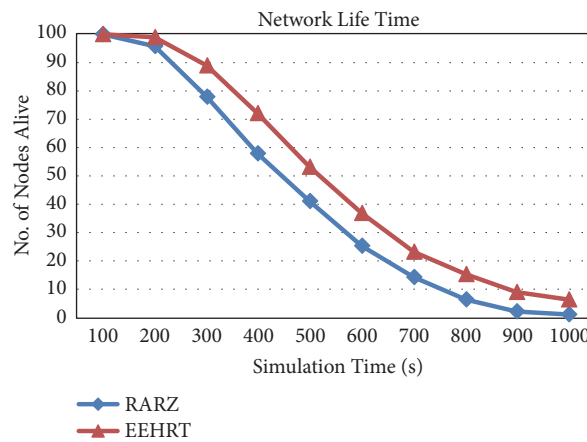


FIGURE 7: No. of nodes alive over time.

tremendous average improvement of 35% in EEHRT against RARZ routing in terms of overall network lifetime. This is because EEHRT, instead of sending multiple copies of the same packet, ensures a distinct copy of each packet received at BS.

The average energy consumption in the system is shown in Figure 8. As mentioned earlier that redundant packets greatly affect the overall network lifetime and other scarce resources like average consumption in the system over time. EEHRT extends the network lifetime by decreasing the energy consumed against the redundant packet's creation and their processing in the network because redundant packets are unwanted traffic which greatly influences the node battery lifetime. As shown in Figure 8, EEHRT outperforms RARZ routing by an improvement of overall 28% of energy efficiency in the network.

The number of data packets successfully received at BS is shown in Figure 9. As per the previous results evaluation, it is generally seen that redundant packets and extra control overhead of ACK packets greatly decrease the overall network lifetime and throughput. As in EEHRT, we removed the concept of duplicate packets creation and their processing in the network. This greatly affects the overall throughput of the network. Figure 9 clearly shows that EEHRT performs better

against RARZ when the total number of messages received at BS is high. An improvement in throughput is seen in a simulation which is 10% high against RARZ routing and 25% improvements against RARZ in unique packet reception at BS.

6. Conclusion

A novel data delivery technique called EEHRT for wireless sensor networks is proposed in this work. It divides the network into static zones by eliminating the control overhead and hence extends the network lifetime. The proposed protocol is a stateless protocol which is completely tableless and nonposition based. Energy efficient nodes in the network are used for data relaying purpose. This results in even distribution of energy consumption and avoids depletion of node's energy in a path. It also ensures distinct data copies of the messages received at the BS by removing the concept of duplicate packets generation in the network. Duplicate packet generation greatly affects the overall network lifetime and data throughput. Moreover, it handles acknowledgment without sending any special ACK packet to the sender by using wireless broadcast advantage (WBA), which significantly reduces the control overhead in the routing process.

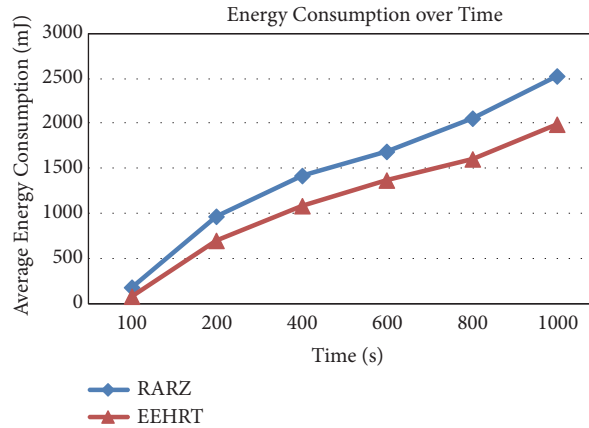


FIGURE 8: Average energy consumption over time.

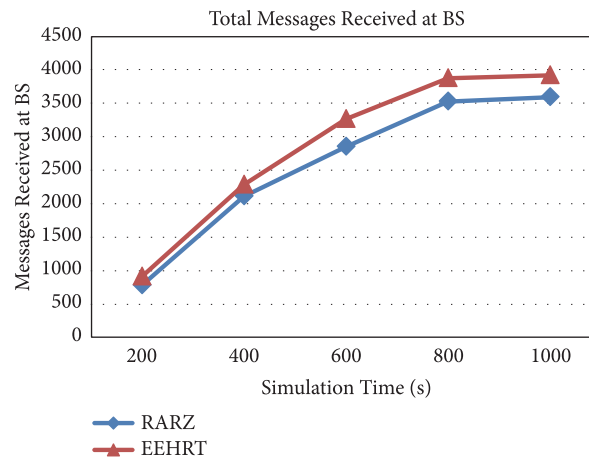


FIGURE 9: Network throughput.

The energy efficiency and ease of deployment make EEHRT a reliable data delivery protocol for wireless sensor networks. Simulation results show that EEHRT achieved 28% improvement in energy efficiency, 35% increase in overall network lifetime, 10% and 25% improvements in data throughput against total and distinct packet reception at BS respectively, and 100% reduction in redundant packets generation and propagation in the network against the RARZ routing.

Data Availability

No data were used to support this study. We have conducted the simulations to evaluate the performance of EEHRT and RARZ protocol. However any query about the research conducted in this paper is highly appreciated and can be asked from the principal author (Rab Nawaz Jadoon) upon request.

Conflicts of Interest

The authors declare no conflicts of interest.

Acknowledgments

We are thankful to CAS-TWAS for supporting this work (CAS-TWAS No. 45, 2016). Also special thanks are due to COMSATS University, Islamabad (Abbottabad Campus), and School of Information Science and Technology, USTC Hefei, China, which fully supported us by providing all key resources during the implementation and all afterward phases of this project. We would also like to personally thank Prof. WuYang Zhou and Dr. Iftikhar Ahmed Khan because of their continuous encouragement and massive support both academically and socially during this project. This work is sponsored by Key Program of National Natural Science Foundation of China (Grant No. 61631018).

References

- [1] W. R. Heinzelman, A. Chandrakasan, and H. Balakrishnan, "Energy-efficient communication protocol for wireless microsensor networks," in *Proceedings of the 33rd Annual Hawaii International Conference on System Sciences (HICSS '00)*, p. 10, IEEE, January 2000.

- [2] M. Guerroumi and A.-S. K. Pathan, "Hybrid data dissemination protocol (HDDP) for wireless sensor networks," *Wireless Networks*, vol. 24, no. 5, pp. 1739–1754, 2018.
- [3] R. E. Mohamed, W. R. Ghanem, A. T. Khalil, M. Elhoseny, M. Sajjad, and M. A. Mohamed, "Energy efficient collaborative proactive routing protocol for Wireless Sensor Network," *Computer Networks*, vol. 142, pp. 154–167, 2018.
- [4] T. Maitra, S. Barman, and D. Giri, "Cluster-based energy-efficient secure routing in wireless sensor networks," in *Information Technology and Applied Mathematics*, vol. 699 of *Advances in Intelligent Systems and Computing*, pp. 23–40, Springer, Singapore, 2019.
- [5] B. Bhushan and G. Sahoo, "Routing protocols in wireless sensor networks," in *Computational Intelligence in Sensor Networks*, vol. 776 of *Studies in Computational Intelligence*, pp. 215–248, Springer, Berlin, Germany, 2019.
- [6] R. N. Jadoon, W. Zhou, W. Jadoon, and I. A. Khan, "RARZ: ring-zone based routing protocol for wireless sensor networks," *Applied Sciences (Switzerland)*, vol. 8, no. 7, article no. 1023, 2018.
- [7] W. B. Heinzelman, A. P. Chandrakasan, and H. Balakrishnan, "An application-specific protocol architecture for wireless microsensor networks," *IEEE Transactions on Wireless Communications*, vol. 1, no. 4, pp. 660–670, 2002.
- [8] J. N. Al-Karaki and A. E. Kamal, "Routing techniques in wireless sensor networks: a survey," *IEEE Wireless Communications Magazine*, vol. 11, no. 6, pp. 6–28, 2004.
- [9] R. Nawaz, S. A. Hussain, S. A. Abid, and J. Shafi, "Beaconless multihop routing protocol for wireless sensor networks," in *Proceedings of the 2011 IEEE 3rd International Conference on Communication Software and Networks, ICCSN 2011*, pp. 721–725, IEEE, May 2011.
- [10] D. J. Baker, A. Ephremides, and J. A. Flynn, "The design and simulation of a mobile radio network with distributed control," *IEEE Journal on Selected Areas in Communications*, vol. 2, no. 1, pp. 226–237, 2003.
- [11] F. Bajaber and I. Awan, "Dynamic/Static Clustering Protocol for Wireless Sensor Network," in *Proceedings of the 2008 Second UKSIM European Symposium on Computer Modeling and Simulation (EMS)*, pp. 524–529, IEEE, Liverpool, UK, September 2008.
- [12] S. Lindsey and C. S. Raghavendra, "PEGASIS: power-efficient gathering in sensor information systems," in *Proceedings of the IEEE Aerospace Conference*, vol. 3, pp. 1125–1130, IEEE, Big Sky, Mont, USA, March 2002.
- [13] M. Hempel, H. Sharif, and P. Raviraj, "HEAR-SN: A new hierarchical energy-aware routing protocol for sensor networks," in *Proceedings of the 38th Annual Hawaii International Conference on System Sciences*, p. 324, IEEE, January 2005.
- [14] W. Heinzelman, A. Sinha, A. Wang, and A. Chandrakasan, "Energy-scalable algorithms and protocols for wireless microsensor networks," in *Proceedings of the 2000 International Conference on Acoustics, Speech and Signal Processing*, pp. 3722–3725, IEEE, Istanbul, Turkey, 2000.
- [15] A. Dwivedi, S. Kushwaha, and O. Vyas, "Performance of Routing Protocols for Mobile Adhoc and wireless sensor networks: A Comparative study," *International Journal of Recent Trends in Engineering*, vol. 2, no. 4, p. 101, 2009.
- [16] M. V. Kumaramangalam, K. Adiyapatham, and C. Kandasamy, "Zone-based routing protocol for wireless sensor networks," *International Scholarly Research Notices*, vol. 2014, Article ID 798934, 9 pages, 2014.
- [17] N. Al-Humidi and G. V. Chowdhary, "Energy-aware approach for routing protocol by using centralized control clustering algorithm in wireless sensor networks," in *Computing, Communication and Signal Processing*, vol. 810 of *Advances in Intelligent Systems and Computing*, pp. 261–274, Springer, Singapore, 2019.
- [18] P. Lalwani, H. Banka, and C. Kumar, "BERA: a biogeography-based energy saving routing architecture for wireless sensor networks," *Soft Computing*, vol. 22, no. 5, pp. 1651–1667, 2018.
- [19] V. Junapudi and S. K. Udgata, "Extended lifetime and reliable data transmission in wireless sensor networks with multiple sinks," in *Smart Intelligent Computing and Applications*, vol. 105 of *Smart Innovation, Systems and Technologies*, pp. 91–100, Springer, Singapore, 2019.
- [20] I. A. Umar, Z. M. Hanapi, A. Sali, and Z. A. Zulkarnain, "Towards overhead mitigation in state-free geographic forwarding protocols for wireless sensor networks," *Wireless Networks*, pp. 1–14, 2018.